


This item was submitted to Loughborough University as a PhD thesis by the author and is made available in the Institutional Repository (<https://dspace.lboro.ac.uk/>) under the following Creative Commons Licence conditions.




creative commons
COMMONS DEED


Attribution-NonCommercial-NoDerivs 2.5


You are free:

- to copy, distribute, display, and perform the work

Under the following conditions:

 **Attribution.** You must attribute the work in the manner specified by the author or licensor.


 **Noncommercial.** You may not use this work for commercial purposes.

 **No Derivative Works.** You may not alter, transform, or build upon this work.

- For any reuse or distribution, you must make clear to others the license terms of this work.
- Any of these conditions can be waived if you get permission from the copyright holder.

Your fair use and other rights are in no way affected by the above.

This is a human-readable summary of the [Legal Code \(the full license\)](#).

[Disclaimer](#) 

For the full text of this licence, please go to:
<http://creativecommons.org/licenses/by-nc-nd/2.5/>

Analysis and Optimal design of Micro-energy harvesting systems for wireless sensor nodes

by

Xin Lu

A Doctoral Thesis

Submitted in partial fulfilment of the requirements

for the award of

Doctor of Philosophy

Of

Loughborough University

September 2012

© by Xin Lu (2012)



CERTIFICATE OF ORIGINALITY

This is to certify that I am responsible for the work submitted in this thesis, that the original work is my own except as specified in acknowledgments or in footnotes, and that neither the thesis nor the original work contained therein has been submitted to this or any other institution for a degree.

..... (Signed)

..... (Date)

ACKNOWLEDGEMENTS

It has been a great pleasure working with the faculty, staff, and students at Loughborough University, during my tenure as a doctoral student. The completion of this thesis would not have been possible without the support, inspiration and encouragement of the following people. The following acknowledgements go a small way to expressing my thanks.

First and foremost, I owe a great debt of gratitude to my supervisor, Professor Shuang-Hua Yang, for his continued encouragement, guidance, inspiration and support. With his advice I was able to focus on the motivation of the research and achieve my goals.

I greatly appreciate and wish to thank all the staff at the Computer Science Department for their assistance during these years, especially Mr Kip Sahnsi, Ms Christine Bagley, and Ms Judith Poulton.

I would like to thank all my colleagues in NCCS groups for providing a stimulating and fun environment in which to complete my PhD. Special thanks go to Ran Xu, Wei Wei He, Kai Cao, Dr Huan-Jia Yang, Dr Yuan-Qing Qin, Dr Yun-Qiu Li, Dr Yan-Ning Yang, Zaid Bin Ahmad, Dr Hesham Abusaimh, Dr Tareq Alhmeida and Dr Khusvinder Gill. I am especially grateful to Dr Fang Yao, who was patiently teaching me the Jennic software design. This is really helpful to my work.

Finally, I would like to thank my family, especially my wife FengYan Wang. It is especially true that during my PhD, without their encouragement and love the PHD would not have been possible.

ABSTRACT

Presently, wireless sensor nodes are widely used and the lifetime of the system is becoming the biggest problem with using this technology. As more and more low power products have been used in WSN, energy harvesting technologies, based on their own characteristics, attract more and more attention in this area. But in order to design high energy efficiency, low cost and nearly perpetual lifetime micro energy harvesting system is still challenging.

This thesis proposes a new way, by applying three factors of the system, which are the energy generation, the energy consumption and the power management strategy, into a theoretical model, to optimally design a highly efficient micro energy harvesting system in a real environment. In order to achieve this goal, three aspects of contributions, which are theoretically analysis an energy harvesting system, practically enhancing the system efficiency, and real system implementation, have been made. For the theoretically analysis, the generic architecture and the system design procedure have been proposed to guide system design. Based on the proposed system architecture, the theoretical analytical models of solar and thermal energy harvesting systems have been developed to evaluate the performance of the system before it being designed and implemented. Based on the model's findings, two approaches (MPPT based power conversion circuit and the power management subsystem) have been considered to practically increase the system efficiency. As this research has been funded by the two public projects, two energy harvesting systems (solar and thermal) powered wireless sensor nodes have been developed and implemented in the real environments based on the proposed work, although other energy sources are given passing treatment. The experimental results show that the two systems have been efficiently designed with the optimization of the system parameters by using the simulation model. The further experimental results, tested in the real environments, show that both systems can have nearly perpetual lifetime with high energy efficiency.

Keywords: WSN, energy harvesting, solar energy harvesting, thermal energy harvesting, maximum power point tracking (MPPT), power management

PUBLICATIONS

X. Lu and S.H. Yang, “Solar Energy harvesting for ZigBee Electronics,” Sustainability in Energy and building, pp. 19-27, 2009.

X. Lu and S.H. Yang, “Thermal energy harvesting for WSNs”, 2010 IEEE International Conference on Systems Man and Cybernetics (SMC), pp. 3045-3052, 2010.

Gill, K., Yang, S., Yao, F., and Lu, X., “A Zigbee-Based Home Automation System”, The Journal of IEEE transactions on Consumer Electronics, Vol. 55, No.2, pp.422 -430, 2009

Abbreviations

WSNs	Wireless Sensor Networks
PCB	Printed Circuit Board
RF	Radio Frequency
TEGs	Thermoelectric Generators
MEMS	Micro-Electro-Mechanical Systems
MPPT	Maximum Power Point Tracking
DCM	Discontinuous Conduction Mode
CCM	Continuous Conduction Mode
SoC	State of Charge
DoD	Depth of Discharge
ADC	Analog Digital Converter
IC	Integrated Circuit
MCU	Micro Control Unit
DTCM	Design Time Component Matching
FOC	Fractional Open Circuit Voltage
FSC	Fractional Short Circuit Current
P&O	Perturb and Observe
PV	Photovoltaic
ESR	Equivalent Series Resistance
RMS	Root Mean Square

OCV	Open Circuit Voltage
-----	----------------------

TABLE OF CONTENTS

Chapter 1. Introduction	1
1.1 Background to the research.....	1
1.2 Energy harvesting technologies	5
1.3 Research challenges	7
1.4 Motivation for the research.....	8
1.5 Research objectives.....	9
1.6 Contributions of the research	10
1.7 Organization of the thesis	13
Chapter 2. Literature Review of Environment Powered Wireless Sensor Nodes	14
2.1 Micro-energy harvesting system overview	14
2.2 Energy harvesting architecture	14
2.3 Review of the existing solar energy harvesting systems	17
2.3.1 Typical solar energy harvesting systems	19
2.3.2 Comparison of the existing solar energy harvesting platforms	24
2.4 Thermal energy harvesting	25
2.4.1 Typical thermal energy harvesting systems	28
2.4.2 Comparison of the existing thermal energy harvesting platforms	31
2.5 Summary	33
Chapter 3. Micro Energy Harvesting System Architecture Design	35
3.1 Background and motivation.....	35
3.2 Features of the proposed System	36

3.3 A generic architecture of energy harvesting system	36
3.4 A design guideline of a micro energy harvesting system	43
3.5 Summary	46
Chapter 4. Energy Harvesting Transducer Modeling	48
4.1 Background and motivation	48
4.2 Solar panel modelling	48
4.3 Thermoelectric generator modelling	52
4.3.1 Constructing a TEG model	53
4.3.2 Model validation	69
4.4 Summary	77
Chapter 5. Modeling micro-energy harvesting systems	79
5.1 Background and motivation	79
5.2 Overview of micro energy harvesting system model	80
5.3 Model of a power conversion circuit	82
5.3.1 Model of the MPPT unit	84
5.3.2 Model of the DC-DC boost converter	85
5.3.3 Model of the entire power conversion subsystem	94
5.4 The model of the energy storage subsystem	95
5.4.1 Model of the super-capacitor	97
5.4.2 Model of the rechargeable battery	106
5.5 The model of the energy consumer	116
5.6 Model of the entire energy harvesting system	117
5.7 Theoretical analysis of an energy harvesting system	125
5.7.1 The lifetime prediction	125
5.7.2 Daily energy conversion efficiency	127

5.8 Model Validation	129
5.8.1 Set up the test environments	129
5.8.2 Evaluate the energy transfer efficiency.....	129
5.8.3 Evaluate the model of the energy storage subsystem	136
5.8.4 Evaluate the entire energy harvesting system model.....	138
5.9 Summary.....	141
Chapter 6. Design and implementation of a power conversion circuit based on MPPT technologies	143
6.1 Background and motivation.....	143
6.2 Feature of proposed work	144
6.3 Proposed MPPT based Power conversion subsystems	144
6.3.1 Regulator circuit design	145
6.3.2 Maximum power point tracking unit	150
6.4 System evaluation	167
6.4.1 Power overhead.....	167
6.4.2 Tracking efficiency	168
6.5 Summary	173
Chapter 7. Design and implementation of a power management system for an energy harvesting system.....	175
7.1 Background and motivation.....	175
7.2 Feature of proposed strategy	178
7.3 Proposed power management system	178
7.3.1 Energy distribution unit	179
7.3.2 Power management algorithm design	183
7.4 System evaluation	195

7.5 Conclusion	200
Chapter 8. Design a wireless Sensor node	202
8.1 Wireless sensor platforms	202
8.2 Data processing subsystem	203
8.3 Sensing subsystem	207
8.3.1 Temperature sensor selection.....	209
8.3.2 CO gas sensor selection	211
8.4 Power supply subsystem	212
8.5 Lifetime calculation	214
8.6 Summary	217
Chapter 9. Solar energy harvesting for wireless sensor nodes	218
9.1 Background and motivation	218
9.2 Feature of the established system	218
9.3 System design considerations	218
9.3.1 Energy storage vs. Energy generation	219
9.4 System design and implementation	229
9.4.1 Energy harvester	230
9.4.2 MPPT based power conversion subsystem.....	230
9.4.3 Power management subsystem	231
9.4.4 Energy consumer	232
9.5 System Evaluation	232
9.6 Summary	237
Chapter 10. Thermal energy harvesting for Wireless sensor nodes.....	238
10.1 Background and motivations	238

10.2 Feature of the proposed system.....	238
10.3 System design considerations	239
10.3.1 Energy consumption of the target sensor node	240
10.3.2 Characteristics of energy source	245
10.3.3 Energy generation characteristics	245
10.3.4 Energy and energy generation	247
10.4 System design and implementation	249
10.4.1 Thermal energy harvesting subsystem.....	250
10.4.2 MPPT based Power conversion subsystem.....	255
10.4.3 Power management subsystem	257
10.4.4 Integrated thermal energy harvesting system	261
10.5 Evaluation	262
10.5.1 Individual component evaluation.....	262
10.5.2 Integrated system evaluation.....	268
10.6 Summary	270
Chapter 11. Conclusion and Future work.....	271
11.1 Summary	271
11.2 Contributions and future work	272
References	278

List of Figures

Figure 1.1 Structure of a typical wireless sensor network (Akyildiz et al., 2002).....	2
Figure 1.2 Ragone plot for comparing the energy storage technologies and their power density versus energy density characteristics (Tester, 2005).....	4
Figure 1.3 Energy harvesting source and their Energy Harvesters (Wan et al., 2010)...	5
Figure 2.1 Energy harvesting system architectures with and without a storage capability (Sudevalayam et, al., 2010).....	15
Figure 2.2 General block diagram representation of energy harvesting system unit (Wan et al. 2010).....	16
Figure 2.3 A general model for micro-solar power system (Jenong, 2009)	17
Figure 2.4 (a) System architecture of Prometheus implementation, (b) Prometheus platform (Jiang et al., 2005).....	20
Figure 2.5 (a) System architecture of Helimote, (b) Helimote platform (Raghunathan et al., 2005)	21
Figure 2.6 (a) System architecture of Everlast, (b) Everlast platform (Simjee and Chou 2006)	21
Figure 2.7 (a) System architecture of Ambimax, (b) Ambimax platform (Park and Chou 2006).....	22
Figure 2.8 (a) System architecture of HydroWatch, (b) HydroWatch platform (Taneja et al., 2008)	23
Figure 2.9 (a) System architecture of Sunflower, (b) Hardware of Sunflower (Stanley-Marbell and Marculescu, 2007)	24
Figure 2.10 Thermo-electrical wristwatch of SEIKO (Kishi et al., 1999).....	28
Figure 2.11 (a) Power conditioning circuit of the TEG (b) Thermal powered wireless sensor node (Lenovo et al. 2007)	29

Figure 2.12 Ground source TEG (Lawrence and Snyder, 2002)	29
Figure 2.13 solar-thermal energy harvesting system (Sodano et al., 2007).....	30
Figure 2.14 (a) system overview of the thermal energy harvesting system, (b) proposed platform (Mateu et al., 2006)	30
Figure 2.15 (a) TEG generator (b) Proposed circuit design with MPPT (Eakburanawat and Noonyaroonate, 2005).....	31
Figure 3.1 Block diagram of energy flow and four energy efficiencies of an energy harvesting system.....	37
Figure 3.2 Block diagram of a micro-Energy harvesting system powered wireless sensor node.....	40
Figure 3.3 Block diagram of a micro-Energy harvesting system powered wireless sensor node.....	43
Figure 3.4 Components of an energy harvesting system	48
Figure 4.1 The equivalent circuit of the one diode model	50
Figure 4.2 (a) I-V characteristic and (b) P-V characteristic of the solar cell.....	52
Figure 4.3 A TEG system	54
Figure 4.4 Typical diagram of a TE module.....	55
Figure 4.5 Scheme of the thermal-electric analogy of the TEG model	58
Figure 4.6 Electrical part of the TE module	59
Figure 4.7 Circuit analysis of the hot side heat exchanger	63
Figure 4.8 Analysis circuit of a heat sink	63
Figure 4.9 (a) Junction with no thermal interface and (b) Junction with thermal interface.....	65

Figure 4.10 Equivalent thermal resistance circuit for two plates with thermal interface material	66
Figure 4.11 The Equivalent circuits of TEGs	67
Figure 4.12 Test prototype of thermal energy harvesting	70
Figure 4.13 Power generated for different ΔT	72
Figure 4.14 (a) Power generated with different Seebeck coefficient (b) Power generated with different internal electric resistances (c) Power generated with different internal thermal resistances (d) power generated with different external thermal resistance of the module.....	74
Figure 4.15 (a) Power generated with different hot side heat exchangers (b) Power generated with different heat sinks (c) Power generated with different ambient air (d) power generated with different contact resistance	76
Figure 4.16 (a) power output with different load resistor (b) maximum power point at different ΔT	77
Figure 5.1 Energy flow of a micro-energy harvesting system	82
Figure 5.2 General Architecture of power conversion circuit	84
Figure 5.3 Simple asynchronous DC/DC boost converter structure	85
Figure 5.4 Synchronous boost converter	86
Figure 5.5 boost converter equivalent circuit including the parasitic components.....	88
Figure 5.6 Output current vs. Efficiency (2.4V and 1.2V input voltage)	93
Figure 5.7 Different input voltages vs. energy transfer efficiency	94
Figure 5.8 Functional diagram of the hybrid combination of energy storage system ..	97
Figure 5.9 Proposed electrical equivalent circuit of super-capacitor.....	98
Figure 5.10 Self-discharging effect of 22F 2.5V super-capacitor.....	104

Figure 5.11 (a) 2.5v constant charging voltage (b) 10mA and 5mA constant charging current	105
Figure 5.12 (a) constant discharge voltages (b) constant discharging current.....	106
Figure 5.13 Electrical battery model (Chen and Rincon-Mora, 2006)	110
Figure 5.14 The relationship of SoC and OCV of NiMH battery (Windarko et al., 2009)	114
Figure 5.15 Battery's Open-circuit voltage with different discharging currents and charging currents.....	116
Figure 5.16 Power transfer in micro-energy harvesting system	118
Figure 5.18 Schematic diagram of MPPT circuit	131
Figure 5.19 schematic diagram of the Power storage subsystem	137
Figure 5.20 The super-capacitors voltages with solar and thermal energy harvesting system	140
Figure 6.1 Block diagram of micro energy harvesting system	145
Figure 6.2 Schematic diagram of the boost converter TPS61222	148
Figure 6.3 Efficiency vs. Input voltage of TPS61222	150
Figure 6.4 Conceptual diagram of the sensor driven MPPT for solar energy harvesting	156
Figure 6.5 The complete Sensor-driven MPPT circuit	157
Figure 6.6 A schematic drawing of the implementation of MPPTs	158
Figure 6.7 Sign of the dP/dV at different position on the power characteristic of a P-V curve.....	159
Figure 6.8 The flowchart of the P&O MPPT method.....	1560
Figure 6.9 Schematic diagram of the lossless current sensor	162

Figure 6.10 The complete MCU based MPPT circuit	163
Figure 6.11 Measurement of the power between two MPPT sampling instance (Sera et al., 2006)	166
Figure 6.12 The flowchart of the enhanced P&O method	167
Figure 6.13 Overall tracking efficiency of the proposed power conversion system	173
Figure 7.1 Generic architecture of power management system.....	179
Figure 7.2 Hardware design for power management subsystem	182
Figure 7.3 System architecture of power management subsystem	188
Figure 7.4 Schematic diagram of the simple solar powered wireless sensor node.....	196
Figure 7.5 Testing results of Power management algorithm	198
Figure 7.6 Experimental results of three different power management.....	200
Figure 8.1 A generic Wireless Sensor node architecture	203
Figure 8.2 JN5139 Module and the block diagram (Jennic 5139, 2009).....	205
Figure 8.3 DS18B20 circuit	211
Figure 8.4 CO gas sensor circuit.....	212
Figure 8.5 Schematic diagram of the Temperature & Co gas sensor	214
Figure 8.6 PCB view of the temperature & CO gas sensor	214
Figure 9.1 Energy flow diagram of solar energy harvesting system	219
Figure 10.1 ZBARV sensor node.....	240
Figure 10.2 Average monthly temperature for Loughborough, UK.....	243
Figure 10.3 A scenario diagram of TE generator	249
Figure 10.4 Function diagram of a Thermal Energy Harvesting System	250

Figure 10.5 Thermal Energy Harvesting Subsystem	252
Figure 10.6 The comparison result of three Heat sinks	252
Figure 10.7 Temperature distribution of the radiator.....	254
Figure 10.8 Hot Side heat exchanger with sponges.....	255
Figure 10.9 Schematic diagram of MPPT based DC-DC converter subsystem	257
Figure 10.10 Schematic diagram of the proposed system	262
Figure 10.11 Experimental setup for thermal energy harvesting system.....	263
Figure 10.12 Output voltage of the TE generator as a function of the hot side temperatures	264
Figure 10.13 The experimental result of the power management system	268
Figure 10.14 Integrated thermal energy powered ZBARV	269
Figure 10.15 The thermal energy harvesting system with ZigBee Based Automatic Radiator.....	269
Figure 10.16 The proposed system test in a real house for 7 days	270

List of Tables

Table 1.1 Energy harvesting opportunities and demonstrated capabilities (Paradiso and Starner, 2005).....	6
Table 2.1 Confirmed terrestrial cell and sub module efficiencies measured under the global AM1.5 Spectrum (Green et. al. 2010).....	18
Table 2.2 Specifications of solar energy harvesting platforms.....	25
Table 2.3 Characteristics of TE power generators (Hudak and Amatucci, 2008).	27
Table 2.4 Specificaitons of thermal energy harvesting platforms.	327
Table 3.1 Proposed dual buffer design vs. single buffer designs.....	42
Table 4.1 Experimental parameters of the AM-5412 solar cell.....	51
Table 5.1 Main technique parameters for TPS61222 and external components	92
Table 5.2 Different types of energy storage elements for micro-energy harvesting system (Taneja et al., 2008)	95
Table 5.3 Specifications of Panasonic Super-capacitor (Panasonic 22F super-capacitor, 2008)	103
Table 5.4 The relationship between the experience OCV and SOC of NiMH battery (Windarko et al., 2009)	113
Table 5.5 NiMH battery parameters	115
Table 5.6 DC current consumption of the DR1048	117
Table 5.7 Charging the super-capacitors with different light irradiances.....	133
Table 5.8 The comparison results of MPP vs. other two working points.....	134
Table 5.9 Charging the super-capacitors with different temperature differences.....	135
Table 5.10 The comparison results of MPP vs. other two working points of TEG....	136

Table 5.11 Charging time of the super-capacitors	138
Table 5.12 Charging the super-capacitors with solar energy harvesting system and TEG.....	138
Table 6.1 Some design specifications of the boost converter	148
Table 6.2 operating voltage of the pilot cell and open circuit voltage of the solar cell under the same light intensity	156
Table 6.3 Power consumption of three proposed MPPT based circuit.....	168
Table 6.4 Comparison of the MPP tracking speed for different MPPT based power conversion systems	169
Table 6.5 Comparison of the MPP tracking efficiency for different MPPT based power conversion system at the constant light condition	171
Table 6.6 Comparison of the MPP tracking efficiency for different MPPT based power conversion system at the slow changing light condition	172
Table 6.7 Comparison of the MPP tracking efficiency for different MPPT based power conversion system at the rapid changing light condition.....	172
Table 7.1 Control and charge DRIVER.....	183
Table 7.2 Specification of the sensor node	189
Table 7.3 Power management algorithm pseudo code	194
Table 7.4 The parameters for the power management algorithm	197
Table 7.5 The parameters of the solar power management algorithm.....	199
Table 7.6 Performance comparison of the power management algorithms.....	200
Table 8.1 ZigBee Chips Comparison.....	204
Table 8.2 Power consumption for the JN5139 microcontroller at different power mode (JN5139, 2009).....	206

Table 8.3 Different power level settings for 2.4GHz transceiver	207
Table 8.4 Temperature sensors	210
Table 8.5 Specification of the door security sensor node	214
Table 8.6 wireless sensor node designs	215
Table 9.1 DC current consumptions of the components of the sensor node.....	221
Table 9.2 Specification of the door security sensor node	221
Table 9.3 The energy consumed by the sensor node during each month of the year .	222
Table 9.4 Average monthly solar radiation for Loughborough, UK	224
Table 9.5 The harvested energy and the available energy of the system in a certain month by using a single solar panel	225
Table 9.6 The comparison results of energy consumption and energy generation through a year by using a single solar panel	226
Table 9.7 The comparison results by using two solar panels	228
Table 10.1 DC current consumption of the ZBARV sensor node	241
Table 10.2 General system specification of ZBARV sensor node	241
Table 10.3 The energy consumed by the ZBARV sensor node during each month...	244
Table 10.4 The harvested energy and the available energy of the system in a certain month by using 8 pieces of the TE modules.	247
Table 10.5 The energy consumed by the ZBARV sensor node during each month...	248
Table 10.6 Physical properties of the TE module.....	251
Table 10.7 Five different configurations of the TE generator (radiator temperature 323K and air temperature 294K)	253

List of Symbols

Symbols	Meanings
I_{ph}	Photocurrent
I_0	Dark saturation current
I_{sh}	Shunt current
R_{sh}	Shunt Resistor
R_s	Series resistance
$V_{s,oc}$	Open circuit voltage of a solar cell
$I_{s,sc}$	Short circuit current of a solar cell
$V_{s,MPP}$	Voltage of a solar cell when it operates at maximum power point
$I_{s,MPP}$	Current of a solar cell when it operates at maximum power point
$P_{s,MPP}$	Power of a solar cell when it operates at maximum power point
$\sigma_{s,V}$ $\sigma_{s,I}$	Coefficients of the linear relationship between $I_{s,MPP}$ and $I_{s,sc}$, $V_{s,MPP}$ and $V_{s,oc}$
$\alpha_{seebeck}$	Seebeck coefficient
$V_{seebeck}$	Generated Seebeck Voltage
τ	Thomson coefficient
$Q_{Thomson}$	Thomson heat
Q_P	Peltier effect
ΔT_g	Temperature difference between the TE
Π	Peltier coefficient
Q_j	Joule heating

ΔT	Temperature difference
K	Thermal resistance
K_j	Joint thermal resistance
$K_{contact}$	Thermal contact resistance
K_{sink}	Thermal resistance of heat sink
$K_{ambient}$	Thermal resistance of ambient
k	Thermal conductivity
Q_F	Fourier conduction
C_{Heat}	Heat capacities
ρ	Density of material
c_p	Specific heat capacity
σ	Stefan-Boltzmann constant (5.67×10^{-8} watt/m ² K ⁴)
ε	Emissivity of the object (0.2-0.31 for aluminium plate at 300K)
m	Asperity slope
k_g	Thermal conductivity of the air (0.024W/mK)
M	Gas parameter
Y	Plane separation
$R_{internal}$	Internal electrical resistance of a TE module
R_n R_p	Electrical resistance of N-type and P-type thermoelectrically material
R_{Cu}	Electrical resistance of Cu
$R_{contact}$	Contact resistance of the TE couple
ρ_c	Specific contact resistance ($1.5 \cdot 10^{-6}$ ohmcm ²)

A_c	Area of the electrical contact of pellets
$Q_{P-hotside}$	The heat generated by Peltier effect at hot side the TE module
$Q_{P-coldside}$	The heat generated by Peltier effect at cold side the TE module
$K_{T,res}$	Total thermal resistance of TE couple
k_n k_p	The thermal conductivity of the N-type and P-type materials
K_{cond}	Total thermal resistance of the TE module without considering the thermal resistance of the TE legs
K_1	Thermal resistance of the ceramic plate
K_2	Thermal resistance of the Cu conductor
K_3	Thermal resistance of the solder
$K_{heatsink}$	Overall thermal resistance of the heat sink
K_{sink}	Thermal resistance of heat sink
$K_{contact}$	Thermal contact resistance
$K_{ambient}$	Thermal resistance of ambient
k_1	Thermal conductivity of the aluminium plate (34.5(W/m°C))
h_{sink}	Thickness of the heat sink
k_{sink}	Thermal conductivity of the heat sink
A_{sink}	Effective surface area of the heat sink
h_c	Convection heat transfer coefficient
$K_{convection}$	Thermal resistance of convection
$K_{radiation}$	Heat body radiation
$h_{radiation}$	Radiated heat transfer coefficient

T_{sink}	Hot body absolute temperature (K) of the heat sink
K_j	Joint thermal resistance
K_b	Thermal resistance of thermal interface material
K_{c1} K_{c2}	Thermal contact resistances of two contact surfaces
K_g	Thermal conductivity of air (0.024W/mK)
ΔT_{total}	Total temperature difference between a TEG system
$P_{\text{transducer}}$	Power extracted from the energy generator
$\eta_{\text{converter}}$	Transfer efficiency of the boost circuit
$P_{\text{harvested}}$	Power harvested by the energy generator
η_{MPPT}	MPPT efficiency of the MPPT circuit
$P_{\text{consume,MPPT}}$	Power dissipation of the MPPT circuit
$V_{\text{consume,MPPT}}$	Voltage crossed the MPPT circuit
$I_{\text{consumer,MPPT}}$	Current consumed by the MPPT circuit
$P_{\text{controller,IC}}$	Power consumed by the boost IC
$V_{\text{controller, IC}}$	Voltage across the boost converter control IC
$I_{\text{controller,IC}}$	Quiescent current of the boost converter control IC
P_{inductor}	Power lost in Inductor of the boost converter
$P_{\text{capacitor}}$	Power lost in output capacitor of the boost converter
$P_{\text{MOSFET},1}$	Power lost in N-MOSFET transistor if the boost converter
$P_{\text{MOSFET},2}$	Power lost in P-MOSFET transistor of the boost converter
f_s	Switching frequency of the boost converter

M	Ratio of the boost converter
D	Duty cycle of the boost converter
T_{on} T_{off}	Duration of the “on” state and “off” state of the boost converter
R_L	Equivalent Series Resistance (ESR) of the inductor
$I_{L,rms}$	Root Mean Square (RMS) current of the inductor
$I_{L,rms}$	Root Mean Square (RMS) current of the inductor
I_{out}	Output current of the boost converter
ΔI_L	Ripple of the inductor current
L	Inductance of the inductor
P_Q	Conduction loss of a N-MOSFET
R_Q	Turn-on resistance of a N-MOSFET
$P_{M,SW}$	Switching loss of a N-MOSFET
$I_{M,RMS}$	RMS current of switching the transistor
t_{rv}	Rise and fall times of drain-source voltage
t_f	Rise and fall times of drain current
$V_{ce(sat)}$	“on” state voltage of a N-MOSFET
V_F	Forward voltage drop in the body diode of a MOSFET
R_{Q2}	on-time drain-to-source resistance of the P-MOSFET
$I_{RMS,Q2}$	RMS current of the P-MOSFET
R_C	ESR of a capacitor
$P_{charging}$	Output power of the power conversion circuit

$V_{W,th1}$	Four voltage thresholds for indicating the state of the super-capacitor
$V_{W,th2}$	
$V_{W,th3}$	
$V_{W,th4}$	
$V_{SC}(t)$	Terminal voltage of the Super-capacitor
$Q_{SC}(t)$	Electrical charges of the super-capacitor
c_{SC}	Capacitance of the super-capacitor.
$Q_{sc}(0)$	Initial charges on the capacitor before charging/discharging
$I_{SC,C}(t)$	Electrical current charging the super-capacitor
$\eta_{capacitor}$	Charge and discharge efficiency of a super-capacitor
$I_{sc,leak}(t)$	Leakage current of the super-capacitor
$I_{c,out}(t)$	Output current of the boost converter
$I_{sc,dis}(t)$	Discharging current of the super-capacitor
$I_{charging}(t)$	Current consumed by the whole energy harvesting system at the time t
$V_{sc}(0)$	Initial voltage of the super-capacitor
$V_{charging,sc}$	Charging voltage of the super-capacitor
S	Notation of Laplace transfer
t_c	Charging time period
t_{dis}	Discharging time period
$R_{SC,self}(t)$	Self-discharge resistance of the super-capacitor
$\Delta V_{sc(self)}$	Super-capacitor's voltage decreased by self-discharging during a time duration Δt
$C_{R-battery}$	Full capacity of a battery

$C_{capacity}$	Nominal capacity of the battery
$f_1(Cycles)$	Cycle number dependent correction factor of a battery
$f_2(Temp)$	Temperature dependent correction factor of a battery
n_{cycles}	Current battery cycles
$R_{Self-Discharge}$	Self-discharging resistance of the battery
$\eta_{c,battery}$	Charging efficiency of the battery
$\eta_{dis,battery}$	Discharging efficiency of the battery
$Q_{B,charging}$	Total energy charged to the battery
$Q_{B,discharging}$	Total energy discharged from battery
$\Delta Q_{Battery}$	Energy used to charge the battery
$\Delta Q_{Battery2}$	Energy consumed by the battery system
SoC(t)	SoC level of the battery
$T_{b,life}$	Lifetime of the rechargeable battery
$V_{B,OC}$	Open circuit voltage of a battery
I_{Batt}	Battery output current
V_{Batt}	Battery voltage
$P_{sensor}(average)$	Average power consumption of the target sensor node
$C_{battery}(t_{initial})$	Initial battery level
$V_{sc}(t_{initial})$	Initial super-capacitor level
$P_{T,consum}$	Total power consumed by the energy harvesting system
$E_{useful}(\Delta t1)$	Useful energy of the energy harvesting system during $\Delta t1$
$C_{B,lost}(\Delta t1)$	Capacity lost in the rechargeable battery in Δt

$E_{useful}(\Delta t1)$	Useful energy of the energy harvesting system during $\Delta t1$
$E_{super}(\Delta t1)$	Energy being stored on the super-capacitor during $\Delta t1$
$C_{B,lost}(\Delta t1)$	Capacity lost in the rechargeable battery in $\Delta t1$
$E_{Battery}(\Delta t1)$	Energy extracted from the battery during $\Delta t1$
$I_{sc}(\Delta t2)$	Charging current of the super-capacitor during $\Delta t2$
$E_{useful}(\Delta t2)$	Useful energy from the energy harvester during $\Delta t2$
$E_{consumed}(\Delta t2)$	Energy being consumed by the system during $\Delta t2$
$E_{super}(\Delta t2)$	Energy being stored in the super-capacitor during $\Delta t2$
$E_{useful}(\Delta t3)$	Useful energy of the energy harvesting system during $\Delta t3$
$E_{consumed}(\Delta t3)$	Energy dissipation of the system during $\Delta t3$
$E_{super}(\Delta t3)$	Energy lost in the super-capacitor during $\Delta t3$
$E_{useful}(\Delta t4)$	Useful energy of the energy harvesting system during $\Delta t4$
$E_{consumed}(\Delta t4)$	Energy dissipated by the system during $\Delta t4$
$E_{super}(\Delta t4)$	Energy lost in the super-capacitor during $\Delta t4$
$E_{useful}(\Delta t5)$	Useful energy of the energy harvesting system during $\Delta t5$
$E_{consumed}(\Delta t5)$	Energy dissipated by the system during $\Delta t5$
$E_{super}(\Delta t5)$	Energy lost in the super-capacitor during $\Delta t5$
$V_{vdd}(t)$	Supply voltage of the energy harvesting system
$T_{lifetime}$	Lifetime of the system
$\eta_{system}(daily)$	Daily energy conversion efficiency
η_{ECE}	Energy conversion efficiency of the energy harvesting system
$L_{(crit)}$	Critical inductor value of a boost converter

D_{max}	Maximum duty cycle of the boost converter
$V_{out,boost}$	Output voltage of the boost converter
$I_{out(max)}$	Maximum output current of the boost converter
f_s	Minimum switching frequency of the converter
C_{out}	Capacitance of the output capacitor used in the boost converter
L	Inductance of the inductor used in the boost converter
V_{pilot}	Output voltage of the pilot cell
$V_{solarcell}$	Output voltage of the solar cell
$K_{solarcell}$	Coefficients between the open circuit voltage and MPP voltages of the solar panel
K_{pilot}	Coefficients between the open circuit voltage and MPP voltages of the miniaturized PV module
R_{esr}	Parasitic resistance of the inductor
V_H V_L	Average voltage produced by the first-order RC low pass filters
R_{esr}	Parasitic resistance of the inductor
V_H V_L	Average voltage produced by the first-order RC low pass filters
$P_{ET}(t)$	Power harvested from the environment at time t by the energy harvester
$E_{leak,b}$	Energy leakage of the rechargeable battery
P_{active}	Power consumption of the sensor node in active mode
P_{sleep}	Power consumption of the sensor node in sleep mode
D_{node}	Duty cycle of the sensor node in active mode

Chapter 1. Introduction

1.1 Background to the research

Since there have been rapid advances in Micro-Electro-Mechanical Systems (MEMS) technology, nanoscale integration, and low energy consumption wireless communication technologies, this has resulted in a new class of miniaturized wireless electronic system which is extremely useful for facilitating monitoring and controlling of physical environments from remote locations. To date, because Wireless Sensor Networks (WSNs), whose individual devices have limited computation, sensing, communication, and energy, based on 802.15.4 wireless standard, represent a significant improvement over wired sensor networks with the elimination of the hard-wired communication cables, are associated easy installation and low maintenance costs, numerous research studies and applications in this area have emerged. Furthermore, the trends in these modern technologies allow the complex sensor systems to decrease in size, power consumption and deployment. Due to these advantages, more and more large scales of such networks are being considered to carry out complex task sets without human intervention in the real world.

The architecture of a WSN typically consists of multiple pervasive sensor node, sink, public networks, manager nodes and end users (Madden et al., 2002). Numerous tiny, smart and inexpensive sensor nodes are scattered in the targeted sensor field to cooperate with each other via a wireless connection to form an ad-hoc network and to collect and analyse data collected from the physical environment. Due to the ad-hoc network, the networks can use multi-hop networking protocols to ensure full connectivity, fault tolerance and long operational life. A typical WSN, which includes sensor nodes, sink node, a connection to the Internet or satellite and a task manager node, is depicted in Figure1.1. Initially, the data collected by sensor nodes is routed within the sensor field by other nodes through wireless communication. When the data reaches the boundary of the sensor field, it is then transferred to the sink node, which

can be treated like a gateway. Typically, the gateway node is powered by a main power source because it has a higher processing capacity and sufficient memory space to supply extra information processing before the data is transferred to the task manager node through the Internet or satellite, and then the end user can process the receiving data when it becomes available (Akyildiz et al., 2002).

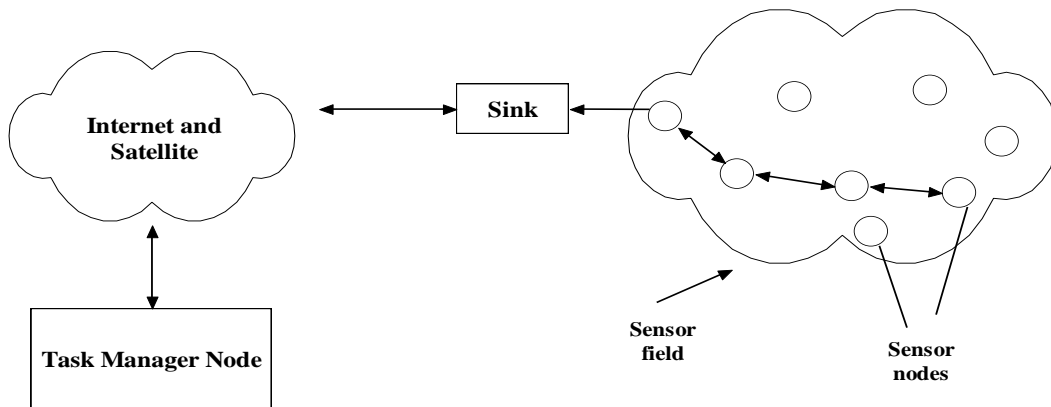


Figure 1.1 Structure of a typical wireless sensor network (Akyildiz et al., 2002)

To date, some very low power wireless sensor productions, which are regarded as stable, inexpensive and computationally efficient, have entered the marketplace. They normally consist of a miniaturized microcontroller, a wireless transceiver, one or several sensors, and one or several power sources. Typically, batteries are considered as the dominant energy source for these wireless applications. However, the disadvantage of using batteries to power the systems is that they need to either replace or recharge them periodically. Despite the stringent constraints on size, WSNs are usually required to operate for several months or years without any human intervention. This makes the frequent battery replacement either unfeasible or prohibitive in these applications. Hence, the mobility and stability of WSNs are restricted by the use of batteries. Since the trend of sensor nodes' design is to make the sensor node as small as possible in order to be conveniently placed and used, size has become one of the most important factors in WSNs. Batteries normally represent a primary percentage of the volume and weight of portable products. On the other hand, as batteries dominate the majority of volume of the sensor nodes, the small volume trend of the device is limited in the amount of energy that the batteries can store. The miniaturized battery means that the entire lifetime of the sensor node is sharply reduced. Hence, the traditional battery with lower power density cannot be utilized to supply power for this micro embedded system. Additionally, a serious environment

impact is created by numerous discarded batteries. As the sensor nodes become dense in the network, the problem in powering the wireless sensor nodes is becoming critical due to these constraints.

Normally, every WSN desires a long lifetime, and thus many efforts have been taken in this area regarding reducing the power consumptions and enhancing the capability of energy sources. In respect of the miniaturization of electronic devices and a high power consumption of WSNs, reducing the physical power consumption of the sensor node is a feasible method. These efforts can be presented by using duty cycling strategies (Ganeriwall et al. 2005), (Dutta et al., 2005), adaptive sensing rates (Liu et al., 2006), tiered system architectures (Ganwali et al., 2006) and redundant placement (Kumar et al., 2008) to reduce the sensor node's power consumption. From the wireless network aspect, depending on the technologies available, there are also some possible solutions presented, such as energy-aware MAC protocols (Ye et al., 2002), power aware storage (Heinzelman et al. 2000) and power aware routing protocols (Abussimeh 2009), to enhance the network's lifetime. Because the WSNs must be able to last for several years, merely reducing the power consumption of the system does not meet the requirements. Hence, it is very important to increase the energy density of the energy storage elements. Many different types of energy storage technologies are shown in Figure 1.2, in which various energy storage technologies and their power density vs. energy density characteristics are depicted by a Ragone plot. Research to increase the energy storage density of both batteries and super-capacitors has been conducted for many years and continues to receive substantial focus (Blomegren, 2002).

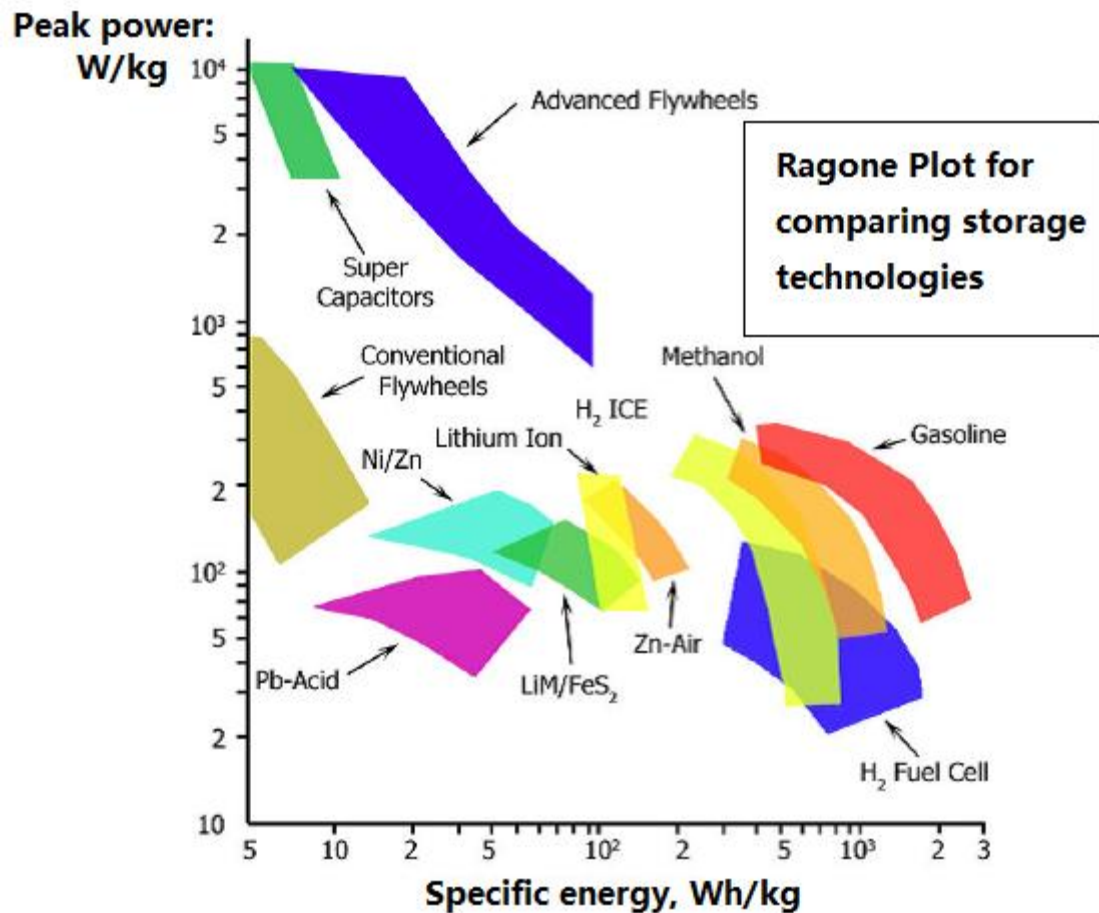


Figure 1.2 Ragone plot for comparing the energy storage technologies and their power density versus energy density characteristics (Tester, 2005)

While these technologies promise to extend the lifetime of WSN, the lifetime is still restricted, especially for wide deployment of WSNs. The maintenance problem is still not solved by using these two kinds of technologies, and hence a perpetual power supply is needed. In order to overcome the major hindrance of WSNs due to the high power consumption of the sensor nodes and the energy storages unpredictable lifetime performance, energy harvesting technologies have emerged to alleviate the energy supply challenge and there have the potential to result in self-powered, perpetual system operations for wireless sensor node. Moreover, unlike a single sensor node with an energy harvesting system, an entire sensor network with energy harvesting systems have been considered in Kar et al. (2006) and Gatzianas et al. (2010). In their works, each sensor node in the network had its own energy harvesting system. Then the lifetime and communication performance of the network had been improved based on the energy generation.

1.2 Energy harvesting technologies

Energy harvesting is a technique that captures or harvests a variety of unused ambient energy sources such as solar light, heat, vibration, radio frequency, and directly converts them into electrical energy. Various ambient energy sources and energy harvesters are shown in Figure 1.3.

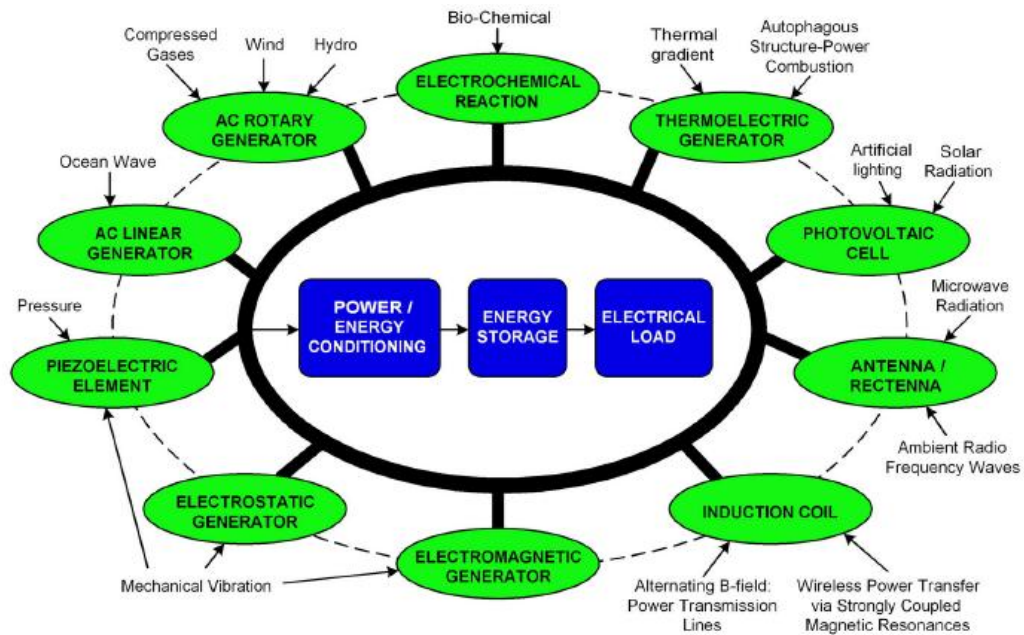


Figure 1.3 Energy harvesting source and their Energy Harvesters (Wan et al., 2010)

Based on Figure 1.3, there are numerous waste and unused ambient energies which can be harvested from the environment. Hence, it is not necessary to expand efforts to generate energy for harvesting. In the last few decades, a lot of researches have been conducted in the investigation of the energy levels of these energy sources in the environment. A compilation of the performance of energy harvesting sources and their energy density factors are listed in Table 1.1. According to the table, solar energy yields the highest energy density in an outdoor environment that can achieve a higher energy density than normal batteries. But, when the solar cells are placed under illuminated indoor conditions, the ambient light energy density drops tremendously. Moreover, the solar energy is sufficient in the day-time but it is unavailable at night. Hence the energy density of the energy sources are highly dependent on the specific application areas and time.

Table 1.1 Energy harvesting opportunities and demonstrated capabilities (Paradiso and Starner, 2005)

Energy source	Performance	Notes
Ambient light	100mW/cm ² (direct sunlight)	Common polycrystalline solar cells are 16%-17% efficient, while standard mono-crystalline cells approach 20%
	100μW/cm ² (illuminate office)	
Thermal	a) 60μW/cm ² at 5K gradient b) 135μW/cm ² at 10K gradient	Typical efficiency of thermoelectric generators are ≤ 1% for ΔT < 313K a) Seiko Thermic wristwatch at 5K body heat, b) Quoted for thermolife generator at ΔT =10K
Blood Pressure	0.93W at 100mmHg	When coupled with piezoelectric generator, the power that can be generated is order of μW when loaded continuously and mW when loaded intermittently
Vibration	4 μW/cm ³ (human, motion-Hz) 800 μW/cm ³ (Machiens-kHz)	Predictions for 1cm ³ generators. Highly dependent on excitation (power tends to be proportional to ω, the driving frequency and y0, the input displacement
Hand linear generator	2mW/cm ³	Shake-drive flashlight of 3Hz
Push Button	50μJ	Quoted at 3V DC for the MIT Media Lab Device
Heel Strike	118J/cm ³	Per walking step on piezoelectric insole
Ambient wind	1mW/cm ²	Typical average wind speed of 3m/s in the ambient
Ambient radio frequency	< 1uW/cm ²	Unless near a RF transmitter
Wireless energy transfer	< 14mw/cm ²	Separation distance of 2 meters

1.3 Research challenges

Powering a sensor node by using an energy harvesting technology can increase the system lifetime and performance. Other benefits are stated and elaborated in (Mathna et al., 2008) and (Thomas et al., 2006) to end user about using these technologies for WSNs, such as reducing the dependency on batteries, installation costs, maintenance costs, and providing sensor nodes in hard-to-access hazardous environments on a continuous basis, providing long term solutions and reducing environmental impact. But there are still some challenges in using these kinds of technologies, especially for designing and implementing a micro energy harvesting system.

Firstly, based on sensor node deployment, there could be two or more energy sources available for harvesting simultaneously. But unfortunately, based on Figure 1.3, there is no unique solution suitable for harvesting all kinds of environmental energy sources. As the energy source varies in relation to time and place, it is very hard to decide which kind of energy should be harvested.

Furthermore, because there are plenty of energy harvesting technologies and devices available, which vary with efficiency, price, and size, there are plenty of trade-offs which should be considered in deciding which kind of energy harvester should be used.

Thirdly, as shown in Table 1.1, the power density of energy sources is extremely small. Thus, designing a highly efficient energy harvesting system is extremely important for micro-scale energy harvesting systems. Since many system parameters should be considered and there is no clear system design guideline in the literature, the system design procedure especially for designing a highly efficient energy harvesting system is unknown. The situation is even worse when the energy harvesting system is used to power a wireless sensor node. Szewczyk's work shows that the lifetime of a sensor node may often be significantly shorter than expected without carefully understanding the electrical characteristics of the sensor node (Szewczyk et al., 2004). Therefore, inaccurate estimates of the power consumption behaviour of the WSN may cause an unexpected error when a new application is placed.

Fourthly, the environmental energy varies with time, even if energy harvesters can ensure a theoretically unlimited amount of energy over time, the energy they provided is hard to predict. In order to design a wireless sensor node with a perpetual lifetime,

the system has been able to recover from blackout periods where energy from the energy harvester is unavailable. Thus, unlike the battery powered wireless sensor node, an energy harvesting system powered wireless sensor node deployment is complex and without taking some proper design considerations into account the system might cause some significant errors or even cause the application to fail.

Last but not the least, WSNs always have numerous sensor nodes which mean that the system is restricted by size and cost. The cost and the size of the system are sometimes even more important than the efficiency of the system in some applications. Hence, the system optimization is very important for reducing the cost and size of energy harvesting systems. But unfortunately, there is a big gap between simulation and application reality. All the proposed systems can only be evaluated by a real experiment. If the system fails, the designers have to re-design and re-test the system. This causes a long design cycle. Hence, a simulation model which can be used to predict the system performance is critical. But it is very hard to design an accurate simulation model because of the diversity of energy harvesting technologies, numerous system architectures and system parameters, which should be considered in the model construction.

1.4 Motivation for the research

As promised by energy harvesting technologies, renewable energy powered wireless sensor nodes can potentially run for a long period of time or even perpetually without requiring any human intervention. Recognizing the possibility of long-term autonomous operation, several energy harvesting implementations have been made during the past few years. These works demonstrate that building a WSN with a type of energy harvesting system is possible. However, these existing works only address particular points in the design domain of the micro energy harvesting system rather than providing general design guidance for system designers. As the system design procedures become complex and a number of system parameters should be considered, it is very hard to develop a system in a short period of time. When a certain type of energy harvesting system is placed in a typical application area, which is different from its desirable environment, the system without proper design guidance might fail to work. Hence, a system-level simulation model which can be used to link the

physical electrical level of the system and the simulation level of the system is critical. But unfortunately, few research efforts have been channelled into this area. Moreover, system efficiency for the current energy harvesting platforms are extremely low and cannot meet the requirement of designing a highly efficient micro system. Additionally, low system efficiency means that the cost, size, weight and lifetime of a system are not as efficient as expected.

The motivation of this thesis is to design and implement highly efficient self-powered, self-sustaining and nearly perpetual operation wireless sensor nodes by utilizing energy harvesting technologies. Based on the restraints of wireless sensor node, the system should be designed following cost and size effective and energy efficient principles. The work also aims to optimize an energy harvesting system using both theoretical analysis and a real implementation. In order to achieve this aim, the methodology of the research is to determine and trade off three factors of the system, which are the energy generation, the energy consumption and the power management strategy of the system, by using an analytical model. Moreover, as this research has been funded by two public projects, which decides that solar and thermal energy harvesting systems should be developed.

1.5 Research objectives

The research objectives of this study can be divided simply into four parts:

- To investigate the existing literature available on micro-energy harvesting system powered wireless sensor nodes in order to obtain a better understanding of the current problems in this area and to find some possible ways to solve the problems.
- Based on the proposed challenges in the existing area, a theoretical analysis of an energy harvesting system is carried out. Some tasks that should be achieved in these areas are as follows:
 - To propose a generic system architecture suitable for different energy harvesting systems
 - To propose efficient and simplified design guidance for an energy harvesting system to meet the energy efficiency and cost-volume efficient requirements.

- To develop a systematic model based on the generic architecture and to use the model predicting the system performance before a real system is developed and deployed in a real physical environment.
- To improve system efficiency and performance based on the simulation results, obtained by the proposed model. The following efforts should be achieved.
 - To design an efficient maximum power point tracking (MPPT) scheme based power conversion circuit which increases the energy transfer efficiency of the system
 - To design an adaptive power management subsystem for an energy harvesting system to enable it have an longer lasting lifespan or even everlasting.
- To develop and implement energy harvesting system powered wireless sensor nodes in a real environment based on system efficient and cost-volume efficient principles. Three processes are considered in this part.
 - To design some wireless sensor nodes without energy harvesting systems to provide a deep understanding of the characteristics of a wireless sensor node
 - To design a solar powered sensor node based on the design guidance proposed in the previous part. The longer lasting lifetime, the energy efficient and cost-volume efficient should be satisfied in this work.
 - To design and develop a thermal energy harvesting system, which is also based on the generic architecture and design guidance. These three system requirements should also be satisfied in the design.

1.6 Contributions of the research

The contributions of this thesis consist of five parts.

- Firstly, a generic system architecture, fitted for all kinds of energy harvesting technologies, has been proposed. As found in the literature review, each energy harvesting application has its own system architecture and none of these system architectures can be adapted for other applications. Furthermore, the efficiency of the existing system architectures is not efficient enough for

micro-energy harvesting systems. Hence, the proposed energy harvesting system architecture has considered all the possible components required to build up an efficient micro-energy harvesting system for powering a wireless sensor node. And the proposed architecture can easily be adapted for other applications. Furthermore, as a dual energy buffer design has been used in the architecture, the lifetime and energy efficiency of the energy harvesting system has greatly improved by a theoretical analysis. Moreover, as the system architecture is highly dependent on the harvested energy types, the architecture for each kind of energy harvesting technology is different. Based on the finding, the main difference of the system architectures can be found in the power conversion part. Hence, this part of the system has been discussed. As solar and thermal are two environment energy sources considered in this thesis, the generic architecture for these two kinds of energy harvesting systems have been developed. The rest parts of the thesis are based on this architecture.

- Secondly, a simplified and efficient system design procedure based on the proposed architecture has been developed. This is because designing an efficient energy harvesting system powered wireless sensor node is much more complex than designing a battery powered sensor node. But unfortunately, there is no clear design guideline in the literature that gives a clear guidance for a system designer to design a cost-size effective and energy efficient system. Most of the design procedures are based on the designers' experience by using a trial-and-error strategy, which might cause a lot of problems. Hence, a simple and efficient system design procedure, which can be easily adopted by all kinds of energy harvesting systems and applications, have been proposed. The methodology of the proposed procedure is that when the system designers determine and apply three factors of the systems into the analytical model, which developed in the next contribution, the optimal sizes of the system can be determined.
- The third contribution of the thesis presents an analysis and experimental evaluation of a generic model representing a micro-energy harvesting system powered wireless sensor node. Generally, the simulation model is considered the best way to help bridge the gap between physical and simulation domains. But rarely are the simulation models presented in literature, and most of them

are focused on one type of energy harvesting technology. In order to make the simulation model fit for all types of energy harvesting technologies, the model is designed based on the generic systematic architecture. By using the proposed model, the energy status of each part of the system can be estimated. In order to demonstrate the model, two energy harvesting technologies, solar energy harvesting and thermal energy harvesting, are employed as two examples.

- The fourth contribution of the thesis is improving the system efficiency and performance by using a Maximum Power Point Tracking (MPPT) scheme and a power management strategy. Because the generated energy is very small by using a micro-scale energy harvester, the energy efficiency of a micro energy harvesting system is critical. Based on the system architecture, the system efficiency can be divided into four parts: energy conversion efficiency, energy transfer efficiency, buffering efficiency and consumption efficiency. The entire system efficiency can be greatly improved by increasing these four types of efficiencies. Hence, two kinds of efforts, designing an MPPT based power conversion circuit and a power management subsystem, have been developed in order to improve the system efficiency.
- In order to prove the proposed work's validity, three different cases have been developed that can be considered as the fifth contribution of the thesis. In the first case study, some wireless sensor nodes without an energy harvesting system have been designed. The characteristics of the wireless sensor nodes, especially for the shortages, have been studied and highlighted. Then two kinds of wireless sensor nodes which are powered by a solar energy harvesting system and a thermal energy harvesting system, respectively, have been developed in the following two cases. The proposed energy harvesting systems have been designed based on the generic system architecture by following the proposed design guidance. The experimental results show that both energy harvesting systems can efficiently harvest solar energy and thermal energy, respectively. The further results demonstrate that both systems can survive for a long period of operation in an extreme environment.

All of the contributions aim to create an efficient way to design and implement a micro energy harvesting systems powered sensor node, which has a perpetual lifespan and satisfies the requirements of the cost-size effectiveness and energy efficiency.

1.7 Organization of the thesis

The structure of this thesis is organized as follows: Chapter 2 reviews the state of existing micro energy harvesting platforms in both solar and thermal energies. Based on the analysis of these existing works, the problems and challenges in designing an efficient micro-scale energy harvesting system are identified. By considering these shortages of the existing works, Chapter 3 proposes a generic system architecture and a design guideline for an energy harvesting system to make the system design procedure more simple and efficient. It is difficult to design and implement a micro energy harvesting system in the real physical world, and a theoretical analysis model of an energy harvesting system is considered as the best way before designing an energy harvesting system. Hence, a simulation model of an energy harvesting system has been developed in Chapters 4 and 5. In Chapter 4, two kinds of energy transducers, which are a solar panel and a thermoelectric generator, are modelled. Subsequently, the whole energy harvesting system is modelled in Chapter 5. The system efficiency can be greatly improved by considering improving four kinds of energy efficiencies. Chapters 6 and 7 show two ways to improve the system efficiency and performance. Three different MPPT approaches have been designed and compared in Chapter 6 and an adaptive power management unit with an energy buffer system has been developed in Chapter 7. Three kinds of case studies to verify the proposed works have been achieved in Chapters 8, 9 and 10, respectively. Chapter 8 shows how to design a wireless sensor node without an energy harvesting system. A solar energy harvesting system and a thermal energy harvesting system are developed in Chapters 9 and 10, respectively. Finally, Chapter 11 summarizes the main contributions of the research and concludes the thesis by identifying areas for future research.

Chapter 2. Literature Review of Environment Powered Wireless Sensor Nodes

2.1 Micro-energy harvesting system overview

Harvesting energy from the environment is a desirable and increasingly important capability in several emerging applications of embedded systems, especially, WSNs. Given the energy-usage profile of a sensor node, energy harvesting techniques could meet part or all of its energy needs by using a proper design procedure. Energy harvesting itself is not new, but the challenges are how to build an efficient energy harvesting capability into a modern embedded system while satisfying all their constraints in terms of systems and application environments. In this chapter, state-of-art solar energy harvesting and thermal energy harvesting technologies are reviewed.

2.2 Energy harvesting architecture

In order to design an electrical system, the architecture of the system is crucial and it should be determined before the system is designed. Based on different energy sources and different design requirements, numerous system architectures can be found in the literature. According to Sudevalayam and Kulkarni (2010), the energy harvesting system can be divided into two categories in terms of a system architecture used: (1) Harvest-Use: energy is harvested just in time for use and (2) Harvest-Store-Use: energy is harvested whenever possible and stored for future used, as shown in Figure 2.1 (a) and (b), respectively. In the Harvest-Use architecture, the harvesting system directly powers the sensor node without any energy buffer, which means that the power output from the energy harvester has to be continuously above the minimum operating point of the sensor node, otherwise the system will die. Dan et

al. (2005) designed a thermoelectric generator to produce light from stoves. In their system, the light in the stove will be lighted when enough power can be harvested by the thermoelectric generator. If the stove is cool down, the light system is automatically turned off. The shortfalls of this design are that the system needs a large energy harvester and requires a continuous energy source. In order to overcome these shortages, a more common system architecture, the Harvest-Store-Use, has been proposed. In this architecture, a storage component or even two energy buffers are added into the system to store excess energy, which is generated by the energy harvester. With the energy buffers, the system can survive when either a harvesting opportunity does not exist or energy usage of the sensor node is higher than the energy generation.

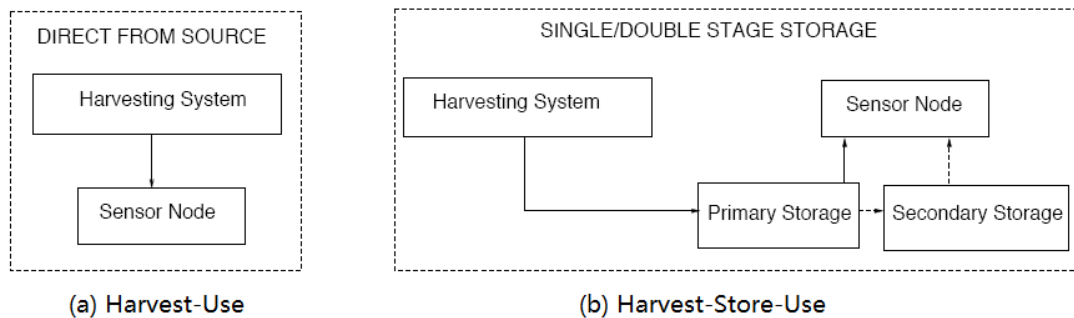


Figure 2.1 Energy harvesting system architectures with and without a storage capability (Sudevalayam et, al., 2010)

Based on the prior analysis, a micro-energy harvesting system for wireless sensor nodes should consist of several components, which are energy collection and conversion mechanisms (energy harvester/energy transducer/energy generator), electrical power management/conditioning circuit, energy storage device and electrical load (wireless sensor node), in an energy harvesting system. There are plenty of different ways to build each component by different designers. A general block diagram of an energy harvesting system is shown in Figure.2.2.

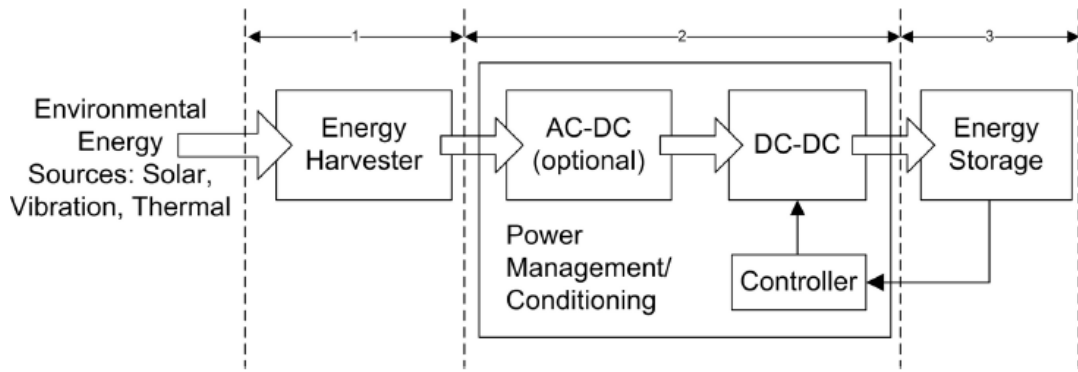


Figure 2.2 General block diagram representation of energy harvesting system unit (Wan et al. 2010)

In Figure 2.2, the function of the energy harvester is to harvest environmental energy sources and convert them into electrical energy. Typical examples of the energy harvesters, as illustrated in Figure 1.2, include the solar cell to collect solar energy, the thermoelectric (TE) generator to harvest thermal gradient energy, piezoelectric material converting vibration energy into electricity, and the rectenna antenna array to capture radio frequency energy from ambient. The harvested electrical energy from an energy harvester is highly dependent on the dynamically changing environment. Hence, the harvested energy is unknown when the system is implemented in the real environment. As the energy efficiency is very important for a small energy harvesting system, the generated energy needs to be conditioned to an appropriate form before powering the entire system in order to improve system efficiency. In this scenario, a power conditioning circuit is normally used and the main objective of the power conditioning circuit is to process and control the energy flow from the source to the load in an efficient way. Another function of the power conditioning circuit involves the conversion and regulation of electrical voltage at high levels into suitable levels for the loads (Tan, 2010). In order to ensure a continuous system operation even when the external energy source is weak or temporarily unavailable, the excess energy of the system should be stored either in a rechargeable battery or a super-capacitor.

A similar argument is presented by Jenong's thesis (Jenong, 2009). The architecture of a micro solar harvesting system is depicted in Figure 2.3, which has been organized by: (a) an external environment that determines the amount of solar radiation available to the micro-solar power system, (b) a solar panel that collects solar energy, (c) energy storage, where extra energy from the solar panel is stored, (d) a load

that will run on top of the power subsystem, consuming energy from the solar panel and the energy storage, (e) an input regulator that maximizes input power by matching the operating point between the solar panel and the energy storage, and (f) an output regulator that regulates the output voltage of the energy storage (Jenong, 2009).

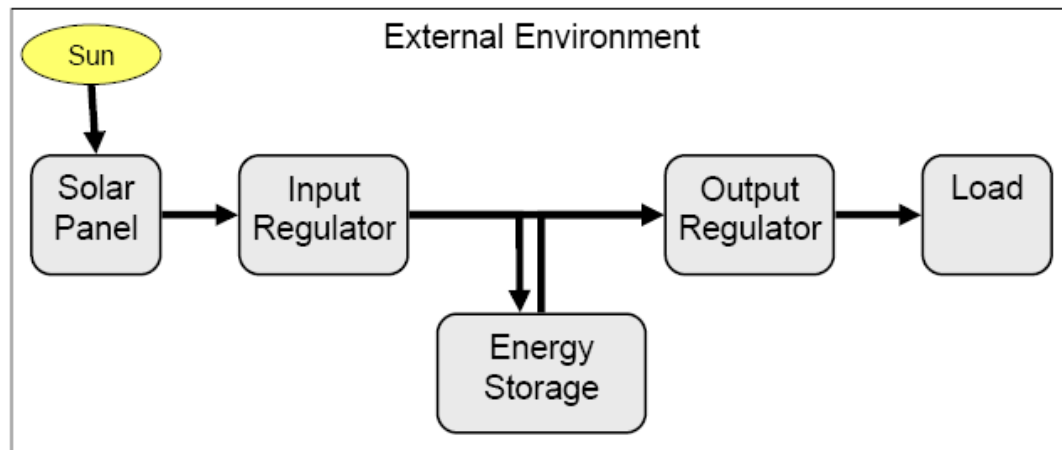


Figure 2.3 A general model for micro-solar power system (Jenong, 2009)

Recently, numerous research studies have been recorded in literature using an energy harvester to obtain energy from the environment to power a wireless sensor node. The goal of these studies is to make the wireless sensor node become truly autonomous and self-sustainable. Because the different nodes in a sensor network may have different energy harvesting opportunities and different environmental energy sources have different characteristics, the selection of the energy harvesting technique is crucial in the design of an energy harvesting system.

2.3 Review of the existing solar energy harvesting systems

Solar energy is both the richest and the most common energy source which can be harvested from the environment. Solar energy harvesters (solar cells), using the photovoltaic effect, convert solar radiation directly into electric energy; this is a widespread technique of solar energy harvesting technology. Generally, the generated voltage of a solar cell is dependent on the module's material and the input solar irradiance level. And on the other hand, the generated current of a solar cell is approximately proportional to the size of the solar cell. Since the voltage and current of a single solar cell is not large enough to meet the power requirement of the sensor

nodes, multiple solar cells are commonly combined in series or parallel into an array (solar panel) to provide suitable voltage and current (Jenong, 2009).

Based on some researches, solar energy of an outdoor incident light at midday holds a power density of roughly 100mW per square centimetre, i.e. in a small volume of 1 cm^2 , 100mW of electrical power can be harvested from the sun by using the solar panel (Wan et al., 2010). Conversely, based on Randall et. al (2003)'s work, the light power density in indoor environments is around $100\mu\text{W}/\text{cm}^2$. Commercially thin film polycrystalline and amorphous silicon solar cells are normally used because of the low cost, but lower conversion efficiency 10-13% is recorded by Randall et. al. (2003). Table 2.1 summaries the best measurements for the latest solar cells and sub modules under the global AM1.5 spectrum ($1000\text{W}/\text{m}^2$) at 25°C . From Table 2.1, it can be observed that the highest conversion efficiency is around 32% (GaInP/GaAs/Ge) by testing in the laboratory (Green et al. 2010). Based on Green's report, some single crystal solar cells offer efficiencies of about 20%. But their prices are much higher than the amorphous silicon solar cells which are very expensive for environmental powered sensor nodes.

Table 2.1 Confirmed terrestrial cell and sub module efficiencies measured under the global AM1.5 Spectrum (Green et. al. 2010)

Classification	Efficiency (%)	Area (cm^2)	V_{oc} (V)	J_{sc} (mA/cm^2)
Si (crystalline)	25 ± 0.5	4	0.706	42.7
Si(multicrystalline)	20.4 ± 0.5	1.002	0.664	38
Si(thin film transfer)	16.7 ± 0.4	4.017	0.645	33
Si(thin film sub module)	10.5 ± 0.3	94	0.492	29.7
GaAS(thin film)	27.6 ± 0.8	0.9989	1.07	29.6
GaAS(multicrystalline)	18.4 ± 0.5	4.011	0.994	23.2
InP(Crystalline)	22.1 ± 0.7	4.02	0.878	29.5
CIGS (cell)	19.6 ± 0.6	0.996	1.107	29.6
CIGS(sub module)	16.7 ± 0.4	16	0.66	33.6
CdTe(cell)	16.7 ± 0.5	1.032	0.845	26.1

CdTe(sub module)	12.5 ± 0.4	35.03	0.838	21.2
Si (amorphous)	10.1 ± 0.3	1.036	0.886	16.75
Si(nanocrystalline)	10.1 ± 0.2	1.199	0.539	24.4
Photochemical	10.4 ± 0.3	1.004	0.729	22
Dye sensitized (sub module)	9.9 ± 0.4	17.11	0.719	19.4
Organic polymer	8.3 ± 0.3	1.031	0.816	14.46
Organic (submodule)	3.5 ± 0.3	208.4	8.62	0.847
GaInP/GaAs/Ge	32.0 ± 1.5	3.989	2.622	14.37
GaAs/CIS(thin film)	25.8 ± 1.3	4	-	-
a-Si/ μ c-Si (thin film cell)	11.9 ± 0.8	1.227	1.346	12.92
a-Si/ μ c-Si (sub module)	11.7 ± 0.4	14.23	5.462	2.99
Organic (2-cell tandem)	8.3 ± 0.3	1.087	1.733	8.03

2.3.1 Typical solar energy harvesting systems

Recently, several implementations of solar energy harvesting powered sensor nodes have been carried out. Prometheus (Jiang et al., 2005), Helimote (Ragunathan et al., 2005), Everlast (Simjee and Chou, 2006), Ambimax (Park and Chou 2006), Sunflower (Stanley-Marbell and Marculescu, 2007), and HydroWatch (Taneja et al., 2008) are different types of solar harvesting sensor nodes

Prometheus and Helimote are two typical prototypes. In both systems, the solar panels are connected with the storage device through a diode. An overview of the system architecture and hardware architecture of the Prometheus are depicted in Figure 2.4 (a) and (b), respectively. The prototype is an autonomous solar energy harvesting system without MPPT technology. By intelligently managing a two-stage buffer design, the system lifetime is prolonged. The working principle is that the solar panel first charges the super-capacitor. When the charge level of the super-capacitor's terminal voltage is higher than a certain value, the capacitor powers the target system only. Otherwise, the system only draws current from the battery. Furthermore, when the capacitor's terminal voltage is higher than another threshold, the capacitor charges the battery and powers the system at the same time. Because Prometheus does not perform MPPT and there is no power management unit on the platform, the harvesting efficiency of this system is not very high.

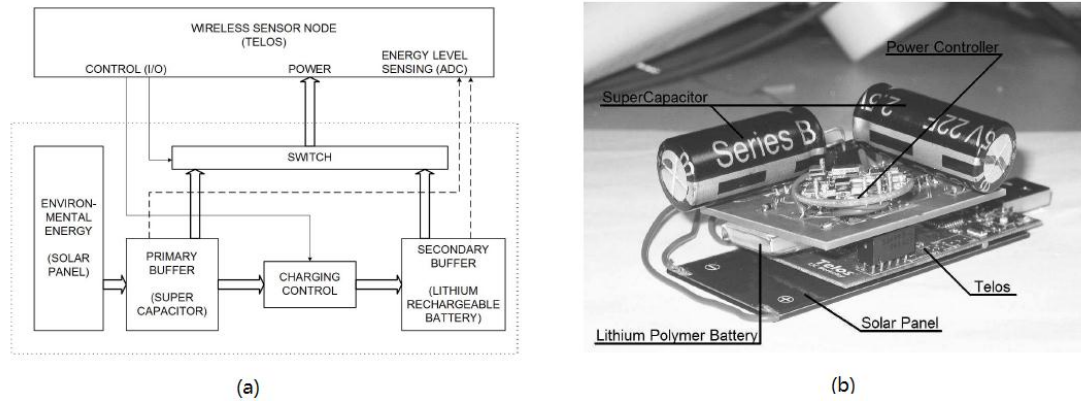


Figure 2.4 (a) System architecture of Prometheus implementation, (b) Prometheus platform (Jiang et al., 2005)

Unlike the Prometheus platform, Heliomote is a single-storage energy harvesting system using NiMH batteries which is built based on the Mica2 sensor node platform (Hill and Culler, 2002). The architecture and the prototype of the system are illustrated in Figure 2.5 (a) and (b), respectively. It uses a solar panel with the following dimensions: 3.75 inches \times 2.5 inches, which outputs 198mW at a voltage of 3.3V. Heliomote has an energy monitoring component which measures and conveys information regarding the magnitude and variance of energy available in the battery (Raghunathan et al., 2005). The gathering battery information is transferred to the sensor node which can learn its energy availability and usage through battery-aware power management. An analysis of the Heliomote platform shows that the perpetual operation of the system can be achieved if the rate of consumption of power is less than the rate of sourced power. Moreover, the Heliomote platform was designed as a plug-and-play enhancement for Crossbow motes. This means that the DC-DC converter is not exactly matched to the battery and the sensor node. Hence, overcharge and undercharge protections are designed in the power management unit. Similarly to the Prometheus platform, there is no MPPT scheme in the system.

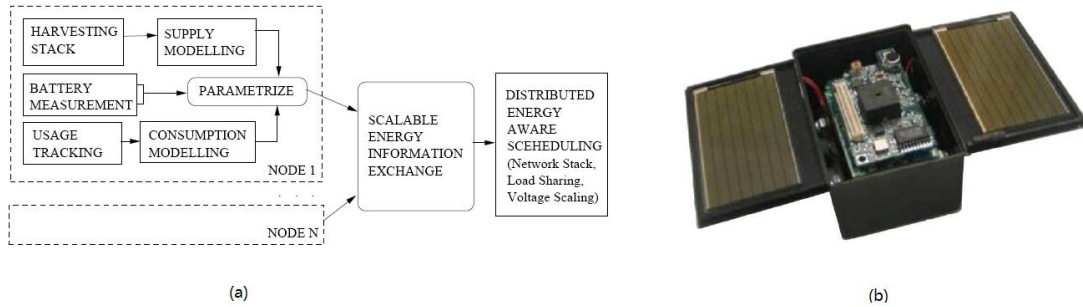


Figure 2.5 (a) System architecture of Helimote, (b) Helimote platform (Raghunathan et al., 2005)

Everlast is a super-capacitor operated energy harvesting platform, as shown in Figure 2.6, which is an integrated system with sensors, radio, low power MCU and the energy harvesting subsystem. The components of the energy scavenging subsystem are: a solar cell, a 100F super-capacitor, a Pulse Frequency Modulated (PFM) controller and a PFM regulator. Unlike the previous platform, an MPPT function is implemented by the PFM regulator. When the solar voltage exceeds the specified MPP reference voltage, the PFM controller pulses the PFM regulator to charge 100F super-capacitor. This process makes the solar panel work at the peak power position. Once the super-capacitor is fully charged, the PFM controller shuts down the PFM regulator by comparing its voltage to a reference voltage. Moreover, since all its components are controlled by the sensor node, the Everlast is not self-controlled. By using this technique, Everlast states a lifetime of 20 years at 50% duty cycle and 1Mbps data rate.

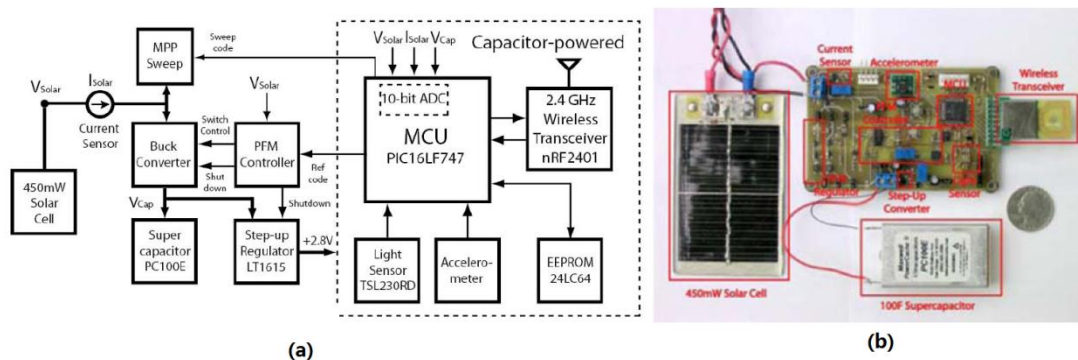


Figure 2.6 (a) System architecture of Everlast, (b) Everlast platform (Simjee and Chou 2006)

Park and Chou proposed an autonomous energy harvesting platform, named Ambimax, for multi-supply wireless sensor nodes. Like the Prometheus platform, it uses the same double-stage storage design. The Ambimax not only harvests solar

energy but also harvests wind energy. Each power source has its own harvesting subsystem that charges a separate super-capacitor. The energy stored in the super-capacitor is used to charge a battery and to supply power to the sensor node. As with Prometheus, the battery is used as a supply only when the super-capacitor voltage is below the minimum allowed input voltage of the sensor node. The energy harvesting subsystem consists of discrete digital and analog components such as comparators, switches and a boost DC-DC converter. The platform uses a variant of the fractional open circuit voltage techniques to achieve MPPT. It assumes a linear relationship between the output of a light sensor and the MPP voltage of the solar panel. The voltage of the solar panel is maintained at around its estimated MPP by a comparator that compares the voltage of the light sensor with the voltage of the solar cell. The comparator output determines whether the boost converter is turned on or off. Based on the MPPT scheme, the system efficiency is higher than the Everlast platform, but there is no power management unit in the Ambimax.

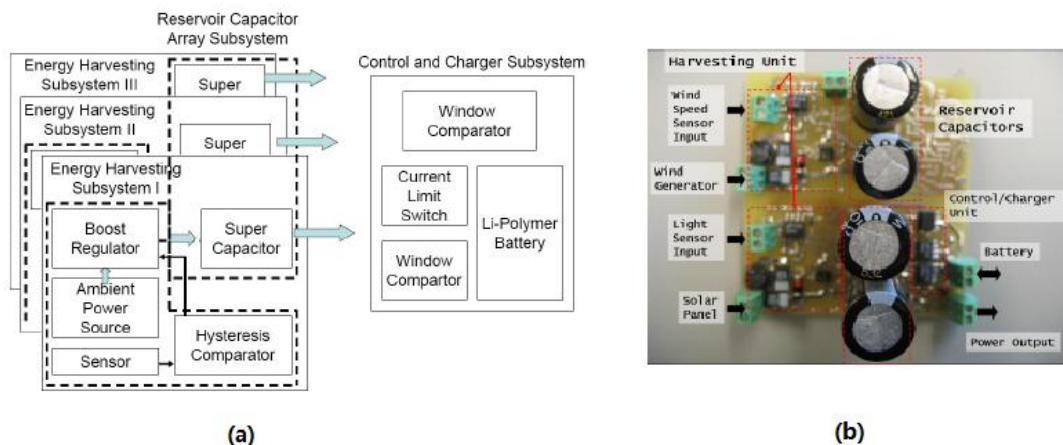


Figure 2.7 (a) System architecture of Ambimax, (b) Ambimax platform (Park and Chou 2006)

Taneja et al. proposed a HydroWatch node, which is a single-storage solar energy harvesting system, for a microclimate sensor network for studies of hydrological cycles in forest watersheds. They created a model for each of the constituent components and calculated that half an hour of sunlight per day is an appropriate requirement for these nodes to operate perpetually (Taneja et al., 2008). Then they designed a solar energy harvesting module based on the energy budget predicted by an astronomical model of the sunlight. The system architecture and the hardware platform are shown in Figure 2.7 (a) and (b). The system uses a solar panel 2.3 inches \times

2.3 inches, of which the maximum output power is 276mW at a voltage of 3.11V. The harvested energy is stored in two 2500mAh NiMH batteries and an input regulator is employed to match the current limit and voltage limit of the battery. The harvesting efficiency is quite low because there is no MPPT circuit and power management unit in the system. Furthermore, since the input regulator is observed to have 50% efficiency, the efficiency of the HydroWatch node is even worse when using this architecture. The proposed platform was evaluated by using two deployments, one of which was placed in an urban environment and the other in a forest watershed. The experimental results show that all nodes received at least half an hour of sunlight ($> 130\text{mWh}$) every day in the urban environment. However, when the system was placed in the forest watershed, most of the nodes did not receive more than 50mWh of energy a day, which was less than the target 79.2mWh/day (Taneja et al., 2008). This means that if the platform is placed in a forest, the sensor node may not have a perpetual life.

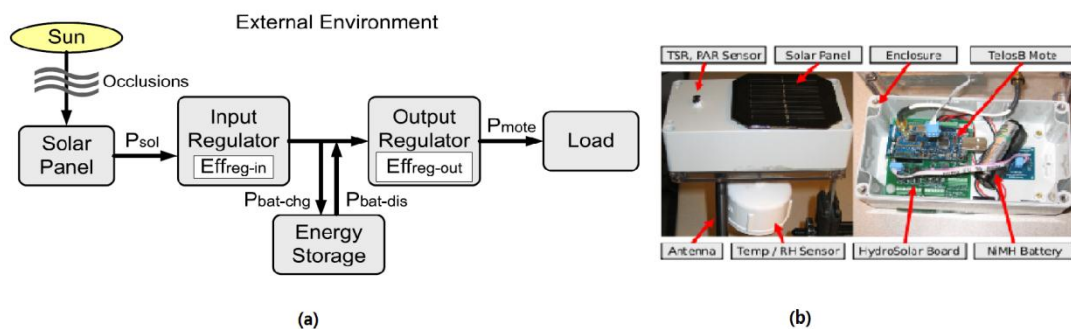


Figure 2.8 (a) System architecture of HydroWatch, (b) HydroWatch platform (Taneja et al., 2008)

Sunflower was designed by using a novel combination of an array of PIN photodiodes to harvest light energy. The harvested energy charges a miniature 0.2F super-capacitor through a switching regulator. There are four types of sensors; a programmable color detector, a microphone, an accelerometer and a temperature sensor, integrated on the sensor node and controlled by a low power MCU. The sensor node is completely powered by the harvested energy. The operating voltages of the sensors are gated with a low-quiescent current FET switch, which can be used to switch off the sensor when not in use. The MCU is entered into a deep sleep mode and uses an external watchdog timer to wake up the MCU.

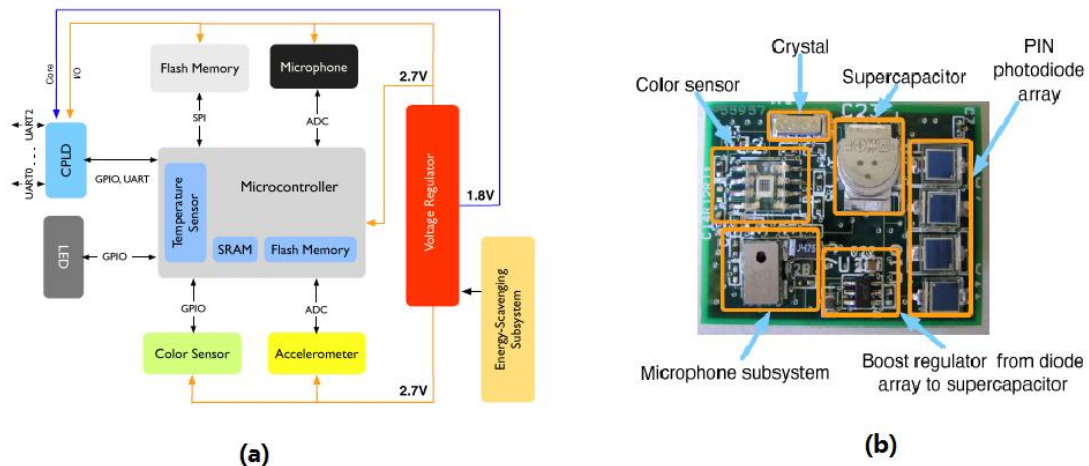


Figure 2.9 (a) System architecture of Sunflower, (b) Hardware of Sunflower (Stanley-Marbell and Marculescu, 2007)

2.3.2 Comparison of the existing solar energy harvesting platforms

Table 2.2 lists the comparative results of the existing solar energy platforms described in the literature. The table is classified by solar panel size and power rating, storage type and storage capacity, sensor node type, and whether to use an MPPT circuit or a power management subsystem. As can be seen from Table 2.2, the Ambimax platform has the largest solar panel, which can generate maximum 400mW, but the Sunflower platform can only generate 20mW power by using 4 PIN photo diodes. The difference is because the power consumptions of the target sensor nodes are different in these applications. From this point of view, it can be seemed that the solar panel size is decided by the energy consumption of the target sensor node. Because a Lithium-polymer battery has better charge-discharge efficiency than a NiMH battery, Prometheus and Ambimax use smaller capacity Lithium-polymer batteries in their design. But, HydroWatch shows that NiMH batteries with a proper voltage regulation is much preferred over the complex pulse charging logic of Lithium batteries for a low energy harvesting requirement (Sudevalayam and Kulkarni, 2010). This is because a Lithium battery with a complex charging circuit costs much more than a simple NiMH charge circuit. This makes a Lithium battery is not suitable for low cost applications. In Ambimax and Prometheus platforms, both platforms are used a dual buffer design. Several advantages of using the dual buffer design are concluded in their works based on their experiments. Firstly, the charging efficiency of the super-capacitor is higher than the energy being directly charged in the rechargeable battery. Secondly, the lifecycle of the super-capacitor can be considered as infinite.

Hence, the dual buffer design can make system lifetime much longer than using a single rechargeable battery design. According to the charging efficiency and the lifetime of the system, the using of high-capacity super-capacitor based two buffer design can be considered as the most viable option for long lifetime micro energy harvesting systems. Since efficiency is the most important factor in designing a micro-scale energy harvesting system, significant efforts such as an MPPT and a power management unit have been made. Unfortunately, there was no system that employed both technologies to achieve higher system efficiency. In these platforms, only Everlast, Ambimax and HydroWatch are employed a simple MPPT circuit in their design. For the power management design, only Heliomote and Sunflower are considered types of power management strategy in their systems.

Table 2.2 Specifications of solar energy harvesting platforms

Node	Solar Panel size(inches × inches) and maximum generated power (mW)	Energy buffer Type/capacity	Sensor node used	MPPT circuit	Power management
Prometheus	3.23×1.45 130	Super-capacitor(two 22F) & Li-poly battery (200mAH)	Telos	No	No
Heliomote	3.75×2.5 190	NiMH battery (1800mAh)	Mica2	No	Yes
Everlast	2.25×3.75 450	Super-capacitor(100F)	NA	Yes	No
Ambimax	3.75×2.5 400	Super-capacitor(two 22F) & Li-poly battery (200mAH)	Telos	Yes	No
HydroWatch	2.3×2.3 276	NiMH (2500mAH)	TelosB	Yes	No
Sunflower	4Pin Photo diodes 20mW	Super-capacitor(0.2F)	NA	No	Yes

2.4 Thermal energy harvesting

Thermal energy is another general energy source that can be harvested from the environment. Several approaches such as the Seebeck effect, thermo-couples, and

Piezo-thermal effect, to convert thermal energy directly into electricity are presently under investigation (Hudak and Amatucci, 2008). Many research studies for thermal energy harvesting have been examined in literature and a thermoelectric generator (TEG) based on the Seebeck effect is one of the popular devices that has been used to harvest thermal gradient energy. A summary of the implemented thermoelectric (TE) modules, capable of generating from $1\text{-}60\mu\text{W}/\text{cm}^2$ at 5K or less temperature difference, is described by Hudak and Amatucci in their review paper (Hudak and Amatucci, 2008). Table 2.3 shows the characteristics of the state-of-the-art TE modules in the Laboratory and commercial market. Both power output and voltage are reported in the table. The highest power density was achieved by RTI International (Watkins et al., 2005) in which the module can harvest $6.1\text{mW}/\text{cm}^2$ at a temperature difference of 2.7K, but the open circuit voltage was only $0.25\text{V}/\text{cm}^2$. Furthermore, two commercially available devices, using Bi_2Te_3 based material, are included in the table. The power generated from Micropelt (TGP v 1.9, 2010) achieved a good open-circuit voltage $6.1\text{V}/\text{cm}^2$ and a relatively high power density $1.2\text{mW}/\text{cm}^2$ by adding a 5K temperature difference on the module (Hudak and Amatucci, 2008). In terms of Hudak and Amatucci's conclusion, the device from Thermo Life (Thermo life, 2009) reached a higher open-circuit voltage $8\text{V}/\text{cm}^2$ but a much lower power density $40\mu\text{W}/\text{cm}^2$. Moreover, employing shorter elements requires higher heat flow to maintain a given temperature difference. For example, the thermo life element, of which the leg length is 1.4mm, is easier in order to maintain a large temperature difference than Micropelt elements, whose the leg length is $20\mu\text{m}$ (70 times lower than the thermo life). But unfortunately, the prices for both modules are around 50 GBP/module, which is too expensive for designing a micro-energy powered sensor node. Hence, a low cost commercial TE module should be considered in the thermal energy harvesting system design.

Table 2.3 Characteristics of TE power generators (Hudak and Amatucci, 2008)

Institution	Materials	Dimensions (μm)	No. of couples	Area (cm^2)	ΔT (K)	Power (μW)	Voltage (V)
University of Wales	Silicon	$4500 \times 20 \times 0.4$	5		5	0.002	0.13
SeiKo Instrumets	Bi_2Te_3 based	$600 \times 80 \times 80$	520	0.4	5		0.3
Fraunhofer Institute for Physical Measurement Techniques	n- Bi_2Te_3 and p-(Bi, Sb) $_2\text{Te}_3$	$20 \times 40 \times 80$	12	0.0112	5	0.67	
Micropelt (MPG D-602)	n- Bi_2Te_3 and p-(Bi, Sb) $_2\text{Te}_3$	$20 \times 35 \times 35$	450	0.082	5	100	< 0.5
Infineon Technologies	Polycrystalline Si		59400	0.06	5	1.5	<0.8
Institut Fur Mikrotechnik	Sb and Bi	$10000 \times 500 \times 7$	30		5	0.8	
DTS	Bi_2Te_3 based	$2800 \times 100 \times 2.5$	2250	0.675	5	1.5	1.1
Thermo Life energy Corporaation	Bi_2Te_3 based	1400(length)	5074	0.679	5	27	2.7
HSG-IMIT	Silicon	$500 \times 7 \times 1$	1000		4	0.2	0.4
Technische University Dresden	Sb and Bi	$20000 \times 40 \times 10$	100		5		<0.042
JPL/Caltech	n- Bi_2Te_3 and p- $\text{Bi}_{2-x}\text{Sb}_x\text{Te}_3$	20×60 (diameter)	63	0.029	1.2 5	1	0.002
ETH Zurich	Cu and Ni	150×210	90	0.49	20	0.0059	0.037

		(diameter)					
RTI International	Bi_2Te_3 based superlattice		30	0.16	2.7	980	<0.04
UC Santa Cruz/UC Santa Barbara	InGa(Al)As superlattice	$5 \times 200 \times 20$	200	0.16	5	10	

2.4.1 Typical thermal energy harvesting systems

Some thermal energy harvesting platforms have been proposed in the literature. One of the first applications of thermal energy harvesting in consumer products was the Seiko thermic watch, shown in Figure 2.10, produced by the Seiko Company (Kishi et al., 1999). It uses a TEG to convert body heat into electrical energy to drive a wrist watch. The system consisted of ten TE modules in series, a lithium-ion battery, and a DC-DC voltage booster. With about a 1 K temperature gradient between the arm and the environment at room temperature, 22 μ W can be harvested. The excess energy from the TE modules is charged into the battery, which was used to keep the watch operation in the absence of heat flow. The authors stated that the DC-DC booster increased the output of the modules from 300mV to 1.5V, but no details of the booster circuit's size or efficiency were given.

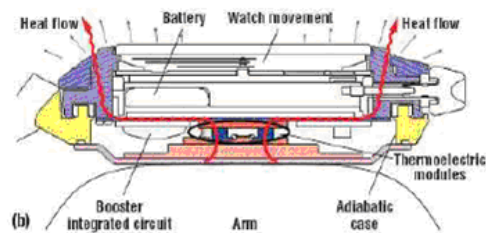


Figure 2.10 Thermo-electrical wristwatch of SEIKO (Kishi et al., 1999)

Similar work has been done by Leonov et al (2007). They designed a thermal energy harvesting system to harvest body heat energy through TE modules, as shown in Figure 2.11 (b). Because the harvested energy is quite low, they designed a power conditioning circuit to boost the harvested energy and store the energy into a single 1.2V NiMH rechargeable battery. The authors stated that the average power generation of the system was around 250 μ W with a 10K temperature difference during the day,

corresponding to about $20\mu\text{W}/\text{cm}^2$, which is better than solar cells in many indoor situations.

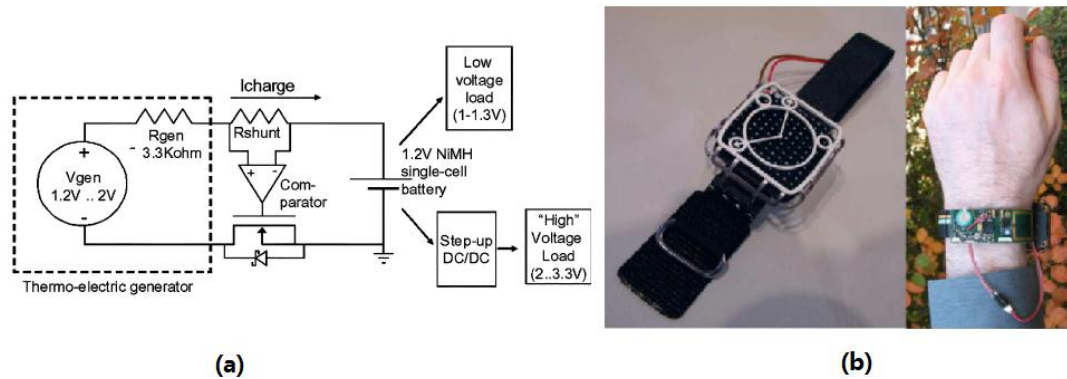


Figure 2.11 (a) Power conditioning circuit of the TEG (b) Thermal powered wireless sensor node (Lenovo et al. 2007)

In another thermal energy harvesting research, Lawrence and Snyder (Lawrence and Snyder, 2002) considered using a heat sink based TEG to harvest the thermal gradient energy between the ground and air, as shown in Figure 2.12. A maximum instantaneous power of approximately 0.4mW could be harvested by the thermoelectric generator, as shown in the results.

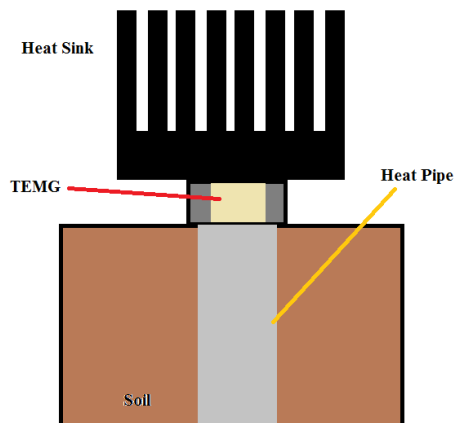


Figure 2.12 Ground source TEG (Lawrence and Snyder, 2002)

Based on the same principle, Sodano et al. (2007) presented a solar-thermal energy harvesting system placed in a greenhouse with a solar concentrator, as seen in Figure 2.13. The TE generator uses eight pieces of TE modules to harvest thermal gradient energy between the heat sink and the ground. The harvested energy is used to charge two 300mA NiMH rechargeable batteries. At an estimated temperature difference of 25K, the harvested energy was able to recharge an 80mAh battery in 33 minutes. The

authors have demonstrated that TEG can be used as an alternative to photovoltaic devices to harvest solar energy. However, there is little discussion on the power management aspects of the solar- thermal energy harvesting system.

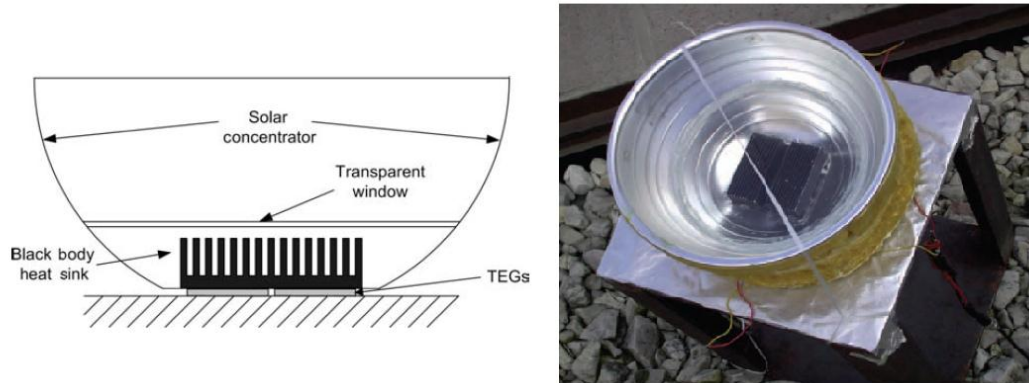


Figure 2.13 solar-thermal energy harvesting system (Sodano et al., 2007)

Mateu et al. (2006) developed an energy harvesting system for powering wireless communication modules. The prototype is shown in Figure 2.14. A thermogenerator module (TEG) is employed to harvest energy from temperature difference between the human body and the ambient. The harvested energy is used to power the EnOcean wireless modules (EnOcean, 2010). In order to dispose of the harvested low voltage energy, a power conditioning unit consisting of a charge-pump and a step-up DC-DC regulator was employed. Based on their results, the minimum 0.236V input energy with 50.53% efficiency can be boosted to charge two rechargeable batteries.

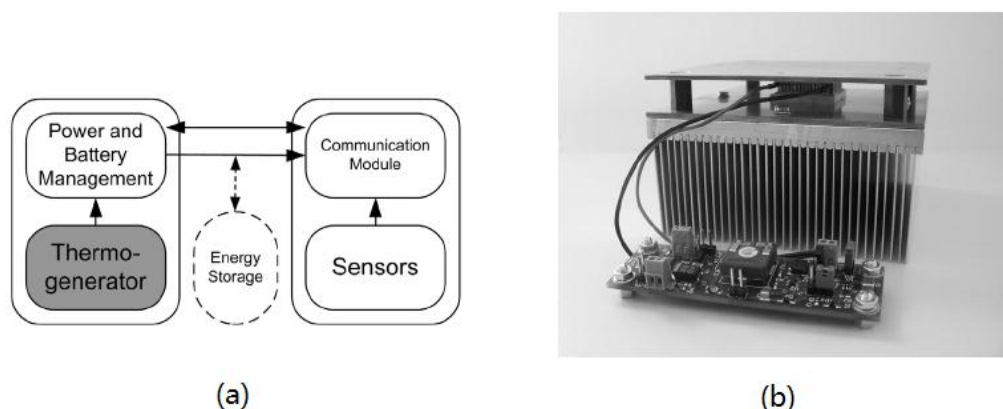


Figure 2.14 (a) system overview of the thermal energy harvesting system, (b) proposed platform (Mateu et al., 2006)

Similar to solar power, there is an MPP problem for the TEG. But unfortunately there are a few thermal energy harvesting systems adding this function in the system.

Eakburanawat and Noonyaroonate (2005) developed a TE generator based battery charging system to convert thermal energy from cook-stove, as shown in Figure 2.15. There is an MPPT circuit added into the system. They stated that the system with the MPPT based converter system has as high as 95.11% transfer efficiency much higher than a direct charging method, which has an efficiency level of approximately 15%. But this platform is used for high power applications, for which the harvested power is around 8W, which is unsuitable for powering the micro sensor node. It was recommended in the research that the MPPT circuit was critical for designing a high efficiency energy harvesting system.

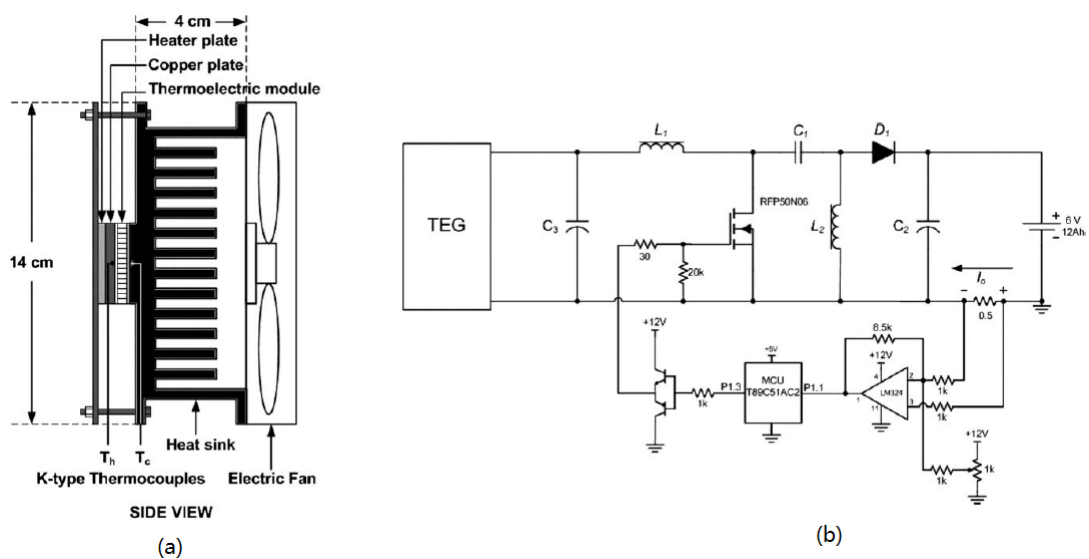


Figure 2.15 (a) TEG generator (b) Proposed circuit design with MPPT (Eakburanawat and Noonyaroonate, 2005)

2.4.2 Comparison of the existing thermal energy harvesting platforms

The comparison of the existing thermal energy harvesting platforms is listed in Table 2.4. Based on the comparison result, the size and the generated energy from the TEGs are different in these platforms. These system parameters are decided by the application requirements. Furthermore, because the harvested energy is highly related to the temperature difference between the TEG, some platforms were employed a heat sink system to maintain a large temperature difference. Thirdly, a lot of platforms had a regular circuit to boost its power to a high voltage level. This is because the voltage of the harvested energy is very low which cannot be used to directly power the target system. Additionally, unlike the solar energy harvesting system, the system architectures of the thermal energy harvesting platforms are simpler. Almost all the

platforms had not considered a power management subsystem into the system and only Eakburannawat's platform had employed a MPPT technology. According to their results, the energy efficiency is greatly improved by using this technology.

Table 2.4 Specifications of thermal energy harvesting platforms

Node	TEG size and maximum generated power	Energy buffer Type	Boost circuit	Sensor node used	MPPT circuit	Power management
Thermo-electrical watch	Small TEG system 22 μ W with 1K temperature gradient	Lithium-ion battery Yes	Yes	Wristwatch	No	No
Leonov's platform	Small TEG system 250 μ W with 10K temperature gradient	NiMH battery	Yes	NA	No	No
Ground source TEG	Large TEG system with a heat sink 0.4mW	NA	NA	NA	No	No
Solar-thermal energy harvesting system	Eight pieces TE modules (medium) with a heat sink unknown	300mAh NiMH battery	Yes	NA	No	No
Mateu's platform	Medium TEG Unknown	Two NiMH batteries	Yes	EnOcean	No	No
Eakburannawat's platform	Large TEG with a heat sink Unknown	Unknown	NA	NA	Yes	No

In conclusion, two problems have to be addressed when power is harvested from ambient heat flow, especially for micro-scale thermal energy harvesting system. Firstly, low ambient temperature difference may produce a voltage output that is too low to recharge a battery or power a device, even to power a boost converter. Hence, finding out how to increase the temperature difference or maintain a large temperature difference between the thermal energy harvesting system is critical. A high efficient heat transfer system should be considered in the thermal energy harvesting system. Secondly, the fluctuations in the ambient temperature will produce fluctuation in the voltage output of a TEG. Hence, a regulator must be used in the system. In summary, a heat sink system and a boost converter system are two essential components in the thermal energy harvesting system. Eakburannawat's work shows that the MPPT circuit

can greatly improve the system performance by maintaining the TEG operation at an MPP.

2.5 Summary

It is evident that the performance of a wireless sensor node can be greatly enhanced by using an energy harvesting technology. However, problems can be identified by analyzing these energy harvesting platforms both on solar energy and thermal energy. Firstly, there are plenty of different ways to build energy harvesting systems, even by using the same components. No researchers stated their system architecture was most efficient. Because each platform is designed for a typical sensor node and just focused on harvesting one type of energy source, the systems cannot easily be expanded to harvest another type of energy and use for other types of applications. Since there are plenty of design considerations and system parameters to be considered when designing a new type of energy harvesting system, the system design procedure is very complex and time consuming.

Secondly, there is no clear system design procedure introduced in the literature to guide a system designer to design a new energy harvesting system. The designer always follows a trial-and-error procedure to develop a new energy harvesting system. This procedure is considered as being inefficient. Hence, if there is a simple and efficient design procedure which can be followed, the energy harvesting system design progress can be simplified and the developing time can be shortened.

Thirdly, unlike the battery powered sensor node system, the system lifetime and performance cannot be easily predicted by examining the residual energy level of the battery, especially for a rapidly changed environment. Generally, a lot of proposed systems failed at the first implementation. For instance, as shown in HydroWatch, the system can only harvest two thirds of the expected solar energy when they are implemented in a forest. While energy harvesting has the potential to enable near-perpetual system operation, designing an efficient energy harvesting system that actually realizes this potential requires an in-depth understanding of several complex tradeoffs. Hence if there is an accurate and efficient system model to model the system performance before the implementation, all three aforementioned problems might be solved.

Moreover, the cost-size effectiveness and system efficiency are two design objectives which should be achieved in designing a micro-scale energy harvesting system for powering the sensor node. Based on the platforms described in the literature, the system efficiency can be divided into four parts, which are the energy conversion efficiency, the energy transfer efficiency, the energy buffering efficiency, and the energy consumption efficiency. By increasing these four types' efficiencies of the system, the performance of the system can be greatly improved by the form of the volume, cost and energy.

The primary goal of this thesis is to design and implement a self-powered and self-sustaining micro-energy harvesting system for powering wireless sensor nodes. This means the system should have a perpetual lifetime. Based on Kansal et al's (2007) findings, the system may have perpetual lifetime by achieving an energy neutral operation, which means the energy consumption of the sensor node is equal to or less than an energy generation of the system at any time. This function can be achieved by using a power management unit. Because energy generation is highly dependent on the environmental energy, which is dynamically changed, an accurate indication of the energy relationship between the energy generation and energy consumption is difficult. By analyzing these proposed systems, some authors stated their system can have a lifespan of as long as 20 years. But this is achieved by using a larger energy harvester and larger energy storage element. This system does not meet the key requirement of cost-size effectiveness. Hence, how to decide the energy harvester size and storage size should be considered.

Chapter 3. Micro Energy Harvesting System Architecture Design

3.1 Background and motivation

A typical energy harvesting system has three components: an energy source, a harvesting architecture and a load. The energy source refers to the ambient source of energy to be harvested and the harvesting architecture consists of the mechanisms to harness and convert the input ambient energy into electrical energy. The load, which is a wireless sensor node, acts as the main energy consumer of the system. Each component has its own characteristics and only when these characteristics work properly with each other, a good energy harvesting system can be designed. According to this point of view, one of the difficulties of building an energy harvesting system is to determine the architecture of the system. As stated in Chapter 2, different energy harvesting systems have different system architectures, and it is hard to say if any particular systems' architectures have the best performance. Moreover, in a distributed system, the energy sources available at different locations vary with the place and time and the sensor nodes in the same network may have different energy harvesting sources. Hence, flexibility and stability are considered two features of a successful micro-energy harvesting system. But unfortunately, none of the existing works meet both of these two features and most of them were designed for a typical application which cannot be easily expanded to other applications. Moreover, in order to design a highly efficient micro-energy harvesting system, a great number of design parameters and choices, such as the cost and size of the system, the lifetime and energy efficiency of the system, should be considered. But there is no clear design guideline proposed in literature to guide the system designer. Most of the existing systems are developed based on the worst-case scenario. The systems are normally oversized and not as efficient as perhaps expected.

3.2 Features of the proposed System

In this chapter, a generic system architecture for a micro-energy harvesting system is proposed. In order to make the architecture useable for all kinds of energy harvesting technologies, it is systematically constructed by five parts. According to this design, the system architecture can be easily expanded to other applications by changing the parameters of the components or adding some additional components into the system. Based on the proposed system architecture, a simple and efficient design guidance has been proposed to guide and optimize the design procedures of an energy harvesting system. Since the small volume, low cost and the highly efficient systems are considered as three factors which need to be satisfied in the micro energy harvesting system design, the proposed guideline considers these factors into the system design procedure.

3.3 A generic architecture of energy harvesting system

The existing energy harvesting systems can be divided into two architectures: harvest-use and harvest-store-use, as shown in Figure 2.1. According to the shortages and advantages of these two types of system architectures in relation with the features of a wireless sensor node, the harvest-store-use architecture is more suitable for powering a wireless sensor node. Hence, the proposed generic architecture is based on the harvest-store-use architecture.

Normally, a micro-energy harvesting system consists of several components which conduct tasks such as collecting an ambient energy, boosting the harvested energy, buffering the excess energy and distributing the harvested energy. Numerous ways of assembling each component of the system have been proposed in Chapter 2, but none of those works can be adapted for another type of application or another type of energy harvesting technology. Moreover, based on their experimental results, the efficiency of these energy harvesting platforms is not efficient enough to sustain an everlasting lifetime of a sensor node. Hence, it is essential to design a generic and efficient system architecture, which can be adapted for different applications.

Regarding micro-energy harvesting systems, the maximum energy out of these micro-scale energy transducers are extremely small, often only a few mW or even μW .

Hence, the energy efficiency of the system is a critical design factor which should be considered in the system architecture design in order to make the system extract as much energy as possible. As stated in Chapter 2, the energy efficiency of the system can be divided into four parts, as shown in Figure 3.1.

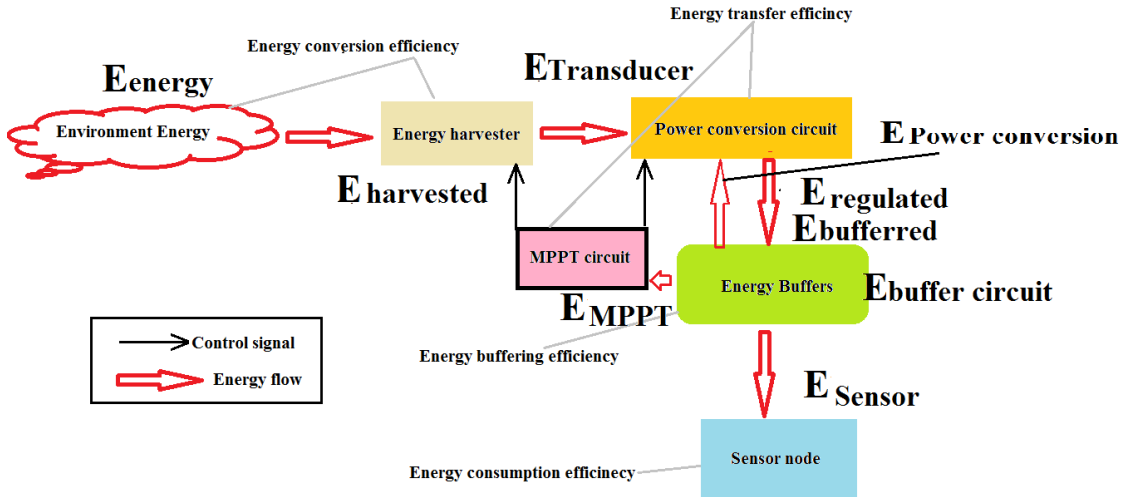


Figure 3.1 Block diagram of energy flow and four energy efficiencies of an energy harvesting system

- Energy conversion efficiency determines the total energy harvested by the energy harvester. It depends on the features of the harvesting technology, the capability of the energy harvester and the environmental factors. This type of energy efficiency can be improved by selecting or designing a high efficient energy harvester. If the environment energy is E_{energy} and the maximum harvested energy of the energy harvester is $E_{harvested}$, then the energy conversion efficiency $\eta_{E,conversion}$ can be expressed as:

$$\eta_{E,conversion} = \frac{E_{harvested}}{E_{energy}} \quad (3.1)$$

- Energy transfer efficiency $\eta_{E,transfer}$ determines how much the harvested energy can be available for using. This can be calculated as:

$$\eta_{E,transfer} = \frac{E_{regulated}}{E_{harvested}} \quad (3.2)$$

where $E_{regulated}$ is the regulated energy of the system by a power conversion circuit. This type of energy is determined by two factors: how much energy can be extracted from the energy harvester and how much the extracted energy can be transferred to the system. As stated in (Park and Chou, 2006) and

(Eakburanawat and Noonyaroonate, 2005), a system with a proper MPPT circuit can greatly enhance system efficiency by maintaining the energy harvester working at its MPP. Hence, a MPPT technology can increase the energy being extracted from the energy harvester. Hence the energy $E_{transducer}$ can be transferred to the power conversion circuit from the energy harvester, which is determined by MPPT efficiency of the MPPT circuit η_{MPPT} . Then $E_{transducer}$ can be expressed as:

$$E_{transducer} = E_{harvested} \cdot \eta_{MPPT} \quad (3.3)$$

Then $E_{transducer}$ will be transferred to the power conversion circuit and a part of this energy could be regulated and transferred $E_{regulated}$ to the next circuit. $E_{regulated}$ can be calculated as:

$$E_{regulated} = E_{transducer} \cdot \eta_{conversion} \quad (3.4)$$

where $\eta_{conversion}$ is the regulating efficiency of the power conversion circuit. By applying Equations 3.3 and 3.4 into Equation 3.2, $\eta_{E,transfer}$ can be rewritten as:

$$\eta_{E,transfer} = \frac{E_{harvested} \cdot \eta_{MPPT} \cdot \eta_{conversion}}{E_{harvested}} \quad (3.5)$$

- Energy buffering efficiency $\eta_{E,buffer}$ determines how much the regulated energy of the system can be stored into the energy buffers. The equation can be expressed as:

$$\eta_{E,buffer} = \frac{E_{buffered}}{E_{regulated}} \quad (3.6)$$

where $E_{buffered}$ is the energy being stored in the energy buffer. By dividing the charging and discharging processes of the energy buffer, $E_{buffered}$ is dependent on the charging efficiency $\eta_{charging}$ and lifecycle of the energy buffer. By ignoring the lifecycle and age effect of the energy buffer, $E_{buffered}$ can be expressed as:

$$E_{buffered} = E_{regulated} \cdot \eta_{b,charging} \quad (3.7)$$

The charging efficiency $\eta_{b,charging}$ is dependent on characteristics of the energy buffers being used in the system. As stated in Chapter 2, the charging efficiency of the super-capacitor is higher than the charging efficiency of the rechargeable battery. In order to enhance the charging efficiency, the super-capacitor should be used to store the regulated energy. But unfortunately, the leakage of the super-capacitor is much higher than the rechargeable battery. The supercapacitor is not suitable to hold energy for a long time. This is why two energy buffer design should be considered in this thesis. This will be described later.

- Energy consumption efficiency $\eta_{E,consumption}$ is defined as the portion of the energy consumed by the sensor node. This can be expressed as:

$$\eta_{E,consumption} = \frac{E_{sensor}}{E_{system}} \quad (3.8)$$

where E_{system} is total energy consumed by the entire system and E_{sensor} is energy consumption of the target sensor node. E_{system} can be calculated by knowing the energy consumption of each component of the system.

$$E_{system} = E_{sensor} + E_{MPPT} + E_{Power\ conversion} + E_{buffer\ circuit}$$

where E_{MPPT} , $E_{Power\ conversion}$ and $E_{buffer\ circuit}$ are the energy overhead of the MPPT circuit, power conversion circuit and buffer controlling circuit, respectively. According to the calculation, in order to make energy consumption of the system as efficient as possible, the sensor node should consume a large portion of the harvested energy. Since most of the proposed energy harvesting platforms have been designed according to the worst scenario, the energy buffer is always being fully charged. Then a proportion of harvested energy is wasted in these platforms. Hence, a power management strategy should be followed in order to increase/decrease the power consumption of the sensor node when there is large/small energy generation.

By considering all the functions and characteristics of an energy harvesting system, a generic micro-energy harvesting system is depicted in Figure 3.2.

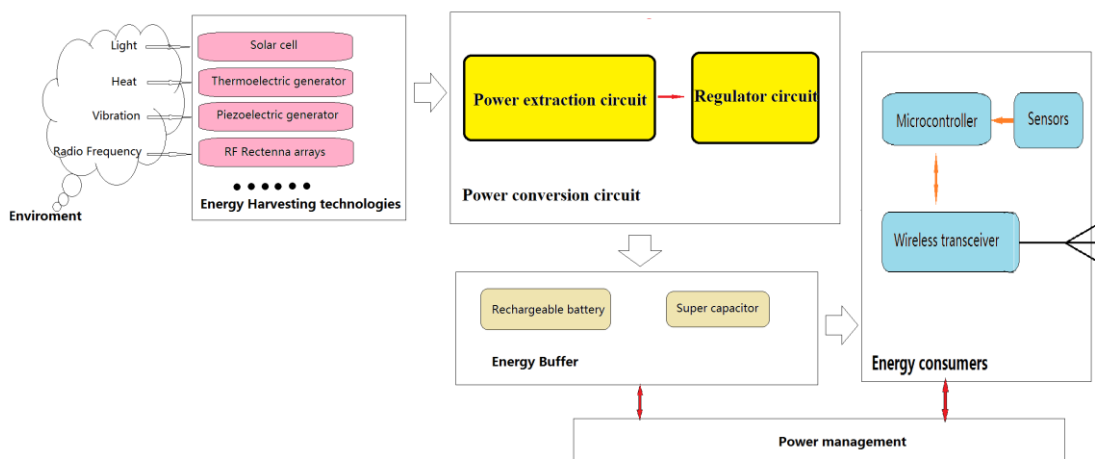


Figure 3.2 Block diagram of a micro-Energy harvesting system powered wireless sensor node

In order for the architecture to be easily adapted to different applications, it consists of five subsystems based on the energy flows. The first part of the system is the external environment; this determines the kind of energy source and the amount of energy available to an energy harvesting system. The second component of the system is an energy harvester, which is determined by knowing the energy source of the environment. For a micro-energy harvesting system, the selected energy harvester normally should be small, low cost and highly efficient. But it is very hard to have all these advantages in one device. Hence, a trade-off should be considered and the energy harvester should be carefully selected and designed to meet the system requirements.

According to the energy flow, the harvested energy is small and sometime the harvested energy is AC power (RF energy harvesters and kinetic energy devices), which cannot directly charging or powering the system. Hence, it needs an interface circuit to transfer the harvested energy can be used by the system. Based on this point, the third component of the system is the power conversion system, which is used to harness and regulate the harvested energy. More in detail, this component can be divided into two parts: a power extraction circuit and a regulator circuit. The main function of the power extraction circuit is to optimal power transfer from the generator to the regular circuit. It also can be called MPPT circuit. For different energy harvesting technologies, the extraction circuits are different, because the harvested energy types are different. For example, kinetic energy devices can be roughly seen as a current source, which the optimal power transfer from the generator to the load is

achieve when the internal resistance of the generator is equal to load. But the situation for solar energy harvesting system is totally different. This is because that the solar cell cannot be considered as a current source. It more like a current and voltage combination device. Hence, the maximum power point of solar cells cannot be equal the resistance of the generator to load. In order to track the maximum power point, some approaches to find the peak power transfer point of the solar cell should be carried out.

The fourth part of the system is the energy buffer system. As mentioned previously, the lifetime of the system is determined by the lifetime of the energy buffer system. If the system want a nearly perpetual lifespan, the lifetime of the energy buffer should as long as possible. According to this point, the dual buffer design with a smart energy distribution circuit is used. The advantage of using the proposed system architecture can be reflected in the dual buffer design. Table 3.1 lists the comparative results of the dual buffer design with other two single buffer designs (single rechargeable battery and single super-capacitor). The table is classified by lifecycle, charging efficiency, leakage and cost. The results show that the lifecycle of the single rechargeable battery is limited by the rechargeable battery, which is around 1000 times. The lifecycle of the dual buffer design and single super-capacitor design are determined by the super-capacitor, which can be seen as infinite. This is big advantage for an energy harvesting system, which desired a long lifespan. By examining the charging efficiency of these three designs, the dual buffer design and the single super-capacitor design have the almost the same charging efficiency. This is because that the energy in both designs is charged in the super-capacitor. The single rechargeable battery design has the lowest charging efficiency. This because that the charging efficiency of batteries is lower than the charging efficiency of supercapacitors. By comparing the current leakage of these designs, the dual buffer design and the single rechargeable battery design have small leakage current. This is because that the most of energy is stored on the rechargeable battery, which the current leakage is smaller than the current leakage of the super-capacitor. Based on this point, the single super-capacitor design has large current leakage, which restrains this design to be used in long time interval energy sources, such as solar. The fourth factor considered is the cost of the system. The single super-capacitor design is the most expensive one in these three designs because the high capacitance super-capacitor is expensive by comparing with

the low cost rechargeable battery. Hence, the single super-capacitor design is not suitable for a low cost system design. For the single rechargeable battery design, it has lowest system cost but it has very expensive maintaining cost such as changing the rechargeable battery or examining the battery lifecycle. This makes that the total system cost of the single battery design is much higher than the dual buffer design, which has a medium system cost in relation with a low maintaining cost. Based on the advantages of the dual buffer design over the single buffer designs, the dual buffer design is more suitable for using in a high efficient micro energy harvesting system.

Table 3.1 Proposed dual buffer design vs. single buffer designs

Name	Lifecycle	Charging Efficiency	Leakage	Cost	Maintaining cost
Dual buffer design	Infinite	High	Small	Medium	Low
Single rechargeable battery	Limited (around 1000 times)	Low	Small	Low	High
Single super-capacitor	Infinite	High	Large	high	Low

The fifth part of the system is the target sensor node. This is the main energy consumer of the system. In order to increase the energy consumption efficiency of the system, a power management strategy is considered. Then the entire architecture of an energy harvesting system can be designed by integrating these five components together. In this thesis, solar and thermal energy harvestings are considered. In order to make the architecture more suitable for these two kind of energies, Figure 3.2 is redrawn, as shown in Figure 3.3. In the figure, the power conversion circuit has been changed as the regular circuit, which includes the MPPT circuit, the DC-DC boost converter and the charge pump circuit (optional). The DC-DC boost converter used in this architecture is because the boost converter is non-resistor device, which can minimize the power consumption of the regular circuit.

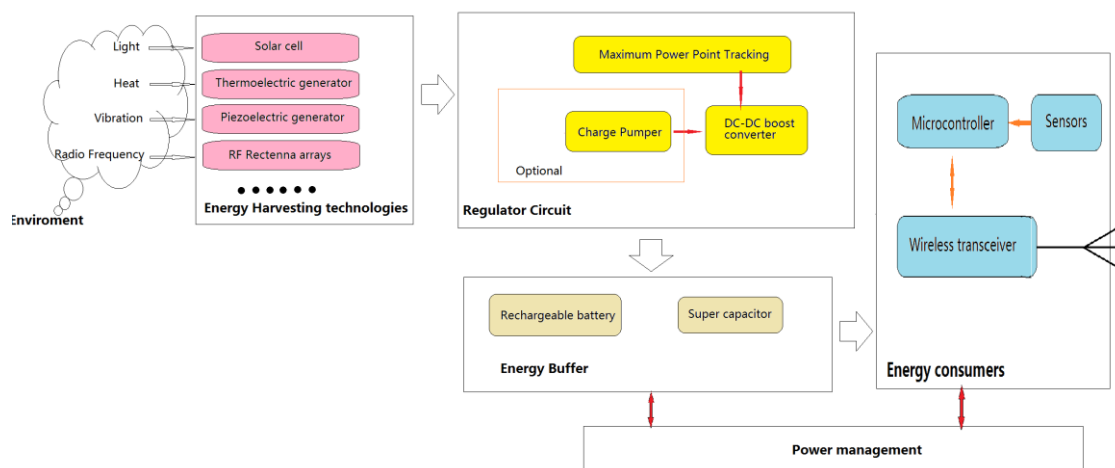


Figure 3.3 Block diagram of a micro-Energy harvesting system powered wireless sensor node

3.4 A design guideline of a micro energy harvesting system

Normally, the design process of an energy harvesting system is complex because numerous system parameters should be considered. This task is harder when designing a highly efficient micro energy harvesting system, because the system should be designed in a holistic way of choosing and designing a micro energy harvester and the constituent circuit, which a number of system factors, such as the relationship of the energy generation and the energy dissipation of the system along with the cost and size of the system should be considered. Recently, most of the existing systems have been designed based on the trail-and-error procedure. As there is no clear design guideline in literature to guide design, the system with this design procedure may cause some problems when it is implemented in a real environment directly. According to these, a simple and an efficient design guideline is urgently required for an energy harvesting system.

Any energy harvesting system, if it has a perpetual lifetime, should satisfy the energy generation equal or larger than the energy consumption all of the time. According to this rule, the design flow of an energy harvesting system based on the proposed system architecture is depicted in Figure 3.4.

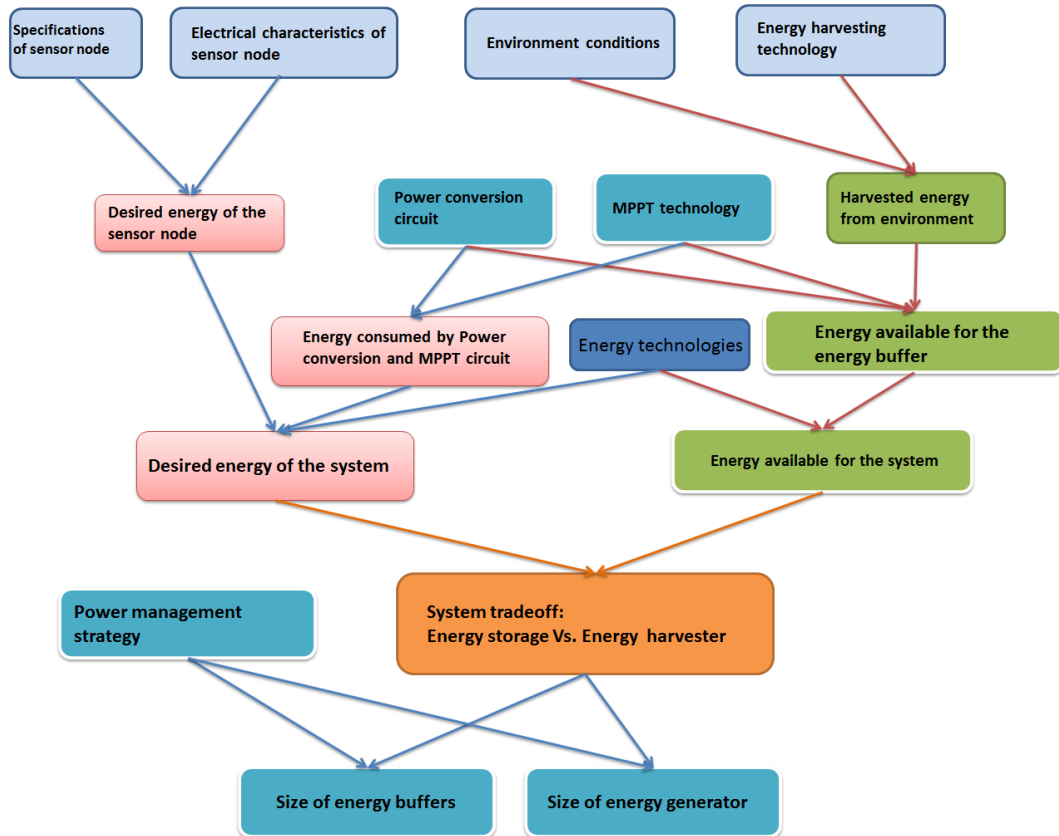


Figure 3.4 Design flow of micro-scale energy harvesting system

Based on the diagram, the design procedure of the energy harvesting system is to find the relationship between the energy generation and the energy consumption. This can be done by knowing the following three factors of the system:

- Determining the energy generation of the system,
- Determining the energy consumption of the system,
- Determining the power management strategy of the system.

Normally, the energy generation and the energy consumption of the system can be obtained by knowing four types of input parameters of the system, provided by the user before designing the system. Based on the energy type, these four types of input parameters can be classified into two parts, as shown in the left hand side of Figure 3.4.

- Energy generation parameters include the target environment conditions such as location, temperature and light level, and the possible energy harvesting technologies, which include the energy harvest capability, size and cost.

- Energy consumption parameters include specifications of the system such as a desired system lifetime, the maximum and minimum duty cycle of the system, and electrical specifications of the sensor nodes such as the maximum and minimum power consumption of the sensor node.

Then the design procedure can be divided into two routes. The first route follows the energy flow of the harvested energy. As shown in Figure 3.4, the harvested energy of the system can be predicted by understanding the environmental conditions and characteristics of the energy harvester. But this is not the exactly energy available for the system because some portion of that energy is dissipated by the mismatching circuit and the working point of the energy harvester. For each environmental condition, there is a unique operation point of the energy harvester at which the maximum harvested energy can be transferred to the next circuit. Any MPPT circuit is used to track and maintain the system working at the Maximum Power Point (MPP). Then the energy transfer to the regulator circuit can be calculated by knowing the MPPT efficiency and the power consumption of the MPPT circuit. After that by knowing the input energy level and the energy conversion efficiency of the regulator circuit, the amount of energy available to the system can be calculated. In order to make the calculation more realistic, the regulated energy is stored into the energy buffer before it being used by the system. Hence, the energy availability in the system is calculated by knowing the buffering efficiency of the system, which can be determined by knowing the parameters of the energy buffers.

On the other energy router, by knowing the desired system specifications (lifetime and duty cycle) and the basic electrical characteristics of the sensor node, the energy consumption of the sensor node can be calculated. By adding the energy dissipation of the MPPT circuit, the power conversion circuit and the control circuit of the energy buffers, the desired energy level of the system can be calculated.

And then by knowing the system requirements proposed by the end user such as the cost, size, lifetime and performance of the system, the power management strategy can be determined by setting different priority level of these parameters. For example, if the end users concern system lifetime more than the performance of the system, than the energy neutral operation should have high priority than maximizing the system performance. Moreover, if the end users want the system has compact size and they do

not care about the cost of the system, then the power management strategy is changed to reduce the sizes of the energy buffers and the energy harvesters. In this thesis, in order to desing an everlasting energy harvesting system, the power management strategy is that the energy neutral operation has high priority level over the system performance.

By applying these three system factors, the energy generaiton, the energy consumption, and the power management strageety, in a simulaiton model, the energy relaitonship of the system can be determined. Then the sizes of the energy buffer and energy harvester can be calculated. Additionally, the energy buffers and the energy harvester are varied in price and volume. Due to optimize the system cost and size, the trade-off between these two components should be considered. According to Figure 3.4, the rest of the system can be designed. By knowing what kind of MPPT technology being selected and what type of DC-DC converter circuit being used, the MPPT based power conversion circuit can be desinged. According to the energy buffer type and the power management strageety, the power managment subsystem can be developed. Then the entire energy harvesitng system can be constructed by integrating these components together, as shown in Figure 3.5.

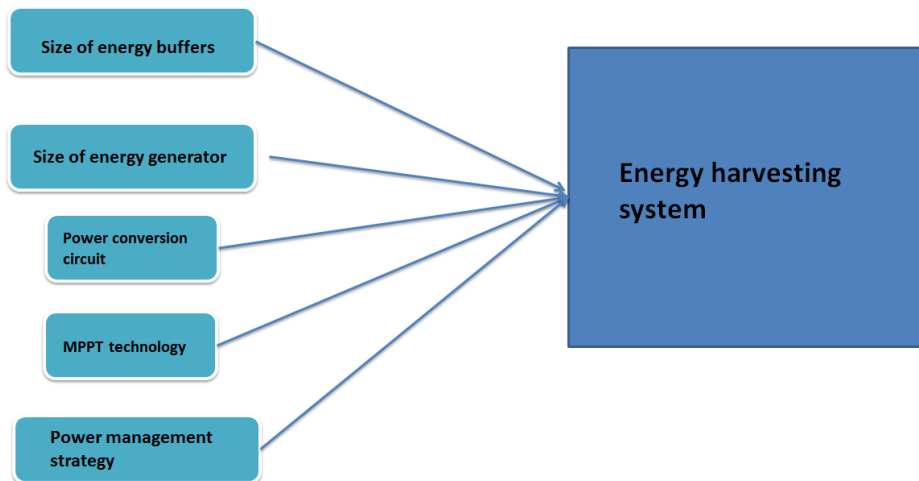


Figure 3.5 Components of an energy harvesting system

3.5 Summary

In this chapter, a generic architecture of an energy harvesting system and the design guideline based on this architecture are proposed, which form the foundation of the

remainder of the chapters. Since the system efficiency is critical for any energy harvesting system, most of the efforts in the following chapters are focused on improving system efficiency and performance.

Chapter 4. Energy Harvesting Transducer Modeling

4.1 Background and motivation

Knowing the energy generation of the system is essential in the design of an energy harvesting system. As stated in Chapter 3, the harvested energy is highly dependent on both the environment where the system is placed and the characteristics of the energy harvester which is used. Normally, the environment conditions can be obtained by some environment sensors or querying the historic data of the environment and the characteristics of the energy harvester can be determined by the datasheet, which is provided by the manufacture of the energy harvester. But the dynamically changed environment makes the electrical characteristics of an energy harvester, especially for a micro scale energy harvester, change rapidly and it is very hard to predict the energy generation of the system by simply knowing the harvesting capability of the energy harvester. Modelling an energy harvester in a mathematic way is considered as an efficient way to analyse and feature the energy generation of an energy harvester. To date, numerous models of energy harvesters have been developed in the literature to predict the energy generation of the energy harvesting system. But the low model accuracy and the complex model structure are the two main shortages in the existing models. In this chapter, two energy harvesters' models, solar and thermal, are developed as two illustrative examples to show energy transducers can be modelled and characterized. The accuracy and the system complexity are the two factors, which are being considered.

4.2 Solar panel modelling

Modelling a solar energy harvester is best way to know the characteristics of the solar energy harvesting technology. Normally, a photovoltaic system (solar panel) is used as a solar energy harvester to directly converter light energy into electricity. The output power of a solar panel highly depends on the environment conditions such as position, light intensity and temperature. The light intensity primarily affects the

amount of current generated and the temperature determines the voltage produced by the solar panel (Dezso et al., 2007). All of these factors need to be taken into consideration when modelling a solar cell. Recently, numerous solar cell models are presented in literature and these models can be roughly classified into a single diode model and a more sophisticated two or more diodes model. The detailed descriptions of these models are summarised in Xiao et al. (2004). The single diode model is the most developed and most common equivalent circuit for a silicon solar cell because of the simple model structure, as shown in Figure 4.1. According to Figure 4.1, five parameters, which are a photocurrent I_{ph} , a dark saturation current I_0 , a shunt current I_{sh} and a shunt resistor R_{sh} and a series resistance R_s , should be determined before modelling a solar cell. But unfortunately, these parameters are not given in the manufactures' datasheets, which normally provide the open-circuit voltage $V_{S,OC}$, the short circuit current $I_{S,SC}$, the panel voltage and current at the maximum power point $V_{S,MPP}$ and $I_{S,MPP}$. Hence, a straightforward approach, which uses the information provided by the data sheet, to construct a model of a solar cell should be considered. According to this idea, (Dezso et al., 2007), (Farivar and Asaei, 2010), (Villalva et al., 2009) and (Petreus et al., 2009) have proposed different solar cell's models to simulate the electrical characteristics of the solar cells. In order to extract parameters easily and to simulate the model rapidly, a solar cell model based on the first empirical model (Petreus et al., 2009), has been adopted in this work. The I-V characteristics of a solar cell can be written as Equations 4.1.

$$V_{solar} = V_{S,OC} \cdot \left[1 + \frac{1}{B} \ln\left(\frac{I_{S,SC} - I}{I_{S,SC}}\right) \right] - R_s \cdot I \quad (4.1)$$

where B and R_s can be expressed by the following equations

$$\begin{cases} B = \left[\frac{I_{S,MPP}}{I_{S,SC} - I_{mpp}} + \ln\left(\frac{I_{S,SC} - I_{S,MPP}}{I_{sc}}\right) \right] / \left(2 \frac{V_{S,MPP}}{V_{S,OC}} - 1 \right) \\ R_s = \frac{P_{S,MPP}}{I_{S,MPP}^2} - \frac{V_{S,OC}}{B} \left(\frac{1}{I_{S,SC} - I_{S,MPP}} \right) \end{cases}$$

And V_{solar} , $P_{S,MPP}$ are the output voltage and the maximum power of a solar cell, respectively.

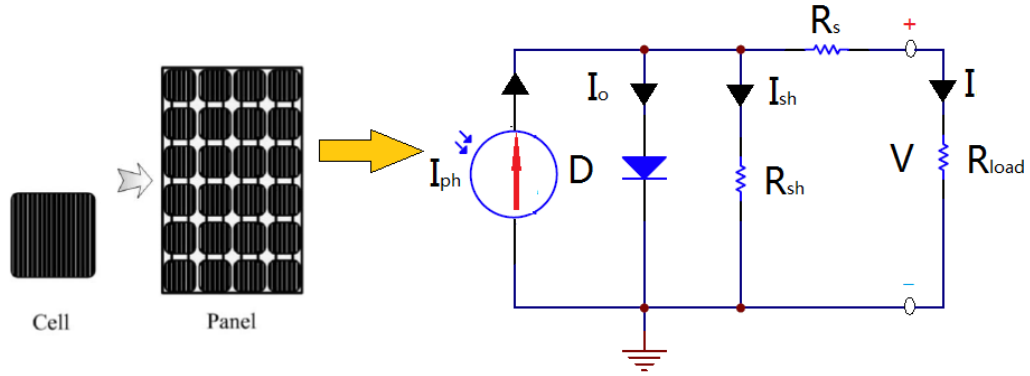


Figure 4.1 The equivalent circuit of the one diode model

According to Equation 4.1, a solar cell model can be constructed by knowing $V_{S,OC}$, $I_{S,SC}$, $V_{S,MPP}$, $I_{S,MPP}$, and $P_{S,MPP}$. Ordinarily, the open circuit voltage $V_{S,OC}$ and short circuit current $I_{S,SC}$ of a solar cell are easily extracted from an experiment. By following two linear relationships between the open circuit voltage and the MPP voltage ($V_{S,MPP}$) of the solar cell, and the short circuit current and MPP current ($I_{S,MPP}$) of the solar cell, the MPP of the solar cell in a certain light condition can be determined (Esram et al., 2007).

$$P_{S,MPP} = V_{S,MPP} \cdot I_{S,MPP} \quad (4.2)$$

$$V_{S,MPP} = \sigma_{s,V} \cdot V_{S,OC} \quad (4.3)$$

$$I_{S,MPP} = \sigma_{s,I} \cdot I_{S,SC} \quad (4.4)$$

where $\sigma_{s,V}$ is the coefficient of a linear relationship between the MPP voltage and the open circuit voltage of a solar cell, and $\sigma_{s,I}$ is the coefficient of a linear relationship between the MPP current and the short circuit current of the solar cell. In this chapter, a SANYO amorphous solar panel AM-5412 (SANY AM-5412, 2008) has been selected to verify the solar cell model. In order to simplify the model description, two fixed coefficients $\sigma_{s,V} = 0.76$ and $\sigma_{s,I} = 0.87$ are employed to estimate the MPP voltage and current of the solar cell. The parameters of the solar panel are illustrated in Table 4.1. The first column is the data when the solar panel is illuminated by a 50kLx standard light. This data is directly provided by the manufacturer. But this is not enough to characterize the solar cell in different situations. Some additional experimental tests should take place to obtain enough information for the model

construction. In this work, three additional tests, which the light intensities are 35kLx, 8.12kLx and 2.93kLx, were tested in the laboratory and the open circuit voltages and the short circuit currents of these three tests were recorded. By using Equations 4.2, 4.3 and 4.4, the other three parameters of the solar cell's model are determined, as shown in Table 4.1.

Table 4.1 Experimental parameters of the AM-5412 solar cell

50kLx		35kLx	8.12kLx	2.93kLx
Parameter	Ratings	Rating	Rating	Rating
V_{oc}	3.4 V	3.14V	2.88V	2.61V
I_{sc}	19.4mA	13.2mA	2.33mA	0.592mA
P_{mpp}	44mW	27.4054mW	4.4369mW	1.008mW
I_{mpp}	16.9mA	11.484mA	2.0271mA	0.515mA
V_{mpp}	2.6V	2.3864V	2.1888V	1.9575V

By applying these parameters into the simulation model, the I-V and P-V characteristics of the solar panel can be depicted. In order to evaluate the accuracy of the model, an experimental test has been taken place at the laboratory to validate the model. A 100W desk lamp has been used to produce a stable light irradiance in the laboratory. The output voltages and currents of the solar panel have been measured with a variable resistor, which can adjust its resistance from 100 ohms to 1Mohms. Figure 4.2 (a) and (b) plot the I-V curves and P-V curves of the solar panel in different light conditions for both the simulation and experiments. According to the figures, the accuracy of the model is around 92% at MPPs. Moreover, by analysing the P-V curve of the solar cell, the output power of the solar cell is highly related to the light irradiance levels and the output power of the solar panel is highly related to the output voltage of the solar cell in a fixed light condition. For each light condition, there is a peak power output point, MPP of the solar panel, where the solar panel can provide maximum output power when it operates at this point.

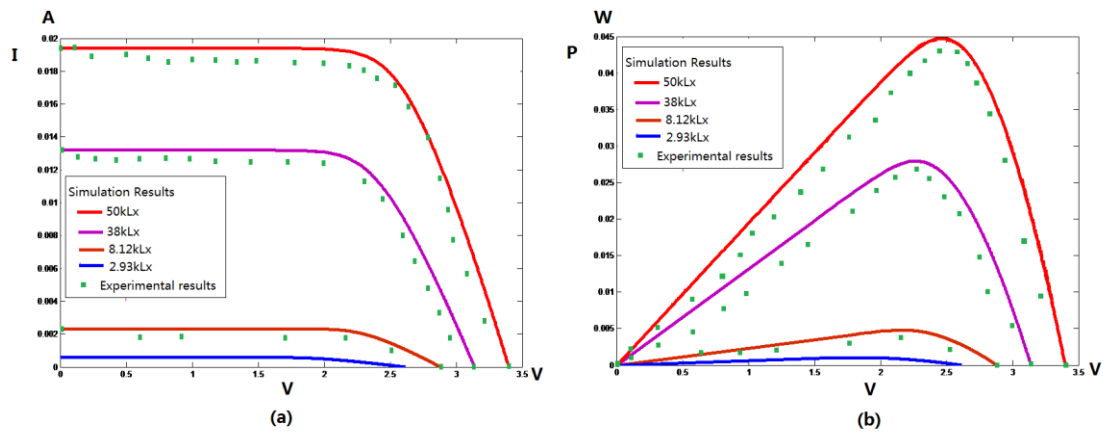


Figure 4.2 (a) I-V characteristic and (b) P-V characteristic of the solar cell

4.3 Thermoelectric generator modelling

The thermal energy harvesting is another energy harvesting technology being considered in this thesis. As stated in Chapter 2, recently TE materials improvements and advanced Micro Electro Mechanical System (MEMS) designed make more and more researches focus on using Thermoelectric Generators (TEGs) to harvest thermal gradient energy from environment. By comparing with other energy harvesting technologies, a TEG has some advantages such as no moving parts, no working fluid, a reduction of maintenance, long system lifetime and silence operation. A TEG is normally comprised by couples of TE modules, which are placed between two thermal transfer systems (a hot side heat exchanger and a heat sink). Unlike solar energy harvesting systems, the energy harvesting efficiency of the TEG system is much lower. Due to this, many researches have been concerned about developing an appropriate TE module and optimizing a TEG geometry design to enhance the energy harvesting efficiency, as shown in (Venkatasubramanian et al., 2011), (Kushch et al., 2001), and (Whalen et al. 2008). All these improving works rely on knowing the behaviour of the thermal energy harvester. According to this point, developing a simple accurate model for TEG is becoming a critical issue for both manufacturers and end users. A good simulation model of a TEG can not only simulate its corresponding behaviours, analyse its performance and improve predictive power of convertible heat energy, but also can optimize the TEG design to cut down the design cycle and the system cost. However, because of the complex system architecture of the TEGs, an accurate and simplified TEG model is one of major challenge in this area.

Recently, numerous analysis models of the TEG have been proposed. In these proposed works, a simple analytical one-dimensional (1-D) model of TEG is very often referred in the literature and these approaches can be derived from both the classical heat transfer theory (Chen et al., 2005) and irreversible thermodynamics (Chen et al., 2009), (Nuwayhid et al., 2000). But the complex heat transfer problems are not solved in these models. According to this point, a popular method of solving the heat transfer problems by converting the thermal equations into an equivalent electrical circuit, which has been proved to be helpful in understanding a complex thermal problems in a simple way, has been used in some research works to construct the TEG model (Chen et al., 2009), (Gao and Rowe, 2007). Based on the equivalent electrical circuit, a mathematical software Matlab (Chen et al., 2005), or a circuit simulator PSPICE (Chen et al., 2009) can be used to build the TEG model. These existing works are basically for analysing a TE module rather than analysing the performance of the entire TEG system that their model did not address the constraints associated with the external heat transfer system. Furthermore, in order for a TEG system to generate a quantity of electric, a comparatively large amount of heat should be moved through the TE module because of its low thermodynamic efficiency. Hence, the design of the hot side and the cold side heat exchangers as well as matching the TEG requirements is critical for a high efficient thermal energy harvesting system. But unfortunately, a proper thermal system design and an optimization of the heat exchangers model have been ignored in the most of TEG models. And hence, some critical factor in determine the efficiency of the system has been neglected in these TEG models.

4.3.1 Constructing a TEG model

In order to develop a TEG model, the structure of the TEG should be determined. A typical configuration of a TEG is depicted in Figure 4.3, where the system is constructed by couples of TE modules, a hot side and a cold side heat exchangers, heat source, cooler (air) and thermal grease. The TE modules are sandwiched between two heat exchangers with two thermal grease layers. The thermal energy flow will conduct from the heat source to the TE module through the hot side heat exchanger and it will release from the cold side heat exchanger (heat sink) into the air. By analysing the function of each part of the system, the model of the TEG system could be divided into a TE module model part and a heat exchanger model part. In order to construct the

simulation model more accurate, two different situations are considered. The first condition is a TEG placed in an effective infinite heat source, such as radiator. In this situation, the maximum power of the TEG can be obtained when the maximum heat flow can be drawn from the heat source. The second situation is that the thermal energy harvesting system is placed in a limited heat environment, such as human body. In this case, the maximum power of the TEG system is when the thermal resistance of the TEG matches the thermal resistance of the heat source. In this thesis, the infinite heat source condition is considered.

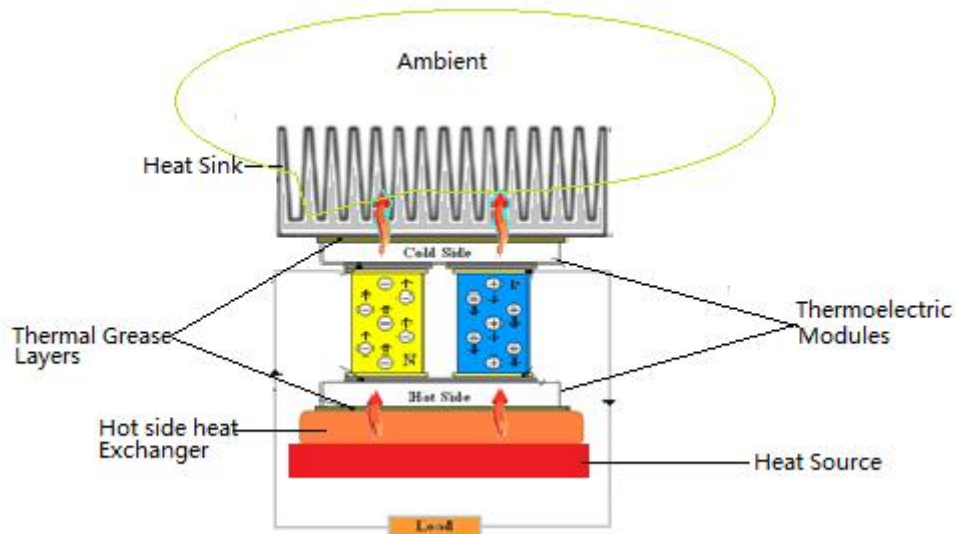


Figure 4.3 A TEG system

4.3.1.1 Constructing a TE module model

For any TEG system, the TE module is the core part, which is used to convert thermal gradient energy directly into electrical energy. Normally, the TE module is constructed with many pairs of P-type and N-type semiconductor legs jointed by metal interconnects (typically Cu) connected in series. These legs are soldered thermally in parallel between two ceramic plates, as shown in Figure 4.4. If ignoring the material difference between the legs, the model of a TE module can be indicated by modelling a P-N type semiconductor couple and multiplying it with the number of couples (N) included in the module.

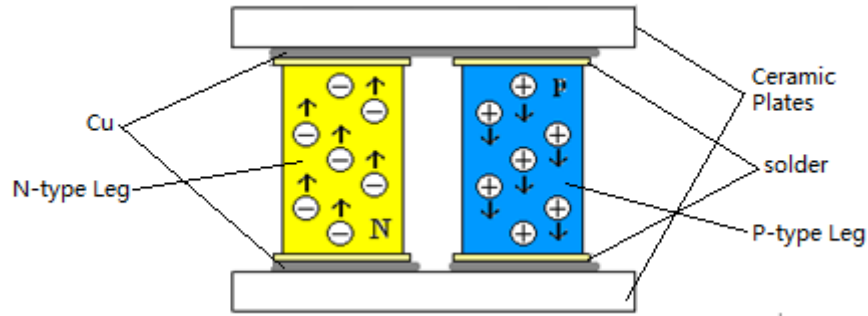


Figure 4.4 Typical diagram of a TE module

Some phenomena, which take place in the TE module, should be determined before constructing a TE module model. In order to simplify the design process, the TE module model is divided into a thermal part and an electrical part. Five thermal phenomena, which are the reversible Seebeck and Peltier effect, Thomson effects, and the irreversible Fourier conduction and Joule heating, can be observed in the thermal part. Seebeck effect is the basic operation principle of a TE module that is the process when the two junctions of two dissimilar materials are held at different temperature conditions and a voltage $V_{Seebeck}$ is generated between the two junctions. The Seebeck coefficient, $\alpha_{seebeck}$, defined as the ratio of the voltage $V_{Seebeck}$ generated by the Seebeck effect and the applied temperature difference ΔT_g , is given by (Lineykin and Ben-Yaakov, 2007).

$$\alpha_{seebeck} = V_{Seebeck} / \Delta T_g \quad (4.5)$$

Meanwhile, an invertible effect, the Peltier effect, occurs when a current I flows through the TE module and the heat Q_p absorbed or generated by the Peltier effect at the junctions is given by Equation 4.6.

$$Q_p = \Pi \cdot I \quad (4.6)$$

where Π is the Peltier coefficient. The relationship between the Peltier coefficient and the Seebeck coefficient is indicated in Equation 4.7.

$$\Pi = \alpha_{seebeck} \cdot T_{tem} \quad (4.7)$$

where T_{tem} is the temperature of the TE module in Kelvin. Moreover, when a temperature gradient is imposed on the TE module, the Seebeck coefficient varies

from place along the length direction of the TE legs. If there is a current flow I , flowing through the TE couples, the Thomson effect occurs. The Thomson heat $Q_{Thomson}$, absorbed or released from the TE module depends on the temperature difference ΔT_g and the current flow I .

$$Q_{Thomson} = \tau \cdot I \cdot \Delta T_g \quad (4.8)$$

The Thomson coefficient, τ , is proportional to both the changes in the Seebeck coefficient and the temperature gradient of the TE module.

$$\tau = \Delta\alpha_{seebeck} / \Delta T_g \quad (4.9)$$

where $\Delta\alpha_{seebeck}$ is a Seebeck coefficient difference. The Joule heating and the Fourier conduction are other two common thermal effects which can be detected in the TE module. The Joule heating is the process of heat dissipation on the resistive loads when an electrical current I pass through the module. This effect can be expressed as:

$$Q_j = I^2 R_{TE} \quad (4.10)$$

where R_{TE} is total internal electrical resistance of the TE leg and R_{TE} can be calculated by:

$$R_{TE} = \rho \cdot h / A \quad (4.11)$$

where ρ is the electrical resistivity of the material using in the TE leg, h is the height of the TE leg, and A is the across section area of the TE leg.

The Fourier conduction states that when a temperature gradient exists within a material, heat energy will flow from the high temperature side to the region of low temperature. The heat absorbed or released by the Fourier conduction Q_F is expressed as:

$$Q_F = \Delta T_g / K_{T,res} \quad (4.12)$$

where $K_{T,res}$ is thermal resistance of the TE leg and it can be calculated by:

$$K_{T,res} = h / (k \cdot A) \quad (4.13)$$

where k is thermal conductivity of the material, h is height of the TE leg and A is the across section area of the TE leg. Then the five thermal phenomena are introduced.

In order to simplify the thermal analysis, a formal analogy between heat and electrical conduction is adopted in this chapter. A list of the analogies between thermal and electric variables and their units are given in Table 4.2. According to the table, a heat flow source and a temperature difference can be modelled as an electrical current and a voltage of an electrical circuit. Moreover, a thermal resistance $K_{T,res}$ can be represented by an electrical resistance R . A thermal mass C_{Heat} can be treated as a capacity in the electrical circuit and it can be described by the expression (Lineykin and Ben-Yaakov, 2007).

$$C_{Heat} = V_{volume} \cdot \rho \cdot c_p \quad (4.14)$$

where V_{volume} is volume of the material, ρ is density of the material and c_p is specific heat capacity of the material.

Table 4.2 Analogies between electrical and thermal variables

Thermal variable		Electrical variable	
Parameter	Unit	Parameter	Unit
Heat flow (Q_F)	W	Current flow (I)	A
Temperature difference (ΔT)	K	Voltage (V)	V
Thermal Resistance ($K_{T,res}$)	Cm^2/W	Electrical Resistance (R)	Ω
Thermal mass (C_{Heat})	J/K	Electrical capacity (C)	F
Absolute zero temperature	0K	Ground	0V

According to Table 4.2, the schematic model of TE module can be transformed into an equivalent electrical circuit scheme by simply changing the variables. The five thermal processes are considered as five different power sources in the circuit. As the model is fabricated for low temperature applications, it can be assumed that the inside of the TE legs is homogeneous and the legs are insulated both electrically and thermally from their surroundings, except at the junction contacts. The proposed thermal model of the TE module is depicted in Figure 4.5. The model is split evenly into two parts: hot side and cold side. As the Joule heat Q_J and the Thomson effect

Q_T generated in the TE module follows its own temperature gradient, these heats can be split evenly between two sides with one half being conducted to the hot side and the other being conducted to the cold side. Moreover, the Peltier heat Q_p is divided into $Q_{P-hotside}$ and $Q_{P-coldside}$ to express the Peltier effect occurs in the hot side and cold side, respectively. The Q_F is used to display the Fourier conduction heat of TE couple. Additionally, Q_1, Q_2, Q_3, Q_4 are used to express the Fourier conduction taking place at the ceramic layer, the Cu layer and the solder of the TE module.

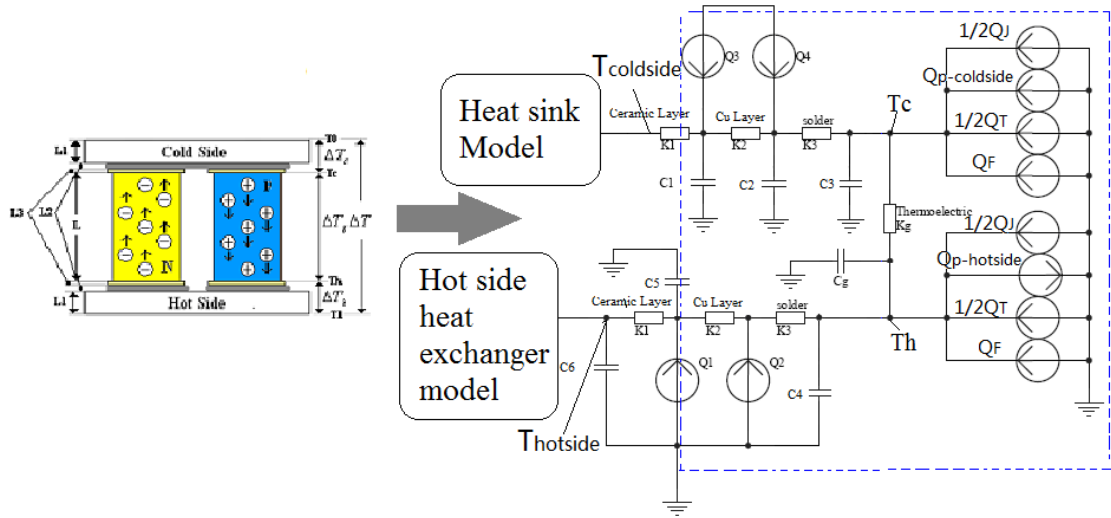


Figure 4.5 Scheme of the thermal-electric analogy of the TEG model

Before taking the numerical analysis of the TE module, the electrical part of the TE module should be determined. This can be presented by using a simple equivalent circuit consisting of a series-connected thermally induced voltage $V_{seebeck}$, which is generated by the Seebeck effect, and an internal electrical resistance of the TE module. As a TE module is formed by N-type and P-type semiconductor materials, the Seebeck voltage $V_{seebeck}$ and the Seebeck coefficient of the TE couple can be expressed by combination of the Seebeck coefficients of the N-type and P-type semiconductor materials.

$$V_{seebeck} = n \cdot (\alpha_p - \alpha_n) \cdot \Delta T_g \quad (4.15)$$

$$\alpha_{seebeck} = \alpha_p - \alpha_n \quad (4.16)$$

where n is the number of thermal couples included in a TE module, and $\alpha_{seebeck}$, α_p and α_n are the Seebeck coefficients of the TE couple, the P- and N-type thermoelements, respectively.

The electrical part of the TE module is illustrated in Figure 4.6, in which the internal resistance of the module consists of the electrical resistance of the P- and N- type thermoelectric materials (R_p and R_n), resistance of interconnects (Cu) R_{Cu} and contact resistances $R_{contact}$ between each interface. In order to simplify the calculation, the contact resistances of the TE couple at each interface is assumed has the same value. Hence, the total contact resistance of the TE couple is expressed by $4 \times R_{contact}$. Then the internal electrical resistance of the TE couple $R_{internal,TE}$ is expressed in Equation 4.17.

$$R_{internal,TE} = [R_n + R_p + (4R_{Cu} + 4 \times R_{contact})] \quad (4.17)$$

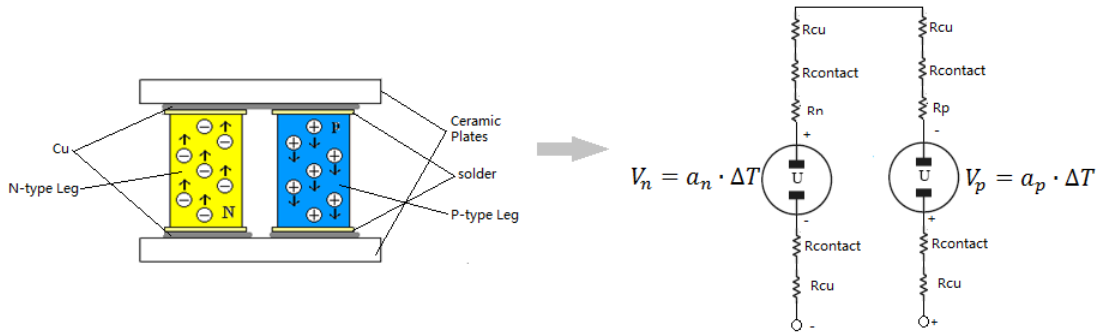


Figure 4.6 Electrical part of the TE module

As shown in (Altazin et al, 2011), the electrical contact resistance in the TE legs causes a growth of the module's electric resistance and results in the drop of their energy conversion efficiency. Hence, an approximate specific contact resistance $\rho_c = 1.5 \cdot 10^{-6} \text{ohmcm}^2$ (Altazin et al., 2011) is adopted in this work to calculate the contact resistance, $R_{contact}$, of the thermo-couples.

$$R_{contact} = \rho_c / A_c \quad (4.18)$$

where A_c is the area of the electrical contact of pellets which is equal to the contact area A .

By integrating the thermal part and the electrical part of the TE couple together, the model of the TE couple can be expressed. The model of a TE module can be calculated by multiplying the model of the TE couple by number of n , which is the number of the TE couples included in the TE module. In order to simplify theoretical analysis of a TE module, the TE parameters (Seebeck coefficient, electrical resistivity

and thermal conductivity) are assumed independent of the temperature. The heat Q_h transfer from the hot side heat exchanger to the hot side of the TE module at temperature $T_{hotside}$ and the heat Q_c release from cold side of the module at temperature $T_{coldside}$ to the heat sink can be expressed as follows by using Equations 4.5-4.14.

$$\begin{aligned} Q_h &= Q_F + Q_{P-hotside} - \frac{1}{2}Q_J - \frac{1}{2}Q_T \\ &= \frac{T_h - T_c}{K_{T,res}} + \alpha_{seebeck} \cdot T_h \cdot I - \frac{1}{2}I^2 R_{internal} - \frac{1}{2}Q_T \end{aligned} \quad (4.19)$$

$$\begin{aligned} Q_c &= Q_F + Q_{P-coldside} + \frac{1}{2}Q_J + \frac{1}{2}Q_T \\ &= \frac{T_h - T_c}{K_{T,res}} + \alpha_{seebeck} T_c I + \frac{1}{2}I^2 R_{internal} + \frac{1}{2}Q_T \end{aligned} \quad (4.20)$$

where Q_F is the Fourier heat, and $Q_{P-hotside}$ and $Q_{P-coldside}$ are the heat generated by the Peltier effect in both hot side and cold side of the TE module, respectively, and T_h and T_c are the temperatures at the hot end and cold end of the TE couples, respectively, and I is current flow into the TE couple. According to Equation 4.13, the total thermal resistance of TE couple, $K_{T,res}$, can be expressed by:

$$K_{T,res} = \frac{h}{A(k_n + k_p)} \quad (4.21)$$

where k_n and k_p are the thermal conductivity of the N-type and P-type materials, respectively. For the low temperature applications, the Thomson effect is very small as compared to the Seebeck effect. Hence, the Thomson effect is neglected in this work because the WSNs are used in the normal environment.

According to Fourier's heat conduction law, the thermal energy enters the hot junction and leaves from the cold junction of the TE module that can be expressed as:

$$Q_h = \frac{T_{hotside} - T_h}{K_{cond}} \quad (4.22)$$

$$Q_c = \frac{T_c - T_{coldside}}{K_{cond}} \quad (4.23)$$

where $T_{hotside}$ and $T_{coldside}$ are the temperatures of the TE module at the hot junction and the cold junction, respectively, and K_{cond} is total thermal resistance of the TE module without considering the thermal resistance of the TE legs. This is sum of thermal resistance of the ceramic plate K_1 , Cu conductor K_2 and solder K_3 .

$$K_{cond} = K_1 + K_2 + K_3 = \frac{L_1}{k_{Al}A} + \frac{L_3}{k_{Cu}A} + \frac{L_2}{k_{solder}A} \quad (4.24)$$

As the thermal balance between the thermal flows entering the hot junction and leaving from the cold junction of the TE module, Equations 4.19 and 4.20 are equal to Equations 4.22 and 4.23 by ignoring the Thomson effect Q_T . By combination these equations, the heat balance equations at two junctions of the TE module are illustrated as:

$$\frac{T_{hotside}-T_h}{K_{cond}} = \frac{T_h-T_c}{K_g} + \alpha T_h I - \frac{1}{2} I^2 R_{internal} \quad (4.25)$$

$$\frac{T_c-T_{coldside}}{K_{cond}} = \frac{T_h-T_c}{K_g} + \alpha T_c I + \frac{1}{2} I^2 R_{internal} \quad (4.26)$$

4.3.1.2 Constructing a heat exchanger model

As the energy conversion efficiency of even the best TE modules available is very low, a proper heat exchanger system design is essential for a good TEG system design. A larger temperature difference between the two sides of the TE module means that more electrical energy can be generated by the TE module. Hence, it is very important to maintain a large temperature difference between the two sides of TE module. When the internal thermal resistance of the TE module is equal to the sum of all external thermal resistance, the maximum output power occurs (Chen et al., 2005). As shown in Figure 4.3, the external thermal resistance is determined by contact resistance between parts and between the surroundings, and the thermal resistance of the exchangers themselves. In order to maximize the efficiency of the heat exchanger system and to predict the performance of the generator, a numerical model of the heat exchangers subsystem should be designed and associated with the TE module model.

A heat exchanger subsystem is composed of two heat exchangers, one is attached to a heat source to harvest heat from the heat source and another is exposed to thermal interface (air) to evacuate the heat from the cold side of the module. Because metals

are good thermal conductor materials, a piece of metal is considered as an ideal hot side heat exchanger. Moreover, as a large temperature difference between the heat source and the TE module can be obtained to compensate an inefficient hot side heat exchanger, a 1.7mm thickness and 160mm^2 square cross-section aluminium plate has been employed as the hot side heat exchanger in this chapter. The diagram of Figure 4.7 is being used to determine the thermal resistance of the hot-side heat exchanger. In Figure 4.7, T_1 and T_2 are the temperature of the hot side and cold side of the hot side heat exchanger, $dT=T_1-T_2$ is the temperature difference between the two sides of the heat exchanger, and Q is heat being absorbed by the hot side heat exchanger. The total thermal resistance of the hot side exchanger K_{hot} is the sum of the thermal resistance of the hot side heat exchanger $K_{hotside}$ and the contact resistance of between the heat source and the hot side heat exchanger, as expressed:

$$K_{hot} = K_{hotside} + K_{contact}$$

$K_{contact}$ will be described in the later section. For the thermal resistance of the hot side heat exchanger, it can be expressed in Equation 4.27.

$$K_{hotside} = \frac{h_1}{k_1 A} = \frac{1.7(\text{mm})}{34.5(\text{W}/\text{m}^\circ\text{C}) \times 160(\text{mm}^2)} = 0.31(\text{K}/\text{W}) \quad (4.27)$$

where k_1 is thermal conductivity of the aluminium plate and the value is $34.5(\text{W}/\text{m}^\circ\text{C})$ according to datasheet of aluminium material (Aluminium, 2010), and A and h_1 is the surface area and the thickness of the aluminium plate, respectively.

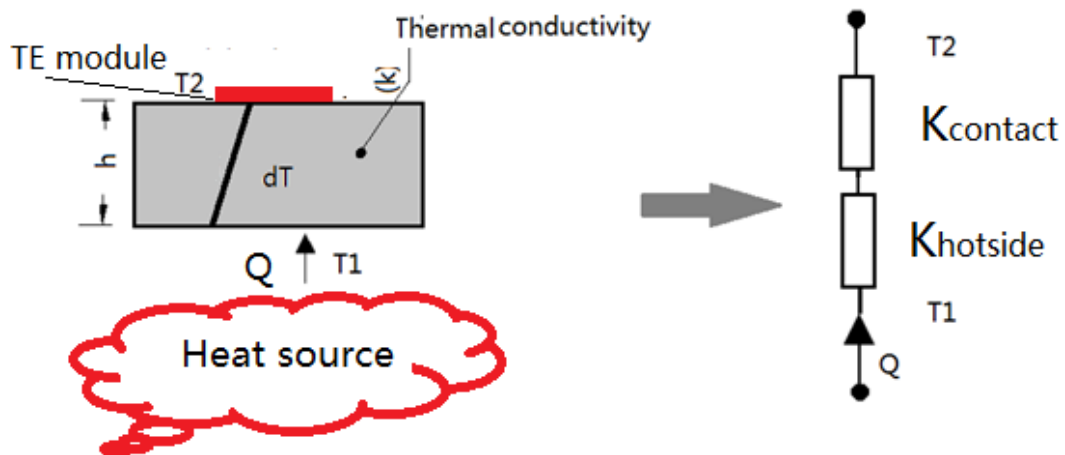
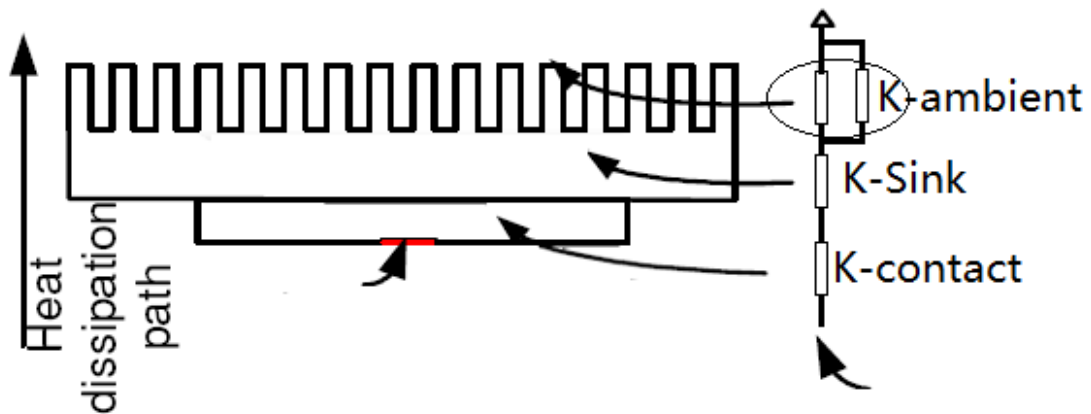


Figure 4.7 Circuit analysis of the hot side heat exchanger

Because the system energy conversion efficiency is dependent on the temperature difference between two sides of the TE module, the cold side heat exchanger is another critical design parameter which should be determined. A solid to air interface is normally used in a lot of TEG systems. But unfortunately, this interface represents the largest barrier for the heat dissipation. Hence, a high efficient heat sink should be used to dissipate the tremendous amount of heat from the cold side of the TE module. The cold side heat exchanger is shown in Figure 4.8 and the overall thermal resistance of the heat sink, $K_{heatsink}$, can further be decomposed into three classical components: thermal resistance of heat sink K_{sink} , thermal contact resistance $K_{contact}$, and thermal resistance of ambient $K_{ambient}$.

$$K_{heat\ sink} = K_{contact} + K_{sink} + K_{ambient} \quad (4.28)$$

**Figure 4.8 Analysis circuit of a heat sink**

Based on Equation 4.13, the thermal resistance of the heat sink is

$$K_{sink} = h_{sink} / (k_{sink} \cdot A_{sink}) \quad (4.29)$$

where h_{sink} is the thickness of the heat sink used in a TEG system, k_{sink} is the thermal conductivity of the heat sink, A_{sink} is the effective surface area of the heat sink.

The thermal resistance between the heat sink and ambient, $K_{ambient}$, is normally estimated by the thermal resistance of convection $K_{convection}$ and the heat body radiation $K_{radiation}$.

$$K_{ambient} = \left(\frac{1}{K_{convection}} + \frac{1}{K_{radiation}} \right)^{-1} \quad (4.30)$$

where the thermal resistance of the convection is:

$$K_{convection} = 1/(h_{conversion} \cdot A_{sink}) \quad (4.31)$$

where $h_{conversion}$ is the convection heat transfer coefficient, which depends on the type of media (gas or liquid) and the flow properties such as flow velocity. Generally, the convective heat transfer coefficient for ambient air h_c is within the ranges of 5-25 W/m²K and $h_c = 10\text{W}/\text{m}^2\text{K}$ (AN-1057, 2009) has been chosen in this chapter. The heat sink radiates the heat to air by the hot body radiation and the thermal resistance of the radiation $K_{radiation}$ is expressed as (AN-1057, 2009).

$$K_{radiation} = \frac{1}{h_{radiation} \cdot A_{sink}} \quad (4.32)$$

where the radiated heat transfer coefficient $h_{radiation}$ is expressed in Equation 4.33.

$$h_{radiation} = \varepsilon\sigma(T_{sink} + T_a)(T_{sink}^2 + T_{ambient}^2) \quad (4.33)$$

where T_{sink} is the hot body absolute temperature (K) of the heat sink, $T_{ambient}$ is the cold surrounding absolute temperature of air, σ is the Stefan-Boltzmann constant ($5.67 \times 10^{-8} \text{ watt}/\text{m}^2\text{K}^4$) and ε is the emissivity of the object, which normally is 0.2-0.31 for an aluminium plate when it has a temperature of 300K .

Thirdly, attaching a heat sink to a semiconductor package requires two solid surfaces being brought together into intimate contact. Unfortunately, no matter how well-prepared, solid surfaces are never really flat or smooth enough to permit intimate contact because all surfaces have a certain roughness. When two rough surfaces are pressed together, they actually touch only at a limited number of discrete parts of the interface, leaving the untouched area filled with air, as shown in Figure 4.9 (a).

Therefore, the real heat transfer area of the joints only occurs at several points of the apparent contact area and the thermal contact resistance is relatively high when the two rough surfaces are placed together. Because two ceramic plates are used as the two surfaces of the TE module to isolate electrical contact of the P- and N- type semiconductor, the surfaces of the TE module is very rough. The thermal contact resistance between the TE module and the hot side heat exchanger, as well as the thermal contact resistance between the TE module and the heat sink are considered in this chapter. As air is poor conductor of heat, it should be replaced by a more conductive material to increase the joints conductivity and to enhance the heat flow across the thermal junctions. Thermal joint compounds, typically bulk properties material, are usually used to enhance the contact area of the junction. Then the surface contact area can be redrawing as illustrated in Figure 4.9 (b).

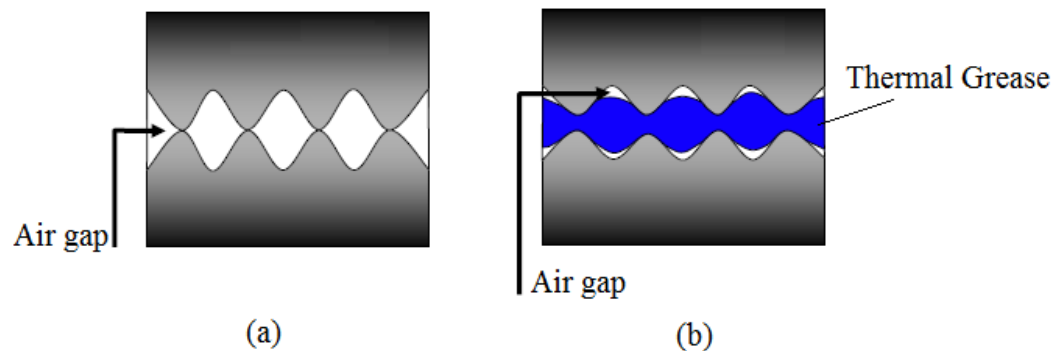


Figure 4.9 (a) Junction with no thermal interface and (b) Junction with thermal interface

Based on the simplified assumption of homogeneous properties of the materials, the joint thermal resistance to the heat flow that incorporates the thermal joint compounds of the interstitial layer can be schematically shown in Figure 4.10.

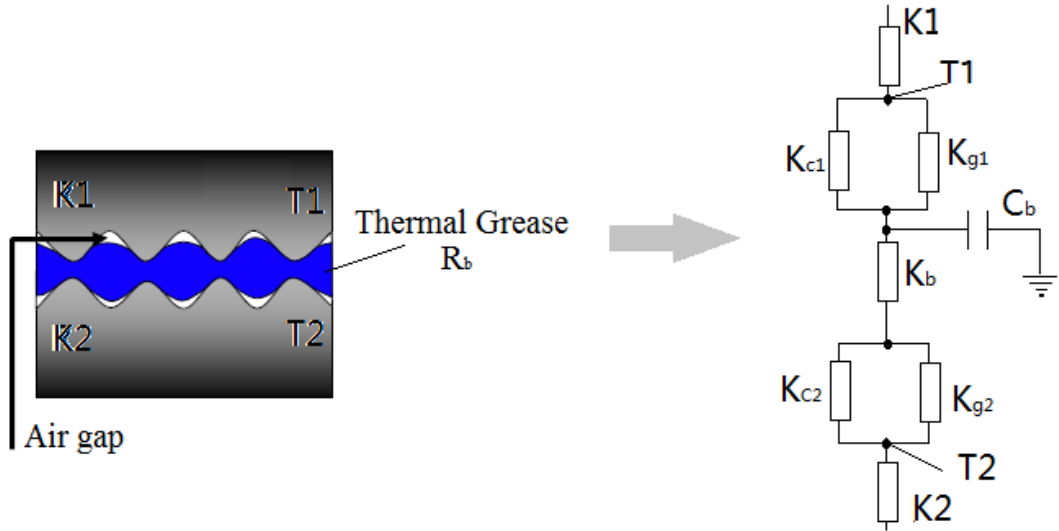


Figure 4.10 Equivalent thermal resistance circuit for two plates with thermal interface material

The joint thermal resistance, K_j , at the interface can be defined as (Marotta et al., 2002)

$$K_j = \left(\frac{1}{K_{c1}} + \frac{1}{K_{g1}} \right)^{-1} + K_b + \left(\frac{1}{K_{c2}} + \frac{1}{K_{g2}} \right)^{-1} \quad (4.34)$$

where K_b is the thermal resistance of thermal interface material, which is determined by the thermal grease used in the system and the thermal contact resistances K_{c1} and K_{c2} can be calculated by using Equation 4.35 (Wang et al., 2010).

$$K_c = \left[\frac{2.5k_1k_2}{k_1+k_2} \left(\frac{m}{\sqrt{\sigma_1+\sigma_2}} \right) \left(\frac{P}{H} \right)^{0.95} \right]^{-1} \quad (4.35)$$

where k_1 and k_2 are the thermal conductivity of the two contacting surfaces, respectively, P is the contact pressure (MPa), H is the surface micro-hardness (MPa) of the softer of the two contacting surface, and σ_1 and σ_2 are the surface roughness (m) of the two adjoining surfaces, respectively. The effective absolute mean asperity slope m can be obtained from the approximate correlation equation from (Antonetti et al., 1993)

$$m = 0.125(\sqrt{\sigma_1 + \sigma_2} \cdot 10^6)^{0.402} \quad (4.36)$$

K_{g1} and K_{g2} from Equation 4.34 are the thermal gap resistances at each interface. They can be calculated by using Equation 4.37 (Antonetti et al., 1993).

$$K_g = (Y + M)/k_g \quad (4.37)$$

where $k_g = 0.024W/mK$, which is the thermal conductivity of air, and M is gas parameter, which is assumed to be zero for the two plates with thermal interface material and Y is the mean plane separation, estimated to be 0.05mm (Antonetti et al., 1993). The model of the heat exchanger subsystem is constructed by integrating the hot side heat exchanger and the heat sink together.

4.3.1.3 Integrated TEG model

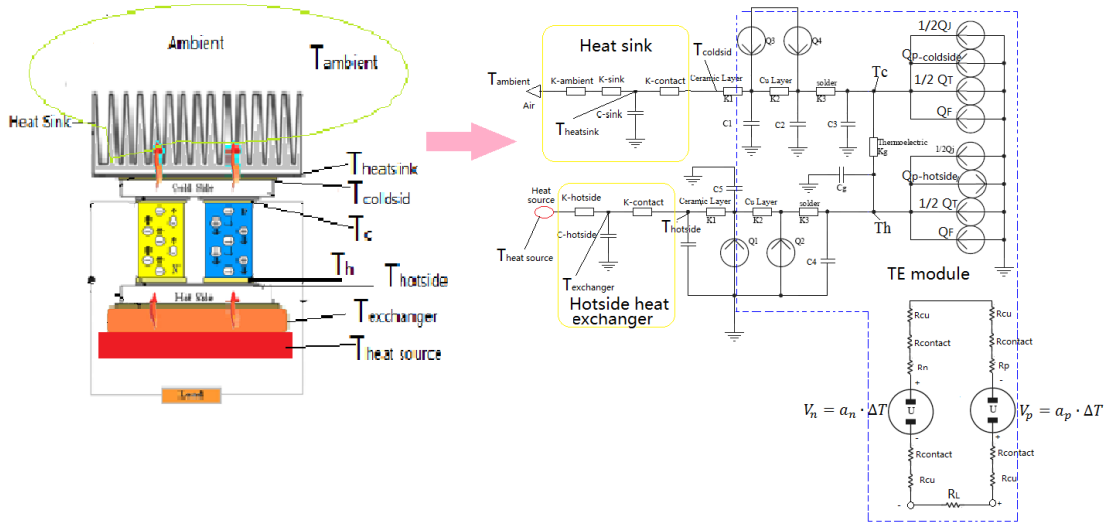


Figure 4.11 The Equivalent circuits of TEGs

The integrated TEG model is comprised of the TE module model and the model of the heat exchanger system, as shown in Figure 4.11. In order to simplify the numerical model, the ideal hot and the cold sources are employed in this work. It is assumed that the hot side heat exchanger is attached to an ideal heat source with a constant temperature $T_{heat\ source}$, while the heat sink is open to an ideal cold source (ambient air) with a constant temperature $T_{ambient}$. $Q_{exchanger}$ is the rate of heat transfer from the heat source to the hot side heat exchanger at temperature $T_{exchanger}$, and Q_{sink} is the rate of heat releasing from the heat sink at temperature T_{sink} to ambient. Then Equations 4.19 and 4.20 can be rewritten as follows:

$$Q_h = \frac{T_{heatsource} - T_h}{K_{hotside} + K_{contact} + K_{cond}} \quad (4.38)$$

$$= \frac{T_h - T_c}{K_g} + \alpha_{seebeck} T_h I - \frac{1}{2} I^2 R_{internal}$$

$$Q_c = \frac{T_{ambient} - T_{coldside}}{K_{sink} + K_{ambient} + K_{contact} + K_{cond}} \quad (4.39)$$

$$= \frac{T_h - T_c}{K_g} + \alpha_{seebeck} T_c I + \frac{1}{2} I^2 R_{internal}$$

The total temperature difference ΔT_{total} applied to the TEG can be expressed as:

$$\Delta T_{total} = \Delta T_g + \Delta T_h + \Delta T_c \quad (4.40)$$

$$\Delta T_h = Q_h (K_{hotside} + K_{contact} + K_{cond})$$

$$\Delta T_c = Q_c (K_{sink} + K_{ambient} + K_{contact} + K_{cond}) \quad (4.41)$$

A cubic equation for ΔT_g can be obtained by combining Equations (4.38-4.41).

$$\Delta T_g^3 + p \Delta T_g + q = 0 \quad (4.42)$$

where

$$p = \frac{T_{heatsource} + T_{ambient}}{\alpha^2 K_{cond}} \frac{(R_g + R_L)^2}{R_L} - \frac{(R_g + R_L)^3}{\alpha^4 K_{cond}^2 R_L} \left(\frac{2K_{cond}}{K_g} + 1 \right) \quad (4.43)$$

$$q = \frac{\Delta T (R_g + R_L)^3}{\alpha^4 K_{cond}^2 R_L} \quad (4.44)$$

Three roots can be obtained from Equation 4.42.

$$\Delta T_{g1} = 2 \sqrt{\frac{-p}{3}} \cos \left[\frac{1}{3} \arccos \frac{q}{2 \sqrt{-\left(\frac{p}{3}\right)^3}} \right] \quad (4.45)$$

$$\Delta T_{g2,3} = -2 \sqrt{\frac{-p}{3}} \cos \left[\frac{1}{3} \arccos \frac{q}{2 \sqrt{-\left(\frac{p}{3}\right)^3}} \pm \frac{\pi}{3} \right] \quad (4.46)$$

Only one real root ΔT_{g1} is meaningful. Hence, the output voltage, current and power of the TEG can be calculated by integrating the real root.

$$U = n \cdot \alpha_{seebeck} \cdot \Delta T_{g1} \quad (4.47)$$

$$I = \alpha_{seebeck} \cdot \Delta T_{g1} / (R_g + R_{Load}) \quad (4.48)$$

$$P_{Out} = I \cdot U \quad (4.49)$$

4.3.2 Model validation

A laboratory prototype of a TEG was built, as shown in Figure 4.12, to determine the accuracy of the computational model. As stated in the previous work, a Bi₂Te₃ TE module is well suited for low temperature applications. The prototype was built by using a commercially available TE module TEC1-12706 (TEC1-12706, 2008) with a size of 40mm × 40mm. The TE module has been inserted between the massive aluminium plate with the size of 85mm × 76mm × 1.7mm and an aluminium heat sink with size of 57mm × 60mm × 40mm. An electric heater was employed to simulate the constant heat source. A thermal insulation box, which is designed by using some pieces of sponge to surround the TE module, has been employed in the prototype in order to thermally insulate the TE module from air. Then the heat flow of the TEG can be consider only be dissipated from the cold side of the TE module through the heat sink to air. In order to maintain a constant room temperature, the prototype has been set in the room with air conditioning, where the room temperature is maintained at 21°C. According to the experimental test, the thermal balance is reached in around 30 minutes. Hence, the prototype of TEG has been tested after the thermal equilibrium was reached. Moreover, in order to demonstrate the maximum power point of the TEG, a 1K potentiometer has been connected to the TEG to imitate the electrical load R_{Load} .

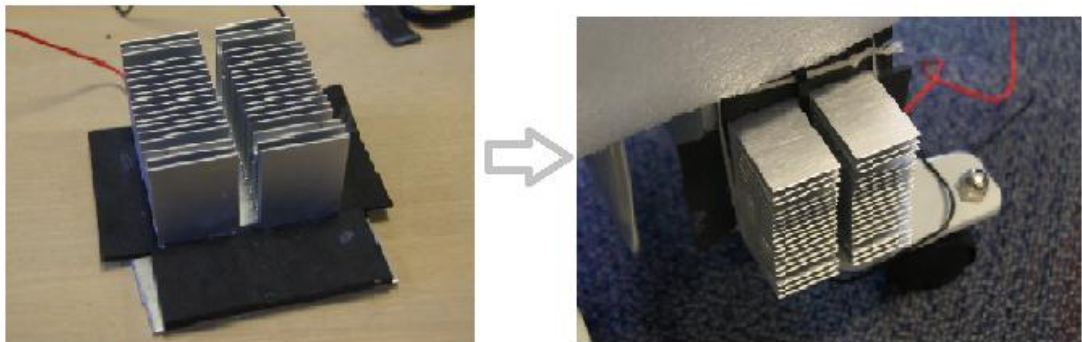


Figure 4.12 Test prototype of thermal energy harvesting**4.3.2.1 Parameter setting**

In order to simulate the experimental conditions by using the proposed model, some parameters of the system should be determined. Normally, the TE properties for both p-type and n-type Bi₂Te₃ semiconductors, which are the Seebeck coefficient (α_{Module}), the thermal resistance of the thermal couple (K_{cond}) and the internal resistance of the module ($R_{internal}$), should be determined before simulation. But unfortunately, the manufactures of TE modules use the following parameters to specify their products, as shown in Table 4.3.

Table 4.3 Performance specifications of TEC1-12706 module

Parameters	Description	Value
T_h	Hot side temperature	50°C
ΔT_{max}	The largest temperature differential that can be obtained between the hot and cold ceramic plates	75°C
I_{max}	The maximum input current added on the TEM to produce the maximum possible ΔT	6.4 A
V_{max}	The maximum DC voltage that will deliver the maximum possible ΔT at the supplied I_{max}	16.4 V
Q_{max}	The maximum amount of heat that can be absorbed at TEM's cold plate at I_{max} and ΔT equal 0°C	57 (watts)

Three equations could be used to calculate the parameters of the proposed model (Lineykin and Yaakov, 2004).

$$\alpha_{module} = n \cdot \alpha_{seebeck} = \frac{2Q_{max} + I_{max}V_{max}}{I_{max}(\Delta T_{max} + 2T_h)} \quad (4.50)$$

$$K_{Module} = \frac{K_g}{n} = \frac{\Delta T_{max}(\Delta T_{max} + 2T_h)}{2Q_{max}T_h - \Delta T_{max}(Q_{max} + I_{max}V_{max})} \quad (4.51)$$

$$R_{module} = n \cdot R_{internal} = \frac{2(I_{max}T_hV_{max} - \Delta T_{max}Q_{max})}{I_{max}^2(\Delta T_{max} + 2T_h)} \quad (4.52)$$

By inserting the parameters from Table 4.3 into Equations 4.50, 4.51 and 4.52, the parameters of the proposed model can be calculated. And thus: $\alpha_{module} = 0.047$ V/K, $R_{internal} = 2.3$ ohms and $K_g = 2.19$ K/W and $n=127$. The other parameters of the TEG system are listed in Table 4.4. A thermally conductive heat sinking compound fills the gaps between the surfaces to lower the contact thermal resistance. And then the thermal resistance of a contact between the TE and the plate is estimated at $K_j = 0.2$ K/W (AN-1057, 2009).

Table 4.4 The parameters of the TEGs

Parameters	Value	Parameters	Value
Effective Area of TE leg	$A = 6.29mm^2$	Thermal resistance of the TEM without TE legs	$K_{cond} = \frac{2.34K}{W}$
Ceramic plate's Height	$L_1 = 0.3mm$	Thermal resistance of the heat sink	$K_{heat\ sink} = 1K/W$
Solder Height	$L_2 = 0.3mm$	Thermal resistance of the hot side heat exchanger	$K_{hotside} = 0.31(K/W)$
Cu lead Height	$L_3 = 0.1mm$	Thermal contact resistance	$K_j = 0.2 K/W$
Thermal conductivity of Ceramic	$k_{aluminumoxide} = 30 W/(m \cdot K)$	Thermal conductivity of solder	$k_{solder} = 67 W/(m \cdot K)$
Thermal conductivity of Cu	$k_{copper} = 401 W/(m \cdot K)$		

The experimental results of physical TE modules are compared with the computer simulation result shown in Figure 4.13. According to the figure, the accuracy of the

computational model can be observed to be around 89%, which means there is a great agreement between measurement and simulation.

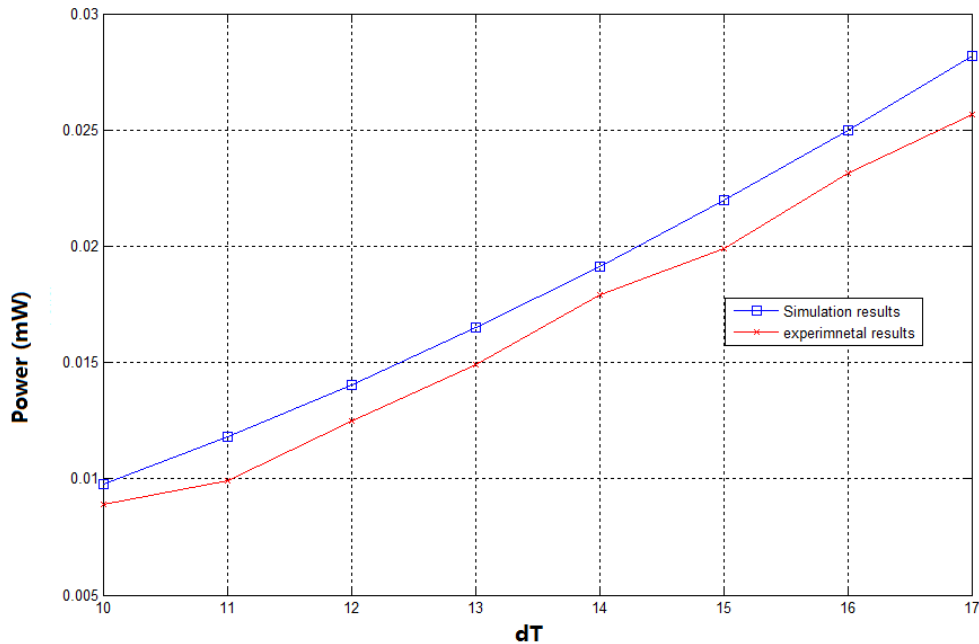


Figure 4.13 Power generated for different ΔT

4.3.2.2 Capabilities of a TE module

As stated in the previous sections, the capability of a TE module is the crucial factor in determining the TEG's conversion efficiency. The capability of a TE module is determined by the TE material parameters, including Seebeck coefficient, internal electrical resistance, and thermal resistance. For the limited heat environment, the maximum system performance can be obtained when the thermal resistance of the TE module equals to the thermal resistance of the heat exchanger system. For the infinite heat environment, the following parameters have been evaluated by the model.

In order to determine the relationship between Seebeck coefficient and the power generated by the TEG, four groups of Seebeck coefficients have been compared by using the simulation model, as shown in Figure 4.14 a. By observing the curves, when the Seebeck coefficient improved 35%, more than 80% of power can be generated by the same system. This is why plenty of research works focus on developing high coefficient TE materials for improving TEG's efficiency. The experimental results of

$a_{seebeck} = 0.047\text{V/K}$ have been compared with the simulation results to show the accuracy of the model, and the results show this to be 90%.

The second parameter being considered in this chapter is the internal resistance of the TE module. Figure 4.14b shows different internal resistances of the TE module influences the output power of the TEG. It can be seen that, the less internal resistance of the TE module has, the more electric power can be generated. According to this rule, the TE module with less internal resistance is preferred in a highly efficient thermal energy harvesting system design. The corresponding internal resistance of 2.3ohms has been evaluated in the laboratory. The accuracy of the model is 91%.

Thirdly, in order to determine how the thermal resistance of the TE module affects the system performance, the thermal resistance of the TE legs and the external thermal resistance of the TE module have been simulated respectively. The simulation results are shown in Figures 4.14 c and d, respectively. In these two figures, the same trend has been found by examining the curves. The maximum power can be generated when the lowest thermal resistance of the module exists. The corresponding experimental results ($K_g = 2.19\text{ K/W}$ and $K_{module} = 2.34\text{ K/W}$) are obtained in the laboratory. The accuracy in these two cases are 91.2% and 90.6%, respectively. Hence, a conclusion can be made that a good TE module should combine a high Seebeck coefficient, a low thermal resistance and a low electric resistance. The simulation results match the corresponding experimental results.

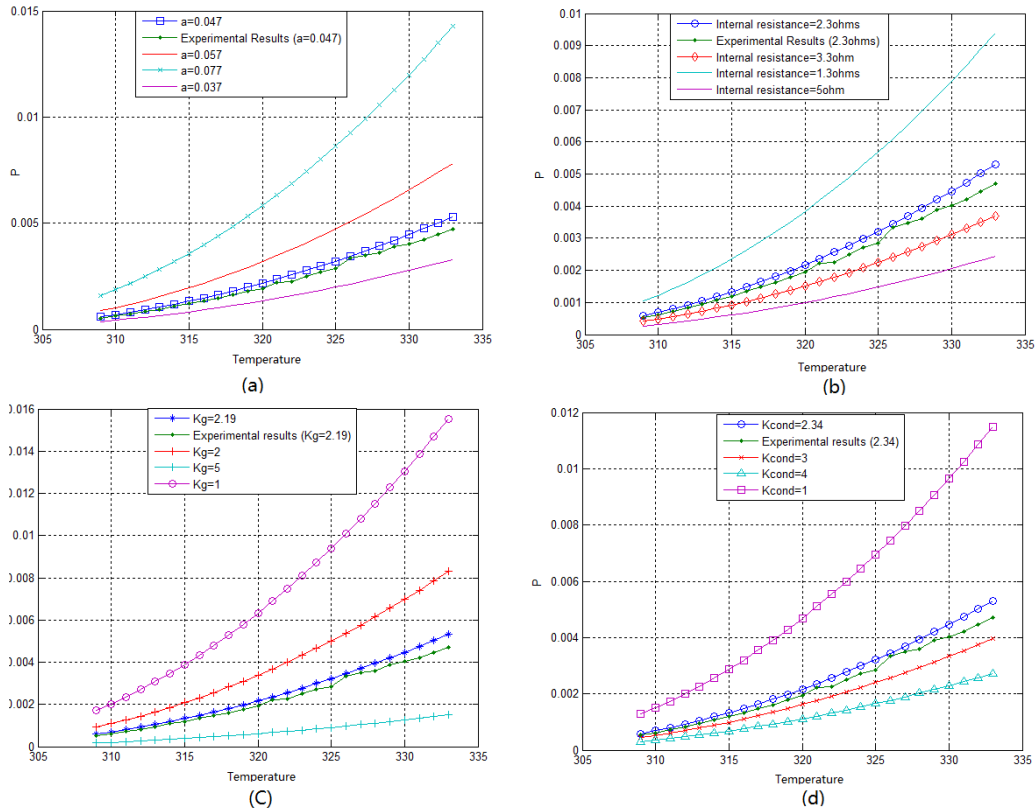


Figure 4.14 (a) Power generated with different Seebeck coefficient (b) Power generated with different internal electric resistances (c) Power generated with different internal thermal resistances (d) power generated with different external thermal resistance of the module

4.3.2.2 Capabilities of a heat exchanger systems

The second evaluation process is to simulate the heat exchanger system and find the corresponding relationship between the performance of the heat exchanger system and the whole TEG system. Similar to evaluate the TE module, four different situations have been considered respectively and the corresponding experimental tests have been carried out to validate the accuracy of the model. Figure 4.15 a, b, c, and d show the results of these four situations. With respect to the material being used in TEG construction, a good thermal conductor is required in order to transfer the heat from the heat source to TE module to achieve high system efficiency. Three kinds of hot side heat exchangers are compared in the model, as shown in Figure 4.15 a. The most efficient one is copper plate, because the thermal behaviour of copper is better than the other two types of metal plates. The corresponding experimental test, which uses an aluminium plate, has been tested in the laboratory with the test setup to show the

accuracy of the model. The results show the accuracy of the proposed model is around 89.7% in the worst case.

As the energy conversion efficiency of the TEG is highly relative to the heat dissipation capability of the heat sink, three types of heat sinks have been simulated by the model, respectively. The simulation results are depicted in Figure 4.15 b. The energy generation of electric power of the TEG is increased by around 50% when the heat dissipation capability has been improved 40%. In order to examine the model, a real experiment, using a 1K/W aluminium heat sink, has been tested in the laboratory and the result shows that the accuracy of the model is around 89.4%. Furthermore, in order to show that the ambient temperature can affect the system performance, the model has been simulated with five different air temperatures. The result is illustrated in Figure 4.15 c. By examining the curves, the generated electrical power is sharply increased by reducing the air temperature. Figure 4.15 d shows that system performance can be affected by the thermal contact resistance of the TEG system. Two different contact resistance values have been integrated into the model to see the difference. According to the curves, the lower thermal contact resistance the system has, the higher generated power the system can achieve. By analysing the contact resistance in Equation 4.34, several critical parameters such as surface roughness of two touching surfaces, contact pressure, density of interstitial gas, heat capacity, thermal and mechanical properties of the filling thermal grease, could be used to determine the value of the contact resistance when two surfaces are attached together. In conclusion, the electric power of the TEG increases considerably when these heat exchangers' thermal resistances, surrounding air temperature, and contact resistance decrease. These results illustrate that how critical of designing a high efficient heat exchanger system (hot side heat exchanger and heat sink), reducing temperature of the surrounding air and reducing the thermal contact resistance in TEG applications. The properly design of the heat exchanger system can easily generated more than double power than the improperly design. This is critical in low temperature TEG applications, which the harvesting efficiency is quite low.

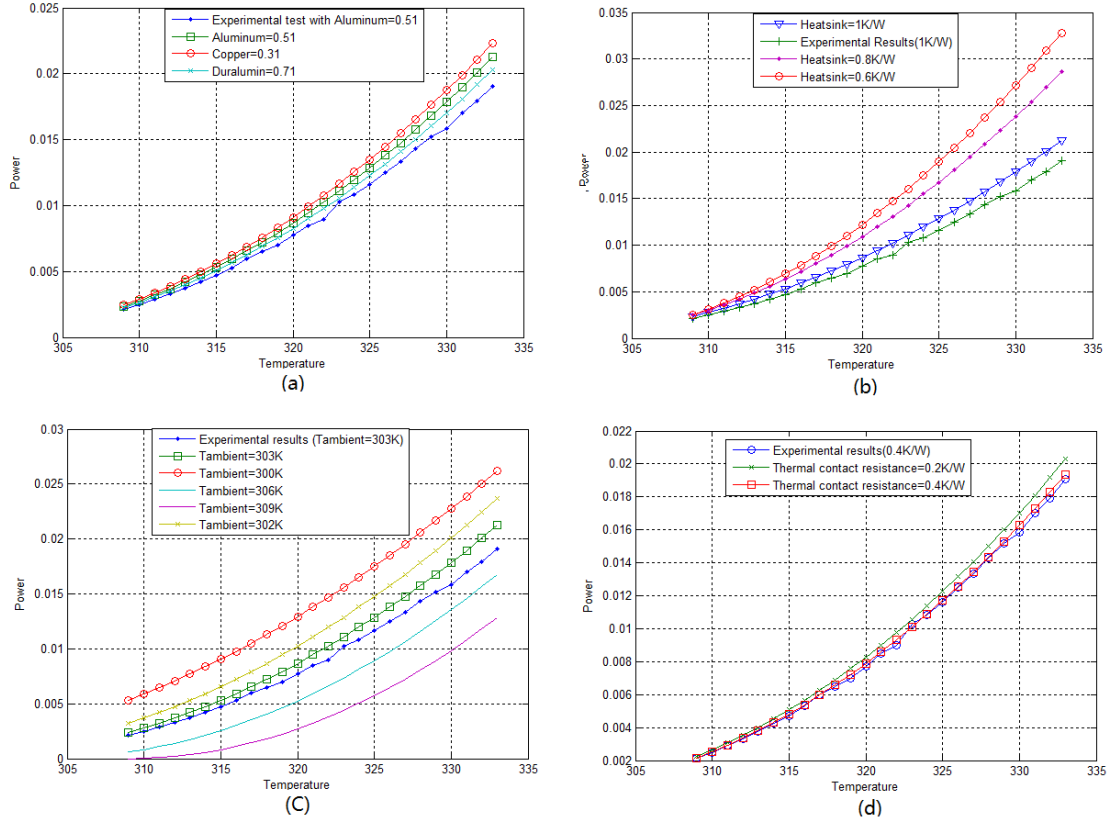


Figure 4.15 (a) Power generated with different hot side heat exchangers (b) Power generated with different heat sinks (c) Power generated with different ambient air (d) power generated with different contact resistance

Whilst keeping the heat source and sink at a stable temperature, change the status of the circuit with different load resistors. The current, voltage and power characteristics of the TEG for different ΔT are plotted in Figure 4.16. As shown in the figure, variations in temperature difference result in variations in output power of the TEG. The same as solar panels, there is a unique MPP for the system at a fixed temperature difference. For instance, the output voltage of the TEG is in the range of 0-0.16V when there is a 10°C temperature difference between the TE module and at the MPP, in which maximum power output is around 0.023W when the system is working at 0.0806V. If the design requires a TEG system working at the MPP, the output voltage of the TEG should always satisfy the half of its open circuit voltage $V_{TEG,OC}$. This can be shown in Equation 4.53

$$V_{TEG,MPP} = \sigma_{TEG} \cdot V_{TEG,OC} \quad (4.53)$$

where $\sigma_{TEG} = 0.5$.

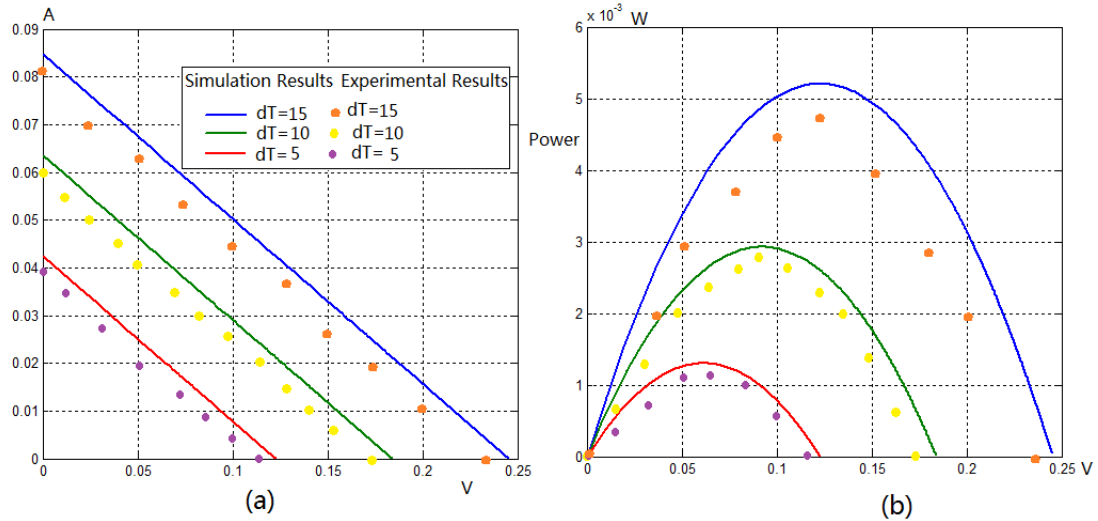


Figure 4.16 (a) power output with different load resistor (b) maximum power point at different ΔT

4.4 Summary

In this chapter, two computational models of a solar panel and a TEG system have been developed, respectively. The feature of these two models is that they are designed based on manufacturers' specification datasheets. This allows the proposed model to be quickly constructed. For the model of a solar panel, the simulation model of a solar cell developed by Petreus et al (2009) is adapted in this chapter because of the fast way to extract five parameters from a solar panel. The test results show that the model is well related with the solar cell placed in the real environment.

For a thermal energy harvesting system, a new computational model, based on manufacturers' specification datasheets, has been developed based on an equivalent circuit which several non-electrical processes are emulated by electrical analogies. The numerical model is used at a system level optimization to determine the optimal design of both the heat exchangers system design and the TE module selection. Two main components, which are a TE module model and the heat exchanger system model, assembly together to emulate the performance of the TEG. The proposed model has been evaluated by the experiments tests held in the laboratory. The accuracy of the model is around 89.4% by showing in the comparison results. Then the model has been simulated in three different ways at the infinite heat situation to show the performance of the TEG is highly dependent on the TE material, the heat exchanger system and load. Based on these findings, the system designers can improve the TEG's

energy conversion efficiency by selecting a proper TE module, designing a high efficient heat exchanger system and tracking MPP of TEG.

By examining the accuracy of the two computation models, the results show that there is a good agreement between the real measurements and simulations. Hence, these two models, which can be used to express the harvested energy in a known environment, will be adopted in the later chapter as the models of energy harvesters.

Chapter 5. Modeling micro-energy harvesting systems

5.1 Background and motivation

The difficulties of building a micro-energy harvesting system are that the complex design process, and the system development and deployment take a long time, especially when a trial-and-error approach is being used. By using this approach, the performance of the developed system highly depends on the designers' experience. Designing a highly efficient micro energy harvesting system needs to face a great number of design parameters and component selections that make even an experienced designer spend a lot of time and effort to figure out a proper solution to enhance the system efficiency. The design processes become harder when the energy harvesting system is designed for a distributed system, in which numerous sensor nodes are randomly placed in a big area. This is because not only the energy sources available at different locations are varied in relation with time, but also the energy consumption of the sensor nodes in the distributed system. Due to the complex system architecture, it is difficult to quickly evaluate the performance of the system at the early design phase and the performance can only be evaluated at a very late stage. If the evaluation result shows a poor system performance or even a functional failure, a new design cycle is needed that normally prolongs the design cycle and increases the expenditure. Moreover, most of the proposed energy harvesting systems are designed based on the worst case scenario which means the systems are oversized and energy inefficient. The compact size, the low system cost and the high energy efficiency are three basic factors which should be included in a micro energy harvesting system, an energy-size-cost efficient design process should be considered in the energy harvesting system design. Additionally, as the everlasting lifetime is desired by the wireless sensor nodes, no existing energy harvesting platforms can provide this capability to the sensor nodes. According to these shortages of the existing energy harvesting platforms,

it is essential to theoretically analyse the performance of the energy harvesting system before it is developed and implemented in a real environment.

Normally, a good simulation model for an energy harvesting system allows the system designers to quickly examine the performance of the proposed energy harvesting system in the early design phase. It can also be used to evaluate the system performance at the different system parameters and design choices. On the other hand, as the simulation model enables systematic design space exploration by various actions, such as lowering the system cost, improving the system efficiency and reliability, it can significantly reduce the inherent design complexity and greatly shorten the development time and cost. Hence, a theoretical analysis by using a simulation model is becoming more and more critical for designing an efficient energy harvesting system. But unfortunately, the system level methods to exploit these sources for optimizing an energy harvesting design are lacking in literature.

5.2 Overview of micro energy harvesting system model

To date, numerical energy models of a wireless sensor node powered by battery have been proposed to support design space exploration (Egea-Lopez et al., 2006), (Merrett et al., 2009). But unfortunately, none of these works have been considered to employ an energy harvesting system as a power source. Since the environmental energy varies and is unpredictable, and the average harvested energy is extremely small, design and optimization of energy harvesting circuits in a wireless sensor node ask for a careful understanding of all aspects of the system, such as energy harvesting capability, battery behavior, DC-DC converter efficiency and energy consumption of sensor nodes. According to this, some energy harvesting system models have been developed in the literature to tune system performance. A general overview of energy device modeling and combination was given in Weddell et al. (2009). They show that the system model can be divided into energy source part, energy storage part and energy consumer's part, but the detail system model was not addressed. An analytical prediction of harvested energy and consequence for battery charge level was examined in Kruger et al. (2009). The presented results show that the model is not accurate enough to optimize system design. Bader et al. (2009) present a simulation model of micro-energy harvesting system, in which the sizing of modules and the sizing of the

system were addressed and their work focused on a simple system architecture, which just has an energy harvester and a super-capacitor. The accuracy of the model was not addressed in their work. A commercial PV cell and a TEG were modelled in Lu et al. (2005). They characterized two commercially available micro-scale energy transducers and based on the characterizations, an optimized power converter system for such ultra-low voltage energy transducer was developed. They stated that the proposed power converter results in an increase in harvested power by up to 30% compared to linear topology charge pump based designs. But the entire energy harvesting system model was not considered in their work. Later, Jeong described modeling a micro-solar power system in his thesis (Jeong, 2009) and the primary goal of his model was used to validate his system architecture rather than a dimension of a given system architecture. A further work described by Jeong was published in Taneja et al. (2008), which addressed capacity planning of micro solar energy harvesting systems. But their work focused on how to implement a micro-system rather than analyse the system.

By analysing the existing works of the simulation model for energy harvesting systems, it can be found that some of them have focused only on a particular component of an energy harvesting system and in this case the performance of the entire system cannot be predicted. Other works focus on using the models to validate the system but they do not consider using the model to guide an energy harvesting system design. In this chapter, a high level simulation model is developed to capture the inherent design parameters and choices to tune the system performance of an energy harvesting system. In order to make the model adaptable for other applications or other types of energy harvesting technologies, the model is designed based on the generic system architecture, proposed in Chapter 3. Distinguished from the existing works, the simulation model can be used to guide the system design and the selection of the system components, such as the energy harvester, the power converter circuit, the energy storage elements and the target sensor node. Two energy harvesting technologies, solar and thermal energy harvesting technologies, have been chosen as examples to validate the proposed model. The performances of the two models have been compared with corresponding experiments.

The model is considered the best way to bridge the gap between the physical world and the theoretical analysis. It enables a system designer to quickly evaluate the

impact of various design choices and the system parameters of an energy harvesting system at an early design phase. It can also be used to estimate the energy status of each component of the system without measuring it by physical connection. In order to simplify the model design procedure, an energy flow of an energy harvesting system based on the proposed generic system architecture has been proposed, as depicted in Figure 5.1. Firstly, the energy harvesting device harvesting energy from environment and converter it into electrical energy. By using a MPPT device, the maximum power of the harvested energy can be delivered to a DC-DC converter circuit, which boost this energy to a proper voltage level. The regulated energy will charge the supercapacitor. With a decision generated by a control unit of energy storage subsystem, the supercapacitor will directly power the target sensor node or charge the rechargeable battery. Then the model of the entire energy harvesting system can be divided into the model of an energy harvester, the model of the power conversion circuit, the model of the energy storage subsystem, and the model of the target sensor node. In this chapter, the models of two types of energy harvesters, solar and thermal, developed in Chapter 4, are adopted. Then the system modelling procedure can be focused on modeling the electrical circuit parts of the energy harvesting system.

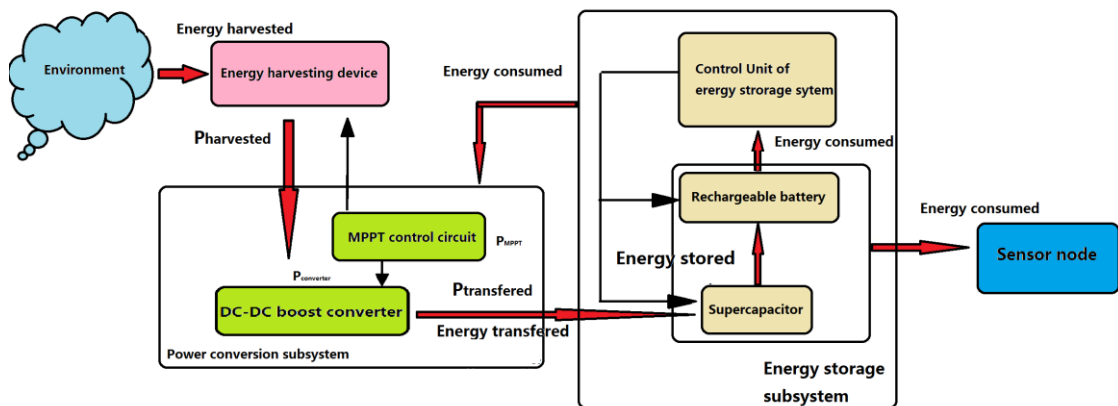


Figure 5.1 Energy flow of a micro-energy harvesting system

5.3 Model of a power conversion circuit

As said in Chapter 3, the power conversion circuit is used to extract as much energy as possible from the energy harvester and convert this energy into a useful level to charge or power the system. In this thesis, because the power conversion

circuit is designed for solar and thermal energy harvestings, the proposed model cannot be used for other type of energy sources, such as kinetic energy.

The complete power conversion circuit has two main components, which are the DC-DC converter circuit and the MPPT circuit, as shown in Figure 5.1. Due to an ultra-low harvested energy generated from a micro energy generator, a switching power DC-DC boost converter is used to regulate the input voltage to a constant high output voltage for the target system. This is because this type of converters is commonly available on the market with high energy conversion efficiency. Based on the different harvesting technologies, some energy transducers' output power is alternating current (AC) power, which cannot be directly used to power the electronics. An optional rectifier circuit is used to convert AC power into DC power. Because only solar and thermal energy harvesting technologies, which are DC power generators, are considered in this thesis, the rectifier circuit is neglected. The second component of the power conversion circuit is an MPPT unit, which is designed to maintain the energy harvester operating at its peak power mode.

If the energy transfer efficiency of the power conversion circuit is identified, the available energy for the next circuit of the energy harvester system can be determined. According to the proposed generic system architecture given in Chapter 3, three kinds of energy losses in the power conversion circuit can be identified, as shown in Figure 5.2. The first energy loss in the power conversion circuit is a mismatching between the energy generator and the power conversion circuit, which reduces the energy extracted from the energy generator. Despite the fact that an MPPT unit can significantly improve the energy being extracted from the energy generator, there is a mismatch still between the system operation point and the MPP. Normally, an MPPT efficiency η_{MPPT} is used to identify the energy loss between the operation point and the MPP of the energy harvester. Since no electrical circuit is seen as ideal, no boost converter circuit can completely transfer the input energy to the output energy. The second energy lost that in the DC-DC converter circuit. This can be illustrated by the transfer efficiency of the boost circuit $\eta_{converter}$. Because the harvested energy is extremely small, the energy dissipated by the MPPT circuit cannot be neglected. The third energy loss in the power conversion circuit is the energy consumed by the MPPT circuit. In order to simplify the model construction process, the model of the power conversion

circuit can be divided into the model of the MPPT unit and the model of a DC-DC boost converter.

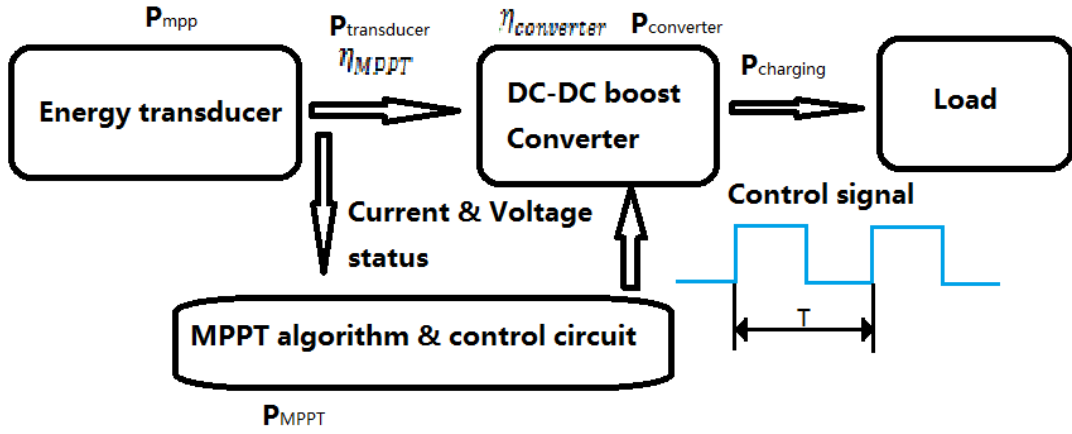


Figure 5.2 General Architecture of power conversion circuit

5.3.1 Model of the MPPT unit

The model of the MPPT circuit can be divided into two parts: (1) energy loss caused by the mismatching between the MPP and the operation point of the energy harvester and (2) the energy consumed by the MPPT circuit. Numerous MPPT technologies have been proposed in literatures which vary at the MPPT efficiency and the circuits' overhead. Hence, the power extracted from the energy generator $P_{transducer}$ can be expressed as:

$$P_{transducer} = P_{harvested} \cdot \eta_{MPPT} - P_{consume,MPPT} \quad (5.1)$$

where $P_{harvested}$ is the power harvested by the energy generator, and η_{MPPT} is the MPPT efficiency by using a type of MPPT unit, and $P_{consume,MPPT}$ is the power dissipation of the MPPT circuit. In this work, a typical $\eta_{MPPT} = 0.85$ is used to identify the MPPT efficiency. $P_{consume,MPPT}$ is assumed independent of the load condition and it can be expressed in Equation 5.2.

$$P_{consume,MPPT} = V_{consume,MPPT} \cdot I_{consumer,MPPT} \quad (5.2)$$

where $V_{consume,MPPT}$ and $I_{consumer,MPPT}$ are the voltage crossed and current consumed by the MPPT circuit, respectively.

5.3.2 Model of the DC-DC boost converter

In order to provide a sufficient voltage for a portable system from a micro-scale energy harvester, boost DC-DC pulse width modulated (PWM) converters are widely used. The boost converters can be classified into the asynchronous type and the synchronous type. A general diagram of an asynchronous boost converter is depicted in Figure 5.3. It consists of a power semiconductor switch Q , a diode D , an input filter inductor L , an output capacitor C , and a resistor R . A control signal, which has a switching cycle duration T_{time} , is applied to the semiconductor switch Q to turn the converter on/off.

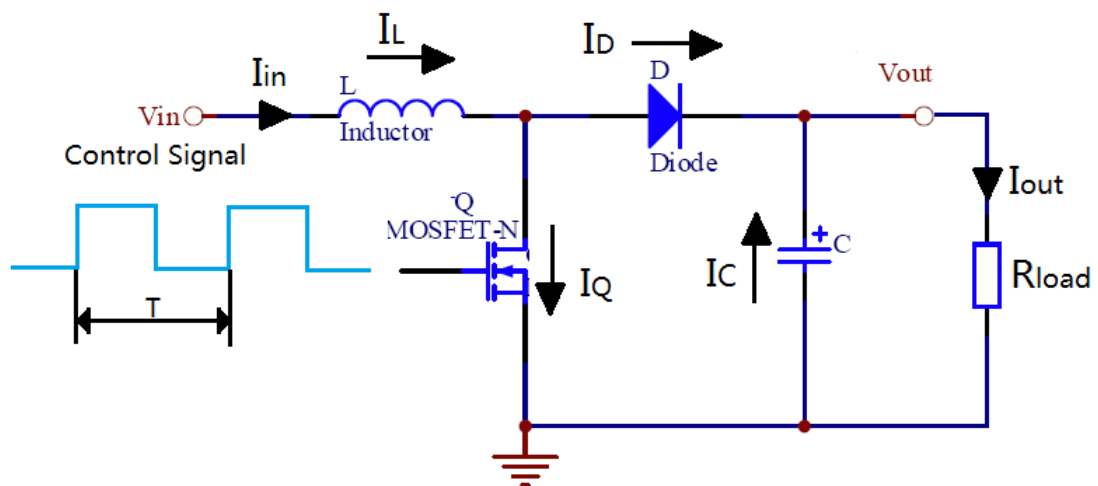


Figure 5.3 Simple asynchronous DC/DC boost converter structure

A synchronous boost converter circuit is shown in Figure 5.4. It has the same working principle as the asynchronous one. The difference between the two types of boost circuits is that a synchronous boost converter uses a p-type MOSFET Q_2 with a proper control signal, depicted in Figure 5.4, to replace a diode D , as shown in Figure 5.3. Normally, a synchronous one is considered more efficient than an asynchronous one, because of avoiding using a big energy consuming diode in the circuit. Due to the high energy efficiency desired by the system, a synchronous type boost converter is selected as the power regulator circuit in this thesis.

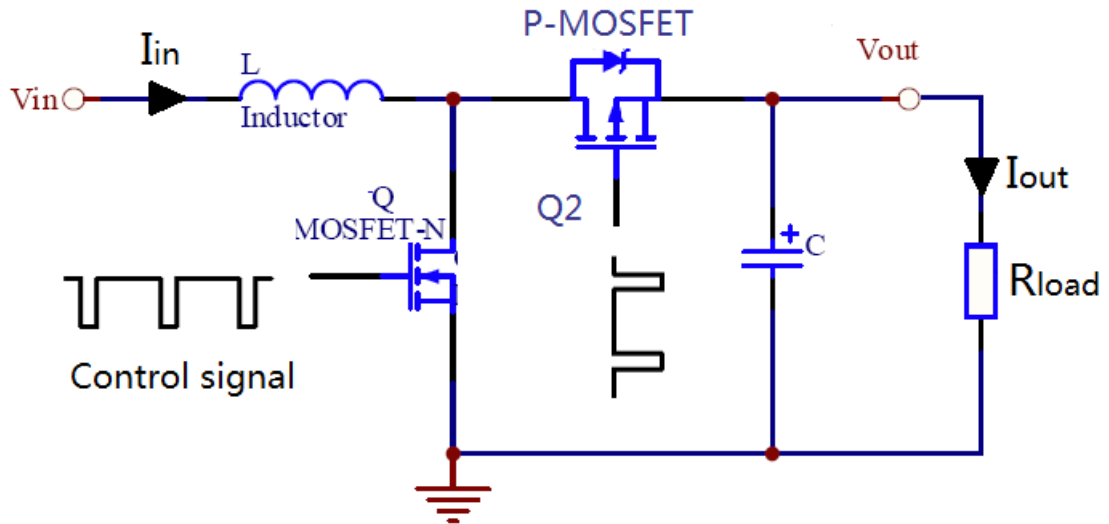


Figure 5.4 Synchronous boost converter

Normally, a commercial boost converter is used to build a power conversion circuit for boosting a low input voltage to a constant high output voltage because of its high system efficiency, low cost and compact size. Hence, the boost converter should operate over a wide range of input voltages. However, the datasheets provided by the manufacturer, which only depict the energy efficiency curve of the circuit at a certain operation point. This is not sufficient for calculating the energy transfer efficiency of the boost converter, because the same device may be used at different input voltages. Thus, in order to predict the performance of the boost converter in any input voltage conditions, a simulation model, which can provide a quick and easy way to obtain the system's efficiency without needing to make laboratory measurements, is needed. Over the last two decades various approaches to model DC-DC converters in continuous conduction mode (CCM) and discontinuous conduction mode (DCM) have been developed. Based on these existing works, an approach by identifying all of the individual power losses in the converter circuit as proposed in Aloisi and Palumbo (2005) and Liu et al. (2008) has been adopted in this chapter. The power losses in the inductor $P_{inductor}$, the capacitor $P_{capacitor}$, the two MOSFET transistors $P_{MOSFET,1}$ and $P_{MOSFET,2}$ are the main power dissipation sources in a DC-DC converter circuit. Despite many manufacturers stating that the power dissipation of the control circuit and the power lost in the miscellaneous circuit in the commercialized DC-DC converter IC are extremely low, these energy consumptions cannot be neglected in a micro energy harvesting system because of an ultra-low harvested energy. Similarly, the energy consumed by the MPPT control circuit, the static power dissipation of the

boost IC can be consumed independent of the load condition. Hence, the power consumed by the boost IC $P_{controller,IC}$ is expressed as:

$$P_{controller,IC} = V_{controller, IC} \cdot I_{controller, IC} \quad (5.3)$$

where $V_{controller, IC}$, $I_{controller,IC}$ are the voltage across the boost IC and the quiescent current of the boost IC, respectively.

Then the power dissipation of the boost converter circuit can be expressed as adding these power dissipation sources together, as expressed in Equation 5.4.

$$P_{converter} = P_{inductor} + P_{capacitor} + P_{MOSFET,1} + P_{MOSFET,2} + P_{controller,IC} \quad (5.4)$$

And the efficiency of the boost converter can be written as:

$$\eta_{converter} = \frac{P_{transducer} - P_{converter}}{P_{transducer}} 100\% \quad (5.5)$$

where $P_{transducer}$ is the power extracted from the energy generator, introduced in the previous section.

To achieve a simple numerical model, a generic model is adopted from Aloisi and Palumbo (2005). The advantage of using this model is that all the parasitic components and their power losses of the boost converter are considered. Figure 5.5 shows all the components of the boost converter in relation to their own parasitic resistance. In order to simplify the analysis, some assumptions, which are made by (Aloisi and Palumbo, 2005), have been used in this chapter.

- The N-type transistor Q is seen as a capacitor, C_Q parallel connection with a series combination of a linear resistor R_Q , and a switch S_1 , which can switch on or off by a control signal.
- Similar to N-type transistor Q, the P-type transistor Q_2 is assumed as the capacitor C_{Q2} connected with a series combination of a linear resistor R_{Q2} and switch S_2 . S_2 is controlled by the boost IC.
- Passive components like inductors and capacitors are assumed to be linear, time invariant and frequency independent. In addition, the equivalent series resistance (ESR), R_L and R_C , of the inductor and the capacitor, respectively, are supposed to be independent from their operating temperature.

- Power dissipation in the control circuit is consumed at a constant value $P_{controller,IC}$ in this work
- Assuming the transistor Q is turned on and off at the constant switching frequency, $f_s = 1/T$, where T is the entire switching cycle.
- R is the load resistor.

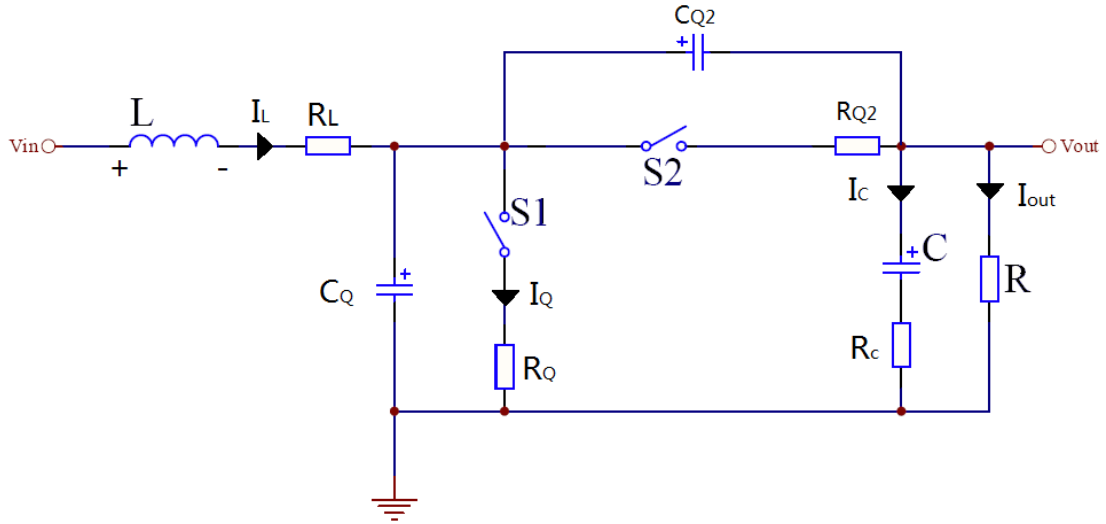


Figure 5.5 boost converter equivalent circuit including the parasitic components

As stated in the previous part, a boost converter can operate in DCM and CCM modes. These two modes are defined based on the inductor current condition of a boost converter circuit. The operation mode of DCM can be classified in terms of the energy stored in the inductor, which is delivered to the load during each switching cycle and the inductor current ramps down all the way to zero during the switch off time. Otherwise the mode is classified as CCM when only part of the energy is delivered to the load. As shown in many research works, the performance of a boost converter in the CCM and the DCM are significantly different in terms of voltage regulation and energy transfer efficiency. Thus, the model of a boost converter should be constructed in both of the CCM and the DCM, respectively.

(A) Boost converter in the CCM

Assume the boost converter is working in CCM. The ratio M, related to the input and output voltage can be obtained as follows:

$$M = \frac{V_{converter,out}}{V_{converter,in}} = \frac{1}{1 - D} \quad (5.6)$$

where $V_{converter,out}$ and $V_{converter,in}$ are the output and input voltage of the boost converter and D is duty cycle of the boost converter, which is expressed as:

$$D = \frac{T_{on}}{T_{on} + T_{off}}$$

where T_{on} and T_{off} are the duration of the “on” state and “off” state of the converters, respectively.

(1) Power dissipation in the inductor

The power dissipation in the inductor is caused by the conduction loss in it and this can be expressed as (Aloisi and Palumbo, 2005)

$$P_{inductor} = R_L \cdot I_{L,rms}^2 \quad (5.7)$$

where $P_{inductor}$, R_L , and $I_{L,rms}$ are the power dissipation, Equivalent Series Resistance (ESR) and Root Mean Square (RMS) current of the inductor using in the boost converter circuit, respectively. $I_{L,rms}$ can be expressed by Equation 5.8.

$$I_{L,rms} = [(M \cdot I_{out})^2 + \frac{\Delta I_L^2}{12}]^{\frac{1}{2}} \quad (5.8)$$

where I_{out} is the output current of the boost converter and ΔI_L is the ripple of the inductor current, which is given by:

$$\Delta I_L = \frac{V_{out}}{L \cdot f_s} \frac{M - 1}{M^2} \quad (5.9)$$

where V_{out} is the output voltage of the boost converter and L is the inductance of the inductor. In order to simplify calculation, an assumption of $\Delta I_L = 0.3 \cdot I_{out}$ is typically used to calculate ΔI_L . This is adopted in this work. By applying these in Equation 5.8, the inductor current can be calculated by Equation 5.10.

$$I_{L,rms} = I_{out} \times 1.00375 \quad (5.10)$$

(2) Power dissipation in N-type MOSFET

The power consumption of N-type MOSFET $P_{MOSFET,1}$ consists of a conduction loss P_Q , which is caused by the turn-on resistance R_Q , and a switching loss $P_{M,SW}$,

which is caused by V-I overlapping and parasitic capacitances charge and discharge (Aloisi and Palumbo, 2005)

$$P_{MOSFET,1} = P_Q + P_{M,SW} \quad (5.11)$$

$$P_Q = R_Q I_{M,RMS}^2 = R_Q \frac{M-1}{M} I_{L,RMS}^2 \quad (5.12)$$

where $I_{M,RMS}$ is RMS current of switching the transistor. It is assumed that either the switching transistor current or voltage rises or falls linearly when the transistor switches. Then, the switching loss caused by parasitic capacitances and overlapping is

$$P_{M,SW} = \frac{1}{2} (V_{ce(sat)} + V_F) \left(M I_{out} + \frac{\Delta I_L}{2} \right) (t_{rv} + t_f) f_s \quad (5.13)$$

where t_{rv} and t_f are the rise and fall times of drain-source voltage and drain current, respectively, and $V_{ce(sat)}$ and V_F represent the “on” state voltage of the MOSFET switch and the forward voltage drop in the body diode, respectively.

(3) Power dissipation in the P-type MOSFET

The power consumption of the P-type MOSFET Q_2 ($P_{MOSFET,2}$) is similar to the N-type MOSFET and it can be expressed as:

$$P_{MOSFET,2} = P_{Q,2} + P_{M,SW} \quad (5.14)$$

$$P_{Q,2} = I_{RMS-Q2}^2 \times R_{Q2} = \frac{V_{converter,out}}{V_{converter,in}} I_{L,RMS}^2$$

where R_{Q2} is the on-time drain-to-source resistance of the P-MOSFET and I_{RMS-Q2} is RMS current of the P-MOSFET.

(4) Power dissipation in the output capacitor

For the power dissipated by the output capacitor $P_{capacitor}$, it is caused by the ESR of the capacitor R_C . The expression can be written as:

$$P_{capacitor} = \frac{R_C}{M} I_{L,RMS}^2 - R_C I_{out}^2 \quad (5.15)$$

(5) Power dissipation in the entire boost converter circuit

The switching loss of the converter IC is neglected in the model in order to simplify the calculation. By collecting these power dissipation sources of the boost converter together, the total power dissipated by the circuit can be written as follows.

$$\begin{aligned}
 P_{converter} &= P_{inductor} + P_{capacitor} + P_{MOSFET,1} + P_{MOSFET,2} + P_{controller,IC} \quad (5.16) \\
 &= R_L \cdot I_{L,rms}^2 + \left(\frac{R_C}{M} I_{L,RMS}^2 - R_C I_{out}^2 \right) + R_Q \frac{M-1}{M} I_{L,RMS}^2 + V_F \cdot I_{out} + \frac{R_D}{M} I_{L,RMS}^2 \\
 &\quad + V_{controller} \cdot I_{controller}
 \end{aligned}$$

(B) Boost converter in the DCM

When the boost converter is operating at the DCM, the formulae of the power dissipation of the inductor, the output capacitor and the N-type MOSFET switches are the same as expressed in the CCM. The differences are the expressions of $I_{L,rms}$ and $P_{M,SW}$ (Aloisi and Palumbo, 2005).

$$I_{L,rms} = I_{out} \cdot \left[\frac{8}{9} \cdot \frac{M(M-1)V_{out}}{L \cdot f_s \cdot I_{out}} \right]^{1/4} \quad (5.17)$$

$$P_{M,SW} \approx \frac{1}{2} (V_{out} + V_{F,Mosfet}) I_{out} \sqrt{\frac{2V_{out}}{L \cdot f_s \cdot I_{out}} \frac{M-1}{M}} (t_{rv} + t_f) \quad (5.18)$$

By ignoring $P_{M,SW}$, the simulation model can be developed by integrating Equation 5.17 with Equation 5.16.

(C) Model Validation

A commercial synchronous boost converter TPS61222 (TPS61222, 2010) from TXAS instruments is employed in this chapter to evaluate the proposed model of the boost converter. This is because the TPS61222 has high system efficiency with an ultra-low input voltage, which can be operated as low as 0.7V input voltage range. The technical parameters are listed in Table 5.1 and all the parasitic parameters of the circuit components are extracted from their datasheets.

Table 5.1 Main technique parameters for TPS61222 and external components

Parameters	Value
L, R_L	4.7uH, 145mohms
C, R_C	10uF, 2ohms
R_{Q2}	1000m Ω
R_Q	600m Ω
$f_{s(\max)}$	2000kHz(2.4V)
TPS61222 Quiescent current $I_{controller}$	5.5 μ A
$V_{controller}$	3.3V
Output voltage	5V

In order to identify the converter operating at the CCM or DCM, an approximation equation from the datasheet (TPS61222, 2010), has been used.

$$\frac{V_{out} \times I_{out}}{V_{in}} > 0.8 \times 100mA \quad (5.19)$$

As long as the in-equation 5.19 is true, the boost converter operates in the CCM, otherwise the converter operates in the DCM. Then the model has been validated by comparing the efficiency curves, which are provided by the manufacturer in order to examine the accuracy of the model. A 5V constant output voltage has been set by the model. Then three types of input voltages (2.4V, 1.2V and 0.7V) have been simulated, respectively. The simulation results have been compared with the corresponding experimental results, supplied by the manufacturer, as shown in Figure 5.6. By examining the curves, the error of the model is around 5% in the worst case scenario. Furthermore, in these three input voltage ranges, the converter circuit is most efficient when the 2.4V input voltage is applied and the 0.7V curve shows the circuit has the

lowest power conversion capability. This trend shows that when the input voltage is closer to the output voltage, the boost converter has a higher energy transfer capability.

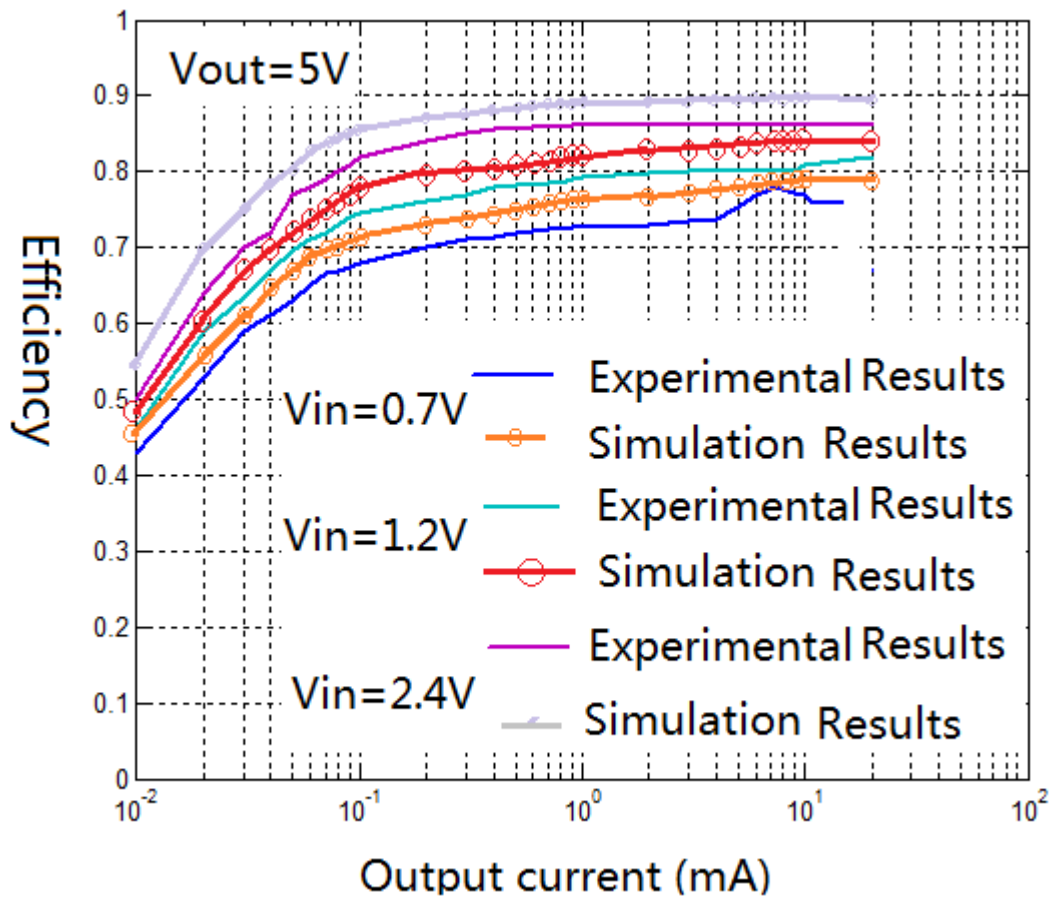


Figure 5.6 Output current vs. Efficiency (2.4V and 1.2V input voltage)

Figure 5.7 shows the efficiency of the boost converter by the fixed output power in relation to the various input voltages. In order to show the difference, three output conditions (10mA, 1mA and 100uA) have been simulated. The simulation results have been compared with the corresponding efficiency curves described in the datasheet. The error of the model is around 5% when comparing the results. In these three cases, the most efficient curve is found when the output current is fixed at 10mA. This is because the efficiency of the boost converter is increased with the increase of input power. In summary, the proposed model of the boost converter can be used to predict the energy condition of the regulator circuit.

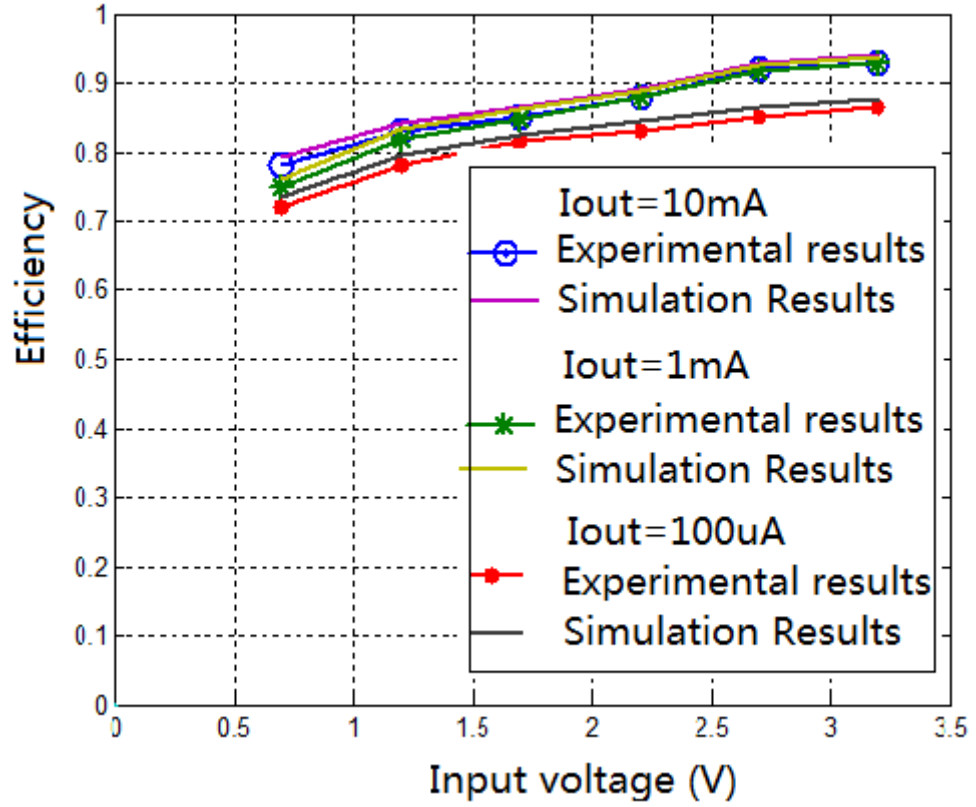


Figure 5.7 Different input voltages vs. energy transfer efficiency

5.3.3 Model of the entire power conversion subsystem

According to the figure shown in Figure 5.2, the model of integrated power conversion circuit can be developed by integrating the model of the MPPT circuit and the model of the boost converter together. The output power of the power conversion circuit $P_{charging}$ can be determined by knowing the power lost in the individual components of the power conversion circuit and the formula of $P_{charging}$ can be expressed as:

$$\begin{aligned}
 P_{charging} &= P_{transducer} - P_{converter} & (5.20) \\
 &= P_{harvested} \cdot \eta_{MPPT} - V_{consume,MPPT} \cdot I_{consumer,MPPT} - (P_{inductor} + P_{capacitor} \\
 &\quad + P_{MOSFET,1} + P_{MOSFET,2} + P_{controller,IC})
 \end{aligned}$$

5.4 The model of the energy storage subsystem

The energy storage subsystem is designed to accumulate the available energy and to sustain the system when no energy can be harvested. According to the generic architecture described in Chapter 3, a hybrid energy storage design (Park and Chou 2006), which combines super-capacitors and rechargeable batteries, are considered in this work to take advantage of two complementary technologies providing an everlasting lifetime to the system. Table 5.2 lists some commonly used energy storage elements and their characteristics, along with energy density, power density, volume, weight, self-discharge rate, charge-discharging efficiency, cycle life, cost, and charging method.

Table 5.2 Different types of energy storage elements for micro-energy harvesting system (Taneja et al., 2008)

Type	Lead Acid	NiCd	NiMH	Li-ion	Li-polymer	Super-capacitor
Make	Panasonic	Sanyo	Energizer	Ultralife	Ultralife	Maxwell
Model No.	LC-R061R3P	KR-1100AAU	NH15-2500	UBP053048	UBC433475	BCAP0350
Nominal voltage	6 V	1.2V	1.2V	3.7V	3.7V	2.5V
Capacity	1300mAh	1100mAh	2500mAh	740mAh	930mAh	350F
Energy	7.8Wh	1.32Wh	3.0Wh	2.8Wh	3.4Wh	0.0304Wh
Weight energy density	26Wh/Kg	42Wh/Kg	100Wh/Kg	165Wh/Kg	156Wh/Kg	5.06Wh/Kg
Volume energy density	67Wh/L	102Wh/L	282Wh/L	389Wh/L	296Wh/L	5.73Wh/L
Weight	300g	24g	30g	17g	22g	60g
Volume	116.4cm ³	8.1cm ³	8.3cm ³	9.3cm ³	12.8cm ³	53cm ³
Self-discharge (per month)	3%-20%	10%	30%	<10%	<10%	5.9%/day
Charge-discharge efficiency	70%-92%	70%-90%	66%	99.9%	99.8%	97%-98%
Capital cost (\$/kWh)	100-200	800-1000	450-1000	600-2500	600-2500	20,000-50,000
Cycle life	500-800	2000-2500	500-1000	1000-10,000+	1000-10,000+	50,000+

(cycles)						
Memory effect	No	Yes	No	No	No	No
Charging method	Trickle	Trickle/pulse	Trickle/pulse	Pulse	Pulse	Trickle

Figure 5.8 schematically shows the structure of proposed active hybrid energy storage subsystems which comprise input and output stages, a rechargeable battery and a super-capacitor associated with a control circuit. In order to provide a high buffering efficiency in relation with an everlasting system lifetime, the energy storage subsystem will be operated in four different states:

- Sustaining the system by directly using environment energy when enough energy can be harvested from the environment;
- Charging the rechargeable battery and meanwhile powering the system when a sufficient harvested energy is available on the system;
- Using rechargeable batteries to power the system when insufficient energy or no energy can be harvested from the environment;
- Disconnect rechargeable battery when the battery is overcharged or over-discharged.

In order to achieve these functions, the following processes should take place. Firstly, the entire energy harvesting system draws energy from the rechargeable battery and uses the energy to sustain the whole system operation. The super-capacitor is directly connected to the power conversion subsystem and it is charged with a constant output voltage from the boost converter. When sufficient energy is available on the super-capacitor, which can directly power the whole energy harvesting system, the system stops drawing energy from the rechargeable battery and switches to using the super-capacitor powering the system. Due to the linear relationship between the voltage and the energy of the super-capacitor, a voltage threshold $V_{W,th1}$ is set for the system to indicate if the super-capacitor can directly power the system. In this situation, the super-capacitor is still being charged when sufficient energy is harvested by the energy generator. As long as the energy level of the super-capacitor is rising, when the second charge threshold $V_{W,th2}$ is reached, the super-capacitor charges both the rechargeable battery and powers the sensor node at the same time. According to

the electrical characteristics of the super-capacitor, the energy on the super-capacitor could quickly be transferred to the rechargeable battery. After the super-capacitor quickly charges the rechargeable battery, the capacitor's voltage drops rapidly. When it drops below the third threshold $V_{W,th3}$, the super-capacitor stops charging the rechargeable battery but still powers the entire system. If there is no harvested energy, or the harvested energy is not enough to power the system, the energy of the super-capacitor drops. As soon as it drops below the fourth voltage threshold $V_{W,th4}$, the system switches to using the rechargeable battery to power the system and the super-capacitor is charged.

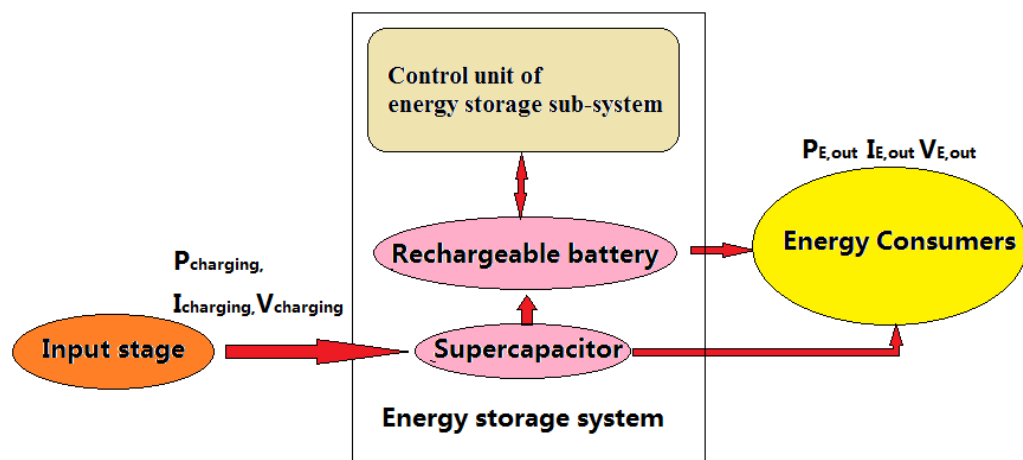


Figure 5.8 Functional diagram of the hybrid combination of energy storage system

According to Figure 5.8, the model of the energy storage subsystem can be divided into three parts: the energy model of the super-capacitor, the energy model of the rechargeable battery and the energy consumption of the control circuit. In this chapter, in order to simplify the model description, the detailed control circuit of the storage subsystem is neglected and the power consumption of the control circuit $P_{E,control}$ is assumed as a constant value. Then the energy storage subsystem can be simplified as modelling the super-capacitor and the rechargeable battery.

5.4.1 Model of the super-capacitor

A super-capacitor, often referred to an electrical double layer capacitor, has similar characteristics to a normal capacitor, but offers significantly higher capacitance values per unit volume. According to Table 5.2, the super-capacitors have a superior cycle efficiency which reaches around 97%-98% and more than 50,000 cycle life. Since the

model of super-capacitors is introduced for fast lifetime calculation, it is inconvenient to use a complex super-capacitor's model. In this work, for achieving fast simulation, a simple super-capacitor model, which is just taking into account the super-capacitor parameters from the datasheet, is developed. The equivalent circuit of the super-capacitor is shown in Figure 5.9. From the figure, a series resistor $R_{SC,S}$ can be determined by measuring the potential difference ΔV between the two terminals at the beginning when charging the super-capacitor with a large constant charging current. $R_{SC,S}$ is very close to the equivalent resistance value provided by the super-capacitor datasheet (Zhang and Yang, 2011). Thus, it is assumed that $R_{SC,S}$ is equal to the equivalent resistance of the super-capacitor. Since the charging frequency is quite low in energy harvesting systems, the series inductor L_{SC} is neglected in this work. The parallel capacitor $C_{SC,S}$ value can be determined by the capacitance of the super-capacitor. As the super-capacitor has a high self-discharge behaviour, a high parallel resistor $R_{SC,P}$ is used to model a leakage resistor. In order to identify the value of $R_{SC,P}$, the self-discharge process has been conducted in the laboratory.

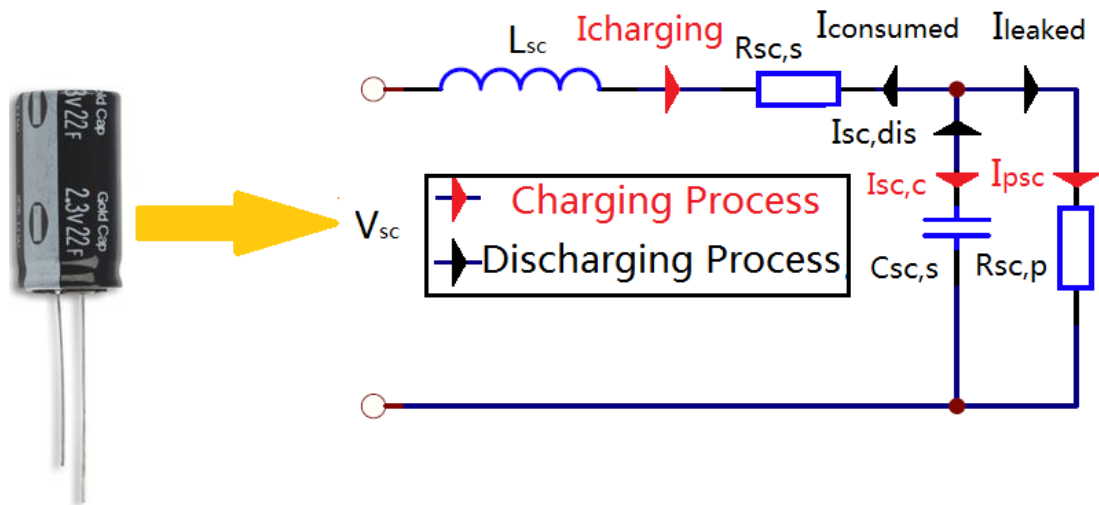


Figure 5.9 Proposed electrical equivalent circuit of super-capacitor

Normally, the capacitor model description can be divided into the charging mode and discharging mode, as illustrated in Figure 5.9. The relationship for the electrical charges of the super-capacitor $Q_{SC}(t)$ and the terminal voltage of the super-capacitor $V_{SC}(t)$ is

$$Q_{SC}(t) = c_{SC} \cdot V_{SC}(t) \quad (5.21)$$

where c_{SC} is the capacitance of the super-capacitor. From the current side of view, the charges of the capacitor can be expressed as:

$$Q_{SC}(t) = \int_0^t I_{SC,C}(t)dt + Q_{sc}(0) \quad (5.22)$$

$$I_{SC,C}(t) = \frac{dQ_{SC}(t)}{dt}$$

where $Q_{sc}(0)$ refers to the initial charges on the capacitor before charging/discharging and $I_{SC,C}(t)$ is electrical current charging the super-capacitor at time t , and $dQ_{SC}(t)$ is electrical charge difference during a time interval dt . As shown in Table 5.2, a capacitor is not an ideal electrical circuit, the charge and discharge efficiency of a super-capacitor $\eta_{capacitor}$, is considered. According to the super-capacitor's characteristics, $\eta_{capacitor}$ is around 97%-98%. Based on Figure 5.9, the charging current $I_{SC,C}(t)$ is approximately equal to the output current of the power conversion circuit $I_{c,out}(t)$ times charge and discharge efficiency $\eta_{capacitor}$. By considering the leakage current of the super-capacitor $I_{sc,leak}(t)$. The relationship between $I_{c,out}(t)$ and $I_{SC,C}(t)$ can be expressed as:

$$I_{c,out}(t) = \frac{I_{SC,C}(t) + I_{sc,leak}(t)}{\eta_{capacitor}} \quad (5.23)$$

The discharging current $I_{sc,dis}(t)$ from the super-capacitor is:

$$I_{sc,dis}(t) = \frac{I_{charging}(t) + I_{sc,leak}(t)}{\eta_{capacitor}} \quad (5.24)$$

where $I_{charging}(t)$ is the current consumed by the whole energy harvesting system at the time t . Equation 5.22 can be rewritten as:

$$V_{SC}(t) = \frac{1}{c_{SC}} \int_0^t I_{SC,C}(t)dt + V_{sc}(0) \quad (5.25)$$

$$V_{SC}(t) = V_{sc}(0) - \frac{1}{c_{SC}} \int_0^t I_{sc,dis}(t)dt \quad (5.26)$$

where $V_{sc}(0)$ refers to the initial voltage of the super-capacitor. Generally, to characterize the model with different I-V inputs, the model description can be extended to have a constant voltage charging/discharging phase.

(1) Charging/discharging using a constant voltage

By using a constant voltage to charge a super-capacitor, the previous equations can be rewritten by using Kintowff's voltage laws to analyse Figure 5.9. The charging voltage $V_{charging,sc}$ of the super-capacitor can be expressed mathematically as:

$$V_{charging,sc} = I_{c,out}(t) \cdot R_{SC,S} + \frac{1}{c_{SC}} \int_0^t I_{sc,c}(t) dt + V_{sc}(0) \quad (5.27)$$

$$= \frac{I_{sc,c}(t) + I_{sc,leak}(t)}{\eta_{capacitor}} R_{SC,S} + \frac{1}{c_{sc}} \int_0^t I_{sc,c}(t) dt + V_{sc}(0)$$

By assuming $I_{sc,leak}(t)$ is a constant value which is equal to $I_{sc,leak}$, Equation 5.27 can be rewritten as:

$$V_{charging,sc} = \frac{I_{sc,c}(t)}{\eta_{capacitor}} R_{SC,S} + \frac{1}{c_{SC}} \int_0^t I_{sc,c}(t) dt + V_1 \quad (5.28)$$

where $V_1 = V_{sc}(0) + \frac{I_{sc,leak}}{\eta_{capacitor}} R_{SC,S}$. By multiplying c_{sc} between two sides of Equation 5.28, the equation can be rewritten as:

$$V_{charging,sc} \cdot c_{SC} = \frac{I_{sc,c}(t)}{\eta_{capacitor}} \cdot R_{SC,S} \cdot c_{SC} + \int_0^t I_{sc,c}(t) dt + V_1 \cdot c_{SC} \quad (5.29)$$

By using the Laplace transform, Equation 5.29 can be expressed as

$$\frac{V_{charging,sc} \cdot c_{SC}}{S} = \frac{I_{sc,c}(s)}{\eta_{capacitor}} \cdot R_{SC,S} \cdot c_{SC} + \frac{1}{S} I_{sc,c}(s) + \frac{V_1 \cdot c_{SC}}{S} \quad (5.30)$$

where S is the notation of Laplace transfer. By writing the equation as the expression of $I_{sc,c}(s)$, Equation 5.31 can be obtained.

$$I_{sc,c}(s) = \frac{R_{SC,S} \cdot c_{SC}}{\frac{R_{SC,S} \cdot c_{SC} \cdot S}{\eta_{capacitor}} + 1} \cdot \frac{[V_{charging,sc} - V_1]}{R_{SC,S}} \quad (5.31)$$

Because

$$\frac{R_{SC,S} \cdot c_{SC}}{\frac{R_{SC,S} \cdot c_{SC} \cdot S}{\eta_{capacitor}} + 1} = \frac{\eta_{capacitor}}{S + \frac{\eta_{capacitor}}{R_{SC,S} \cdot c_{SC}}}$$

, then the express $I_{sc,c}(s)$ becomes:

$$I_{sc,c}(s) = \frac{\eta_{capacitor}}{S + \frac{\eta_{capacitor}}{R_{SC,S} \cdot c_{SC}}} \cdot \frac{[V_{charging,sc} - V_1]}{R_{SC,S}} \quad (5.32)$$

Equation 5.32 can be inverse-transformed into:

$$I_{sc,c}(t) = \eta_{capacitor} \cdot \frac{[V_{charging,sc} - V_1]}{R_{SC,S}} \cdot e^{\left(-\frac{\eta_{capacitor}}{R_{SC,S} \cdot c_{SC}} \cdot t\right)} \quad (5.33)$$

By integrating Equation 5.33 into Equation 5.25, the equation is rewritten as:

$$\begin{aligned} V_{SC}(t) &= \eta_{capacitor} \cdot \frac{[V_{charging,sc} - V_1]}{R_{SC,S} \cdot c_{SC}} \int_0^{t_c} e^{\left(-\frac{\eta_{capacitor}}{R_{SC,S} \cdot c_{SC}} \cdot t\right)} dt + V_{sc}(0) \quad (5.34) \\ &= -(V_{charging,sc} - V_1) \cdot \left[e^{\left(-\frac{\eta_{capacitor}}{R_{SC,S} \cdot c_{SC}} \cdot t_c\right)} - 1 \right] + V_{sc}(0) \end{aligned}$$

The charging time period t_c , which is the time that the supercapacitor is charged from $V_{sc}(0)$ to V_{target} , can be expressed as:

$$t_c = -\frac{R_{SC,S} \cdot c_{sc}}{\eta_{capacitor}} \times \ln \frac{V_{target} - V_{charging,sc} + V_1 - V_{sc}(0)}{V_1 - V_{charging,sc}} \quad (5.35)$$

If using a constant voltage $V_{discharging,sc}$ to discharge the super-capacitor, it yields similar results to the charging process. By assuming $I_{sc,leak}(t) = I_{sc,leak}$, the discharge voltage $V_{discharging,sc}$ can be expressed by using Kinhowff's voltage laws:

$$\begin{aligned} V_{discharging,sc} &= -\frac{1}{c_{sc}} \int_0^t I_{sc,dis}(t) dt + V_{sc}(0) - I_{sc,dis}(t) \cdot R_{SC,S} \quad (5.36) \\ &= -\frac{1}{c_{sc}} \int_0^t I_{sc,dis}(t) dt + V_{sc}(0) - [\eta_{capacitor} \cdot I_{sc,dis}(t) - I_{sc,leak}] \cdot R_{SC,S} \end{aligned}$$

By using $V_2 = V_{sc}(0) + I_{sc,leak} \cdot R_{SC,S}$, Equation 5.36 can be simplified as:

$$V_{discharging,sc} = -\frac{1}{c_{sc}} \int_0^t I_{sc,dis}(t) dt + V_2 - \eta_{capacitor} \cdot I_{sc,dis}(t) \cdot R_{SC,S} \quad (5.37)$$

By using Laplace transform, Equation 5.37 can be rewritten as:

$$I_{sc,dis}(s) = \frac{R_{SC,S} \cdot c_{sc}}{1 + \eta_{capacitor} \cdot S \cdot R_{SC,S} \cdot c_{sc}} \frac{[V_2 - V_{discharging,sc}]}{R_{SC,S}} \quad (5.38)$$

$$= \frac{\frac{1}{\eta_{capacitor}}}{S + \frac{1}{\eta_{capacitor} \cdot R_{SC,S} \cdot c_{sc}}} \frac{[V_2 - V_{discharging,sc}]}{R_{SC,S}}$$

By inverse transforming Equation 5.38, $I_{sc,dis}(t)$ can be expressed as

$$I_{sc,dis}(t) = \frac{1}{\eta_{capacitor}} \cdot \frac{[V_2 - V_{discharging,sc}]}{R_{SC,S} \cdot c_{sc}} e^{\left(\frac{-1}{\eta_{capacitor} \cdot R_{SC,S} \cdot c_{sc}} t\right)} \quad (5.39)$$

By integrating Equation 5.39 into Equation 5.26, the expression can be written as:

$$V_{sc}(t) = V_{sc}(0) - \frac{1}{\eta_{capacitor}} \cdot \frac{[V_2 - V_{discharging,sc}]}{R_{SC,S} \cdot c_{sc}} \int_0^{t_{dis}} e^{\left(\frac{-1}{\eta_{capacitor} \cdot R_{SC,S} \cdot c_{sc}} t\right)} dt \quad (5.40)$$

$$= (V_2 - V_{discharging,sc}) \cdot \left[e^{\left(\frac{-1}{\eta_{capacitor} \cdot R_{SC,S} \cdot c_{sc}} t_{dis}\right)} - 1 \right] + V_{sc}(0)$$

The discharging time period t_{dis} needed to discharge the super-capacitor to a certain voltage V_{target} can be given by:

$$t_{dis} = -\eta_{capacitor} \cdot R_{SC,S} \cdot c_{sc} \times \ln \frac{V_{target} - V_{discharging,sc} + V_2 - V_{sc}(0)}{V_2 - V_{discharging,sc}} \quad (5.41)$$

(2) Charging and discharging with a constant current

Similar to using a constant voltage to charge/discharge a super-capacitor, it can also be charged or discharged by using a constant current I_1 . Then Equations 5.23, 5.24, 5.25, and 5.26 can be rewritten as:

$$I_{sc,c} = \eta_{capacitor} \cdot I_1 - I_{sc,leak} \quad (5.42)$$

$$I_{sc,dis} = \frac{I_1 + I_{sc,leak}}{\eta_{capacitor}} \quad (5.43)$$

$$V_{SC}(t) = \frac{I_{sc,c}}{c_{sc}} \cdot t_c + V_{sc}(0) \quad (5.44)$$

$$V_{SC}(t) = V_{sc}(0) - \frac{I_{sc,dis}}{c_{sc}} \cdot t_{dis} \quad (5.45)$$

The duration t_c or t_{dis} it takes by using a constant current to charge or discharge the super-capacitor to a certain voltage V_{target} can be calculated by Equations 5.46 and 5.47, respectively.

$$t_c = \frac{c_{sc} \cdot [V_{target} - V_{sc}(0)]}{I_{sc,c}} \quad (5.46)$$

$$t_{dis} = \frac{c_{sc} \cdot [V_{sc}(0) - V_{target}]}{I_{sc,dis}} \quad (5.47)$$

(3) Model evaluation

In order to evaluate the model, the leakage resistance of the super-capacitor under various states should be determined. As stated in (Guan and Liao, 2008), charge on the super-capacitor drops by around 35% per month due to the leakage. . The self-discharge resistance of the super-capacitor $R_{SC,self}(t)$ can be estimated as (Guan and Liao, 2008):

$$R_{SC,self}(t) \approx \frac{\Delta t_{self}}{c_{sc} \times \ln \left[\frac{V_{sc}(0)}{V_{sc}(0) - \Delta V_{sc}(self)} \right]} \quad (5.48)$$

where $\Delta V_{sc}(self)$ is super-capacitor's voltage decreased by self-discharging during a time duration Δt_{self} . $\Delta V_{sc}(self)$ and Δt_{self} can be determined by experiments. For the evaluation of the model, a 2.3V 22F super-capacitor from Panasonic (Panasonic 22F super-capacitor, 2008), was used in this work. The specifications of the super-capacitor are listed in Table 5.3.

Table 5.3 Specifications of Panasonic Super-capacitor (Panasonic 22F super-capacitor, 2008)

Parameter	Specification	Unit
Capacitance	22	F

Internal resistance at 1KHz	0.1	Ω
Maximum operating voltage	2.5	V

In order to determine the self-discharging resistance of the super-capacitor, experiments have been conducted in the laboratory with constant environmental factors (25°C and 30% humidity). Initially, the super-capacitor was fully charged by using a DC power supply and the self-discharge process has been taking place for two hours after removing the power source. In order to reduce random measurement errors, the experiment has been repeated ten times by using four 22F super-capacitors. The average value gained from these experiments and the testing results are shown in Figure 5.10. By integrating the parameters into Equation 5.48, the self-discharging resistor can be estimated. By comparing the simulation results with the experimental results, the error of the self-discharging model is around 2.7%.

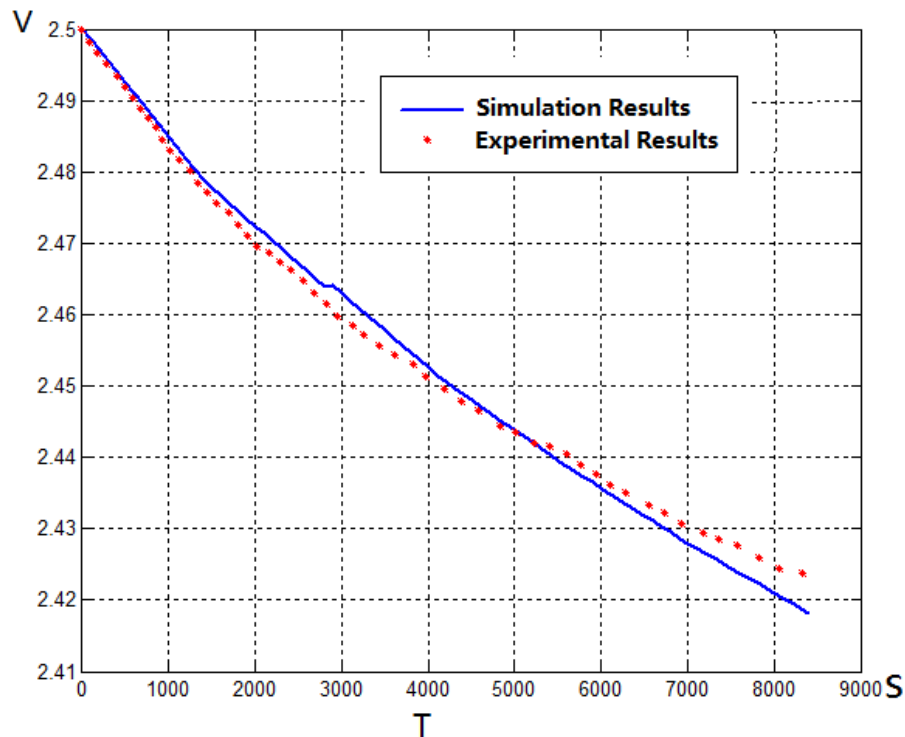


Figure 5.10 Self-discharging effect of 22F 2.5V super-capacitor

The accuracies of the proposed model during the charging and the discharging processes have been evaluated by using experiments. Firstly, the model was validated with a 2.V constant charging voltage and the result is depicted in Figure 5.11(a). The corresponding experimental test, which used a 2.5V battery as the constant voltage

source to directly charge the super-capacitor, has been carried out in the laboratory. The accuracy of the proposed super-capacitor model is 96.1% by comparing the simulation result with the experimental result. Figure 5.11 (b) shows the model, in which the super-capacitor is charged by a constant current source. In order to see the difference, 10mA and 5mA input currents have been simulated, respectively. Initially, the voltage level of the super-capacitor is set to be 1.3V. By using these two current sources to charge the super-capacitor with the same time interval (3200s), respectively, the final voltages of the super-capacitor in these two cases are 2.49V and 1.9V, respectively. The corresponding experiments have been tested and the final voltages of the super-capacitor in these two experiments are 2.39V and 1.79V, respectively. By comparing the simulation results and the experimental results, a 6% error could be found in the worst case scenario.

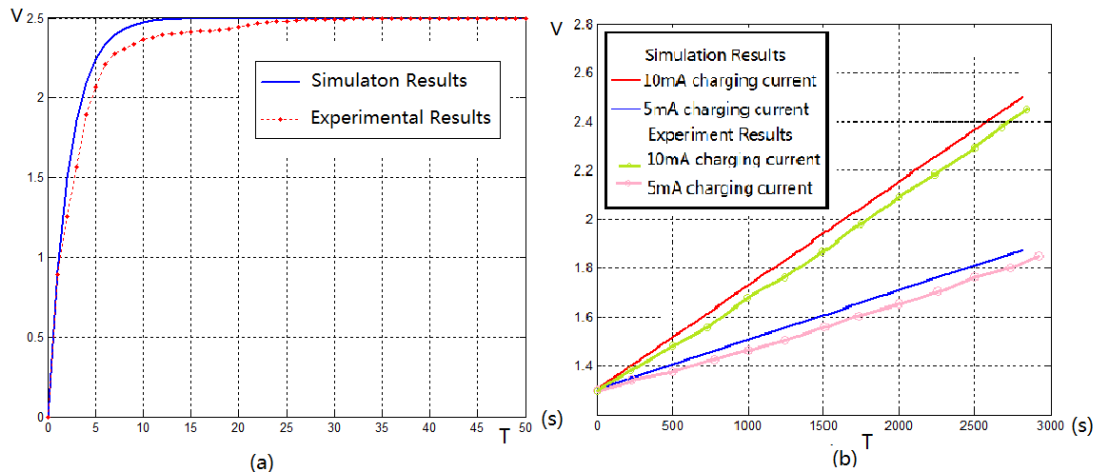


Figure 5.11 (a) 2.5v constant charging voltage (b) 10mA and 5mA constant charging current

The discharging processes were simulated and tested with constant discharge voltages and constant discharge currents, respectively. Figure 5.12 shows that fully charged super-capacitors were discharged by 1.1V and 1.2V batteries. The simulation results show that the time periods for discharging the capacitors from 2.5V to 1.5V are 2.5s and 3.2s, respectively. The corresponding test results are 3s and 3.5s, which indicate the error of the model is around 20%. The increase of the model error is caused by a measurement error, which is normally caused by the equipment and those running the tests. The discharging model was evaluated by constant current sources, for which 5mA and 10mA were selected. The simulation results show that the capacitor needs 2680s and 1448s to discharge from 2.5V to 1.8V respectively. In order

to evaluate the accuracy of the proposed model, experimental tests have been held. The comparison results show that the capacitor needs 2200s and 1309S to discharge from 2.5V to 1.8V by using these two current sources and the error of the model is around 10%.

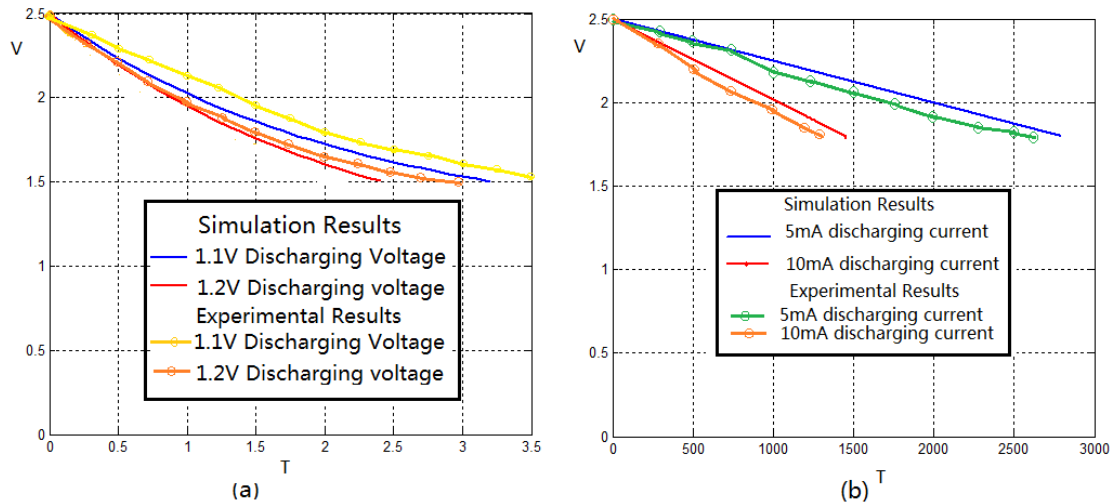


Figure 5.12 (a) constant discharge voltages (b) constant discharging current

5.4.2 Model of the rechargeable battery

Since the lifetime of the micro-energy harvesting system is highly related to the lifetime of the rechargeable batteries, an accurate rechargeable battery model is critical to predict the lifetime of the system. The performance of the battery highly depends on which type of battery technology is used and in what external environment it is operated in. Hence, before designing a battery model, the battery type being used in the energy harvesting system should be determined. Some popular rechargeable battery technologies such as Lead Acid, Nickel Cadmium (NiCd), Nickel Metal Hydride (NiMH) and Lithium Ion (Li-ion) are normally used in energy harvesting systems. The typical values of parameters across different battery technologies are shown in Table 5.2. In these technologies, NiMH and Li-based batteries emerged as good choices for energy harvesting applications based on their advantages. As shown in the table, Li-ion batteries have the highest output voltage, energy density, power density, charge-discharge efficiency and moderately low self-discharge rate (Sudevalayam and Kulkarni, 2011) and they do not suffer from memory effect-loss of energy capacity due to repeated shallow recharge. These make them become a very popular energy buffer option for an energy harvesting system application. However, Li-ion batteries normally require a complicated charging circuit that makes this

technology unsuitable for some micro energy harvesting systems, which require small, compact and simple circuits.

On the other hand, NiMH batteries can be trickle charged and they do not need a complex pulse charging circuit. This means NiMH batteries can be directly connected to an energy source being charged. This is why NiMH batteries are more suitable for use in micro energy harvesting systems. Furthermore, by comparing the cost of the NiMH battery with other battery technologies, it has a reasonably high energy density and a high number of recharge cycles. But the charge-discharge efficiency of NiMH batteries is lower than Li-based batteries. In summary, both Li-ion and NiMH batteries have their own advantages and disadvantages; the battery selection depends on the application requirements and energy constraints. In this thesis, because the small size, low cost and less circuit complexity are concerned in the energy harvesting system design, a NiMH battery is chosen.

NiMH batteries require simple maintenance to maintain batteries for optimal performance and extension of battery life. NiMH batteries are good for 500 to 1000 cycles if properly used. Below are some methods on NiMH battery maintenance.

- NiMH batteries should be discharged fully before first used and the new battery requires charging and discharging three to five times to activate battery internal cathode and anode materials.
- NiMH batteries do not accept full charge and discharge if the temperature is above 50°C or below 0°C. It should maintain the battery temperature around 0 – 40°C, otherwise the battery lifetime will be sharply reduced.
- NiMH batteries can hold full charge for a month if store in normal temperature. If the battery is kept near hot objects or exposed in sunlight for hours, the charge will drop in one day. In this case, in order to maintain the charge on the NiMH battery, it should avoid facing the sunlight and nearing the hot source.
- NiMH batteries should avoid over-charged and over-discharged. This is because these two processes could damage the battery.

According to these, it can be observed that the battery lifecycle and the self-discharging rate are highly dependent on the maintenance of the battery. The battery can have long lifecycle and small self-discharging rate when it has good maintenance. Thus, the battery modelling is highly related to the maintenance of the

battery. In order to simplify the modelling process, it assumed that the NiMH battery has been properly maintained in an ideal environment, where the temperature, humidity, and light are constant.

As stated in the previous part, the performance of the battery depends on how and where it being used. Some undesirable effects, including the loss of rated capacity, faster temperature rises during operation, less charge acceptance, higher internal resistance, lower voltage, frequency self-discharge, overcharge, and over discharge, will significantly shorten the lifetime of the battery. There are several parameters associated with battery modelling, and these parameters are briefly explained below.

- State of Charge (SoC) is an expression of the present battery capacity as a percentage of the maximum capacity. The open circuit voltage of the battery depends on its present SoC.
- Depth of Discharge (DoD) of a battery is defined as the percentage of the battery capacity that has been withdrawn from a battery compared to the maximum capacity. The DoD, which is the inverse of SoC, is an alternate way to indicate a battery's SoC. It is a measurement of how deeply a battery is discharged. When a battery's SoC is 100%, then the DoD is 0%. Conversely, when the battery is 100% empty, the DoD is 100%.

For further understanding of the rechargeable battery, some specifications from the manufacturer's datasheet should be understood when choosing a battery (MIT Electric Vehicle Team, 2008).

- Nominal voltage ($V_{nominal,B}$) is the reported or referenced voltage of the battery.
- Cut-off voltage ($V_{cutoff,B}$) is the minimum allowable voltage, which is also defined as the empty state of the battery.
- Nominal capacity (Ah) is the total Amp-hour available when the battery is discharged at a certain discharge current (specified as a C-rate) from 100% SoC to the cut-off voltage (MIT Electric Vehicle Team, 2008). It is also called coulometric capacity, which is calculated by multiplying the discharge current (in Amps) by the discharge time (in hours).
- Self-discharge rate is a phenomenon in batteries in which the electrical capacity is lost when the cell is not in use. It is used to measure how quickly a cell will lose

its energy while not in use. The rate depends on the battery chemistry, the temperature and age.

- Internal Resistance of the battery is illustrated as the total resistance of the battery when it is charging or discharging
- Overcharging and Over-discharging resistance indicate that when the battery is overcharged or over-discharged, the internal resistance will be increased significantly due to the electrolyte dissuasion.
- Cycle-life is defined as the number of complete charge-discharge cycles a battery can perform before its nominal capacity falls below 80% of its initial rated capacity. The cycle life of a battery is estimated for specific charge and discharge conditions.
- The C rate is the measure of the rate at which a battery is discharged related to its maximum capacity (MIT Electric Vehicle Team, 2008). For instance, if a 2000mAh rechargeable battery discharges at its 1C rate, the rechargeable battery will discharge the entire capacitance in one hour. And the discharging current 1C rate for this type of rechargeable battery is 2000mA.

Nowadays, a wide variety of battery models with varying degrees of complexity have been developed for different applications. These models can be classified into three different categories. The electrochemical models (Gomadani et al., 2002), are considered as the most accurate battery models, and are based on the chemical processes taking place in the battery to describe battery processes in detail. However, the proposed models are too complex. Oppositely, to predict the performance of a battery, many different mathematical models exist (Rong and Pedram, 2003) and (Rakhmatov et al., 2003). Although these models are useful to system designers to quickly predict system level behaviour such as battery runtime, they are considered too abstract to express the practical process of the battery. Furthermore, mathematical models cannot offer any I-V information which is important for circuit simulation and optimization. By considering these limitations, electrical models have been proposed. This technology has accuracy between electrochemical and mathematical models. There are three kinds of electrical models in the existing literature, including a runtime based model (Benini et al., 2001), impedance-based model (Buller et al., 2003) and Thevenin-based model (Valvo et al., 1996) and (Chen and Rincon-Mora, 2006). By comparing the advantages and disadvantages of each approach, an electrical model

provided by (Chen and Rincon-Mora, 2006) has been adopted in this work to model a NiMH battery. This is because this model has a capability of predicting lifetime and I-V performance of the rechargeable battery. The equivalent schematic battery model is shown in Figure 5.13. The model is divided into battery lifetime part and voltage-current characteristics part.

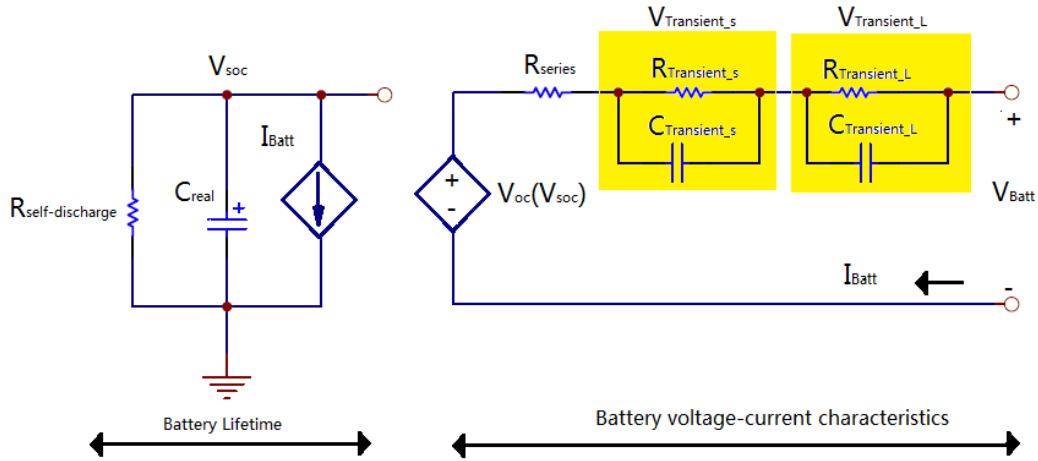


Figure 5.13 Electrical battery model (Chen and Rincon-Mora, 2006)

On the left side of Figure 5.13, a capacitor C_{real} and a current source I_{batt} , inherited from runtime based models, represent the present SoC and discharge current of the battery, respectively (Chen and Rincon-Mora, 2006). In order to represent the usable capacity decreasing slowly with time when no load is connected to the battery, a self-discharge resistor $R_{Self-Discharge}$ is used. The right side of the circuit emulates the voltage and current characteristics of the battery. The two series connected RC parallel networks, similar to a Thevenin-based model, are used to indicate the transient response of the battery. In the first RC network, it was used $R_{Transient_S}$ and $C_{Transient_S}$ to describe the short-time constant of the step response. The later RC network uses $R_{Transient_L}$ and $C_{Transient_L}$ to response a long-time constant of the step response. Furthermore, in order to show the response of the instantaneous voltage drop of the step response, a series resistor R_{Series} , which is assumed to be the constant part of the internal resistor, is used (Chen and Rincon-Mora, 2006). A controlled voltage source V_{SOC} whose value depends on the open circuit voltage V_{OC} of the battery is used to bridge SoC of the battery to an open circuit voltage. The full capacity of a battery $C_{R-battery}$, when the SoC is 100%, represents the whole charge stored in the battery and can be expressed as (Chen and Rincon-Mora, 2006).

$$C_{R-battery} = 3600 \times C_{capacity} \times f_1(Cycles) \times f_2(Temp) \quad (5.49)$$

where $C_{Capacity}$ is the nominal capacity of the battery in Ahr and $f_1(Cycles)$ and $f_2(Temp)$ are cycle number and temperature dependent correction factors of the battery, respectively. Due to the aging effect, the full capacity of the battery is reduced as the battery goes through cycles of charging and discharging, especially for deep discharging. Hence, in order to achieve a long battery lifespan, the SoC of the battery is desirably kept within appropriate limits. By searching the NiMH battery datasheet, the life cycles of the battery are around 700 times when the battery is discharged when it reaches DoD=80%. By considering there is a linear relationship between the cycles and usable capacity of the battery, $f_1(Cycles)$ can calculate by:

$$f_1(Cycles) = n_{cycles} \cdot \left(1 - \frac{20\%}{700}\right) \quad (5.50)$$

where n_{cycles} is present battery cycles. Similarly, in order to express temperature affecting the usable capacity of the battery, a temperature factor $f_2(Temp)$ is used. Because wireless sensor nodes are normally designed for using in a normal environment, the usable capacity of the battery is not affected by the environment temperature. To simplify the simulation, $f_2(Temp) = 1$ is assumed in this work. As the NiMH battery has a high self-discharge rate, 1% of the capacity lost in the battery per day is used. Hence, the self-discharging resistor of the battery $R_{Self-Discharge}$ can be simplified as a large resistor. Because rechargeable batteries can step into charging or discharging phases, the battery efficiency can be divided into the charge efficiency $\eta_{c,battery}$ and the discharge efficiency $\eta_{dis,battery}$ parts:

$$\eta_{c,battery} = \frac{\Delta Q_{Battery1}}{Q_{B,charging}} \quad (5.51)$$

$$\eta_{dis,battery} = \frac{Q_{B,discharging}}{\Delta Q_{Battery2}} \quad (5.52)$$

where $Q_{B,charging}$ and $Q_{B,discharging}$ are the total energy which are charged in or discharged from the battery, and $\Delta Q_{Battery1}$ is total energy adding on the battery when it being charged, and $\Delta Q_{Battery2}$ is total energy being lost in the battery when it being discharged. Their units are the charge in coulombs.

According to Table 5.2, the NiMH battery has a charging/discharging efficiency of around 66%. In this work, in order to make the charging/discharging process more clear, the charging and discharging efficiency are separated into $\eta_{c,battery} = 0.9$ and $\eta_{dis,battery} = 0.7$. When the battery is being charged by using a current source $I_{b,charging}(t)$, the SoC of the battery is changed dynamically. The present SoC of the battery is calculated by using the original capacity plus the charged capacity, as shown in Equation 5.53.

$$\text{SoC}(t) = \text{SoC}(0) + \frac{1}{C_{R-battery}} \int_0^t \eta_{c,battery} \cdot I_{b,charging}(t) dt \quad (5.53)$$

where t is the charging or discharging period, and $\text{SoC}(t)$ and $\text{SoC}(0)$ are SoC value at time t and 0, respectively. If using a discharge current $I_{b,discharge}(t)$ to discharge the battery, the $\text{SoC}(t)$ is expressed as the original capacity minus the discharged capacity.

$$\text{SoC}(t) = \text{SoC}(0) - \frac{1}{C_{R-battery}} \int_0^t \frac{I_{b,discharge}(t)}{\eta_{dis,battery}} dt \quad (5.54)$$

Normally, the lifetime of the rechargeable battery $T_{b,life}$, can be simply calculated based on the total amount of energy C_{total} , which can be put into and taken out of a battery over all the cycles in its lifetime before its capacity reduces to 80% of SoC. It is assumed that rechargeable batteries are discharged in a constant current $I_{b,discharge}$ and the self-discharge effect is neglected; then the $T_{b,life}$ can be calculated.

$$T_{b,life} = \frac{C_{total} \cdot \eta_{dis,battery} \cdot DoD}{I_{b,discharge}} = \frac{\sum_{n=1}^{700} C_{R-battery}(n) \cdot \eta_{battery} \cdot DoD}{I_{b,discharge}} \quad (5.55)$$

where $DoD=80\%$ means this is the end of lifecycle of the rechargeable battery.

In order to determine the lifetime as well as the I-V character of the battery, the present SoC of the battery is a key point. However, it is very hard to accurately predict the battery SoC because it depends on many factors such as temperature, battery capacitance, and internal resistance. One approximate way to estimate the SoC of the battery is through the open circuit voltage of the rechargeable battery $V_{B,OC}$, which is a function of SoC and can be described as:

$$V_{B,OC}(SoC) = f(SoC) \quad (5.56)$$

By knowing the SoC of the battery, the open circuit voltage can be determined. Unlike an ordinary battery, the relationship between the SoC and open circuit voltage of NiMH battery is non-linear. In order to achieve a more precise battery model, a piecewise linear approach proposed by Windarko et al. (2009), has been adopted in this chapter. According to their experiments, in which 10 NiMH batteries were tested respectively, the relationship between SoC and open circuit voltage of the NiMH battery is plotted in Figure 5.14. It can be observed that the relationship can be divided into three linear segments, which are 0 to 10%, 10% to 80%, and 80% to 100% in terms of SoC. Table 5.4 shows the open circuit voltage (OCV) values in these points. Based on these estimations, a piecewise linearization formula has been proposed.

$$SoC(t) \begin{cases} \frac{V_{B,OC} - 1.2}{1.28 - 1.2} \cdot 10\% & 0 \sim 10\% \\ \frac{V_{B,OC} - 1.28}{1.35 - 1.28} \cdot 70\% + 10\% & 10\% \sim 80\% \\ \frac{V_{B,OC} - 1.35}{1.39 - 1.35} \cdot 20\% + 80\% & 80\% \sim 100\% \end{cases} \quad (5.57)$$

Table 5.4 The relationship between the experience OCV and SOC of NiMH battery (Windarko et al., 2009)

OCV (V)	1.2	1.28	1.35	1.39
SoC (%)	0	10	80	100

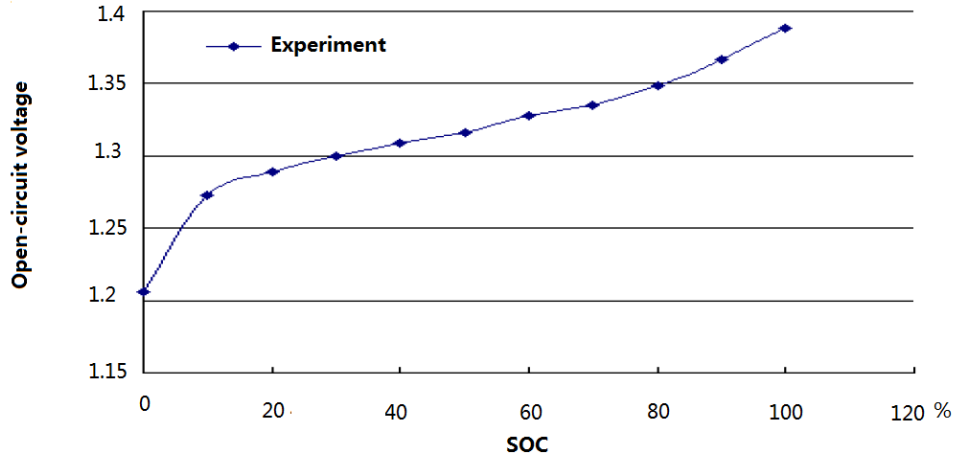


Figure 5.14 The relationship of SoC and OCV of NiMH battery (Windarko et al., 2009)

Typically, open circuit voltage of a battery $V_{B,OC}$ can be obtained by a direct measurement, by temporarily disconnecting the battery charging or discharging processes, which is considered inconvenient. Thus the left side circuit of Figure 5.13 is used to calculate $V_{B,OC}$ by knowing the battery output current I_{Batt} and battery voltage $V_{Batt}(t)$. By using Kirchoff laws, the $V_{B,OC}(t)$ can be expressed by using a constant current I_{Batt} to discharge and charge the battery. In the discharging mode, $V_{B,OC}(t)$ can be expressed as:

$$\begin{aligned}
 V_{B,OC}(t) = & V_{Batt}(t) \\
 & + \left\{ I_{Batt} \cdot R_{Series} + I_{Batt} \cdot R_{Transient_S} \left[1 - e^{-\left(\frac{t}{\tau_D}\right)} \right] + I_{Batt} \right. \\
 & \left. \cdot R_{Transient_S} \left[1 - e^{-\left(\frac{t}{\tau_K}\right)} \right] \right\} \quad (5.58)
 \end{aligned}$$

In the battery Charging mode, $V_{B,OC}(t)$ can be expressed as:

$$\begin{aligned}
 V_{B,OC}(t) = & V_{Batt}(t) \\
 & - \left\{ I_{Batt} \cdot R_{Series} + I_{Batt} \cdot R_{Transient_S} \left[1 - e^{-\left(\frac{t}{\tau_D}\right)} \right] + I_{Batt} \right. \\
 & \left. \cdot R_{Transient_S} \left[1 - e^{-\left(\frac{t}{\tau_K}\right)} \right] \right\} \quad (5.59)
 \end{aligned}$$

where $\tau_D = R_{Transient_S} \cdot C_{Transient_S}$ and $\tau_K = R_{Transient_L} \cdot C_{Transient_L}$.

where $\tau_D = R_{Transient_S} \cdot C_{Transient_S}$ and $\tau_K = R_{Transient_L} \cdot C_{Transient_L}$. The rest of the symbols are illustrated in Figure 5.13.

Before simulating the model, some parameters of the NiMH battery must be identified. A Duracell HR03 NiMH battery (HR03, 2008) rated at 1.2V and 800mAH is used as an example. In order to calculate the open-circuit voltage of the battery, R_{Series} , $R_{Transient_S}$, $C_{Transient_S}$, $R_{Transient_L}$ and $C_{Transient_L}$ should be determined. Based on (Chen and Rincon-Mora, 2006), the parameters extracted from their work have been adopted in this model to calculate the open-circuit voltage. Table 5.5 shows the battery simulation parameters.

Table 5.5 NiMH battery parameters

Parameters	Value
R_{Series}	30m Ω (SoC 100% – 20%) 40m Ω (SOC 20% – 0%)
$R_{Transient_S}$	0.05 Ω
$R_{Transient_L}$	0.1 Ω
$C_{Transient_S}$	600F
$C_{Transient_L}$	1.5kF
Maximum Voltage	1.49V
Minimum voltage	1.2V
Capacity	800mAH
Cycles	700 times
DoD	80% (1.29V)

Experiments have taken place at the laboratory to evaluate the accuracy of the proposed NiMH battery model. In order to avoid the environment factors affecting the experiments, the temperature and humidity of the laboratory are maintained at the same level. To evaluate the model, the simulation results of open circuit voltage with different charge and discharge currents are plotted in Figure 5.15. The open circuit

voltages of the batteries were recorded every 500 seconds. Due to the recovery effect of the battery, the open circuit voltages vary significantly after rapidly charging or discharging. In order to get stable results, the battery was allowed to discharge for one hour. This is because there is no significant change in the open circuit voltage after one hour of resting. By examining the curves, the simulation results are close to the experimental results. And the error of the model is around 6% in the worst case scenario. By using the simulation model to calculate the lifetime of the battery by using 1C and 0.5C discharge rate, the lifetime of the batteries are 3453s and 7282s, respectively. The relatively experimental results are 3275s and 7150s, respectively. The error of the model is around 5.4%.

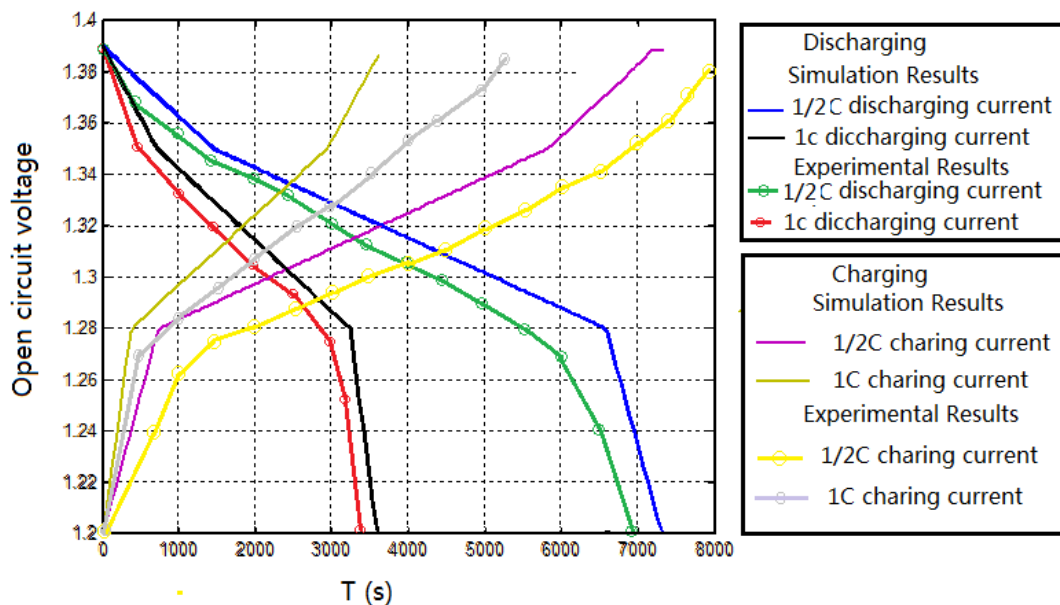


Figure 5.15 Battery's Open-circuit voltage with different discharging currents and charging currents.

5.5 The model of the energy consumer

Normally, a wireless sensor node is the primary energy consumer in the micro-energy harvesting system. In this chapter, a Jennic 5139 MCU based platform is chosen as a target energy consumer. A popular low power sensor node, DR1048 (Jennic DR1048, 2008), from NXP company, has been chosen as an example to demonstrate and verify the proposed model. The electrical characteristics of DR1048 board are listed in Table 5.6.

Table 5.6 DC current consumption of the DR1048

Description	Current
CPU Sleep mode	0.0035mA
CPU active mode	7.41mA
Radio (Receiving mode)	37mA
Radio (Idle mode)	37mA
Radio (Transmission mode)	38mA
Temperature & Humidity sensor (Idle Mode)	3.5uA
Temperature & Humidity sensor (Sleep Mode)	0.3uA
Light sensor (active mode)	0.35mA
Light sensor (power down mode)	10uA
LED	2mA

Using a voltage and current meter to monitor the power consumption of the DR1048 board, the active power consumption and the sleep power consumption of the sensor node are measured at 35.23mW and 6.63mW, respectively. If using duty cycle $D=25\%$, the average power consumption of the sensor node $P_{sensor}(average)$ is:

$$P_{sensor}(average) = 35.23 \times 25\% + (1 - 25\%) \times 6.63 = 13.78mW \quad (5.60)$$

5.6 Model of the entire energy harvesting system

The model of the whole energy harvesting system has been constructed based on Figure 5.16 by integrating each component of the model together. In order to highlight the energy flow, the efficiency of each component is tracked. The power consumptions in the control circuits have been taken into account and deduced the available power from the system. The energy model of the entire system can be described based on the three different states of the energy storage subsystem, which are using the battery to power the system, using the capacitor to power the system, using the capacitor to power the system and to charge the battery at the same time. The following are descriptions of these three states.

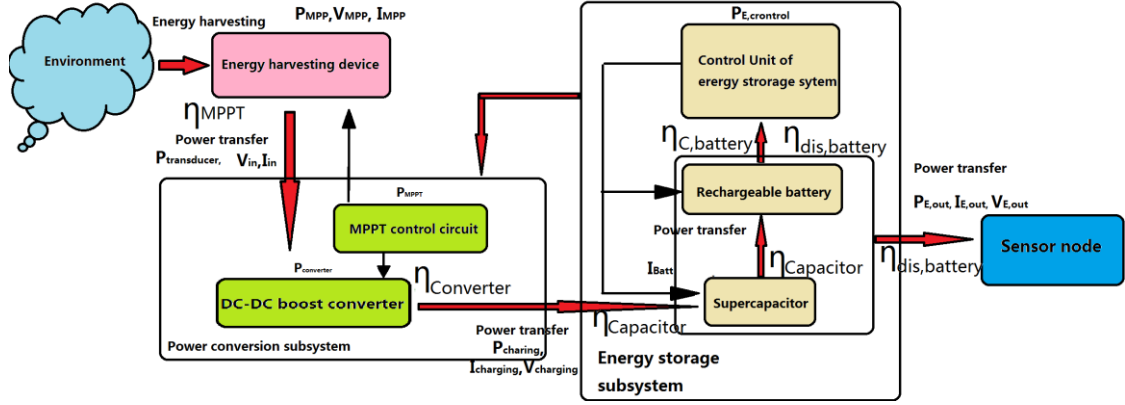


Figure 5.16 Power transfer in micro-energy harvesting system

It can be assumed that the system starts at a given time instant $t_{initial}$ and the initial energy level of the rechargeable battery and the super-capacitor are recorded as $C_{battery}(t_{initial})$ and $V_{sc}(t_{initial})$, respectively. By assuming $V_{sc}(t_{initial}) < V_{W,th1}$, the system draws energy only from the rechargeable battery. Then the total power consumed by the energy harvesting system $P_{T,consum}$ can be calculated by adding the power consumption of MPPT circuit $P_{consumer,MPPT}$, the power consumption of the boost converter $P_{controller,IC}$, the power consumption of the control unit from the power conversion subsystem $P_{E,control}$, and the average power consumption of the sensor node $P_{sensor}(average)$ together. This can be expressed as shown in Equation 5.61.

$$P_{T,consume} = P_{consumer,MPPT} + P_{controller,IC} + P_{E,control} + P_{sensor}(average) \quad (5.61)$$

Because the whole system is powered by the same energy source, Equation 5.61 can be rewritten as a current form, as shown in Equation 5.62.

$$I_{T,consume} = I_{consumer,MPPT} + I_{controller,IC} + I_{E,control} + I_{sensor}(average) \quad (5.62)$$

where $I_{T,consume}$, $I_{consumer,MPPT}$, $I_{controller,IC}$, $I_{E,control}$, $I_{sensor}(average)$ are the current consumption of the entire system, the MPPT circuit, the boost converter, the control unit of the energy storage system, and the sensor node, respectively. Based on the energy harvester's characteristics and the environment, the harvested energy $P_{MPP}(t)$ can be determined. By using the MPPT circuit, the exact power $P_{transducer}(t)$ transferred from the energy harvester to the boost converter can be calculated by Equation 5.1. $P_{transducer}$ is the input power of the DC-DC boost converter. By considering all the power dissipation sources in the DC-DC converter

circuit, the efficiency of the converter $\eta_{converter}(t)$ can be calculated and therefore, the output power of the boost converter $P_{charging}(t)$ can be obtained as:

$$P_{charging}(t) = \eta_{converter}(t) \cdot P_{transducer}(t) \quad (5.63)$$

The system can step in different states by knowing the energy level of the supercapacitor, as shown in Figure 5.17. If the terminal voltage of the super-capacitor $V_{SC}(t) < V_{W,th1}$, the system draws energy from rechargeable battery and the harvested energy is stored in the super-capacitor. This can be observed as the black curve in Figure 5.17. If $V_{W,th1} < V_{SC}(t) < V_{W,th2}$, the system switches to use super-capacitor as the main power source. This can be seen as the red curve in Figure 5.17. As soon as $V_{SC}(t) \geq V_{W,th2}$, the super-capacitor charges the rechargeable battery and powers the system at the same time. The charging battery process will stop when $V_{SC}(t) \leq V_{W,th3}$. This can be displayed by the green curve. In this time period, the system is still powered by the super-capacitor and this process will be stopped when $V_{SC}(t) \leq V_{W,th4}$. According to the figure, the theoretical analysis can be divided in three different cases.

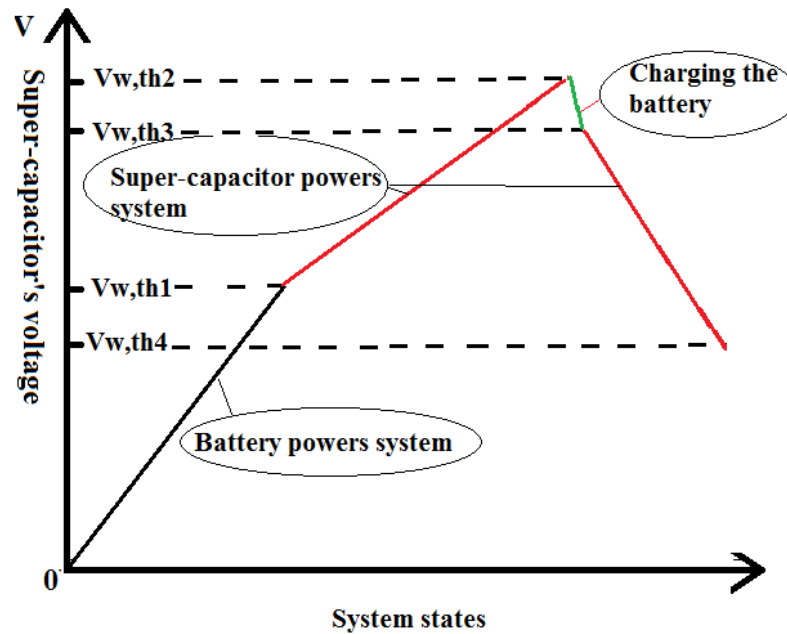


Figure 5.17 System states Vs. four voltage thresholds.

(1) $V_{SC}(t) < V_{W,th1}$

In the case one, $V_{SC}(t) < V_{W,th1}$, the system only draws energy from the rechargeable battery. As long as the super-capacitor voltage rise, the system will extract energy from the super-capacitor until $V_{SC}(t) \geq V_{W,th1}$. By assuming energy harvesting system is a constant current source in a short time interval dt , the terminal voltage of the super-capacitor $V_{SC}(t)$ can be expressed as:

$$V_{SC}(t) = \frac{1}{C_{SC}} \int_0^t I_{sc}(t) \cdot dt + V_{SC}(t_{initial}) \quad (5.64)$$

where C_{SC} is the capacitance of the super-capacitor. By considering the charge and discharge efficiency $\eta_{capacitor}$ of the super-capacitor and the self-discharging current of the super-capacitor $I_{leaked}(t)$, the exactly charging current $I_{sc}(t)$ can be expressed

$$I_{sc}(t) = \eta_{capacitor} \cdot I_{charging}(t) - I_{leaked}(t) \quad (5.65)$$

Then the time interval between the initial systems to this point $\Delta t1$ can be calculated as:

$$\Delta t1 = \frac{C_{SC} \cdot [V_{W,th1} - V_{SC}(t_{initial})]}{\int_0^{\Delta t2} I_{sc}(t) dt} \quad (5.66)$$

Where $I_{sc}(t)$ is the charging current in the time period $\Delta t1$. During the time period $\Delta t1$, the useful energy of the energy harvesting system $E_{useful}(\Delta t1)$ is the energy being stored on the super-capacitor $E_{super}(\Delta t1)$, which is expressed in Equation 5.67.

$$E_{useful}(\Delta t1) = E_{super}(\Delta t1) = \left(\frac{1}{2}\right) \cdot C_{SC} \cdot [V_{SC}^2(\Delta t1) - V_{SC}^2(t_{initial})] \quad (5.67)$$

On the other hand, the total energy consumed by the system in this time interval is drawn from the rechargeable battery. By assuming energy harvesting system is a constant current consumer, the energy consumed in this time period can be expressed as:

$$E_{consumed}(\Delta t1) = \int_0^{\Delta t1} V_{Batt}(t) \cdot I_{T,consum} dt \quad (5.68)$$

where V_{Batt} and $I_{T,consum}$ are the terminal battery voltage and the current drawn from the rechargeable battery. By considering the discharging efficiency of the

rechargeable battery, total capacity lost in the rechargeable battery in $\Delta t1$ $C_{B,lost}(\Delta t1)$ is:

$$C_{B,lost}(\Delta t1) = \int_0^{\Delta t1} \frac{I_{T,consum}}{\eta_{b,discharge}} dt \quad (5.69)$$

where $\eta_{b,discharge}$ is discharging efficiency of the rechargeable battery. Then the energy extracted from the battery $E_{Battery}(\Delta t1)$ during this time interval is:

$$\begin{aligned} E_{Battery}(\Delta t1) &= \int_0^{\Delta t1} V_{B,OC}(t) \cdot \frac{I_{T,consum}}{\eta_{b,discharge}} dt \\ &= \frac{V_{B,OC}(0) + V_{B,OC}(\Delta t1)}{2} C_{B,lost}(\Delta t1) \end{aligned} \quad (5.70)$$

where $V_{B,OC}(t)$ is open circuit voltage of the rechargeable battery in a time instance t . By knowing the open circuit voltage is a function of SoC, Equation 5.57 can be rewritten as:

$$V_{B,OC}(\Delta t1) = V_{B,OC}(SoC) = \varphi \cdot \frac{C_{battery}(t_{initial}) - C_{B,lost}(\Delta t1)}{C_{R-battery}} + V_{B,min} \quad (5.71)$$

where

$$\varphi = \begin{cases} 0.08 & (V_{B,min} = 1.2V, SoC \in 0\sim 10\%) \\ 0.1 & (V_{B,min} = 1.27V, SoC \in 10\% \sim 80\%) \\ 0.2 & (V_{B,min} = 1.19V, SoC \in 80\% \sim 100\%) \end{cases}$$

$$(2) V_{W,th1} \leq V_{SC}(t) < V_{W,th2}$$

In the second state, the energy harvesting system detected that the super-capacitor's voltage higher than $V_{W,th1}$, the system uses only the energy from the super-capacitor to power the system. In this state, there are two different cases which should be considered respectively. In the first case, the charging current of the super-capacitor $I_{sc}(t) > (I_{T,consum}/\eta_{capacitor}) + I_{leaked}(t)$, and then the super-capacitor continues to increase its terminal voltage until the second voltage threshold $V_{W,th2}$ is met. In this case, the charging current of the super-capacitor $I_{sc}(\Delta t2)$ can be rewritten as:

$$I_{sc}(t) = \eta_{capacitor} \cdot I_{charging}(t) - (I_{T,consum}/\eta_{capacitor}) - I_{leaked}(t) \quad (5.72)$$

The time interval in this situation is Δt_2 and it can be expressed as:

$$\Delta t_2 = \frac{C_{SC} \cdot [V_{W,th2} - V_{W,th1}]}{\int_0^{\Delta t_2} I_{sc}(t) dt} \quad (5.73)$$

In order to simplify the model, the self-discharging and the recovery effect of the rechargeable battery are ignored in this period. Then the energy level of the battery is maintained in this time period. In this time period, the useful energy from the energy harvester $E_{useful}(\Delta t_2)$ is the sum of the energy being consumed by the system $E_{consumed}(\Delta t_2)$ and the energy being stored in the super-capacitor $E_{super}(\Delta t_2)$, as shown in Equation 5.74.

$$E_{useful}(\Delta t_2) = E_{consumed}(\Delta t_2) + E_{super}(\Delta t_2) \quad (5.74)$$

where $E_{consumed}(\Delta t_2) = \int_0^{\Delta t_2} V_{SC}(t) \cdot \frac{I_{T,consume}}{\eta_{capacitor}} dt$ and $E_{super}(\Delta t_2) = \left(\frac{1}{2}\right) \cdot C_{SC} \cdot [V_{w,th2}^2 - V_{w,th1}^2]$.

In the second case, the charging current of the super-capacitor is less than the current drawn from the super-capacitor; the system draws energy from the super-capacitor until the fourth voltage threshold $V_{W,th4}$ is met. The fourth voltage threshold $V_{W,th4}$ is set because frequently switching energy sources generates a lot of noise to the sensor node which makes the system performance unstable. After the system detects $V_{sc}(t) < V_{W,th4}$, the system uses the battery to power the system again. In this case the current draw from the supercapacitor $I_{sc,dis}(t)$ can be expressed as:

$$I_{sc,dis}(t) = I_{T,consume} - \eta_{capacitor} \cdot I_{charging}(t) + I_{leaked}(t)$$

By assuming the discharging process of the super-capacitor is using a constant current source, the time period Δt_3 can be obtained by

$$\Delta t_3 = \frac{C_{SC} \cdot [V_{W,th1} - V_{W,th4}]}{\int_0^{\Delta t_3} I_{sc,dis}(t) dt} \quad (5.75)$$

Moreover, the useful energy of the energy harvesting system $E_{useful}(\Delta t3)$ is the energy difference between the total energy dissipation of the system $E_{consumed}(\Delta t3)$ and the energy lost in the supercapacitor $E_{super}(\Delta t3)$.

$$E_{useful}(\Delta t3) = E_{consumed}(\Delta t3) - E_{super}(\Delta t3)$$

where $E_{consumed}(\Delta t3) = \int_0^{\Delta t3} V_{SC}(t) \cdot \frac{I_{r,consume}}{\eta_{capacitor}} dt$ and $E_{super}(\Delta t3) = \left(\frac{1}{2}\right) \cdot C_{SC} \cdot [V_{w,th1}^2 - V_{w,th4}^2]$. In this case, the battery voltage is maintained at the same level.

(3) $V_{SC}(t) > V_{W,th2}$

In order to use the super-capacitor to power the system and meanwhile charge the rechargeable battery, sufficient energy should be harvested by the energy harvester. As soon as the voltage condition of the super-capacitor $V_{SC}(t) > V_{W,th2}$ is met, this state will occur. Normally, a charging window is used to stabilize the system charging process. A stop charging voltage threshold $V_{W,th3}$ is used to indicate the stop charging battery point of the super-capacitor. If $V_{SC}(t) < V_{W,th3}$, the capacitor stops charging the rechargeable battery but it still powers the system. The charging battery process can be considered as using a constant voltage source to discharge the supercapacitor. The discharging voltage $V_{discharging}(t)$ is equal to battery voltage $V_{battery}(t)$. In order to simplify the calculation, $V_{battery}(t)$ can be seemed as a constant value $V_{battery}(t) = 2.5V$. Then the charging battery time $\Delta t4$ is:

$$\Delta t4 = -\eta_{capacitor} \cdot (R_{SC,S} + R_{battery}) \cdot C_{SC} \quad (5.76)$$

$$\times \ln \frac{V_{W,th3} - V_{battery} + V_2 - V_{W,th2}}{V_2 - V_{battery}}$$

According to the electrical characteristics of the super-capacitor, the charging process is very quick and it can be seemed as an instantaneous process by comparing with other processes. In order to simplify the analyses, it is assumed no energy consumption in this time period. The total electrical charge $Q_{c,lost}$ lost in the super-capacitor during the charging process in the rechargeable battery.

$$Q_{c,lost} = C_{SC} \cdot (V_{W,th2} - V_{W,th3}) \cdot \eta_{capacitor} \quad (5.77)$$

where $\eta_{capacitor}$ is discharging efficiency of the super-capacitor. Furthermore, by considering the charging efficiency of the rechargeable battery $\eta_{b,charge}$, only a part of $Q_{c,lost}$ could be charged in the rechargeable battery. The energy being charged in the rechargeable battery $C_{B,charging}$ can be expressed as:

$$C_{B,charging} = \eta_{b,charge} \cdot Q_{c,lost} \quad (5.78)$$

The SoC of the battery $SoC_{battery}(t + 1)$ in this period can be expressed as

$$SoC_{battery}(t + 1) = SoC_{battery}(t) + \Delta SoC_{battery} \quad (5.79)$$

Where $SoC_{battery}(t)$ is the previous SoC of the rechargeable battery. $\Delta SoC_{battery}$ is adding SoC in this time period and it can be calculated by

$$\Delta SoC_{battery} = \frac{C_{B,charging}}{C_{R-battery}}$$

where $C_{R-battery}$ is nominal full battery capacitor.

Furthermore, if the energy harvester can still supply sufficient energy to raise the voltage of the super-capacitor from $V_{W,th3}$ to $V_{W,th2}$, the charging current of super-capacitor $I_{sc}(t)$ in this case can be expressed as:

$$I_{sc}(t) = \eta_{capacitor} \cdot I_{charging}(t) - (I_{T,consum}/\eta_{capacitor}) - I_{leaked}(t)$$

The time interval in this process $\Delta t5$ can be expressed as:

$$\Delta t5 = \frac{C_{SC} \cdot [V_{W,th2} - V_{W,th3}]}{\int_0^{\Delta t5} I_{sc}(t) dt} \quad (5.80)$$

The useful energy from the system $E_{useful}(\Delta t5)$ in this time period is the sum of energy dissipated by the system and energy stored into the super-capacitor.

$$E_{useful}(\Delta t5) = E_{consumed}(\Delta t5) + E_{super}(\Delta t5) \quad (5.81)$$

where $E_{consumed}(\Delta t5) = \int_0^{\Delta t5} V_{SC}(t) \cdot \frac{I_{T,consume}}{\eta_{capacitor}} dt$ and $E_{super}(\Delta t5) = \left(\frac{1}{2}\right) \cdot C_{SC} \cdot [V_{w,th2}^2 - V_{w,th3}^2]$.

On the other hand, if there is less energy or no energy to be harvested by the system, the voltage of the super-capacitor drops rapidly. As soon as the super-capacitor's voltage drops below $V_{W,th4}$, the system switches to use battery power the system again. The discharging current $I_{sc,dis}(t)$ draws from super-capacitor is:

$$I_{sc,dis}(t) = I_{T,consum} - \eta_{capacitor} \cdot I_{charging}(t) + I_{leaked}(t)$$

The time interval Δt_6 of this period is expressed as:

$$\Delta t_6 = \frac{C_{sc} \cdot [V_{W,th3} - V_{W,th4}]}{\int_0^{\Delta t_6} I_{sc,dis}(t) dt} \quad (5.82)$$

Similar to Δt_3 process, the useful energy in this period $E_{useful}(\Delta t_6)$ can be expressed as:

$$E_{useful}(\Delta t_6) = E_{consumed}(\Delta t_6) - E_{super}(\Delta t_6) \quad (5.83)$$

where $E_{consumed}(\Delta t_6) = \int_0^{\Delta t_6} V_{SC}(t) \cdot \frac{I_{T,consume}}{\eta_{capacitor}} dt$ and $E_{super}(\Delta t_6) = \left(\frac{1}{2}\right) \cdot C_{SC} \cdot [V_{w,th3}^2 - V_{w,th4}^2]$. And the battery energy is maintained at the same level.

5.7 Theoretical analysis of an energy harvesting system

After the entire model construction, the performance of a micro-energy harvesting system can be analysed. As shown in previous chapters, the lifetime and the energy efficiency of the system are the two critical factors for any energy harvesting platform. Hence, the system performance can be analysed in terms of the two metrics: the lifetime prediction and the daily energy conversion efficiency.

5.7.1 The lifetime prediction

The lifetime of the system is the key performance factor to indicate whether the proposed system is successful or not. Based on previous analysis, the lifetime of the system is determined by the lifetime of the energy buffers. The energy profile of the environment energy source can be obtained by the historical record or experience tests. By integrating the environment energy data into the integrated energy model of an energy harvesting system, the available energy of the system can be determined. On the other hand, the energy dissipation of the system can be calculated by using the

model as well. By comparing the energy difference between the energy generated and the energy dissipation, and comprehensively considering the residual energy level of the energy buffers, the lifetime of the system can be calculated. In order to simplify the description, it assumes that the system is powered by the rechargeable battery all the time and the harvested energy is stored into the super-capacitor before it charging the rechargeable battery. Then the total energy dissipation of the system $E_{consumed,T}(t)$ and the total energy generated by the system $E_{generated}(t)$ can be expressed as

$$E_{consumed,T}(t) = I_{T,consume} \cdot V_{vdd}(t) \cdot T_{lifetime} \quad (5.84)$$

$$E_{generated}(t) = E_{harvested} \cdot \eta_{capacitor}^2 \cdot \eta_{b,charge} \cdot \eta_{dis,battery} \quad (5.85)$$

where $V_{vdd}(t)$ is the supply voltage of the energy harvesting system and $T_{lifetime}$ is the lifetime of the system. The total energy harvested by the energy harvester through the lifetime $T_{lifetime}$, $E_{Harvester}(\text{total})$ is:

$$E_{Harvester}(\text{total}) = \int_0^{T_{lifetime}} P_{MPP}(t) dt \quad (5.86)$$

where $P_{MPP}(t)$ is the peak power of the energy harvester. At the same time, the residual energy of the rechargeable battery $E_{residual,B}(t)$ can be calculated by Equation 5.87.

$$E_{residual,B}(t) = SoC(t) \cdot C_{R-battery} \cdot V_{nominal,B} \quad (5.87)$$

where $SoC(t)$ is the current SoC of the battery, and $C_{R-battery}$ is the full capacitor of the battery, and $V_{nominal,B}$ is the nominal battery voltage. The lifetime $T_{lifetime}$ can be calculated by when Equation 5.88 is true.

$$E_{generated}(t) + E_{residual,B}(t) - E_{consumed,T}(t) = 0 \quad (5.88)$$

And the calculated t is the lifetime of the system.

$$T_{lifetime} = t$$

Moreover, in order to make the system have a perpetual lifetime, an energy neutral operation (Kansal, et. al., 2007) is introduced here. When the available energy of

system is equal to the energy dissipation of the system in a cycle, the system is considered to operate at the energy neutral operation, as shown in Equation 5.89.

$$E_{generated}(t) + E_{residual,B}(t) - E_{consumed,T}(t) \geq 0 \quad (5.89)$$

If the system in any test cycle Equation 5.89 is true, the system can be considered having an everlasting life system. But unfortunately, the energy generation of the system varies rapidly with the dynamic environment conditions and it is very hard to make the system operate at the energy neutral operation all the time. Hence, a power management algorithm should be considered in the system to achieve energy neutral operation.

5.7.2 Daily energy conversion efficiency

The efficiency of the energy harvesting platform is another factor to indicate the system performance. This is extremely important for the micro-scale energy harvesting system, because the higher efficiency the system can shrink the system cost and size. In this chapter, daily energy conversion efficiency, which is defined as 24 hours energy conversion efficiency, is introduced to evaluate the system performance. A 24 hour test window is selected in this work because the energy availability from the environment is normally daily based. The daily energy conversion efficiency $\eta_{system}(daily)$ refers to the ratio between the energy delivered to the system $E_{delivered}$, which is the sum of energy consumed by the system and energy stored in the energy buffers, and the energy harvested by the energy harvester $E_{harvester}$ in a day.

$$\eta_{system}(daily) = \frac{E_{delivered}}{E_{harvester}} 100\% \quad (5.90)$$

$$E_{delivered} = E_{consumed}(total) + [E_{system}(Remain) - E_{system}(initial)]$$

where $E_{consumed}(total)$ is total energy consumed by the system in 24 hours, and $E_{system}(Remain)$, $E_{system}(initial)$ are the residual energy and initial energy level of the system, respectively. The initial energy stored in the energy harvesting system is

$$E_{system}(initial) = E_{Battery}(initial) + E_{capacitor}(initial) \quad (5.91)$$

where $E_{Battery}(initial)$ and $E_{capacitor}(initial)$ are the pre-stored energy on the rechargeable battery and the supercapacitor, respectively. The initial energy on the rechargeable battery can be calculated by knowing $V_{nominal,B}$ and the initial battery capacitance $C_{battery}(t_{initial})$

$$E_{Battery}(initial) = V_{nominal,B} \cdot C_{battery}(t_{initial}) \quad (5.92)$$

On the other hand, the initial energy stored on the super-capacitor can be calculated as:

$$E_{capacitor}(initial) = \frac{1}{2} \cdot C_{SC} \cdot V_{SC}^2(t_{initial}) \quad (5.93)$$

After 24 hours of operation, the remaining energy in the energy storage elements are:

$$E_{system}(Remain) = E_{Battery}(Remain) + E_{capacitor}(Remain) \quad (5.94)$$

$$E_{Battery}(Remain) = V_{B,OC}(0) \cdot C_{battery}(t_{final}) \quad (5.95)$$

$$E_{capacitor}(Remain) = \frac{1}{2} \cdot C_{SC} \cdot V_{SC}^2(t_{final}) \quad (5.96)$$

where $C_{battery}(t_{final})$ and $V_{SC}(t_{final})$ are the final capacitor of the battery and final voltage of the super-capacitor, respectively. Total energy consumed by the system during a day can be expressed as:

$$E_{consumed}(total) = \int_0^{24\text{hours}} P_{T,consume}(t) dt \quad (5.97)$$

where $P_{T,consume}(t) = I_{T,consume} \cdot V_{T,consume}(t)$. To simplify the calculation, $V_{T,consum}(t)$ is considered as a constant value 2.8V which is the terminal voltage of the two series connected NiMH batteries. The total energy harvested by the energy harvester through a day is:

$$E_{Harvester}(total) = \int_0^{24\text{hours}} P_{MPP}(t) dt \quad (5.98)$$

Then the daily efficiency of the system can be calculated according to Equation 5.90.

5.8 Model Validation

In the model evaluation, the component and entire system model are validated against reference experiments to show the accuracy of the model which is expected to predict the system performance. The system simulation could be carried out to simulate system behaviour in different situations and with different dimensioning parameters of components used by the system. The mathematical model is simulated by Matlab, which provides a strong capability of mathematic calculation and flexibility for simulation. As stated in the previous sections, individual components of the energy harvesting system were validated. In order to validate the entire system model, two actual deployments, solar and thermal energy harvesting systems, have been implemented in the laboratory. The evaluation processes can be divided into different steps based on the function of each subsystem.

5.8.1 Set up the test environments

Before designing the prototypes to evaluate the simulation mode, a controllable test environment should be developed. This is because the harvested energy is extremely dependent on the environment where the energy harvester is deployed. For instance, the performance of a solar panel depends on the solar irradiance levels, dust and the environment temperature. And the harvested energy from the TEG system is highly related to the surrounding temperature and air flow. As these environment factors are difficult to predict in a certain place at a certain time, it is hard to evaluate the proposed model in a real environment. But if the environment factors are controllable and being known by the designer, the model evaluation can be carried out. For solar energy, a 100W controllable desk lamp has been employed to emulate a controllable solar light in door. The different light conditions can be obtained by adjusting the output of the lamp or varying the distance between the solar cell and the lamp. For emulating a controllable thermal energy in the laboratory, a 50 W electric heater has been used. The temperature of the heater can be adjusted by the on board controller and the room temperature has been maintained at a constant value by an air condition.

5.8.2 Evaluate the energy transfer efficiency

As concerned by all the energy harvesting researchers, the system transfer efficiency is critical in designing any energy harvesting system. Hence, the first evaluation step is to verify the energy harvester with the MPPT based power

conversion system. This is because the energy harvester and the power conversion subsystem are the two main parts to determine the system's efficiency. In this part, the energy consumer and the energy storage subsystem are ignored. As mentioned in previous parts, the amorphous solar cell AM-5412 from SANYO and eight pieces of Bi₂Te₃ TE modules TEC1-12709 from the Taicang TE cooler company have been used to harvest the light energy and the thermal energy, respectively. Hence, these devices have been used as the energy harvester in both the simulation models and the evaluation prototypes. In this chapter, the synchronous boost converter TPS61221 from TEXAS instrument has been employed as the regulator circuit for boosting the low input voltages and regulated the voltages to a constant 5V output voltage. In order to calculate the harvested energy, two 22F super-capacitors from Panasonic, series connected, have been used as the energy buffer. There are some reasons to use super-capacitor as the energy accumulator. First, the charging efficiency of the super-capacitor is near 100%, which the energy lost in charging process can be neglected. Secondly, the energy stored on the super-capacitor can be easily calculated by knowing the voltage level of the super-capacitor. In order to ensure the initial state of the super-capacitors at the same level in all the experiments, the super-capacitors have been pre-charged to 1.3V.

For the MPPT circuit, in order to simplify the evaluation test setup, the open circuit voltages of the solar panel and the TEG for each test environment have been measured. Based on the results in relation with the linear relationship between the open circuit voltages to the MPP of the energy harvesters, the MPPs of the energy harvesters in these test conditions can be calculated. These results have also been used as the peak power, harvested by the energy harvesters, to calculate the energy efficiency of the system. By knowing the MPPs in these test conditions, an ultra-low power single comparator LTC1440 from Linear (Linear technology LTC1440, 2008) has been used as the MPPT circuit to make the system working at MPPs. The schematic diagram of the MPPT unit is shown in Figure 5.18. The on chip 0.5V reference voltage is connected to the Pin 4 as one input of the comparator. This is the reference voltage to indicate the output voltage of the energy harvester, which has been reached MPP. Another input Pin3 is connected to the output voltage of the energy harvester through two adjustable resistors R_1 and R_2 . Their resistances can be adjusted based on the calculation shown below:

$$V_{reference} = \frac{R1}{R1 + R2} V_{MPP}$$

where V_{MPP} is the voltage of the MPP of the energy harvester in a test condition, $R1$ and $R2$ are the resistances of two adjustable resistors, and $V_{reference} = 0.5V$. By comparing these two inputs values, when the output voltage of the energy harvester is equal to the voltage of the MPP, the comparator sends a control signal to switch on the DC-DC boost converter. Based on this principle, the simplified MPPT based power conversion circuit has been developed. By ignoring the power consumption of the periphery circuit of the comparator, the overhead of the MPPT circuit can be calculated by knowing the quiescent current of the comparator circuit, which is $2.1\mu A$ according to the datasheet. In order to avoid the MPPT circuit extracting energy from the energy harvesting system to make calculation complicate, an external 3V battery has been used to sustain the MPPT circuit. Then the power consumption of the MPPT circuit can be estimated $P_{MPPT,C} = 6.3\mu W$.

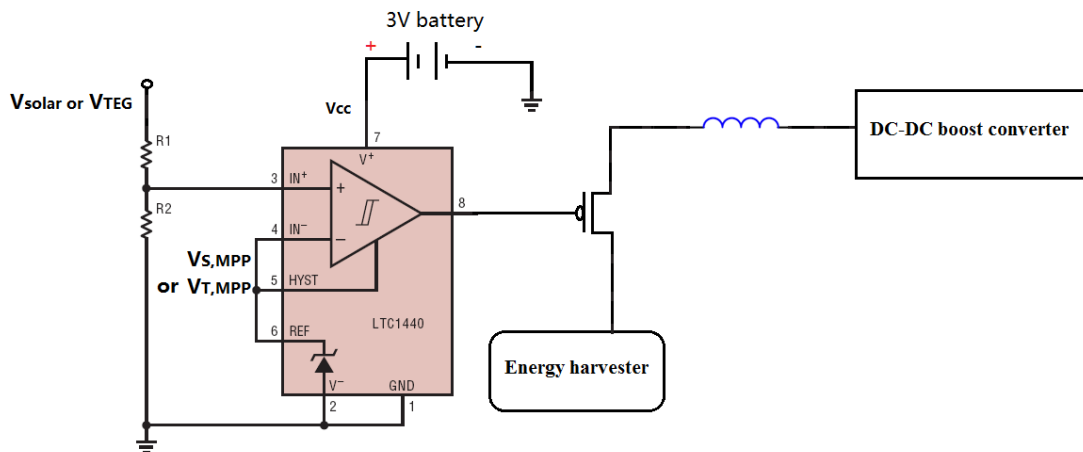


Figure 5.18 Schematic diagram of MPPT circuit

Three different light levels, 50kLx, 35kLx and 8.12kLx, have been used to evaluate the energy transfer efficiency of the solar energy harvesting system. According to the tests, the open circuit voltages of the solar panel in these three conditions are 2.6V, 2.39V and 2.19V, respectively, when the environment temperature is set at 25°C. Based on the Equations 4.3 and 4.4, shown in Chapter 4, the MPP of the solar panel in these three conditions are 1.976V, 1.864V and 1.664V, respectively. By typing these energy sources into the model of the boost converter, the corresponding converter efficiencies are 81.2%, 80.1% and 79.8%, respectively. By considering the $\eta_{MPP} =$

85% and $P_{consumer,MPPT} = P_{MPPT,C} = 6.3\mu W$, the regulated energy of the solar energy harvesting system can be calculated. Normally, the charging time is the best way to indicate system efficiency. Table 5.7 shows the charging time of simulation and experimental results. By examining the comparison results, the accuracy of the model is around 81.5% in the worst case. The accuracy of the model is acceptable. It is noticed that there are some differences between the simulation and the real measurement. This is caused by an idealistic modelling of the individual subsystems. But the simulation results capture the trend that the energy conversion efficiency is roughly increased in proportion to the strength of the harvested energy. Based on analysing results, the charging time is proportional to the harvested energy. Furthermore, the energy conversion efficiency of the energy harvesting system η_{ECE} could be calculated by knowing the total energy harvested from the environment, total energy stored into the capacitors $\Delta E_{capacitor}$, and total energy consumed by the MPPT circuit during a time interval t .

$$\begin{aligned}\eta_{ECE} &= \frac{\Delta E_{capacitor} - E_{MPPT}}{E_{Harvester}(\text{total})} \\ &= \frac{\frac{1}{2} C_{sc} \cdot [V_{sc}^2(t) - V_{sc}^2(t_{initial})] - \int_0^t P_{consumer,MPPT} dt}{\int_0^t P_{mpp}(t) dt}\end{aligned}\quad (5.99)$$

where $C_{sc} = 22F$ and $P_{mpp}(t)$ is the peak power of the energy harvester. By applying charging times into Equation 5.99, the efficiency of the system can be calculated, as shown in Table 5.7. Based on the results, the energy conversion efficiency of the system is highest when the light level is 50kLux. This indicates the system efficiency is highly related to the input level of the light energy. It also can be observed that the highest system efficiency can be found when the super-capacitor's voltage is in range of 4.1V to 5V and the lowest system efficiency is in the range of (1.3V to 3V). This is because when the super-capacitor is charging from 1.3V to 3V, the charging current drawn from the boost converter is the maximum output current of the boost convert. And the conversion efficiency of the boost converter in this condition is the lowest, which are around 40%. When the terminal voltage level of the super-capacitor approaches the charging voltage 5V, the charging current drops but the energy transfer efficiency increases. Based on this point of view, the higher system efficiency can be obtained when the charging voltage is set to near the highest voltage

threshold of the super-capacitor. Moreover, based on the experimental result, when the light input level is 8.12kLux, the supercapacitor cannot be charged to 5V. This is because the leaking current of the super-capacitor is higher than the charging current.

Table 5.7 Charging the super-capacitors with different light irradiances

Input power	Charging time (From 1.3V to 3V)		Charging time (From 3V to 4.1V)		Charging time (From 4.1V to 5V)	
	Efficiency		Efficiency		Efficiency	
	Simulation	Experimental	Simulation	Experimental	Simulation	Experimental
44mW (50kLux)	2791 (s) 32.74%	2820 (s) 32.4%	1805 (s) 54.08	2294 (s) 42.55%	1476 (s) 69.35%	1606 (s) 63.7%
27.41mW (35kLux)	4720 (s) 31.07%	4758 (s) 30.8%	3053 (s) 51.3%	3947 (s) 39.7%	2606 (s) 63.308%	3000 (s) 54.77
4.44mW (8.12kLux)	70122 (s) 12.9%	84146 (s) 10.76%	45383 (s) 21.3%	68074 (s) 14.21%	27186 (s) 37.31%	Capacitor can only be charged to 4.4V

Moreover, in order to show the MPPT circuit is critical in enhancing energy efficiency of the system, two different working points (3V and 2V) of the solar panel have been selected when the solar energy harvesting system is illuminated under 50Klx light condition. When the system operates at the MPP, the solar panel has 44mW output power. But when the 3V working point has been set by the system, the output power drops to 9.3mW. The simulation and the corresponding experimental test results are shown in Table 5.8. By comparing charging times, when the system works at MPP, it has the most efficient charging time. By integrating the simulation results into Equation 5.99, the system conversion efficiencies at 3V and 2V working points are 7.86% and 22.89%, respectively. By integrating the experimental results in Equation 5.99, the efficiencies are 6.8% and 20.88% at the points 3V and 2V, respectively. By comparing with the system efficiency of 41.57% at the MPP, the system efficiency rapidly decreased when the solar energy harvesting system is not working at the MPP. According to this point, the MPP circuit is critical for an energy harvesting system which requires high system efficiency.

Table 5.8 The comparison results of MPP vs. other two working points

Input power	From 1.3V to 5V	
	Simulation (second)	Experimental (second)
44mW (Maximum Power point)	6072	6720
9.3mW (3V, 3.1mA)	37000	42678
26.4mW (2V, 13.2mA)	12718	13950

The same processes have been used to evaluate the model of thermal energy harvesting system, which use the TEG model to replace the solar panel model in the previous part. Because of the ultra-low harvester voltage, eight pieces of TE modules were connected in series to enhance the harvester voltage in this test. In order to show the difference, 10K and 15K temperature differences have been used. Similar to the solar energy harvesting system, the open circuit voltage of the TEG have been measured before the simulation. Based on Equation 4.53, showed in Chapter 4, the MPPs of the TEG system under these two temperature conditions can be calculated. Similar to the solar energy harvesting system, the testing and simulation results of the charging time and efficiency are listed in Table 5.9.

By comparing the simulation and the testing results, the accuracy of the model is around 83.1% in the worst case. The energy conversion efficiency of the system in these two conditions is 40.31% and 36.46% by integrating the experimental results in the Equation 5.99. By comparing the efficiency with the solar energy harvesting system, the conversion efficiency of the thermal energy harvesting system is much lower than the solar energy harvesting system. This is why this energy harvesting technology is not as popular as the solar one.

Table 5.9 Charging the super-capacitors with different temperature differences

Input power	Charging time (From 1.3V to 3V)		Charging time (From 3V to 4.1V)		Charging time (From 4.1V to 5V)	
	Efficiency		Efficiency		Efficiency	
	Simulation	Experimental	Simulation	Experimental	Simulation	Experimental
41.6mW (dT=15K)	3512 (s)	4218 (s)	2271 (s)	2895 (s)	1857 (s)	2055 (s)
	27.52%	22.91%	45.46%	35.66%	58.3%	52.69%
23.4mW (dT=10K)	6885 (s)	8269 (s)	4454 (s)	5791 (s)	3644 (s)	6167 (s)
	24.96%	20.77%	41.21%	31.7%	52.8%	31.21%

In order to see the MPPT circuit affects the performance of the thermal energy harvesting system, the comparison results of the TEG system which works at MPP and other two selected (0.8V and 1.6V) working points are showed in Table 5.10. According to the results, the system efficiencies have been dropped to 29.22% and 20.61% in the real experimental tests. By comparing the conversion efficiency of 40.31% when the system is working at MPP, the system efficiency drops significantly when the system is not working at the MPP. It can be observed that 0.8V working point has much more efficient than the 1.6V working point. This is because the 0.8V working point is much closer to the MPP. In summary, the system efficiency can be rapidly enhanced when the working point of the energy harvester is close to the MPP of the energy harvester.

Table 5.10 The comparison results of MPP vs. other two working points of TEG

Input power	From 1.3V to 5V	
	Simulation Results (second)	Experimental Results (second)
41.6mW (0.98V)	7640	9168
38.9mW (0.8V)	8956	10536
24.1mW (1.6V)	12679	14916

5.8.3 Evaluate the model of the energy storage subsystem

The second evaluation step is to verify the model of the energy storage subsystem. In this part, the models of the power storage subsystem and the sensor node have been integrated together. In order to evaluate the model in a real environment, an experimental system has been developed based on the schematic diagram shown in Figure 5.19. Two 850mAH NiMH batteries and two 22F super-capacitors have been chosen as the power storage elements and the DR1048 sensor node has been employed as the energy consumer. The control circuit has been designed by using a PIC16F688 MCU from Microchip INC (PIC16F688, 2008), a MAX890L P-channel switch from MAXIM (Max890, 2007), and a dual P-channel MOSFET FDS9933A from Fairchild (Fairchild, FDS9933A, 2007). The functions of each component are described below:

- The PIC16F688 MCU has been used to monitor super-capacitors' voltage and batteries' voltage levels. As stated in the previous part, the power storage system can be in one of three states, which are using batteries powering the system, using capacitors powering the system, using capacitor powering system meanwhile charging the batteries, by examining the voltage level of the super-capacitor. Hence, the monitored super-capacitor voltages have been compared with four pre-setting voltage threshold 3V, 4.1V, 3.8V and 2.8V. By calling the UART function on the PIC MCU, the monitoring results can display on the computer.

- The MAX890L P-channel switch has been used to achieve charging or stop charging the NiMH batteries.
- The FDS9933 dual P-channel MOSFET has been used to supply a select function of the system, which the system can decide to use the battery or the super-capacitor to power the system.

The power consumption of the control circuit can be simply assumed as the power consumed by the PIC16F688 MCU and the MAX890L microchip. Based on their specifications, the current consumptions at 3.3V are $100\mu\text{A}$ and $10\mu\text{A}$, respectively. Then the total overhead of the control circuit

$$P_{E,control} = I_{E,control} \cdot V_{VCC}$$

where $V_{VCC} = 3.3\text{V}$ and $I_{E,control} = 110\mu\text{A}$.

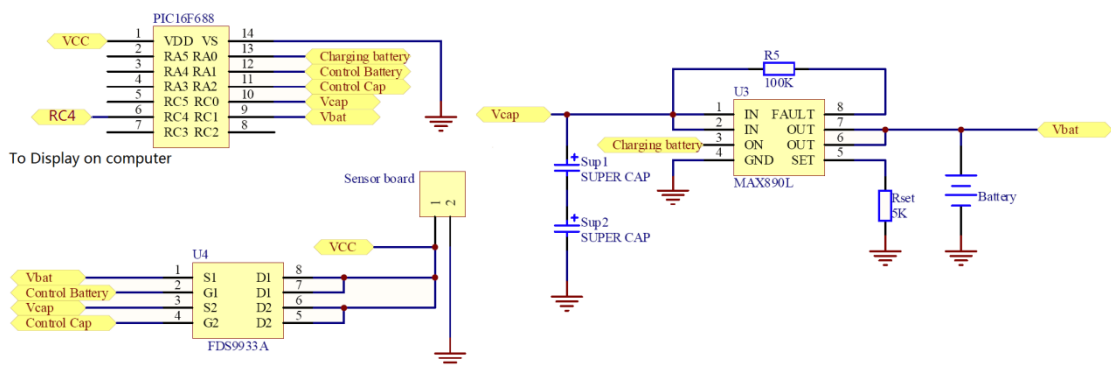


Figure 5.19 schematic diagram of the Power storage subsystem

In order to ensure the state of the super-capacitors and rechargeable batteries at the beginning of each experiment were the same, the super-capacitors and the rechargeable batteries have been pre-charged to 1.3V and 2.7V (SoC 80%), respectively. A programmable DC power supply (62000P Series, 2008) has been used to directly charge the super-capacitors. Two output levels 5V, 10mA and 5V, 20mA, have been selected respectively to emulate the harvested energy. Initially, the system draws energy from the rechargeable battery. When the voltage of the super-capacitors reaches four different voltage thresholds, the system decides to use battery or super-capacitor to power the system or charge the battery. Table 5.11 shows the charging time of the super-capacitors to reach 3V, 4.1V voltage thresholds with these two energy sources. The corresponding experiments show the accuracy of the model is around 93.4%.

Table 5.11 Charging time of the super-capacitors

Input power	From 1.3V to the first threshold voltage 3V (Second)		From 3V to the second threshold 4.1V (Second)		From 3.8V to 4.1V (Second)	
	Simulation	Experimental	Simulation	Experimental	Simulation	Experimental
50mW	1870	2002	2114	2263	576	617
100mW	935	1001	769	823	209	224

5.8.4 Evaluate the entire energy harvesting system model

For the hybrid model evaluation, both energy harvester model and the power conversion model have been implemented with the energy storage model. The energy levels of the super-capacitors and the rechargeable batteries have been recorded with different time stamp. In order to evaluate the model, two deployments of each system have been tested in the laboratory, where the solar panel was illuminated by a constant 50Klx light irradiance and the temperature difference of the TEG system has been maintained at 15K. To examine the accuracy of the model, the experimental and the simulation results are compared in Table 5.12. By comparing with the charging times, the accuracy of the model is around 81.4% in the worst case.

Table 5.12 Charging the super-capacitors with solar energy harvesting system and TEG

Input power	From 1.3V to the first threshold voltage 3V (Second)		From 3V to the second threshold 4.1V (Second)		From 3.8V to 4.1V (Second)	
	Simulation	Experimental	Simulation	Experimental	Simulation	Experimental
Solar cell 44mW (50kLx)	3080	3850	6748	8477	1840	2300
TEGs 41.6mW (dT=15K)	3747	4683	16970	21453	4628	5850

In order to calculate the daily conversion efficiency of the system, the prior test setups have been tested in the laboratory for 24 hours. Figures 5.20 and 5.21 show the complete voltage curves of the super-capacitors and the rechargeable batteries in these

conditions both by simulation and experiment. By examining the voltage curves of the super-capacitors in Figure 5.20, the super-capacitor's terminal voltage rises rapidly when the terminal voltage is less than 3V. After the terminal voltage is higher than the 3V, the slope of the voltage curves becomes flat. This is because the system switches to using the super-capacitors to power the system. When the terminal voltage is higher than 4.1V, it drops rapidly to 3.8V. This is because the energy from the super-capacitors is charging the rechargeable battery. By calculating the times of super-capacitors charging the batteries, the simulation results show the batteries have been charged 42 and 15 times during one day operation by solar energy and thermal energy, respectively. The experimental results show the batteries have been charged 28 and 12 times during a 24 hours test. Figure 5.21 depicts the corresponding battery voltage of the two prototypes. It can be observed that the battery voltage rises as expected. The simulation results show the terminal battery voltage are 2.727V and 2.703 for solar and thermal energy harvesting system. The experimental results show the final battery voltages of the two platforms are 2.721V and 2.702V, respectively. In order to calculate the daily conversion efficiency of the platform, the simulation and the experimental results are integrated into Equations 5.90-5.98, respectively. The daily conversion efficiencies of the solar and the thermal energy harvesting systems are 41.07% and 36.8%, respectively. The corresponding experimental results show that the daily energy conversion efficiency of the system are 36.8% and 32.85% in these two cases. The accuracy of the model is around 80% which is acceptable to predict the performance of an energy harvesting system.

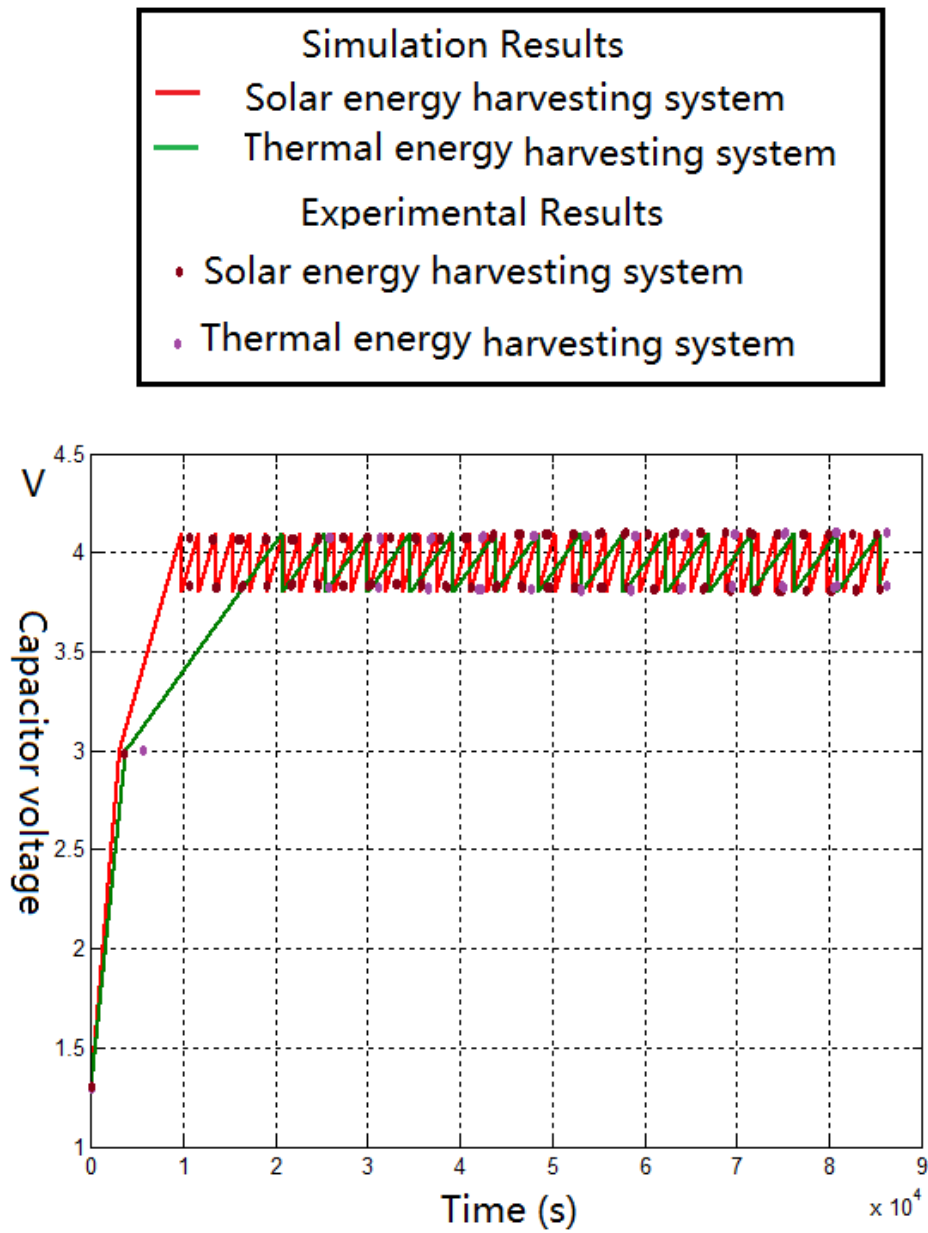


Figure 5.20 The super-capacitors voltages with solar and thermal energy harvesting system

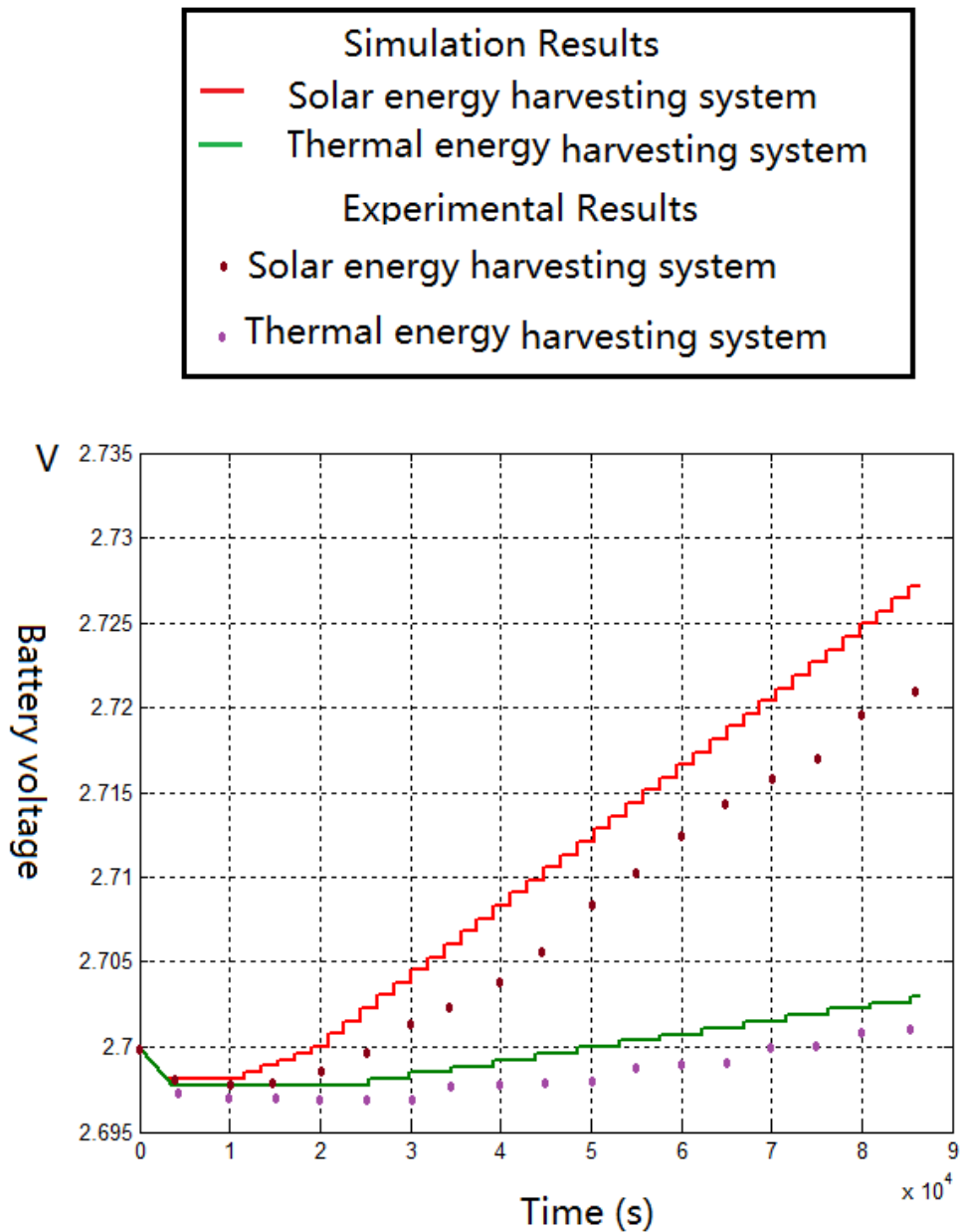


Figure 5.21 The terminal battery voltage of the system by using the solar panel and the TEG

5.9 Summary

When designing and deploying a micro-energy harvesting system, a careful understanding of numerous parameters of the system, such as the energy level of the harvested power, the power consumption of the system and the efficiency of the system is required. Due to the price and volume constraints of wireless sensor nodes, and the fact that it normally a perpetual lifetime, the design procedure becomes more

complex and difficult. Hence, using an analytical model to theoretically analyse the performance of a proposed system is critical. In this chapter, based on the architecture and energy flows, each building block of the system has been modelled. The accuracy of each component model has been validated in the laboratory. In order to explore how these components impact the system performance, a hybrid system model has been established by compositing these component models. Solar and thermal energy harvesting systems have been selected as two examples to show how to create the model. The models have been evaluated in the laboratory with the controllable environments. The experimental results show the accuracy of the model is no worse than 80%, which is acceptable for evaluate an energy harvesting system design. According to the results, the model could be used to prevent excessive system testing or undesired results from miss-dimensioning. The model also shows the system performance is highly related to some key system parameters, such as environment conditions, the efficiencies of the MPPT circuit and the regulator circuit. These findings can be used to guide the designers to make decisions on selecting components under a known environment. As mentioned before, energy harvesting systems are always over-designed by using larger energy transducers and energy storage elements than necessary. Hence, the model could be used to derive a cost-effective and energy efficient design for an energy harvesting system.

Chapter 6. Design and implementation of a power conversion circuit based on MPPT technologies

6.1 Background and motivation

Energy efficiency is a critical factor in designing a micro energy harvesting system. The existing energy harvesting platforms are low energy efficient in terms of energy conversion efficiency. As the cost and volume are constrained by designing a micro energy harvesting system, it is necessary to use a highly efficient circuit design to scale down the cost and volume in term of using small and compact energy generators and energy storages. As stated in the previous chapters, system efficiency can be divided into four parts: energy conversion efficiency, energy transfer efficiency, buffering efficiency and consumption efficiency. In this chapter, improving both the energy conversion efficiency and the energy transfer efficacy are considered.

Normally, the energy conversion efficiency is determined by the capability of the energy harvester and the energy level of the energy source, in which the energy harvester is placed. Once the energy harvester has been designed, the energy conversion efficiency is determined. Then the available energy of the system is decided by knowing how much of the harvested energy can be transferred to the system. The energy conversion efficiency is especially low for a micro energy harvesting system because of the difficulty of tracking the maximum power point of the micro-scale energy harvester. On the other hand, for the energy transfer efficiency, it is determines how much the generated energy can be transferred as useful energy, which can be used to power the system or be stored into the energy buffer. As illustrated in Chapter 5, an energy harvesting system can achieve a high performance by using an efficient power conversion system with a proper Maximum Power Point Tracking (MPPT) technology. Nowadays, many researches focus on this area to extract as much energy as possible from the energy harvesters. But the efficiency of

the intermediate circuit is low which is considered as a bottleneck in designing and deploying a micro energy harvesting system.

6.2 Feature of proposed work

In this chapter, a power conversion circuit, based on the proposed system architecture illustrated in Chapter 3, has been designed. In order to enhance the energy harvesting system's performance in terms of the energy efficiency, both the MPPT technology and the boost converter circuit are considered. In the first part, a high efficient boost converter, which is used to regulate the ultra-low input voltages at a constant value, is designed. In order to make the system meet the cost-size and the energy efficiency requirements, the components of the boost converter are chosen based on the proper design considerations. Secondly, in order to track and maintain the system working at peak power level, an efficient MPPT circuit is needed. Three existing MPPT technologies, which are normally used for micro energy harvesting systems, are compared with each other in various conditions to show the characteristics of these technologies. As power consumption is the main concern factor in designing a micro energy harvesting system, low power consumption is considered in both parts of the power conversion circuit.

6.3 Proposed MPPT based Power conversion subsystems

A generic block diagram of MPPT based power conversion circuit is illustrated in Figure 6.1. The circuit is divided into two parts: the regulator circuit and the MPPT control circuit. The regulator circuit is built by a boost converter IC with its peripheral components to boost the low input voltages to a constant higher output voltage, which can be used to directly power or charge the system. The MPPT circuit is used to track the peak power of the energy harvester. The working principle is that the MPPT circuit generates a proper control signal to turn on or off the boost converter circuit through a MOSFET device G_1 according to make the peak energy from the energy harvester which can be transferred to the regulator circuit.

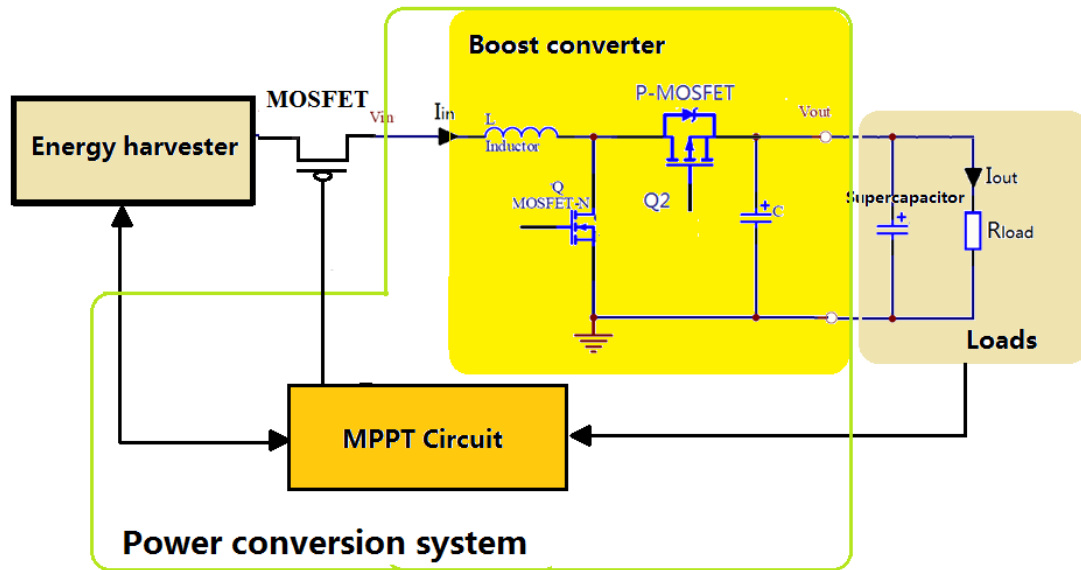


Figure 6.1 Block diagram of micro energy harvesting system

6.3.1 Regulator circuit design

Since the amount of harvest energy is limited, an efficient regulator circuit, which operates at a high efficiency over a wide load range, is a key in the design of any high efficient power conversion subsystem. A DC-DC boost converter is employed as the regulator circuit in this study. By considering the constraints of the micro energy harvesting system, the regulator circuit should be made extremely energy efficient, low cost and compact size in order to be integrated into an energy harvesting system.

6.3.1.1 Design considerations for a regulator circuit

The efficiency is a critical factor in designing a regulator circuit. Based on the datasheets, for a specific range of loads, some boost converters can be designed with efficiency greater than 90%. But with variations of loads and input power levels, their efficiency might vary significantly. Hence, optimizing a DC-DC boost converter design is very important for designing a highly efficient energy harvesting system. As shown in Chapter 5, a boost converter circuit can be optimized by decreasing energy losses caused by its components, which are the MOSFET switches, the inductor, the capacitors and the control IC. By choosing a set of proper components to reduce their energy loss, the performance of the boost converter can be enhanced.

(1) Inductor selection

Since the boost converter is used to provide a stable high output voltage from a given low input voltage, the power inductor selection is very important in designing a

highly efficient regulator circuit. Based on the datasheet of the boost converter (TPS61222, 2010), the boost converter, which works at Continuous Conduction Mode (CCM), can have high energy efficiency. In order to keep the converter working at CCM all the time, it is necessary to make the inductor's value higher than a boundary condition. The critical inductor value, $L_{(crit)}$, is selected based on Equation 6.1 (Hasaneen and Elbaset, 2008).

$$L_{(crit)} = \frac{V_{out,boost}}{2 \times f_s \times I_{out(max)}} D_{max}(1 - D_{max})^2 \quad (6.1)$$

where D_{max} is the maximum duty cycle of the boost converter and $V_{out,boost}$ and $I_{out(max)}$ are the output voltage and the maximum output current of the boost converter and f_s is the minimum switching frequency of the converter. Normally, the size and the performance of the inductor is highly dependent on the switching frequency f_s , which the higher switching frequency the boost converter has, then the smaller inductor can be used. But the high switching frequency causes a large switching loss in the boost circuit. On the other hand, a larger inductor means the boost circuit is more energy efficient. But the size of the system is also increased. Hence, there is a trade-off between the performance and size of the inductor. Choosing a proper switching frequency with a proper size of the inductor is very important in designing a high efficient regulator circuit. Moreover, because the main contributor of power loss in the inductor is caused by the Equivalent Series Resistance (ESR) of the inductor, the small ESR of the inductor should be used to reduce the power loss. Based on this point, the inductors with a coil and low resistance should be used for achieving high system efficiency.

(2) MOSFET selection

The power losses in the MOSFET switches (Q and Q2), shown in Figure 6.1, are other energy loss sources in the boost converter circuit. In order to limit these energy losses, a low power N-channel MOSFET and P-channel MOSFET should be used in the circuit. In this chapter, a synchronous boost converter TPS61222 from Texas Instruments is selected as the control Integrated Circuit (IC) of the boost converter. These two MOSFET switches are integrated into the boost IC that saves time for selecting a proper MOSFET switches for the boost circuit.

(3) Selection of the required capacitor

There are two functions of the output capacitor. Firstly, it used to deliver energy to the load during switch on time of the boost converter. Second, it can be used as a filter to reduce the output ripple voltage. The primary criterion for selecting the output capacitor is its capacitance and ESR. This is because that the capacitance decides the volume of the capacitor and ESR decides the energy dissipation of the capacitor. Typically, the output capacitor is chosen to meet an output voltage ripple specification. An approximate equation for the required capacitance can be expressed as (Hasaneen and Elbaset, 2008):

$$C_{out} \geq \frac{L}{2} \quad (6.2)$$

where C_{out} is the capacitance of the output capacitor and L is inductance of the inductor which is used in the converter circuit. Capacitors' ESR affects conversion efficiency and a good performance can be produced by using low ESR capacitors. Hence, a ceramic capacitor with a low ESR has been normally used in designing a high efficient DC-DC converter. Moreover, connecting a few capacitors in parallel is considered as a possible way to reduce ESR of the capacitor.

6.3.1.2 Design and implementation of a regulator circuit

The synchronous boost converter TPS61222 has been selected as the regulator IC because of its low quiescent current of 0.5uA and high system efficiency even at low input powers. And it saves time for choosing two MOSFET switches. Based on Figure 6.1, the input voltage of the boost converter is equal to the output voltage of the micro energy harvester, which is dependent on the characteristics of the energy harvester, the environment condition and the MPPT control circuit. Based on the datasheet, the schematic diagram of TPS61222 is shown in Figure 6.2.

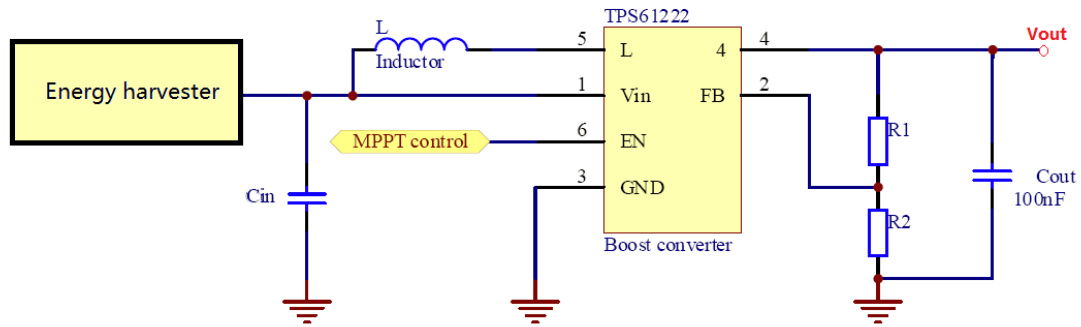


Figure 6.2 Schematic diagram of the boost converter TPS61222

The boost converter circuit must have low power overhead because of micro-scale energy harvesting used. The parameters of the boost converter IC are listed in Table 6.1. The peripheral components can be decided by knowing these parameters.

Table 6.1 Some design specifications of the boost converter

Parameters	Value
Maximum switching frequency	100Khz
Input voltage (V_{in}) Range	1.2-2.5V
Max ripple current	200mA
Output current	19.2mA
Output voltage V_{out}	4.1V

According to the results shown in Chapter 5, the system efficiency is highly dependent on the output voltage of the super-capacitor, which the highest system efficiency can be obtained when the output voltage of the boost converter is equal to the highest voltage threshold of the super-capacitor. As illustrated in (TPS61222, 2010), a 100nF ceramic capacitor are normally used as the input capacitor, which improves the transient behaviour and the Electro-Magnetic Interference (EMI) behaviour of the regulator circuit by reducing its input impedance and stabilizing the input power. Moreover, the input capacitor also can be used as a voltage sensor to indicate the power status of the energy harvester.

Two resistors R_1 and R_2 are used to adjust output voltage of the boost IC, V_{out} . Equation 6.3 shows the relationship between these two resistors and V_{out} .

$$R_1 = R_2 \left(\frac{V_{out}}{V_{FB}} - 1 \right) \quad (6.3)$$

where V_{FB} is 0.5V, provided by the datasheet (TPS61222, 2010). In this chapter, $V_{out} = 4.2V$ is set by the system. Then the value of R_1 and R_2 can be calculated.

As said before, in order to make the system work at a high efficiency mode, the converter circuit should work in CCM all the time., This means the inductance value should be higher than the critical value, calculated by Equation 6.1. However, TPS61222 boost IC is not a fixed frequency converter IC, which operates by regulating the ripple current in the inductor around 200mA. The datasheet provides an easy way to estimate whether the boost converter work at CCM or Discontinue Conductance Mode (DCM), as shown in Equation 6.4.

$$\frac{V_{out,boost} \times I_{out,boost}}{V_{in}} > 0.8 \times 100mA \quad (6.4)$$

where $V_{out,boost}$ and $I_{out,boost}$ are the output voltage and current of the boost circuit and V_{in} is input voltage of the boost circuit. As setting $V_{in} = 1.2V$ and $V_{out} = 4.1V$, the boundary output current of the converter, operating at CCM, is 19.2mA. In order to calculate the critical value of the inductor, the maximum duty cycle D_{max} should be determined. The D_{max} can be calculated by introducing the minimum input voltage $V_{in(min)} = 1.2V$ and the constant output voltage $V_{out} = 4.1V$ into Equation 6.5. The calculation result shows D_{max} is equal 0.76.

$$D_{max} = 1 - \left(\frac{V_{in(min)}}{V_{out}} \right) \quad (6.5)$$

By adopting 100Khz working frequency for the converter, the critical value of the inductor can be obtained:

$$L_{(crit)} = 5.7\mu H \quad (6.6)$$

When an inductor higher than the critical value is selected, the boost converter works at CCM. In this chapter, a 10uH choke coil inductor with a high permeability and a high flux density ferrite core from Murata power solutions (29L103C Inductor,

2007), has been selected. Based on the inductor's datasheet, the DC parasitic resistance of the coil is $15\text{m}\Omega$, which is very small by comparing with other circuit.

In this design, two series connected 22F super-capacitors have been chosen as the output capacitor to accumulate the regulated energy from the boost converter. Normally, the boost converter needs the output capacitor being placed close to the boost IC. But considering the size, these two capacitors cannot be placed close to the boost IC. Hence, an extra small ceramic capacitor is placed close to the IC to reduce the output voltage ripple. Based on Equation 6.2, the value of the output capacitance value needs to be no less than half the inductance value. Hence, a $10\mu\text{F}$ capacitor has been chosen as the output capacitor in this design.

The efficiencies of the proposed boost converter have been calculated by using the DC-DC converter model explained in Chapter 5. Figure 6.3 illustrates the efficiency graph of the TPS61222 with different power inputs. In order to validate the accuracy of the simulation results, the corresponding experiments have been tested in the laboratory. The comparison result shows that the simulation results highly match the experimental results.

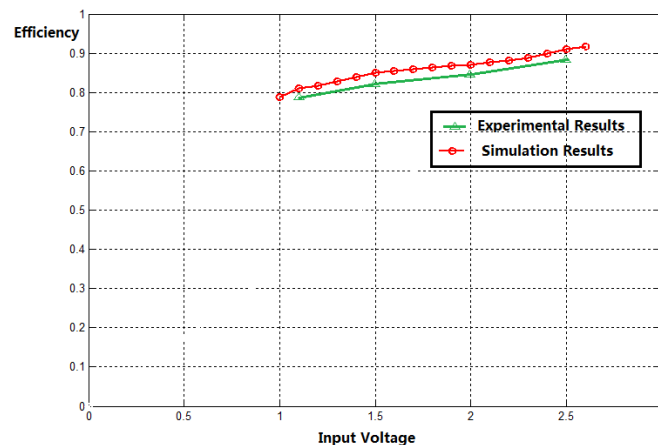


Figure 6.3 Efficiency vs. Input voltage of TPS61222

6.3.2 Maximum power point tracking unit

The MPPT control unit decides how much the harvested energy can be delivered to the power conversion circuit. But sometimes this goal is hard to achieve because there are some obstructions in this area. Firstly, the MPP for an energy harvester varies with the strength of the environmental energy sources, which rapidly changed with time and location. The dynamic energy sources make a simple MPPT scheme hardly to locate

the exact MPP of the energy harvester or even mislead the system. Secondly, as the location of the MPP in the I-V plane is unknown a priori, normally a complicated MPPT algorithm and a high capability MCU should be used to trace the MPP of the system during various situations. Since the size of the energy harvesters is scaled down, the harvested power drops into the range of micro watt, which presents a new design challenge for low power MPPT circuit design. Based on these analyses, the design specifications for an MPPT circuit in a micro energy harvesting system are efficiently tracking the MPP of the energy harvester and ensuring the minimal power overhead.

6.3.2.1 Conventional MPPT methods

MPPT controlled energy harvesting systems have been widely implemented and their effectiveness is well proven (Simjee and Chou, 2006, Park and Chou 2006, Eakburanawat and Noonyaroonate, 2005). Ordinarily, these approaches can be roughly divided into the analog and digital parts. An analog MPPT circuit uses an analog circuitry and a classical feedback control to make the energy harvesting system approaching MPP. They are mainly characterized by their simplicity, low overhead and low cost, but are more problematic to control (Tanouti et al., 2010). A digital MPPT circuit use a MCU based with digital and adaptive algorithm to track MPP of the system. The benefits of this design are that it is normally more reliable and more efficient than an analog one. But the power consumption is the main challenge for using this approach in the micro energy harvesting systems. In this section, an overview of several existing MPPT approaches, which can be used for a micro energy harvesting system, is described below.

(1) Design time component matching (DTCM) approach

The DTCM MPPT approach is used in Heliomote solar harvesting platform (Raghunathan et al., 2005). The MPP operation is achieved by careful selection of the specific solar cell and the rechargeable battery. In their platform, the terminal voltage of the batteries is around 2.8V when they are charged. Meanwhile, the solar panel's MPPs varied between 2.5V-3V. They stated that the Heliomote system can always operate with few tenths of a voltage difference of its exact MPP. The zero tracking overhead is the main advantage of using this approach. But the drawbacks of this approach are obvious. Firstly, direct connection makes the system has very low

efficiency, because the solar panel stops charging the rechargeable batteries when the panel's terminal voltage is lower than the rechargeable battery. Secondly, without MPP tracking system, the system can just work around the MPP of the system. This makes the MPPT efficiency of the system very low by comparing with other precise MPPT approaches.

(2) Fractional Open Circuit Voltage (FOC) approach/ Fractional Short Circuit current (FSC) approach

FOC and FSC approaches are two automatic MPPT approaches proposed in the literature. The principle of the algorithms is based on that there are approximately constant ratios between the MPP's voltage to open circuit voltage and the MPP's current to short circuit current. By either measuring the open circuit voltage or measuring the short circuit current of an energy harvester, the MPP voltage or MPP current can be approximated. Based on these linear relationships, simple approaches to estimate V_{mpp} or I_{mpp} by momentarily disconnecting the solar cell from the load to sense open circuit voltage or short circuit current were proposed in (Masoum et al., 2002), (Simjee and Chou, 2006) and (Bekker and Beukes, 2004). An interface circuit, which is a charge pump or a boost converter, is used to adjust the operation point of the energy harvester. The MPPT is complete once the energy harvester's output voltage or output current reaches the reference voltage or current. Because the simple open-loop control and does not require any intensive computation in these approaches, they are considered as suitable MPPT approaches for micro energy harvesting systems. But the main drawback of these two approaches are that periodically disconnected the energy harvester from the system causes temporary energy loss, which restricts the efficiency of the system. In order to address this shortage, an improved design was presented in (Park and Chou, 2006), where an additional tiny solar cell is used in the energy harvesting system as a pilot cell. This is also called the sensor driven MPPT approach. The open-circuit voltage of the pilot cell is used in place of the open-circuit voltage of the main solar cell. This approach eliminates doing any open circuit voltage sensing on the main solar cell to improve system efficiency. While the shortage of this approach is straightforward, the pilot cell covers a much smaller area than the main solar panel that might not yield a representative MPP of the main solar panel, if dust or shadow on the panel does not cover the pilot cell in the same proportion. Thus, with

this approach, the pilot cell should be carefully chosen and placed to ensure that the voltage relationship is close to the main solar cell (Esrām and Chapman, 2007).

(3) Hill-climbing/Perturb and Observe (P&O) approach

In order to solve the problems facing by previous approaches, an alternative tracking method by using a hill climbing or Perturb and Observe approach (P&O) has been proposed in (Esrām and Chapman, 2007), (Eakburanawat and Noonyaroonate, 2005), and (Lu et al., 2010). The essential working principle of this method is adopting an iterative trial and error approach to track MPP (Esrām and Chapman, 2007). It can be achieved by continuously sensing the output current and voltage at either the output of the transducers or the output power of the converter, and multiplying them to obtain the current power output of the system. A small perturbation is applied to the interface circuit by varying the duty cycle of the boost converter (Eakburanawat and Noonyaroonate, 2005) or the switching frequency of a charge pump (Shao et al., 2009), and then the effect on the output power of the energy harvester is noticed. The working principle is described as below. It assumed that the perturbation results in an increase in the terminal voltage of an energy harvester and the output power is recorded and compared to the previous power output before the perturbation. If the perturbation results indicates the power increasing, another perturbation in the same direction is applied, which results in a further increasing the terminal voltage of the energy harvester. Otherwise, a perturbation in the opposite direction is performed. The MPPT process is continuously repeated until the MPP is reached. There is a tradeoff, which is the relation between responding speed and MPPT efficiency, should be considered in the algorithm design. The large step size corresponds to a rapid response time to the environmental variances, but oscillates with a large swing near the MPP. A small step size can minimize the oscillation swing, but slow down the tracking speed (Lu et al., 2010). By contrasting to the advantages, the circuit complexity and the power consumption with respect to the FOC approach are considered as two main drawbacks of this approach. Moreover, because the algorithm has many steps to approach the MPP, this technique is unsuitable for those energy transducers under rapidly changing atmospheric condition. Hence, in the rapidly changing environment, an improvement P&O approach should be considered (Sera et al., 2006).

(4) Commercial DC-DC boost converter with built-in MPPT algorithm

Recently, several types of commercially available DC-DC boost converter with built-in MPPT algorithm have been developed, such as SPV1020 from ST Microelectronics (SPV1020, 2010), LTC3105 from LINEAR Technology (LTC3105, 2010), and SM72441 from TEXAS Instruments (SM72441, 2010). Based on their datasheets, they state that these devices can easily be used in low voltage, high impedance alternative power sources such as photovoltaic cells and TEGs, because of a small start-up capability and integrated MPP controller. The advantages of using this technology are simple design process and short time for debugging the circuit. But the MPPT efficiencies of the circuits are unknown.

6.3.2.2 The comparison of three MPPT approaches

A number of existing MPPT approaches for a micro energy harvesting system have been described in the previous section. But there is no consensus on which approach is most efficient. The most of the present systems were just compared with a direct connection approach. The lack of comparison between the MPPT approaches comes from the fact that the literature did not know the absolute efficiencies of MPPT approaches. Furthermore, as the environment energy sources have different characteristics, the MPPT scheme suits in one type of energy may not suit for another one. Hence, a selecting guidance in this area is needed. But unfortunately, no guidance has been proposed in literature to guide the designer selecting a proper MPPT technology in their application. According to these two reasons, the system designers are hard to select and design a proper MPPT technology for their system. Hence, three commonly used MPPT approaches have been designed and compared in this thesis to show the characteristics of each approach. And a guidance of selecting a proper MPPT technology for a micro energy harvesting application has been proposed.

According to the previous analysis, some general design considerations, both on the systematic aspect and the component aspect should be considered to optimize the MPPT circuit design. Firstly, MPPT circuit may incur nontrivial overhead, sometimes even higher than the amount of the harvested energy by the micro energy harvester. Hence, the MPPT circuit for a micro system must consider the amount of power that can be transferred after subtracting the MPPT circuit overhead. Moreover, based on some research works (Shao et al., 2009), the most efficient working point of the energy harvesting system may different from the MPP of the energy harvester. This is

because the working point of the converter circuit also affects the energy efficiency. Therefore, the MPPT circuit should ensure that the energy harvester operates at the MPP of the entire system instead of operating at the MPP of the energy harvester alone. Thirdly, as described in the previous chapters, the system is targeted for micro energy harvesting system, which usually imposes strict constraints on cost, weight, volume and lifetime. Hence, it is desirable to avoid using any high power, large size current and voltage sensors, time multiplexing hardware and the power hungry MCU. Fourthly, the sensor nodes placed at different positions may have different opportunities to harvest various ambient energies. The MPPT scheme should have a capability of easily expanding for other energy harvesting systems. In conclusion, a simple, low cost, low overhead, high MPPT tracking efficiency and compact size MPPT circuit is desired in a micro energy harvesting system to force the energy harvester operating over the various environment conditions. Because the MPP of a solar panel has typical characteristics of other energy harvesting technologies, three types of MPPT circuits are designed for a solar energy harvesting system to simplify the work.

(1) *Sensor driven MPPT*

A sensor driven approach is the first MPPT scheme adopted in this chapter. This is an analog MPPT approach and the conceptual diagram is depicted in Figure 6.4 by adopting the same design principle described in (Park and Chou, 2006). It uses an additional small PV module, which has the same material of the main solar panel, as a pilot cell to present the characteristics of the solar panel in the various conditions. In more detail, the fundamental relationship between the MPP voltages of the solar panel can be represented to the open-circuit voltage of the pilot cell when they are exposed to the same light condition. The output voltage of the pilot cell V_{pilot} is acted as a reference voltage, sent to a low-power comparator. By matching the V_{pilot} to the solar cell's operating voltage $V_{solarcell}$, the MPP operation can be achieved. Equation 6.7 shows the basic relationship between V_{pilot} and $V_{solarcell}$.

$$V_{MPP} \approx K_{solarcell} \cdot V_{OC} \approx K_{solarcell} \cdot (K_{pilot} \cdot V_{pilot}) \quad (6.7)$$

where $K_{solarcell}$ and K_{pilot} are the coefficients between the open circuit voltage and MPP voltages of the solar panel and the miniaturized PV module, respectively.

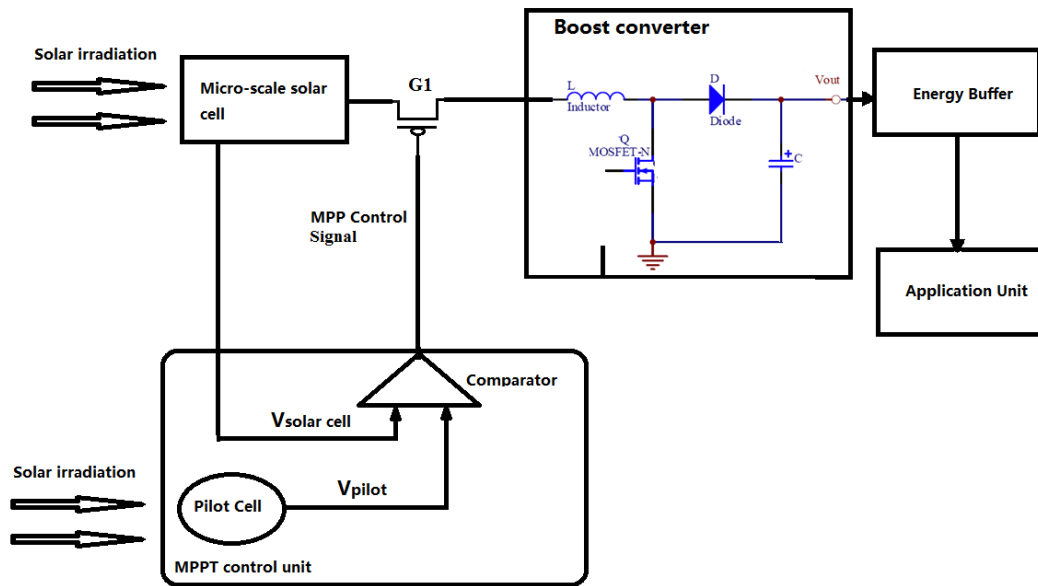


Figure 6.4 Conceptual diagram of the sensor driven MPPT for solar energy harvesting

Some design considerations should be satisfied when designing and implementing a proper sensor driven MPPT circuit. Firstly, a proper type of pilot cell, which meets the requirement of Equation 6.7, should be selected. As shown in Chapter 5, the amorphous solar panel AM-5412 from SANYO was chosen as the solar energy harvester for the solar energy harvesting design. Based on its specification, the same material photodiode S1087 from Hamamatsu (Hamamatsu S1087, 2007) has been selected as the pilot cell in this work. Table 6.2 lists the comparing result of the output parameters of the solar panel and the S1087 photodiode in the same test environment. It displays the output voltage of the pilot cell is near linear of the open circuit voltage of the solar cell.

Table 6.2 operating voltage of the pilot cell and open circuit voltage of the solar cell under the same light intensity

Light intensity	Open circuit voltage of the solar cell	Output voltage of the pilot cell
50Klx	2.6V	0.54V
35Klx	2.39V	0.48V
8.12Klx	2.19V	0.44V

The power overhead of the MPPT circuit is the second design consideration to be considered. An ultra-low power comparator LTC1440, used in Chapter 5, has been adopted as a core control part of the sensor driven MPPT circuit. As the comparators have a hysteresis window for operation, the actual operating point of the solar cell is oscillates around its MPPs. Hence, the third design consideration is that which tunes the hysteresis window of the comparator to make the system become more efficient. The narrow hysteresis window means the system can operate closer to the MPP than the large hysteresis window being used that means more energy can be transferred from the energy harvester to the regulator circuit. But on the other hand, the narrow window size indicates the system operating at high switching frequencies, which may lead to more power consumption and more system noise. Hence, a proper hysteresis window being used is very important. According to (Brunelli et al., 2008), a band of 15mV is shown as the best performance for the sensor driven MPPT scheme. Hence, a 15 mV hysteresis window has been selected in this work. By considering the boost converter circuit, the completed prototype of the sensor driven MPPT is shown in Figure 6.5.

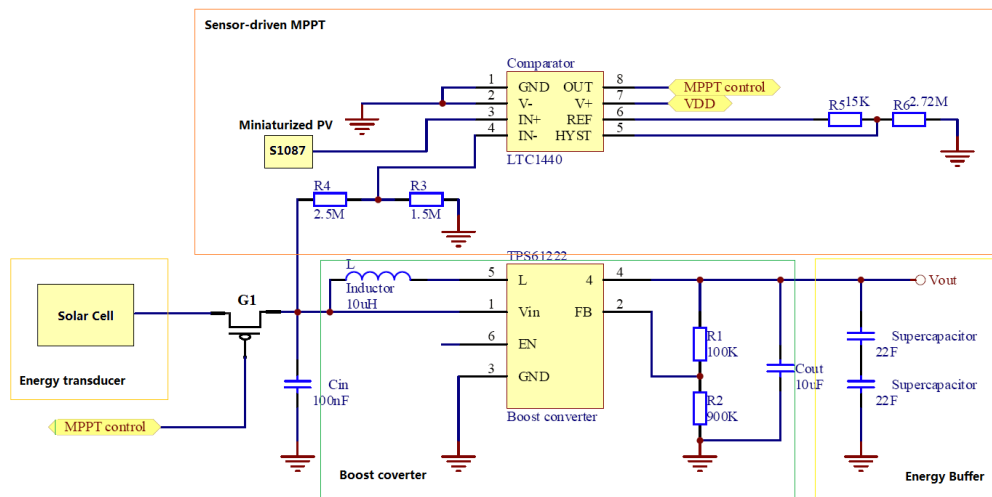


Figure 6.5 The complete Sensor-driven MPPT circuit

(2) A classical P&O MPPT approach

The second MPPT circuit being chosen is based on a classical P&O method, which uses a digital MCU as core control part. The system architecture is shown in Figure 6.6. In order to reduce the power overhead of the circuit, a low cost and low power consumption MCU should be used. It also must have capability to process an

analog-to-digital converter function, which can be used to capture the feedback signals sending from the voltage and current sensors.

According to these signals, a classical P&O MPPT algorithm can be designed and implemented in the MCU. The design principle is based on the trend of the output power level by comparing the current power level to the previous power level of the energy harvester, the MCU chip generates a control signal to turn on/off the boost converter approaching the MPP of the system.

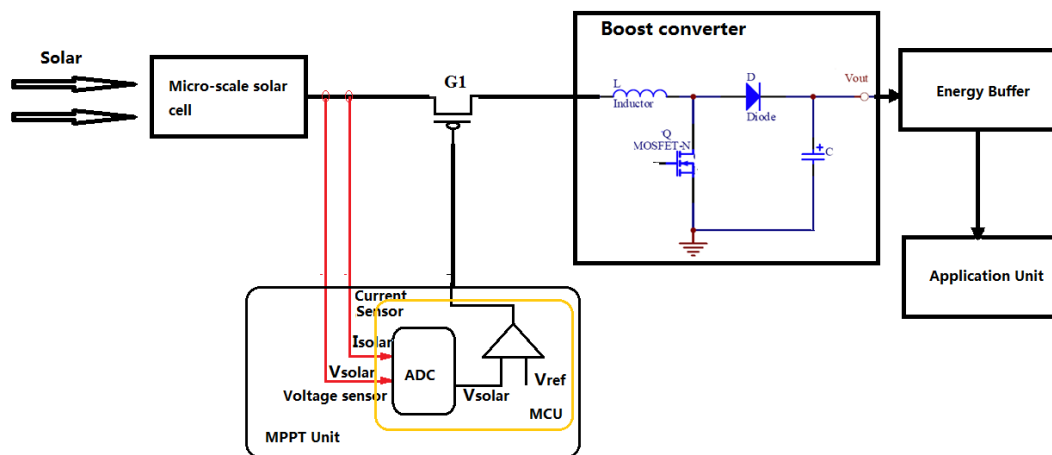


Figure 6.6 A schematic drawing of the implementation of MPPTs

Figure 6.7 shows the relationship between the terminal voltage and output power generated by a solar cell. It can be observed that the MPP of the solar cell under a certain environment is obtained when the condition $dP/dV = 0$ is met, which is point C in Figure 6.7. If the operating voltage of the solar cell is perturbed in the increasing condition and the operation point of the solar cell is in the position A, where $dP/dV > 0$, the perturbation moves the solar cell's operation point toward the MPP of the solar cell. If $dP/dV < 0$ is found, it can be assumed that the system is working at point B. If the algorithm keeps increasing the operating voltage of the solar cell, the operation point of the solar cell is away from the MPP. The output power of the solar cell is decreased in this case. Hence, the P&O algorithm should reverse the direction of the perturbation, which reduces the operation voltage of the solar cell to increase the output power. But all these analysis is according to a fixed environment condition.

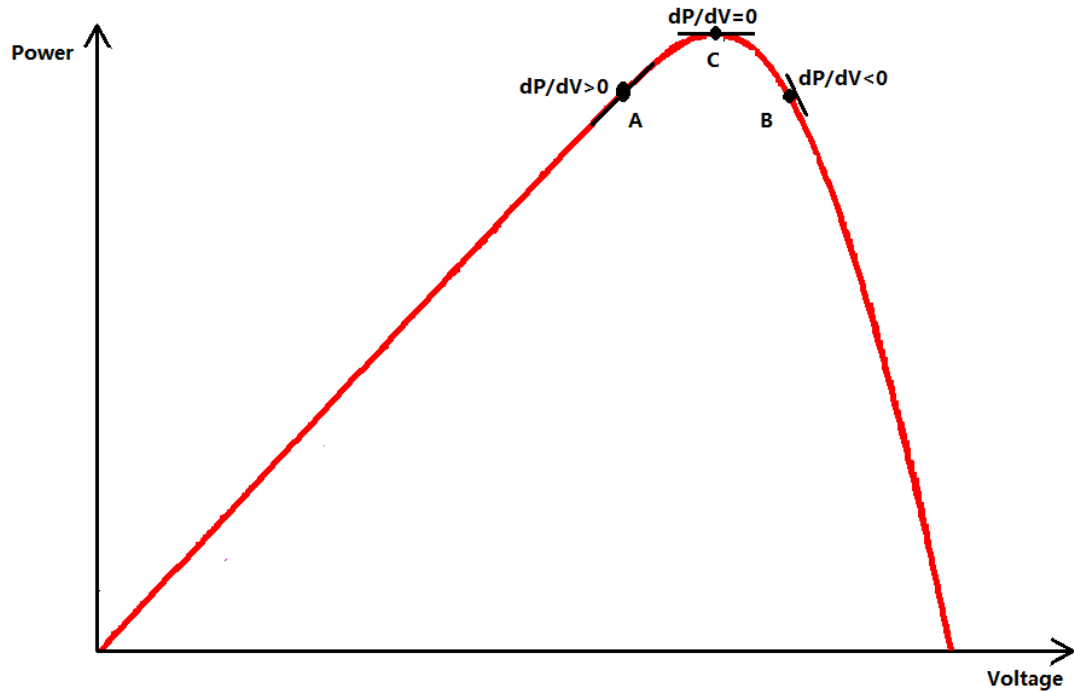


Figure 6.7 Sign of the dP/dV at different position on the power characteristic of a P-V curve

According to the previous analysis, the flowchart of the classical P&O algorithm is depicted in Figure 6.8. Initially, the algorithm sets a reference voltage V_{ref} for the solar panel, which is at the operating point A or B. The corresponding output power of the solar cell, $P_{(k)}$, is calculated by sensing the output voltage $V_{(k)}$ and current $I_{(k)}$ of the solar panel in this term. In the first perturbation cycle, a positive increment of voltage dV is added on the reference voltage V_{ref} . The voltage and the current sensors measuring the current power status of the solar cell $P_{(k+1)}$, based on the new operating point $V_{ref} + dV$. By comparing $P_{(k+1)}$ with the previous power reading $P_{(k)}$, the algorithm can decide the system's working point. If $P_{(k+1)} \geq P_{(k)}$ is observed, it indicates the starting point of the system is A and V_{ref} will keep on increasing in the next iteration until the MPP is reached. In contrast, if $P_{(k+1)} < P_{(k)}$, it indicates that the start point of the system is B. In order to obtain a higher power in the next iteration dV is subtracted from the current voltage point. By repeating this searching process, which maintains the direction if the new power is not less than the previous one, whereas reverses the direction if the new one is less than the previous one, the MPP will be tracked and the system will approach the MPP. It should be known that the system is eventually operating around MPP when the steady state is

reached. As this algorithm is designed for slowly changing environments, the algorithm might track in the wrong way when the system is placed under rapidly changing environment. This is the big drawback of using this type of algorithm.

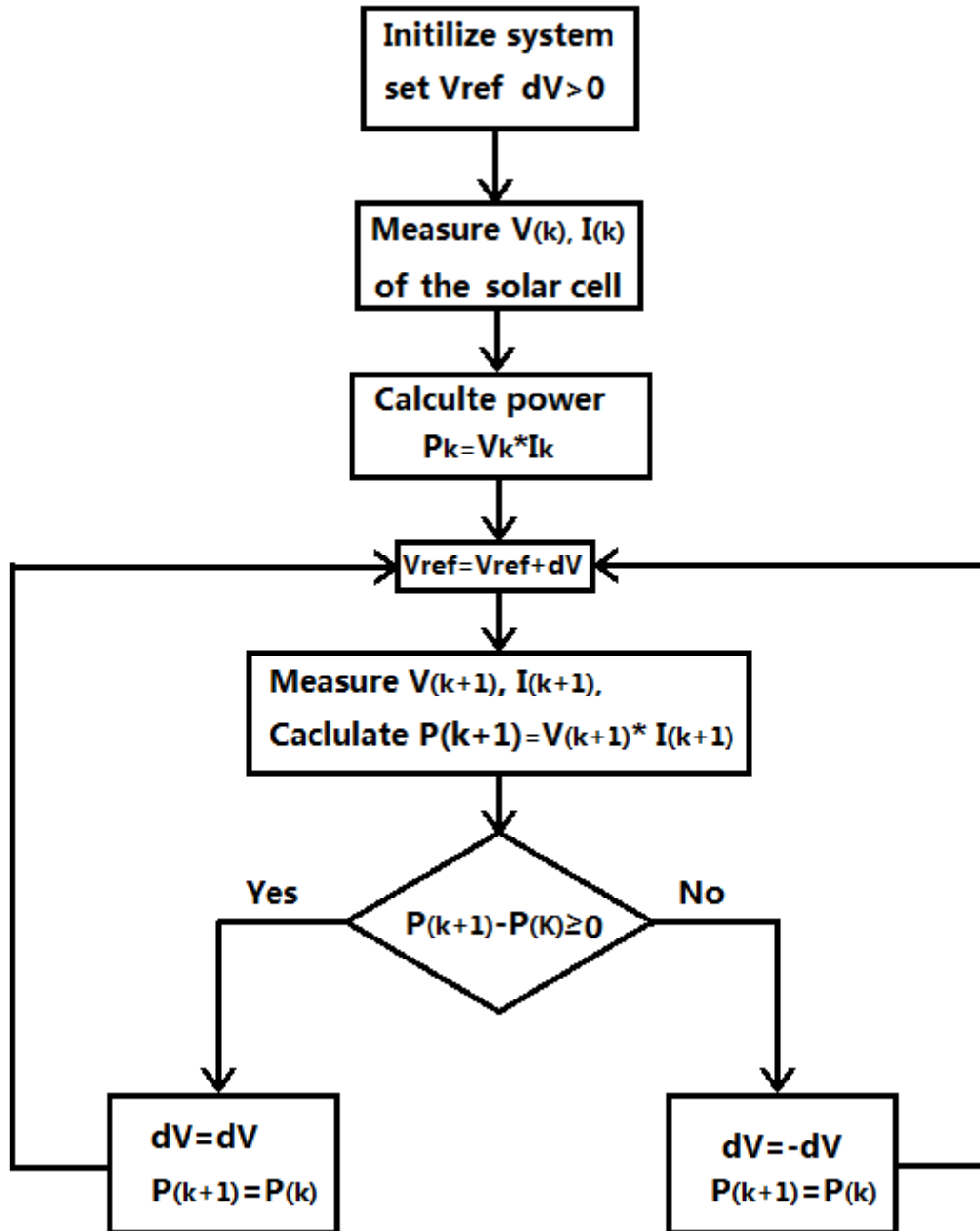


Figure 6.8 The flowchart of the P&O MPPT method

Before completing the hardware design of the classical P&Q MPPT scheme, some design considerations should be concerned. Firstly, in order to reduce the total overhead of the MPPT circuit, a low power MCU PIC16F688 from Microchip (PIC16F688, 2008) has been chosen as the control IC. The chip provides 12 I/O pins

with individual direction control, two analog comparators and a multiplexed 10-bit ADC. The MCU has a capability to handle a variety of functions. This is very beneficial in the low power application, which the power loss of the auxiliary components can be kept to a minimum.

Secondly, the voltage and the current sensors are other two components should be determined in this design. According to the simplify the circuit design and minimizing the power consumption rules, simple, low cost and low power consumed sensors should be used. Based on these rules, the voltage sensor can be simplified by using a capacitor, which is placed between the solar cell and the boost converter as the input capacitor of the boost converter. As the small capacitor is used, the terminal voltage of the capacitor can be considered as the output voltage of the solar panel. The voltage can be monitored by using an ADC pin of the PIC MCU.

For the current sensor parts, a small current sensor, series connected into circuit, is normally used. By measuring the small voltage drop of the current sensor, the current flows into the circuit can be determined. But, an extra low noise and high gain amplifier should be used in this design. This will cause some drawbacks in the micro energy harvesting system. Firstly, by considering the additional power consumption of the low noise amplifier together with the added power loss of the current sensor, the power consumption of the MPPT circuit is quite high, especially by comparing with the ultra-low harvested energy. Secondly, the auxiliary components used for the amplifier makes the system become more complex and bigger. Hence, an alternative current sensor design should be investigated. The P&O algorithm traces the MPP of the system by knowing the value dP/dV is positive or negative. The value of dV can be obtained by the voltage sensor. Then the system just want to know the value of dP is positive or negative. dP can be calculated by:

$$dP = V_n \cdot I_n - V_{n-1} \cdot I_{n-1} \quad (6.8)$$

where V_n , I_n , V_{n-1} , and I_{n-1} are two adjacent voltage and current readings of the energy harvester. By supplying $V_n = V_{n-1} + dV$ in 6.8, the equation can be rewritten as:

$$dP = V_{n-1} \cdot (I_n - I_{n-1}) + dV \cdot I_n = V_{n-1} \cdot dI + dV \cdot I_n \quad (6.9)$$

where dI is the current difference between these two current readings. Then the value of dP is positive or negative that can be determined by knowing a relative changing of the current dI of the solar cell. This means the current sensor does not require the absolute accuracy of the current reading or any instantaneous current values. It just needs to know the difference between the two measurements. Based on this view, a lossless current sensing technology (Pilawa et al., 2010), which uses the inductor's voltage to measure the inductor's current, can be adopted here to measure the current difference of the system between the different working points. The inductor current can be calculated by knowing the average voltage drop across the inductor and the relationship between inductor current I_L and sensed voltage drop ΔV is given by (Pilawa et al., 2010).

$$I_L \cdot R_{esr} = \Delta V = (V_H) - (V_L) \quad (6.10)$$

where R_{esr} is the parasitic resistance of the inductor, which is a constant value. The average voltage V_H and V_L are produced by the first-order RC low pass filters (Pilawa et al., 2010), as shown in Figure 6.9. By using two different ADC pins of the MCU with a built-in gain amplifier, the V_H and V_L can be obtained directly. The current reading can be determined by integrating V_H and V_L into Equation 6.10. Then the value of dP can be calculated. The benefits of using this design are that the current sensing circuit is achieved without integrating a power consuming series current sensor into the circuit and an additional amplifier. The power consumption of this design is much lower than using the current sensor.

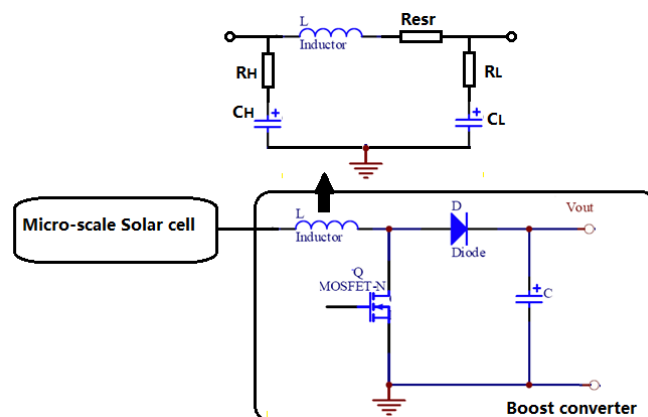


Figure 6.9 Schematic diagram of the lossless current sensor

By integrating the voltage and current sensors into the system, the completely prototype has been designed, as shown in Figure 6.10.

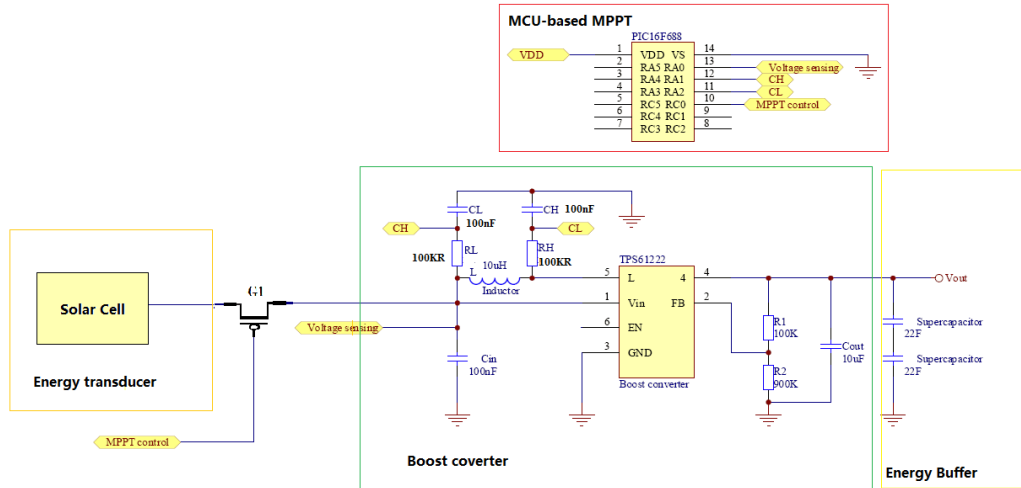


Figure 6.10 The complete MCU based MPPT circuit

In order to ensure a high performance of the MPPT hardware design, several steps have been considered in the algorithms. As the output voltage and current of the solar cell varies rapidly when the boost converter stays at the ON state. The proposed algorithm should sample the solar panel's voltage and current at the same time instance in the switching period to ensure consistent values of voltage and current. This could be done by using high capacitance capacitors of C_L and C_R and high resistance resistor R_L and R_H . Based on the datasheet of (TPS61222, 2010), the frequency of the TPS61222 boost converter is around 1.25 MHz, which the switching cycle of the boost converter t_{cycle} is:

$$t_{cycle} = \frac{1}{1.25\text{Mhz}} = 0.8\mu\text{s}$$

In order to ensure the current sensor reading is equal to the mean current through the inductor, the RC time constants of the C_L and R_L , and C_H and R_H , should much larger than t_{cycle} . In this application, $C_L = C_H = 100\text{nF}$ and $R_L = R_H = 100\text{K}$ have been selected. The RC time constants of these two RC circuits τ_L and τ_H are:

$$\tau_L = \tau_H = C_L \cdot R_L = 100\text{nF} \cdot 100\text{k}\Omega = 10\mu\text{s}$$

Based on the calculation, τ_L and τ_H are ten times bigger than t_{cycle} . Then the current reading of the current sensor can be seen as the mean current through the inductor. And this value can be used to calculate ΔP of the solar cell. When the MPPT algorithm starts to work or restarts from an error condition, the initial reference

voltage of the MPP is set automatically by the system. By choosing a proper initial reference voltage V_{ref} , the MPPT cycles can be reduced and the system performance can be improved. This can be achieved by knowing the roughly energy profile of the energy harvester in the environment. Furthermore, the MPPT circuit's tracking speed is determined by choosing a proper value of dV . The large perturbation dV increases the response speed of MPPT but it reduces the MPPT accuracy of the system. Hence, a trade-off between the peak power operation and the response speed of the MPPT circuit should be considered. Fourthly, the cycle period of the proposed algorithm affects the system efficiency. In the rapidly changing environment, a long time interval between two cycles will cause the algorithm to be inefficient or even to fail to track MPP. In order to achieve the high performance, the sampling rate should be set as fast as possible. But on the other hand, a short cycle time, increases the power overhead of the whole MPPT circuit. Hence, a trade-off according to this point should be considered in the MPPT algorithm design. In conclusion, a good MPP algorithm can optimize the system efficiency by choosing a proper initial reference voltage, a proper perturbation dV and a proper cycle period. By examining the experimental results of the solar cell show in Chapter 5, the parameters of the MPPT algorithm have been set as: $V_{ref} = 2V$, $dV = 15mV$ and the cycle period is 50ms in this work.

As stated in previously, the actually achieved peak point of the system by using the MPP algorithms oscillates around the exact MPP of the system. In order to avoid the system oscillating around the MPP when MPP has been reached, a simple improvement from (Hohm and Ropp, 2003), which adds a waiting function into the algorithm to avoid the system oscillating at the MPP, has been adopted in this work. If the MCU records the algebraic sign of the perturbation reversed several times in consecutive sample cycles, the system is considered that has reached the MPP. In this design, if the reversed dV has been found four times continuously, the system will be considered to have approached MPP. Then the MPPT circuit will stop varying V_{ref} for couple of cycles until the output power of the transducer is changed. This improvement approach can reduce the oscillation about the MPP in the steady state and improve the system efficiency under constant irradiance conditions. But for rapidly changed environments, the MPPT circuit still has a chance to mislead the system.

(3) Enhanced P&O MPPT approach

As discussed in the previous section, the classical P&O algorithm might track in a wrong direction in the rapidly changing environments. Hence, some modification algorithms have been proposed in the literature to overcome this shortfall. One possible improvement algorithm presented in (Pilawa-Podgurski et al, 2010), involves measuring the solar panel's power $P1$ at a reference voltage $V1$, and then it perturbs the voltage to a new reference voltage $V2$ and gets the reference power $P2$. After that, it adjusts the reference voltage back to its previous value $V1$ and re-measures the panel's power $P1'$. By comparing the two measurements results at $V1$, the algorithm can determine whether the irradiance of the light is changed or not. According to the same working principle, an improvement P&O method proposed by (Sera et al., 2006) has been adopted in this work to avoid the shortfall of the classical P&O method. The working principle is that the MPPT circuit determines the correct tracking direction by performing an additional measurement at the same reference voltage to make an estimate of how much the irradiance has changed between two sampling periods. The working principle is shown in Figure 6.11. In the first sampling cycle, the recorded power is $P_{(n)}$. The power difference $dP1$ between the previous reading $P_{(n-1)}$ and the current power reading $P_{(n)}$ can be calculated:

$$dP1 = [P_{(n)} - P_{(n-1)}] \quad (6.9)$$

$dP1$ contains the change in power caused by the perturbation of the MPPT plus the irradiation changes. In order to separate the power difference caused by MPPT unit, another measurement has been taken place in the next cycle by maintaining the same reference voltage. Then $P_{(n+1)}$ can be obtained. The power difference $dP2$ can be calculated

$$dP2 = [P_{(n+1)} - P_{(n)}] \quad (6.10)$$

$dP2$ only reflects the change in power due to the environmental changes. By choosing a quite small sample rate, it can be found that the rate of change in the light irradiation is constant over two sampling periods. Hence, the power difference caused by perturbation of the MPPT circuit can be obtained by using Equation 6.11.

$$dP = dP1 - dP2 \quad (6.11)$$

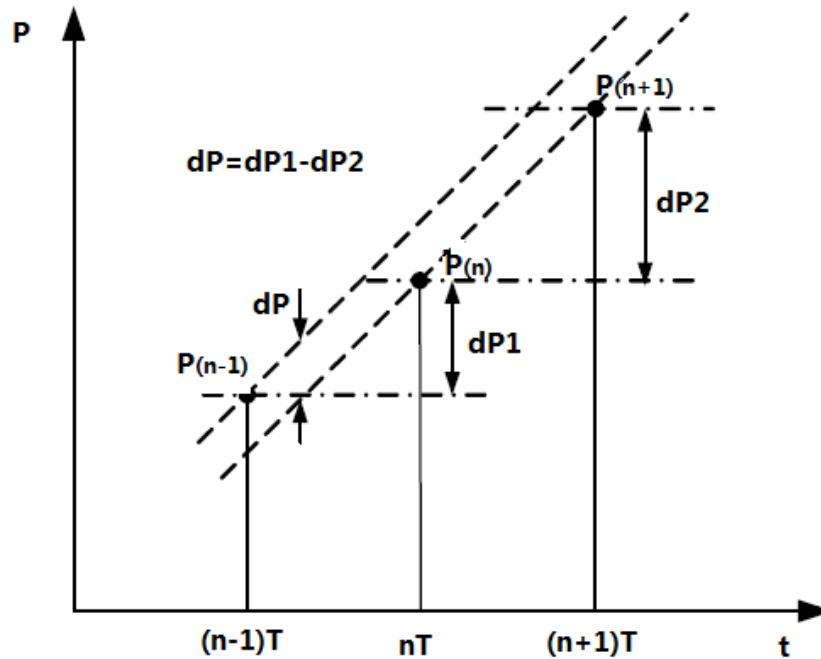


Figure 6.11 Measurement of the power between two MPPT sampling instances (Sera et al., 2006)

According to this principle, the flowchart of the enhanced P&O MPPT approach is shown in Figure 6.12. Initially, the system is tested for three samples, one with the reference voltage V_n and the rest two with the reference voltage V_{n+1} . By using Equation 6.11, the dP can be calculated. If $dP > 0$ is observed, then the algorithm comparing two reference voltages V_{n+1} and V_n . If $V_{n+1} - V_n > 0$, it indicates that the operating point of the solar panel is on the left side of the P-V curve. Then, the algorithm increases the reference voltage and maintains this voltage in the two test cycles. Otherwise, the system decreases the reference voltage. On the other hand, if $dP < 0$ is founded, at the same time if $V_{n+1} - V_n > 0$ is observed, it indicates the system is working at the right side of the P-V curve. In order to approach the MPP, the system decreases its reference voltage. Otherwise, the system increases its reference voltage. In order to avoid making system oscillating at MPP, if $dP = 0$ is founded, the system maintains the same reference voltage in couple of circuits until dP has been changed. Based on this, the shortfall of the classical P&O approach has been solved. But the shortfall of this modification is that it increases the number of sample cycles which slows down the tracking speed. The same hardware and algorithm

considerations, mentioned in the classical P&O MPPT scheme, have been adopted in the enhanced P&O MPPT system design.

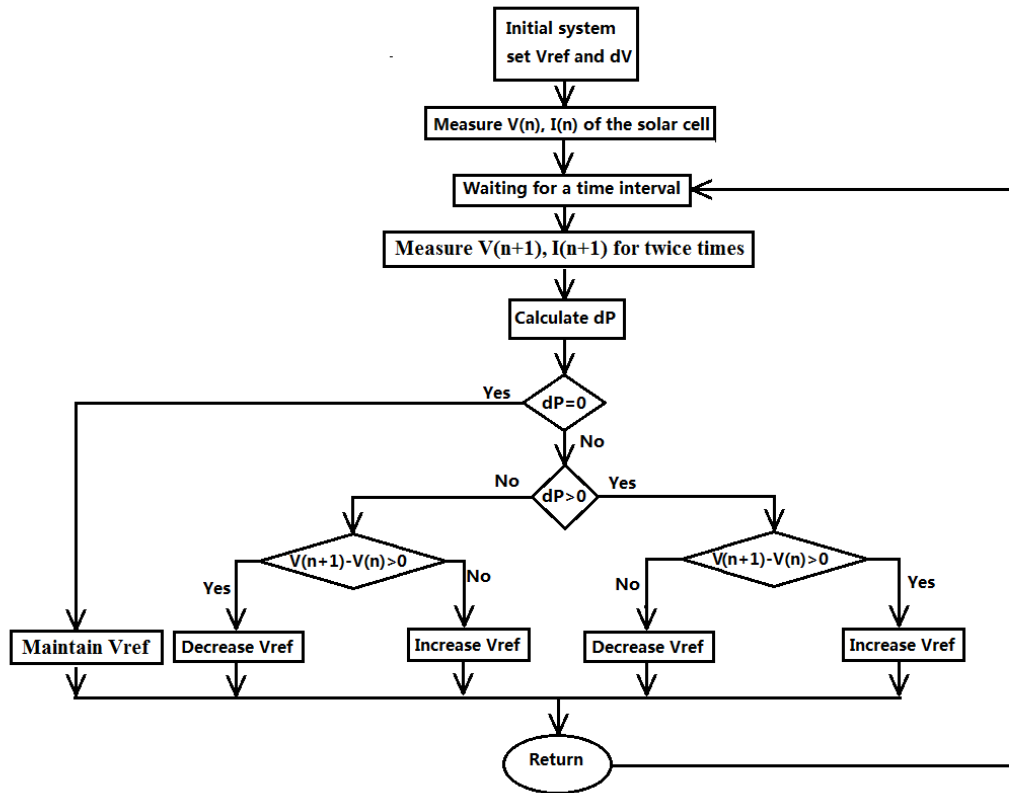


Figure 6.12 The flowchart of the enhanced P&O method

6.4 System evaluation

In order to verify the proposed power conversion circuit, a test environment used in Chapter 5, has been adopted here. In order to compare artificial light with outdoor light, the two solar cells were placed outside during a normal sunny day in Loughborough where the maximum 150mW power could be harvested. As discussed in the previous sections, the power overhead and the MPP tracking efficiency are two critical design factors needed be verified in the system evaluation.

6.4.1 Power overhead

As stated in the previous sections, the power consumption is crucial to design a micro-scale energy harvesting system. In order to distinguish the power consumption of each proposed power conversion circuits, each part of the system and entire system have been tested. As analysed in Chapter 5, the power losses of the boost converter

depend on the input power levels. This means the power consumption of the boost converter is not fixed. But the same boost IC and peripheral circuit are used in these three designs. By neglecting the system differences, the power consumption of the boost converter is assumed the same, which can be neutralized in the power consumption calculation. Then the proposed power conversion system can be simplified to distinguish the power consumption of the MPPT circuits. For the sensor-driven MPPT circuit, the main power consumption part is the ultra-low power comparator LTC1440. Based on the relevant datasheet (LTC1440, 2009), the minimum power consumption is $6.3\mu W$. The real experimental result shows the comparator consumes less than $20\mu W$. For the other two MCU based power conversion circuit, they have the same hardware. By neglecting the power consumption variation caused by different algorithms, these two designs can be assumed have the same power consumption. Based on their hardware design, the power consumed by the MPPT circuit come from the MCU and its peripheral circuit. Based on the datasheet (PIC16F688, 2008), the PICF688 MCU consumes $30\mu W$ when it operates. But it consumes $3nW$ when it stays at standby mode. In order to simplify the design procedure, the MCU is stayed at the operating mode all the time. The experimental result shows the power consumption of the MCU based MPPT circuit is around $45\mu W$. Moreover, the entire power conversion circuits have been tested with a constant DC power input. The power consumption of each proposed systems are shown in Table 6.3. Based on these experimental results, the sensor-driven circuit has the lowest power consumption.

Table 6.3 Power consumption of three proposed MPPT based circuit

Boost converter mode	Sensor-driven MPPT based Power conversion circuit	P&O MPPT based Power conversion circuit	Improved P&O based Power conversion circuit
Switch-off	$220\mu W$	$260\mu W$	$260\mu W$
Switch-on	$500\mu W$	$560\mu W$	$560\mu W$

6.4.2 Tracking efficiency

The tracking efficiency is another critical factor to examine the MPPT technologies. Before determining the tracking efficiency, the MPP tracking speed is examined. Table 6.4 lists the tracking speeds when the solar energy harvesting system is executed

with three MPPT methods under three different light conditions. According to Table 6.4, the elapsed times of the sensor-driven MPPT method are the shortest under all conditions, which is followed by the classical P&O method. This is because the sensor-driven MPPT algorithm uses the sensing result to directly achieve MPP. The enhanced P&O method has the longest elapsed time owing to its more complicated judgment procedure than those of the other two methods.

Table 6.4 Comparison of the MPP tracking speed for different MPPT based power conversion systems

Elapsed time of MPPT			
Light Irradiance	35 Klux	10Klux	5Klux
Temperature	25°C	22°C	22°C
Sensor-driven MPPT	instant	instant	instant
Classic P&O	500ms	650ms	750ms
Enhanced P&O	510ms	665ms	771ms

The MPPT efficiency can be defined as

$$\eta_{MPPT} = \frac{\int_0^t P_{actual}(t)dt}{\int_0^t P_{max}(t)dt} \quad (6.12)$$

where P_{actual} is the actual power produced by the PV array under the control of the MPPT, and P_{max} is the maximum power produced by the PV array under a given temperature and light irradiance. Since it is not easy to measure the energy transferred in a single pulse without a high speed digitizer, P_{actual} and P_{max} are very hard to measure in a real experimental environment. One alternative option is to use the power conversion efficiency of the entire power conversion circuit to indicate the MPPT efficiency. The entire power conversion efficiency can be calculated by knowing the energy being stored in an energy storage element and energy being generated by the solar cell, as shown in Equation 6.12.

$$\eta_{conversion} = \eta_{converter} \cdot \eta_{MPPT} = \frac{E_{transferred}}{E_{MPP}} \quad (6.12)$$

$$E_{MPP} = V_{MPP} \cdot I_{MPP} \cdot T$$

where $\eta_{conversion}$ and $\eta_{converter}$ are the conversion efficiency of the entire power conversion system and the efficiency of the boost converter, respectively. In order to determine $E_{transferred}$, a super-capacitor is used to store the harvested energy. Then $E_{transferred}$ is computed as the value of increasing the energy level from $E_{(t-T)}$ to $E_{(t)}$ during a given time interval T.

$$E_{transferred} = E_{(t)} - E_{(t-T)} = \frac{C_{SC}}{2} [V^2(t) - V^2(t - T)] \quad (6.13)$$

where C_{SC} is capacitance of the energy buffer, and $V(t)$ and $V(t - T)$ are the two voltage levels of the energy buffer during a testing cycle. Hence, the conversion efficiency can be simplified by comparing the energy output by the solar cell with the increase in the capacitor's energy level during a test period T. By using the same boost converter circuit except MPPT circuits in the power conversion system, the only difference in Equation 6.12 is η_{MPPT} of each employed MPPT approach. Hence, the simple way to interpret system efficiency is to compare the capacitor's voltage of each system when there are placed at the same environment. In this chapter, two 22F super-capacitors placed in series are used as the energy storage element. In order to ensure the state of the capacitors at the beginning of each experiment being the same, the capacitors are pre-charged to 1.3V. Generally, the outdoor light irradiance can be roughly divided into three groups, which are constant light conditions, slow changing light condition, and rapidly changing light condition. In order to obtain the overall efficiency of the energy harvesting systems in all these conditions, three trials have been conducted for each system. Each algorithm has been tested three times under the same condition and the equal value of these three tests for each system has been obtained to reduce the testing error.

For a constant light condition, three different light inputs 35kLux, 10kLux and 5kLux have been tested with each system for 20 minutes. Table 6.5 shows the comparison results of experiment tests. The efficiencies for each system under these three different light irradiances are calculated by introducing the parameters into Equation 6.12. The calculation results are shown in Table 6.5. Since the MPP of a solar cell is very sensitive to its temperature, it was very important to ensure the panel's temperature was kept at a constant value during the experiment. Therefore, the tests have been examined when the solar cells had been illuminated by the lamp for

about 30 minutes to ensure that the temperature of the solar panel had reached a stable state. The comparison results show that the sensor-driven MPPT based conversion circuit has the minimum capacitors' voltage which indicates that it has the minimum energy transfer efficiency during these tests. This is because the light sensor's output power is not 100% matching the solar cell's output power. The P&O and the enhanced P&O algorithms have very similar overall efficiencies and the P&O method even has a slightly better efficiency than the enhanced P&O algorithm. This is because the enhanced P&O algorithm is complex and needs more time to decide MPP. This makes the enhanced P&O method not as efficient as the classical P&O method in the constant light condition.

Table 6.5 Comparison of the MPP tracking efficiency for different MPPT based power conversion system at the constant light condition

Terminal voltage of the super-capacitors			
Light Irradiance	35kLux (27.4mW)	10kLux (6.43mW)	5kLux (4mW)
Temperature	25°C	22°C	22°C
Charging time slot	30 mins	30 mins	30mins
Sensor-driven MPPT	2.825V (70.2%)	1.777V (69.8%)	1.601V (67.1%)
P&O	2.887V (74.1%)	1.801V (73.8%)	1.623V (72.1%)
improved P&O	2.886V (74%)	1.8 V(73.7%)	1.623V (72.1%)

If the solar energy harvesting systems were placed outside in a cloudy day, the environment condition could be considered as a slow changing light condition. In order to emulate the dynamic light conditions in the laboratory, a brightness adjusting lamp has been used. The lamp started at 5kLux for 5mins, and then it was suddenly adjusted to reach its maximum 35kLux. It kept the maximum output for 5mins and returned to a low value about 5kLux as a cycle. The experiment lasted for an hour and the results are shown in Table 6.6. Based on the comparison result, the maximum efficiency can be achieved by using the classical P&O algorithm, which is followed by the enhanced P&O method. The difference between the classical P&O and the enhanced P&O methods are much bigger than one when they were placed at a constant

light condition. This is because the P&O algorithm has a simpler algorithm to track the MPP at a slow changing environment. The worst case is found by using the sensor-driven MPPT.

Table 6.6 Comparison of the MPP tracking efficiency for different MPPT based power conversion system at the slow changing light condition

Terminal voltage of the super-capacitors and conversion efficiency	
Sensor-driven MPPT	2.965V (69.3%)
P&O	3.04V (73.48%)
Enhanced P&O	3.01V (71.8%)

For a partly cloudy day, the light condition might changes rapidly. If the proposed system is placed at this environment, the results will be different. The rapidly dynamic light environment has been emulated in the laboratory by rapidly changing the lamp output power between the maximum value (35klux) and the minimum value (5klux) in every 2 seconds. The test lasted for 1 hour. Table 6.7 shows the comparison result of different power conversion systems illuminated in this condition. From the result, the enhanced P&O method achieves the maximum efficiency of the all three MPPT algorithms.

Table 6.7 Comparison of the MPP tracking efficiency for different MPPT based power conversion system at the rapid changing light condition

Terminal voltage of the super-capacitors and efficiency	
Sensor-driven MPPT	2.965V (69.1%)
Classic P&O	2.982V (70.08%)
Enhanced P&O	2.998V (71.2%)

In order to evaluate the proposed system in the real environment, three designed power conversion systems have been tested in an outdoor environment for 5 days. In these five days, the systems have been placed outside of the laboratory through 9am to 7pm. And after each testing days, the systems have been reset back to their initial state. In order to supply enough capacitance for the energy buffer, a large capacitance rechargeable battery has been employed to replace two 22F capacitors as the energy

buffer in these designs. The rechargeable batteries have been pre-charged to 2.1V ensuring that the state of the battery at each experiment is the same. The terminal voltages of the rechargeable batteries in these testing days have been recorded, as depicted in Figure 6.13. Based on the figure, the terminal battery voltage of the enhanced P&O method is the highest in each testing day indicating the enhanced P&O method is the most efficient one in these three MPPT methods when they are placed at outdoor environments. The sensor driven MPPT approach is the most inefficient one. It can be concluded that the enhanced P&O method is the best selection when the solar energy harvesting system is placed at outdoors.

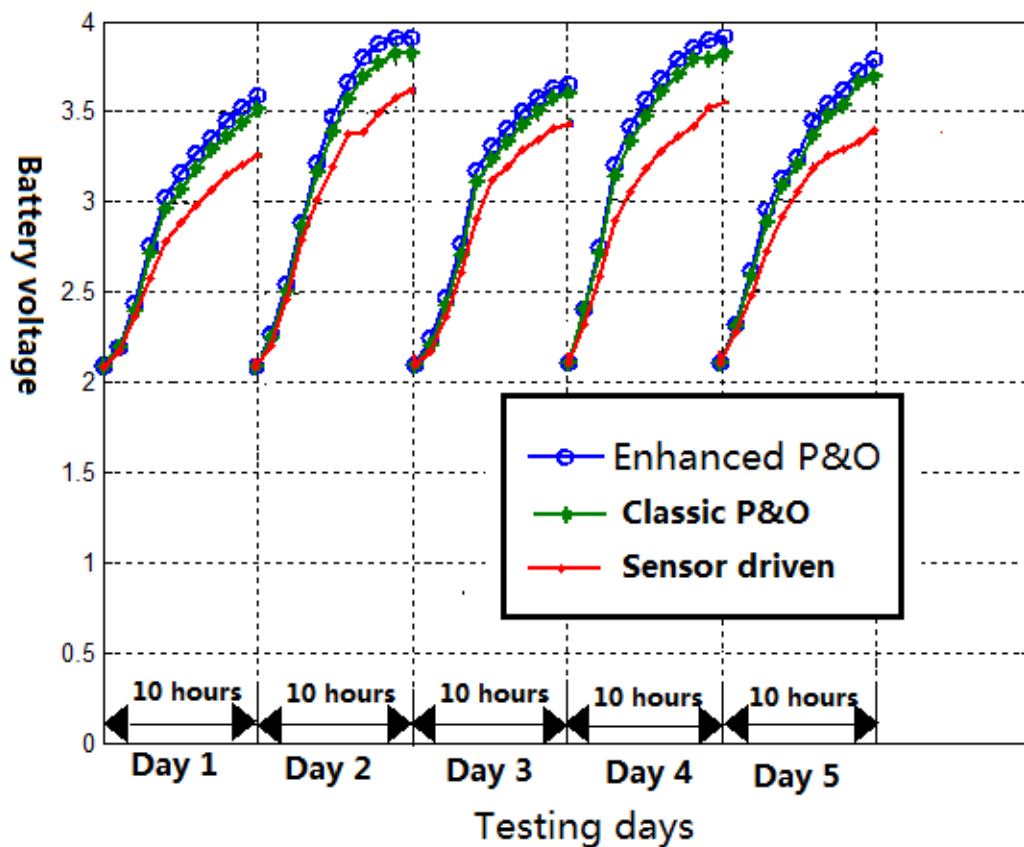


Figure 6.13 Overall tracking efficiency of the proposed power conversion system

6.5 Summary

By analysing the present states of micro energy harvesting systems, a low system performance in terms of energy conversion makes the design of high efficient power conversion subsystem, including the design of efficient power converter and a high

efficient MPPT scheme, becoming an active area of research. In this chapter, three integrated cost-effective MPPT algorithms based power conversion circuits for micro-scale solar energy harvesting systems have been compared. The proposed systems have been tested in the laboratory on both the power overhead and overall system efficiency. The experimental results show that the sensor-driven MPPT based power conversion circuit has a minimum power overhead, but it has the lowest tracking efficiency. The enhanced P&O MPPT system has the same power overhead of the classical P&O MPPT system, but it has the most efficient when the system is using in the rapid changed environment. The classical P&O MPPT system has the maximum system performance when the environment conditions changed slowly or maintained. In order to verify the system performance in the real environment, three systems have been tested outdoor for 5 days. The results show the enhanced P&O based power conversion circuit has the maximum efficiency and it is considered as the best option when the system is placed at the rapidly change environment.

Chapter 7. Design and implementation of a power management system for an energy harvesting system

7.1 Background and motivation

The energy harvesting technologies have the potential to make the WSNs have near-perpetual operation. In order to have this potential, the energy harvesting system requires high energy efficiency with high system reliability. As mentioned in previous chapters, a lot of effort has been proposed in this area to enhance the system performance both on energy efficiency, and on system lifetime. But these efforts are not sufficient to give a perpetual lifetime to the system. In order to make the system becoming everlasting, a power management subsystem is required. There are some reasons to employ a power management subsystem in a micro energy harvesting system. Firstly, the harvested energy depends on the energy available from the environment, but different sensor nodes, which come from the same WSN, placed at different places may have different energy harvesting opportunities. The unstable and uncontrollable environment makes the harvested energy unstable and undependable that makes the existing energy harvesting systems not suitable for other applications. Secondly, as the wireless sensor nodes perform three basic functions: data collection, data communication and sleeping, the power demands for achieving these functions are significantly different. Based on these two reasons, the energy budget and the energy usage of the energy harvesting system are unpredicted. The system, without knowing this energy relationship, may not operate properly as expected. Moreover, by considering the constraints on the cost, size, and energy, the micro energy harvesting system without a proper energy usage strategy may cause some unexpected problems when the system is deployed in the real environment. Hence, an energy management capability is a key factor enabling an energy harvesting system adaptable to any working conditions.

The power management is not new in the design of WSNs. As described in the literature, energy management technologies are extremely useful in the battery powered embedded system in order to prolong the lifetime and maximize the system performance under energy constraints. As shown in Chapter 1, significant research efforts have been dedicated to achieving efficient energy utilization in WSNs in the past year, such as dynamic voltage scaling, reducing the number of bits to transmit and dynamic power management. But power management strategies will be significantly different when the energy source of the sensor node changes from the fixed battery to a harvesting device.

Firstly, unlike a battery driven sensor node, whose performance has been constrained by its limited power sources, an environmental energy driven sensor node with an added capability of a renewable energy makes the system having potentially infinite amount of energy. With appropriate choice of data sampling rate and a routing protocol, the lifetime of the sensor node could be infinite. In conclusion, the power management strategies of a battery system is there to minimize the energy consumption of the system as much as possible under energy constraints that differ from the power management strategies of an energy harvesting system, which make the lifetime and the system performance maximization based on balancing the energy consumption and the energy generation of the system.

Secondly, the power management strategies for the battery driving sensor node are required to have a battery level close to full, but in the case of the sensor node with energy replenishment, a fully charged battery means that no energy could be charged and the system misses the opportunity to utilize the replenishment energy. Due to the limitation of the energy buffer's capacity, conservative energy expenditure may lead the system missing charging opportunities. But on the other hand, the aggressive energy usage of the sensor nodes along with an unstable harvested energy may lead to a lack of coverage or connectivity when the system is working with low residual energy level. Hence, determining the right balance between the residual battery level and the energy consumption of the system becomes a complex issue for a power management algorithm design for an energy harvesting system.

The power management strategies for the sensor node driven by environmental energy must have the capability to balance these contradictory goals in order to maximize the system performance and the system lifetime, simultaneously. Nowadays, a lot of effort is put into developing efficient power management algorithms for sensor

nodes powered by an energy harvesting device. Kar et al. (2006) and Gatzianas et al. (2010) have proposed activation schemes for rechargeable sensors to maximize the network-level utility of sensing networks. Both authors assume that all the sensor nodes have the same energy replenishment possibility and they look at the whole system energy utility instead of focusing on analysing node-level performance. But in the most WSN applications, only parts of sensor nodes have energy replenishments. The power management schemes focusing on individual environment powered sensor nodes become more realistic and more useful for real applications. In relation to this point, Kansal et al. (2006) introduced the concept of energy neutral operation, which has been introduced in Chapter 5, into the power management algorithm design. A power management unit for dynamically adapting the duty cycle of a sensor node with energy harvesting capabilities has been developed according to this concept. They used adequate historical data obtained by experiments to indicate the energy budget of the system. Since the environmental energy is dynamical and unpredictable, the energy budget of the system, which is based on previous experiments, cannot accurately predict the energy generation of the system. Hsu et al. (2006) extended this idea and proposed an adaptive power management algorithm for harvesting-aware duty cycling of wireless sensor nodes. Three objectives have been achieved by their algorithm: (a) achieving energy neutral operation, (b) maximizing the system performance based on an application utility model subject to the above energy neutrality constraint, (c) adapting to the dynamics of the energy source at run-time (Hsu et al., 2006). However, in both works, the authors assumed a priori knowledge of the energy profile which is hardly possible to obtain in a real environment. An improvement approach, which the energy relationship between the energy budget and the energy dissipation is indicated by monitoring the battery level of the system, is proposed by (Vigorito et al., 2007). However, this model-free approach cannot be accurate enough to indicate the energy variations in a short period that prevents this approach from being used in a micro energy harvesting system.

7.2 Feature of proposed strategy

Based on the above discussions, a power management subsystem for an energy harvesting system is proposed. Three objectives have been achieved by the subsystem, which are the energy neutral operation, system performance maximization and a perpetual lifespan of the system. The design process is divided into two parts: an energy distribution and a power management parts. According to this, both hardware and software have been designed based on the entire system perspective. A solar energy harvesting system has been used to evaluate the proposed power management subsystem both in a laboratory and at outdoor environment. The experimental results illustrate the proposed algorithm is able to have the better system performance by comparing with other two simple designs.

7.3 Proposed power management system

Normally, the everlasting life, the energy neutral operation and the maximum system performance are considered as three basic objectives which should be achieved in a high efficient micro energy harvesting system. According to these requirements, the power management subsystem can be divided into the energy distribution and the power management parts, as illustrated in Figure 7.1. An energy harvester is connected with an MPPT based power conversion circuit to create appropriate voltage level for the energy buffers, which is included in the energy distribution part. It is also used to decide which energy buffer being used by the system according to the energy level of the buffers. Then the power management unit is used to monitor energy budget of the system and adapt energy dissipation equal or less than the energy generation of the system.

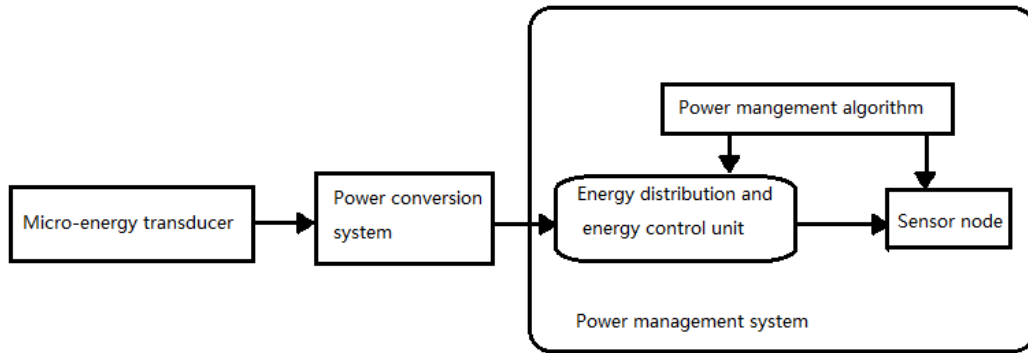


Figure 7.1 Generic architecture of power management system

7.3.1 Energy distribution unit

The main function of the energy distribution part is to use an intelligent control algorithm to efficiently distribute the energy to each part of the system. According to feature of the energy distribution unit, the design processes can be divided into choosing the energy storage elements and designing an efficient charging and discharging mechanism, which satisfy a set of system requirements such as lifetime, capacity, current draw, size and weight.

7.3.1.1 Energy buffer design

The energy buffer system decides the whole system lifetime of the energy harvesting system. This part is very important for designing a long lifetime system. In order to give the system a nearly perpetual lifetime, the hybrid combination energy storage design, mentioned in Chapter 5, is adopted in this chapter. Because of the high charging/discharging efficiency along with infinite charge/discharge cycles, a super-capacitor is employed as the primary buffer, which is directly charged by the harvesting system. It powers or charges the system when enough energy is available on its. The rechargeable batteries are used as the secondary buffer by considering the large capacitance and high capability of holding energy. It is used to cover the black area of the system when there is no or small amount of energy can be harvested by the energy harvester. Based on these special requirements, the super-capacitor should be as large as possible to minimize the charging/discharging process to increase the system efficiency and prolong the lifetime of the rechargeable batteries. But a larger capacitance of the capacitor has a greater leakage current, which is the main energy dissipation of the energy buffer system. Hence, an optimal capacitance level of the

super-capacitor should be considered. By considering the power management unit, which will be described later, there is a minimum value of the super-capacitor should be stratified. The principle is that the minimum capacitance of the super-capacitor should ensure the system can only step into one status at a cycle T . This means that the maximum energy consumption of the entire system through a time interval T , which should be less than the energy that can be drawn from the super-capacitor from the stop charging battery stage to the using battery powering system stage. The mathematical description is shown in Equations 7.1, 7.2 and 7.3.

$$E_{capacitor} > E_{system}(maximum) \quad (7.1)$$

$$E_{system}(maximum) = P_{system}(maximum) \cdot T \quad (7.2)$$

$$E_{capacitor} = \frac{C_{sup-cap}}{2} (V_{w,th3}^2 - V_{w,th4}^2) \quad (7.3)$$

where $C_{sup-cap}$ is the capacitance of the super-capacitors, and $V_{w,th3}$ and $V_{w,th4}$ are the two voltage thresholds of the super-capacitor to indicate the stop charging battery stage and the using battery powering system stage, and $E_{capacitor}$ is the energy drawn from the super-capacitor from $V_{w,th3}$ dropping to $V_{w,th4}$, and $E_{system}(maximum)$ and $P_{system}(maximum)$ are the maximum energy consumption and the maximum power consumption of the system.

The secondary buffer is used when the energy at the primary buffer cannot directly power the system. Hence, a high energy density, a low breakdown voltage and a low leakage current have been considered as the three basic design requirements of the secondary buffer. By considering the charging/discharging efficiency and the complexity of the charging circuit, a NiMH type rechargeable battery is used. In order to use the rechargeable battery as efficiently as possible, several actions should be considered in the system design. A bigger battery size and high cost are not suitable for a micro system. The optimal battery size can be estimated by calculating the difference between the maximum energy consumed and the minimum energy generated through a year. Secondly, if a battery is subjected to a deep discharge cycle, the lifecycle of the battery is degraded. For instance, a NiMH battery yields a lifecycle about 500 cycles, when it is subjected to repeated 100% discharge rate. But, if the battery is cycled at 10% Depth of Discharge (DoD), it will last for over 5000 cycles before it reaches the end-of-life (Karsal et al., 2006). Therefore, the power management system should keep the battery operating at a shallow DoD to preserve

battery endurance (Karsal et al., 2006). Thirdly, rechargeable batteries have two voltage limitations which characterize the maximum and the minimum amount of charge present on the battery. If a rechargeable battery exceeds the upper voltage limitation or drops below the lower voltage limitation, the lifetime of the battery will be significantly decreased. Hence, an over charging and under charging protection should be considered to protect the rechargeable battery.

7.3.1.2 Control Unit

A control unit is quite essential for the buffering system, especially when a hybrid combination energy storage design has been used. Several system requirements should be satisfied when the highly efficient circuit is desired. Firstly, the control circuitry should oversee the operation of the energy transducers, manage the energy buffers and routers the energy consumption of the system with a proper policy. Secondly, in order to enhance the hardware longevity, the overcharge and undercharge protection should be included. Thirdly, because the power management system makes an energy usage decision based on the energy budget, the control unit should have a built-in energy measurement capability to monitor the energy levels of the two energy buffers. Furthermore, the low cost, small size and the simple circuitry are required. Based on these requirements in relation with the characteristic of a digital circuit, which the circuit is simpler than an analog circuit, a low power MCU based control circuit is developed. In this chapter, a multiple function MCU PIC16F688 with very low power consumption is used and the schematic diagram is depicted in Figure 7.2. The rest of the circuit includes a dual P-channel MOSFET FDS9933A playing as an energy source switch, and a 1.2A current limited, P-channel switch Max890L working as a battery charger.

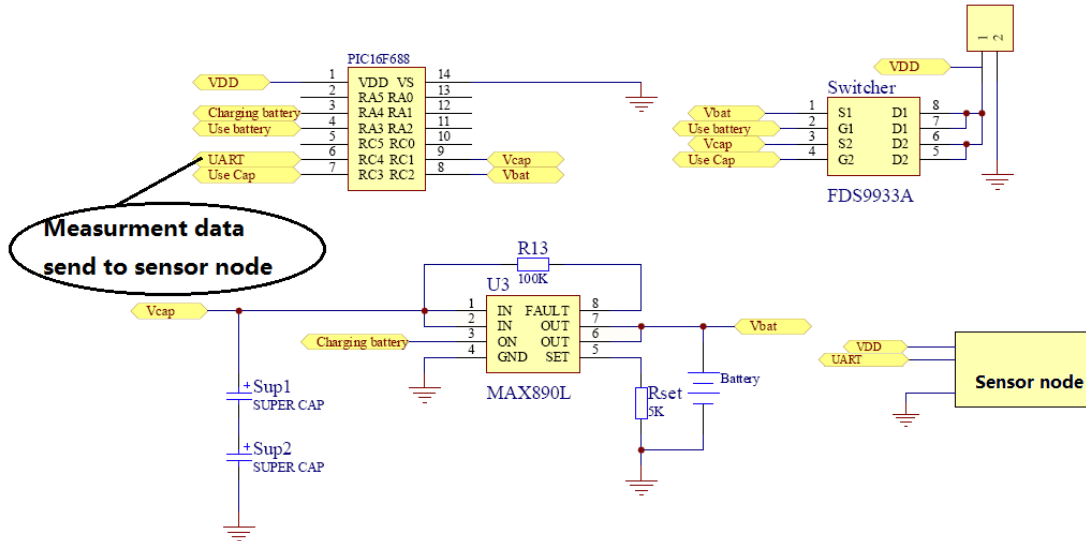


Figure 7.2 Hardware design for power management subsystem

In this circuit, two ADC channels from the MCU are used to monitor energy levels of the super-capacitor and the rechargeable battery. By comparing the terminal voltage of the super-capacitor V_{cap} and using a configured threshold voltage $V_{W,th1}$, the control circuit determines which energy sources, either the super-capacitor or the rechargeable battery should be used to power the system. If the terminal voltage of the super-capacitor is higher than $V_{W,th1}$, the super-capacitor powers the system. Otherwise, the system draws energy from the rechargeable battery. Frequently switching the power sources generates noise, which is harmful for an MCU based system, a 0.6V window has been set by the control unit to stabilize the power stage. When the super-capacitor's voltage drops below the voltage threshold $V_{W,th4} = V_{W,th1} - 0.6V$, the control unit switches to using battery to power the entire system.

Furthermore, in order to charge the rechargeable battery when sufficient energy is available, $V_{W,th2}$ is set by the MCU to indicate the charge status. When the rechargeable battery is not fully charged while $V_{cap} > V_{W,th2}$, the rechargeable batteries are charged by the super-capacitor. In order to avoid frequently charging the batteries, a 0.3V charging window is selected. This means that another voltage threshold $V_{W,th3} = V_{W,th2} - 0.3V$ has been set, which indicates that the system should stop charging the batteries.

As the lifespan of the rechargeable battery is critical for determining the entire system's lifetime, an overcharge and undercharge protection is designed to extend the lifetime of the batteries. Hence, two battery voltage thresholds $V_{B,th1}$ and $V_{B,th2}$ are chosen for the battery to avoid overcharging and undercharging processes. In order to simplify the hardware design, the control logic has been uploaded into the PIC MCU that the number of physical components and quiescent current consumption can be reduced. The software has complete control over buffer selection, charging process, instantaneous energy measurement and communication with the sensor node. The driver for the control unit is shown in Table 7.1 by using simple if-else statement to achieve the functions mentioned above.

Table 7.1 Control and charge DRIVER

	Driver
1	Set $V_{W,th1}$, $V_{W,th2}$, $V_{W,th3}$, $V_{B,th1}$ and $V_{B,th2}$
2	Measure V_{cap} and $V_{R-battery}$
3	If $V_{B,th2} < V_{R-battery} \leq V_{B,th1}$ If $V_{cap} < V_{W,th4}$ Battery powered system=True Charge battery=False Cap powered system=False
4	If $V_{B,th2} < V_{R-battery} \leq V_{B,th1}$ If $V_{W,th1} \leq V_{cap} \leq V_{W,th2}$ Battery powered system=False Charge battery=False Cap power system=True
5	If $V_{B,th2} < V_{R-battery} \leq V_{B,th1}$ If $V_{cap} \geq V_{W,th2}$ Battery powered system=False Charge battery=True Cap power system=True
6	If $V_{B,th2} < V_{R-battery} \leq V_{B,th1}$ If $V_{cap} = V_{W,th3}$ Battery powered system=False Charge battery=False Cap power system=True
7	If $V_{R-battery} \geq V_{B,th1}$ Charge battery=False
8	If $V_{R-battery} \leq V_{B,th1}$ Battery powered system=False
9	Sending V_{cap} and $V_{R-battery}$, number of charging battery n_{charge} and number of using super-capacitor power the system n_{power} to sensor node

7.3.2 Power management algorithm design

The power management part is crucial for adapting the energy usage to the energy budget of the system. This is the core part for an energy harvesting system to achieve the energy neutral operation and maximize the performance.

7.3.2.1 Theoretical analysis of a power management strategy

In order to design a proper power management algorithm for an energy harvesting system, a theoretical analysis should be conducted before the algorithm is designed. The energy neutral operation is the most important function to be achieved by the power management algorithm. It can be determined by knowing the energy status of each part of the system. $P_{ET}(t)$ is defined as the power harvested from the environment at time t by the energy harvester while the power being consumed by the system at that time is $P_{system}(t)$. In order to model the energy budget in a more practical way, a non-ideal power conversion circuit with an MPPT control unit and a non-ideal energy storage buffers are considered in this part. Hence, the MPPT efficiency η_{MPPT} , the regulator circuit's efficiency $\eta_{converter}$, the battery charging and discharging efficiency $\eta_{RB,charging}$ and $\eta_{RB,discharging}$, and the super-capacitor charging and discharging efficiency $\eta_{capacitor.charging}$ and $\eta_{capacitor.discharging}$ are used to indicate the energy losses in the system. In order to simplify the calculation, an efficiency of the entire power conversion circuit $\eta_{conversion}$, which combines η_{MPPT} and $\eta_{converter}$, is introduced.

$$\eta_{conversion} = \eta_{MPPT} \cdot \eta_{converter} \quad (7.4)$$

Based on the same reason, unified buffering efficiency $\eta_{battery}$ is introduced in Equation 7.5

$$\eta_{battery} = \eta_{RB,charging} \cdot \eta_{RB,discharging} \quad (7.5)$$

Normally, the charging and discharging efficiency of the super-capacitor is the same which is expressed as $\eta_{capacitor}$. Then the buffering efficiency of the super-capacitor $\eta_{supercapacitor}$ can be expressed as:

$$\eta_{supercapacitor} = \eta_{capacitor} \cdot \eta_{capacitor} \quad (7.6)$$

Based on the energy flow of the system, shown in Figure 5.16, the rule of the energy neutral operation can be expressed in two different conditions by using these notations.

- Case 1: If the harvested energy is higher than the energy consumed by the system, then the energy relationship can be expressed as

$$E_{battery,initial} + \eta_{battery} \cdot \int_0^T [\eta_{supercapacitor} \cdot \eta_{conversion} \cdot P_{ET}(t) - P_{system}(t)] dt - E_{leak,b} \geq 0 \quad (7.6)$$

where $E_{battery,initial}$ is the initial battery level and T is cycle duration and $E_{leak,b}$ is energy leakage of the rechargeable battery.

- Case 2: If the harvested energy is less than the energy consumption of the system, then the part of the energy consumption is drawn from the rechargeable batteries. The equation in this case is:

$$E_{battery,initial} - \int_0^T [P_{system}(t) - \eta_{conversion} \cdot \eta_{supercapacitor} \cdot P_{ET}(t)] dt - E_{leak,b} \geq 0 \quad (7.7)$$

If the buffer size of the rechargeable battery is limited, Equations 7.6 and 7.7 can be rewritten as:

$$E_{battery,initial} + \eta_{battery} \cdot \int_0^T [\eta_{supercapacitor} \cdot \eta_{conversion} \cdot P_{ET}(t) - P_{system}(t)] dt - E_{leak,b} \leq E_{battery,full} \quad (7.8)$$

and

$$E_{battery,initial} - \int_0^T [P_{system}(t) - \eta_{supercapacitor} \cdot \eta_{conversion} \cdot P_{ET}(t)] dt - E_{leak,b} \leq E_{battery,full} \quad (7.9)$$

where $E_{battery,full}$ is the maximum energy can be stored in the rechargeable battery. Because if the rechargeable battery is full, no harvested energy could be stored in the battery and the harvested energy will be wasted that is considered as an inefficient design for an energy harvesting system. A proper power management strategy should ensure that the system operating at any time t must satisfy Equations 7.8 and 7.9. This can be achieved by that if the system consumes more energy than the energy generation, its performance should be scaled down to meet the requirement of the energy neutral operation. On the other hand, if the harvested energy is sufficient and

the rechargeable battery is near full, the system must enhance its performance in order to maximize system performance by avoiding waste of the harvested energy.

In order to adjust the system performance based on the energy budget, the energy used directly from the harvested source and the energy stored in and used from the battery may be computed as follows. The time axis is discretized into slots of a duration ΔT and the entire window size is N slots. The following energy profile variables are defined with the index i ranging over $\{1, \dots, N\}$ and $P_{ET}(i)$ is the harvested power in the slot i . $E_{battery}(i)$ is the residual battery energy at the beginning of the slot i . similarly, two possible cases for $P_{ET}(i)$ will occur in ΔT .

- Case 1: If $P_{ET}(i)$ is higher than $P_{system}(i)$, all the energy consumed is directly sustained by the harvested source and the excess energy is stored in the battery.

$$E_{battery}(i+1) - E_{battery}(i) = \Delta T \cdot \eta_{battery} [\eta_{supercapacitor} \cdot \eta_{conversion} \cdot P_{ET}(i) - P_{system}(i)] \quad (7.10)$$

- If $P_{ET}(i)$ is lower than $P_{system}(i)$, part of the energy is drained from the battery, and Equation 7.9 can be rewritten as

$$E_{battery}(i+1) - E_{battery}(i) = \Delta T [\eta_{supercapacitor} \cdot \eta_{conversion} \cdot P_{ET}(i) - P_{system}(i)] \quad (7.11)$$

In order to simplify the analysis, the power consumption of the energy harvesting system itself can be roughly assumed to be of a constant value P_c . Hence, the energy consumption of the system only varies based on the performance of the sensor node, which can be scaled/enhanced by using several techniques, such as duty-cycling among different power modes, radio transmit power adjustment and dynamic voltage scaling. These techniques require hardware support and may not be always be available on the resource constrained sensor node. In this work, in order to simplify the algorithm in relation with the hardware limitation, a common performance scaling technique, which uses duty-cycling between active and sleep modes, has been used.

The power consumption for the sensor node at these two modes are P_{active} and P_{sleep} , respectively, and the average power consumption of the sensor node, $P_{node}(i)$,

and the power consumption of the energy harvesting system $P_{system}(i)$ in a time slot i are calculated as:

$$P_{node}(i) = D_{node}(i) \cdot P_{active} + [1 - D_{node}(i)] \cdot P_{sleep} \quad (7.12)$$

$$P_{system}(i) = D_{node}(i) \cdot (P_{active} + P_c) + [1 - D_{node}(i)] \cdot (P_{sleep} + P_c) \quad (7.13)$$

where P_c is the power consumption of the control circuit of the energy harvesting system and $D_{node}(i)$ is the duty cycle of sensor node in active mode. By substituting Equation 7.13 into Equations 7.10 and 11, the equations can be rewritten related to the duty cycle of the sensor node:

$$E_{battery}(i + 1) - E_{battery}(i) \quad (7.14)$$

$$\begin{aligned} = & \Delta T \cdot \eta_{battery} \cdot D_{node}(i) [\eta_{supercapacitor} \cdot \eta_{conversion} \cdot P_{ET}(i) - (P_{active} + P_c)] + \Delta T \\ & \cdot \eta_{battery} \cdot [1 - D_{node}(i)] \cdot [\eta_{supercapacitor} \cdot \eta_{conversion} \cdot P_{ET}(i) \\ & - (P_{sleep} + P_c)] \end{aligned}$$

$$E_{battery}(i + 1) - E_{battery}(i) \quad (7.15)$$

$$\begin{aligned} = & \Delta T [\eta_{supercapacitor} \cdot \eta_{conversion} \cdot P_{ET}(i) - (P_{active} + P_c)] + \Delta T \cdot \eta_{battery} \\ & \cdot [1 - D_{node}(i)] \cdot [\eta_{supercapacitor} \cdot \eta_{conversion} \cdot P_{ET}(i) - (P_{sleep} + P_c)] \end{aligned}$$

The energy neutral operation and maximum system performance can be achieved when the battery level at the end of the test window N is greater than or equal to the initial battery level, as shown in Equation 7.16.

$$E_{battery,full} > E_{battery}(N) \geq E_{battery,initial} \quad (7.16)$$

The system performance can be determined by calculating the average duty cycle of the system $D_{average}$ during the test window.

$$D_{average} = \frac{[\sum_{i=1}^N D_{node}(i)]}{N} \quad (7.17)$$

The power management algorithm can be designed by knowing the power consumption and the power generation of the system at any time.

7.3.2.2 Power management algorithm design

The energy neutral operation in relation with maximizing the system performance is considered as the feature, which should be satisfied in the proposed power management system. In order to distinguish with other works, the proposed algorithm attempts to achieve this function without knowing the whole map of the energy generation. The proposed power management algorithm consists of three basic parts, as shown in Figure 7.3. The first part is the system specification part, which provides the basic requirements of the system, such as the power consumption, the duty cycle and the lifetime. The second part is characterizing the relationship between the power consumption and the power generation of the system, which can be achieved by monitoring the energy status of the energy buffers. The third part of the system is adapting the sensor node's performance in response to the energy budget of the system according to achieve the energy neutral operation in relation with maximizing the system performance.

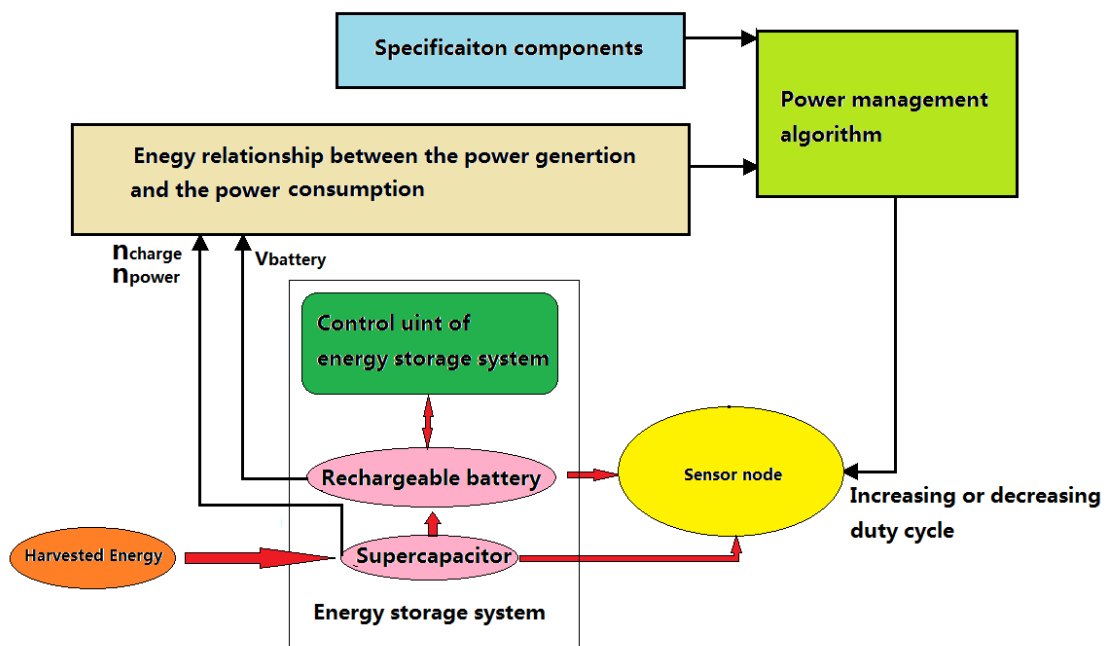


Figure 7.3 System architecture of power management subsystem

(1) The specification component

The specification component in the proposed system provides an interface to the power management strategy and the user policy. Normally, a sensor node has general system requirements, such as network lifetime and the maximum and the minimum

duty cycle of the sensor node. By knowing these requirements, the range of the maximum and the minimum system performance can be addressed. Moreover, the power management algorithm is designed to ensure the system satisfies the requirements, but sometimes the system cannot meet all the requirements at the same time. Hence, the priorities of these requirements should be determined before the algorithm is designed. For instance, if the lifetime of the system is more important than the performance of the sensor node, the power management strategy should maximize the system lifetime rather than to enhance the system performance when the system is operating at the energy restrained condition. The typical requirements of the sensor node for this work are listed in Table 7.2.

Table 7.2 Specification of the sensor node

Priority	Description
1	System lifetime of at least 5 years
2	Sample all sensors at least 30 minutes and send reading to a network coordinator
3	The maximum sample rate is 5 seconds per sample

(2) Characterizing the energy relationship

According to the theoretical analysis, described in the previous section, the energy characteristic of the system is essential for designing a power management algorithm. This characteristic can be determined by having a complete knowledge of the energy generation, the energy consumption and the residual energy in the energy buffers. But unfortunately, all these factors are hard to obtain, especially for the energy generation of the system, which is varied with dynamic environments. Hence, a practical way, which measures the energy level of the energy buffers to indicate the energy relationship, is used in this work. In order to avoid the shortfall by using the battery level to indicate the energy relationship of the system, proposed by (Vigorito et al., 2007), the system monitors the energy level of the super-capacitor used to indicate the instantaneous energy relationship of the power generation and the power consumption.

The sizes of the test window and the time slot should be determined before characterizing the energy relationship. As different environment energy sources have

different energy characteristics, the window size and the time slot size are judiciously chosen based on the characteristics of the energy harvesting system. For instance, as the solar energy has a diurnal cycle, the window size is chosen to be a twenty-four hour duration. Because sunlight is normally changed rapidly, the size of the time slot should be as small as possible in order to increase the accuracy of the algorithm. But frequent comparison increases the overhead of the system, which should be avoided in the micro energy harvesting system. A trade-off should be considered in the algorithm design. In this design, each time slot is taken to be 20 minutes as the variation in generated power by the solar panel using this setting is less than 10% between each adjacent time slot.

In this work, making the sensor node which can adapt quickly changed harvested energy for a long period of time, a simple mechanism for determining both the short-time and long-time energy relationship is proposed. Any time the battery level $E_{battery}(t)$ is higher or less than the initial battery level $E_{battery,initial}$, it donates the energy consumption of the system is less or higher than its generation. But the energy relationship cannot be indicated when the battery level equals to the previous one. In order to recognize the relationship in this situation, the energy level of the super-capacitor is used to indicate the instantaneous energy relationship of the system. As shown in the previous section, the system can work at three different modes, which are using battery, using the super-capacitor or charging the battery modes, by knowing the energy level of the super-capacitor. Hence, the energy relationship of the system can be simplified by knowing the system status. There are two voltage thresholds of the super-capacitor, $V_{W,th1}$ and $V_{W,th2}$, that have been chosen to indicate the system status. If the super-capacitor's voltage $V_{SC}(t) < V_{W,th1}$, the system uses the rechargeable battery to power the system that indicates the energy generation is less than the energy consumption. The system need to reduce its power consumption to adapt its energy generation. At any time slot, if $V_{W,th1} \leq V_{SC}(t) < V_{W,th2}$, the system is powered by the super-capacitor and the energy consumption approximately equals to the energy generation. If $V_{SC}(t) \geq V_{W,th2}$, the super-capacitor powers the system and charges the rechargeable battery at the same time. In this case, the generated energy is higher than the energy consumption. By choosing a proper capacitor size, which can be calculated, based on Equation 7.1, the super-capacitor can only stay at

one status in one time slot and the energy relationship in the time slot can be indicated by examining the energy level of the super-capacitor.

On the other hand, by considering the condition of maximizing the system performance, any situation in which the battery energy is full ($E_{battery}(t) = E_{battery,full}$) indicates that the harvested energy has not been efficiently used. Thus, if the system satisfies $E_{battery}(t) < E_{battery,full}$ at any time, the harvested energy is efficiently being used by the system. By combination the energy neutral operation and maximizing the system performance, the proper power management algorithm should make the battery energy satisfying $E_{battery,initial} \leq E_{battery}(t) < E_{battery,full}$ at any time period.

(3) Algorithm design

By knowing the energy relationship of the system, the power management algorithm can be designed. As the system performance is highly related to the duty cycle of the sensor node, the algorithm adapts its duty cycle by following the energy usage law. The adaptive duty cycle should be restricted in a limited interval, which are the highest duty cycle and the lowest duty cycle of the sensor node. In order to avoid a large variance between neighbouring cycles, which may cause the system performance to become unstable, the algorithm should consider a smoothing function to keep the variance of the duty cycle to a minimum. A duty cycle $D_{initial}$ has been automatically set by the algorithm when the system starts to work. The battery at the first time slot powers the system and the measurements of the energy level of the two energy buffers are taken at the end of the cycle. Then the system compares the current battery voltage reading to a 2.2V voltage threshold. If the battery voltage is higher than 2.2V, which means that the battery is in a healthy state. Then the system goes to the next stage. Otherwise, the system reports the battery energy is almost depleted and the sensor node will report an error message to the local server and then go to sleep.

When the system ensures the battery is in the healthy state, it compares the residual battery energy to the initial battery energy. The system also records the status of the super-capacitor by using n_{power} and $n_{charging}$ to indicate that the system is being powered by the battery and the system is charging the battery, respectively. Based on the previous analysis, three different cases will occur and the corresponding reactions will be considered.

- Case I: if the current battery reading is less than the previous one, the energy is drained from the battery by the sensor node. In order to maintain the energy neutral operation in this shortfall condition, the duty cycle of the sensor node should be reduced. By considering smoothing the duty cycle, three different duty cycle variations ΔD_1 , ΔD_2 and ΔD_3 , are set by the algorithm based on different situations. If the residual battery level $V_{R-battery}$ is lower than a setting threshold $V_{b,th1}$, which indicates that the system cannot last long enough to meet the next testing window, the minimum duty cycle of the sensor node D_{min} is chosen for the system to ensure the system charging the battery. This is because the charging battery process has the top priority in this situation. If $V_{b,th1} \leq V_{R-battery} < V_{b,th3}$, the task of charging the battery still has the higher priority than maximizing the system performance. The largest duty cycle variation ΔD_1 is chosen for the system to reduce the power consumption of the system to make sure more the extra energy could charge the battery. If $V_{b,th3} \leq V_{R-battery} < V_{b,th2}$, which means the residual battery energy is in the good condition, and the system wants to enhance its performance rather than to store energy in the battery. A smaller cycle variation ΔD_2 is defined by the algorithm to reduce the power consumption of the system. If $V_{R-battery} \geq V_{b,th2}$, the residual battery energy is nearly full. In order to maximize the performance of the system and keep a small duty cycle variation between two adaptive processes, the smallest duty cycle variance ΔD_3 is set by the algorithm.
- Case II: when the battery voltage is higher than the previous one, the harvested energy is higher than the energy consumption of the system. In this case, the system will increase the duty cycle in the future time slot to maximize system performance. The same duty cycle variations ΔD_1 , ΔD_2 , and ΔD_3 , as set in the Case I, are used to meet different situations. There are four different situations being considered in the algorithm. If $V_{R-battery} < V_{b,th1}$, the charging battery is the most important task to be achieved. Hence, the minimum duty cycle D_{min} is selected by the algorithm. If $V_{b,th1} \leq V_{R-battery} < V_{b,th3}$, which the charging battery procedure has the higher priority, the smallest ΔD_3 is added onto the previous duty cycle to balance the charging battery procedure and improving the system performance procedure. If $V_{b,th3} \leq V_{R-battery} < V_{b,th2}$, the system performance is more important than the energy neutral operation. A larger duty

cycle variation ΔD_2 is added onto the previous duty cycle to improve the system performance. If $V_{R-battery} > V_{b,th3}$, which means the battery energy is nearly full, the largest duty cycle variance ΔD_1 is added to rapidly increase the power consumption of the system.

- Case III: when the battery voltage is equal to the previous one, the more complex judgements should be concerned to indicate the energy relationship. In this work, the super-capacitors' status has been used to indicate the energy relationship. By considering the residual energy of the batteries, the system is faced with four different situations. If $V_{R-battery} < V_{b,th1}$, the system must charge the batteries. Hence, the minimum power consumption of the sensor node should be used. If $V_{b,th1} \leq V_{R-battery} < V_{b,th3}$, there are three different situations that will be observed by the system. If the charging battery status has been found, which indicates $n_{charging,B} > 0$, the energy generated of the system is higher than the energy consumption of the system. By considering the fact that the charging battery process has the higher priority, the system maintains the same duty cycle in the next time slot to expect energy being store in the battery. At the same situation, if $n_{power,B} > 0$ is detected, which indicates the harvested energy is less than the energy consumption, ΔD_2 is reduced from the previous duty cycle to guarantee more energy could be stored in the battery. The last scenario for this case is that if there is no $n_{power,B}$ or $n_{charging,B}$ being recorded, which means that the energy consumption nearly equals to the energy generation, the smallest duty cycle variation ΔD_3 is reduced from the previous one. For the situation $V_{b,th3} \leq V_{R-battery} < V_{b,th2}$, the system wants to consume more energy than the energy being stored in the battery. The three situations are distinguished by examining the status of the super-capacitors. If $n_{charging,B} > 0$, the energy generation is higher than the energy consumption. In order to increase the system performance, ΔD_2 is added to the previous duty cycle to increase system performance. If $n_{power,B} > 0$, ΔD_3 is taken from the previous duty cycle to maintain energy neutral operation. If $n_{charging,B} = 0$ and $n_{power,B} = 0$, the system maintains its duty cycle. In the last situation, where $V_{R-battery} > V_{b,th3}$, the residual battery energy is nearly full. For efficiently using the harvested energy, ΔD_1 is added onto the previous duty cycle to ensure the system consumes

more energy than it has harvested.

The proposed power management algorithm is shown in Table 7.3 using the simple else-if statements. Moreover, as stated in the previous section, in order to avoid over draining the energy from the battery, the sensor node needs to be switched-off when the battery voltage drops below the lowest voltage threshold.

Table 7.3 Power management algorithm pseudo code

	Driver
1	<p><i>Initial system</i></p> <ul style="list-style-type: none"> ● Measuring initial battery level $V_{R-battery}$, and set initial duty cycle $D_{initial}$ for sensor node ● Setting $V_{B,th1}$, $V_{B,th2}$, $V_{B,th3}$, D_{min}, D_{max}, ΔD_1, ΔD_2, and ΔD_3 ● $n_{power} = 0$ and $n_{charge} = 0$
2	<p>During time slot T, the system recorded $V_{R-battery}$, n_{power}, and n_{charge} respectively</p>
3	<p>If $V_{R-battery} > 2.2V$ { Comparing the battery level $V_{R-battery}$ to the previous battery level reading $V_{R-battery,i}$</p> <p>Case 1: if $V_{R-battery} < V_{R-battery,i}$ { if $V_{R-battery} < V_{B,th1}$, $D = D_{min}$; Else if $V_{B,th1} \leq V_{R-battery} < V_{B,th3}$, $D = D_{initial} - \Delta D_1$; Else if $V_{B,th3} \leq V_{R-battery} < V_{B,th2}$, $D = D_{initial} - \Delta D_2$; Else If $V_{R-battery} \geq V_{B,th2}$, $D = D_{initial} - \Delta D_3$; }</p> <p>Case 2: if $V_{R-battery} > V_{R-battery,i}$ {If $V_{R-battery} < V_{B,th1}$, $D = D_{min}$ Else if $V_{B,th1} \leq V_{R-battery} < V_{B,th3}$, $D = D_{initial} + \Delta D_3$; Else if $V_{B,th3} \leq V_{R-battery} < V_{B,th2}$, $D = D_{initial} + \Delta D_2$; Else if $V_{R-battery} \geq V_{B,th2}$, $D = D_{initial} + \Delta D_1$; }</p> <p>Case 3: If $V_{R-battery} = V_{R-battery,i}$ {If $V_{R-battery} < V_{B,th1}$, $D = D_{min}$; Else if $V_{B,th1} \leq V_{R-battery} < V_{B,th3}$ {If $n_{charge,B} > 0$, $D = D_{initial}$; Else If $n_{power,B} > 0$, $D = D_{initial} - \Delta D_2$; Else if $n_{charge,B}$, $n_{power,B} = 0$, $D = D_{initial} - \Delta D_3$; } Else if $V_{B,th3} \leq V_{R-battery} < V_{B,th2}$ {If $n_{charge,B} > 0$, $D = D_{initial} + \Delta D_2$; Else if $n_{power,B} > 0$, $D = D_{initial} - \Delta D_3$; } Else if $n_{charge,B}$, $n_{power,B} = 0$, $D = D_{initial}$; }</p> <p>If $V_{R-battery} \geq V_{B,th2}$; $D = D_{initial} + \Delta D_1$; } }</p>
4	<ul style="list-style-type: none"> ● $D_{initial} = D$ and $V_{R-battery,i} = V_{R-battery}$ ● $n_{power} = 0$ and $n_{charge} = 0$ <p>Return to step 2</p>
5	<p>Else If $V_{R-battery} < V_{B,th2}$ Report error to coordinator and enter sleep mode</p>
6	<p>end</p>

The reason the algorithm set different rechargeable battery voltage thresholds, $V_{B,th1}$ and $V_{B,th2}$, for the system is that the system wants to save some unused energy

to cover some extremely cases, such as a long term rainy. Moreover, as the super-capacitor is charged by the boost converter, which is powered by the energy harvester, the system can be cold-started from the battery depleted condition.

7.4 System evaluation

In order to evaluate the proposed power management system in a real environment, the power management system for a solar energy harvesting system has been designed and implemented, as shown in Figure 7.4. A Jennic wireless module based sensor node, DR1048 board (DR1048, 2007), was employed as the target system. The power consumption of the sensor node is 43mW in active mode and 6mW in sleep mode, respectively. By adding the overhead of the control circuit, the maximum power consumption of the system is around 14mW when 20% duty cycle is applied on the sensor node. The control and charge algorithm has been designed based on Table 7.1 and implemented in the PIC16F688 MCU to distribute and monitor the available energy in the energy buffers. By considering the specifications of the sensor node and the energy buffers, the six voltage thresholds are set $V_{W,th1} = 3.3V$, $V_{W,th2} = 4.1V$, $V_{W,th3} = 3.7V$, $V_{W,th4} = 2.7V$, $V_{B,th1} = 3V$ and $V_{B,th2} = 2.2V$, respectively. As knowing a 30 minute time duration is selected by the power management algorithm, the capacitance of the super-capacitor can be calculated by using Equations 7.2 and 7.3.

$$E_{\text{system}}(\text{maximum}) = 0.014 \times 1800 = 25.2 \text{ Joule}$$

$$C_{\text{min}} = \frac{2 \times E_{\text{system}}(\text{maximum})}{V_{w,th3}^2 - V_{w,th4}^2} = 7.94F$$

Based on the calculation, the minimum 7.94F super-capacitor can supply sufficient energy capacitance to the system. By considering the energy leakage and charging/discharging efficiency, a much higher capacitance capacitor should be used. In this work, a 22F super-capacitors has been chosen as the primary energy buffer. Moreover, in order to supply a sufficient energy capacitance to the system when no energy can be harvested, two series connected 800mAh NiMH rechargeable battery are used as the secondary energy buffer.

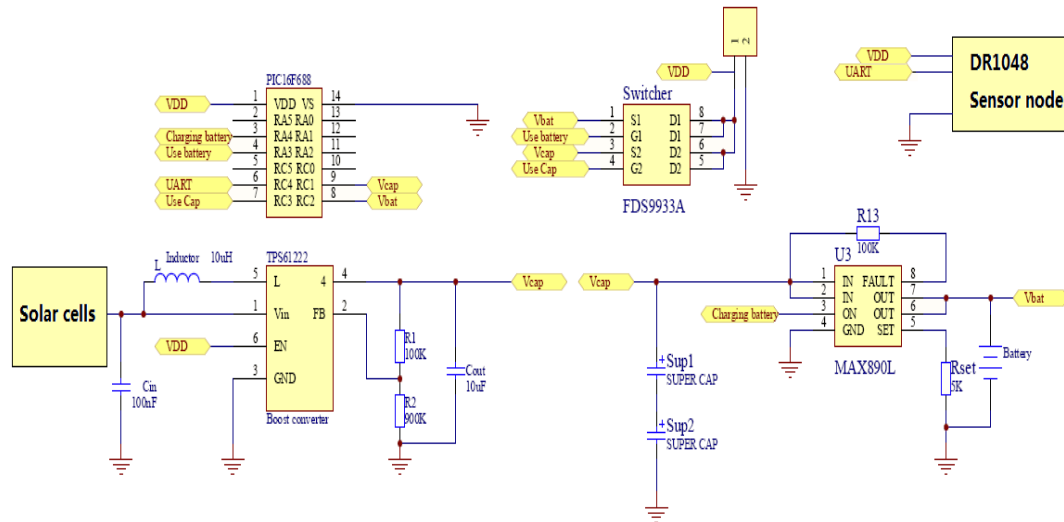


Figure 7.4 Schematic diagram of the simple solar powered wireless sensor node

The first step of the system evaluation is to verify the control and charge algorithm. A bread board circuit has been designed and implemented in the laboratory. In order to simplify the testing procedure, the circuit board is connected and powered by a DC power supply, which is used to emulate the harvested energy from the environment. Initially, the sensor node is powered by the rechargeable batteries while the DC power supplier charges the super-capacitors. It can be observed that when the first voltage threshold $V_{cap} = 3.3V$ is met, the system is powered by the super-capacitor. If the input energy is higher than the energy consumption, this indicates that the super-capacitor's voltage is growing. When it reaches the second charging threshold $V_{cap} = 4.1V$, the PIC16F688 switches on the MAX890L charging chip and the energy from the super-capacitor is rapidly transferred to the rechargeable battery. As long as the capacitor's voltage drops less than $3.7V$, the control and charge circuit stops charging the battery and the terminal voltage of the super-capacitor rises again. After several charging cycles, the DC power supply turns off and the terminal voltage of the super-capacitor drops. As soon as the super-capacitor's voltage drops below $2.7V$, the battery starts to power the system again. In order to examine the overcharge protection and undercharge protection, another experiment has been taken performed. To simplify the testing procedure, the super-capacitor is used to emulate the battery. The experiment results show that the system stops charging the super-capacitor when its voltage level is higher than $3V$ and the system reports an error message to the local controller when the $2.2V$ voltage threshold is met. The experimental results also show

that the MCU monitors the energy buffer's terminal voltage correctly and the sensor node receives the measuring data at each testing cycle. The power overhead of the control and charge circuit is around $600\mu W$ when 3.3V voltage source is supplied.

By knowing the energy characteristics of the system, the power management algorithm has been designed and implemented into the Jennic chip in order to achieve energy neutral operation and maximize the system performance. The same hardware has been used to evaluate the power management algorithm. In order to simplify the testing procedure and reduce the testing time, a 10 minutes testing window has been chosen and each iteration of the power management algorithm is run every minute. The duty cycle range is set between [2%, 100%] and the maximum power consumption and the minimum power consumption of the system are 43.6mW and 7.34mW, respectively. The initial duty cycle of the sensor node is 20% and the corresponding power consumption of the system is 14mW. The battery is pre-charged to 2.7V and the rest of the parameters are set by the algorithm which is listed in Table 7.4.

Table 7.4 The parameters for the power management algorithm

Parameters of the algorithm					
$V_{B,th1} = 2.2V$	D_{max} = 50%	D_{min} = 0.05%	$\Delta D_1 = 1\%$	$\Delta D_2 = 0.5\%$	$\Delta D_3 = 0.1\%$
$V_{B,th2} = 2.9V$					
$V_{b,th3} = 2.7V$					

The system is powered by the DC power supply and the evaluation results are depicted in Figure 7.5 (a) and (b). Initially, a constant 10mW power, which is less than the power consumption of the system, is supplied to the system for running 3 hours. In this case, the majority of the energy is drained from the rechargeable batteries, as shown in Figure 7.5(a). Since the batteries' voltage drops, the algorithm reduces its duty cycle to adapt available energy during the time interval 0-152 minutes, as depicted in Figure 7.5(b). It can be observed that the battery voltage has risen when the power consumption drops below the input energy. After 3 hours, the system switches to be powered by 20mW power source. It can be observed from the curves that the batteries' voltage has risen faster after the new power source was added to the system. Because the input energy level is far more than the power consumption, the duty cycle

of the sensor node has risen simultaneously to adapt the new input energy. The maximum 3V battery voltage was achieved at 253 minutes and then the system stopped charging the battery. In order to attain maximum the system performance to reduce the energy wastage, the sensor node continues to raise its duty cycle to consume more energy than the input energy. At last the duty cycle maintains around 37%, which the power consumption equals to the input energy source. Based on the testing results, the proposed power management algorithm has the ability to maintain an energy neutral operation in relation with maximizing the system performance.

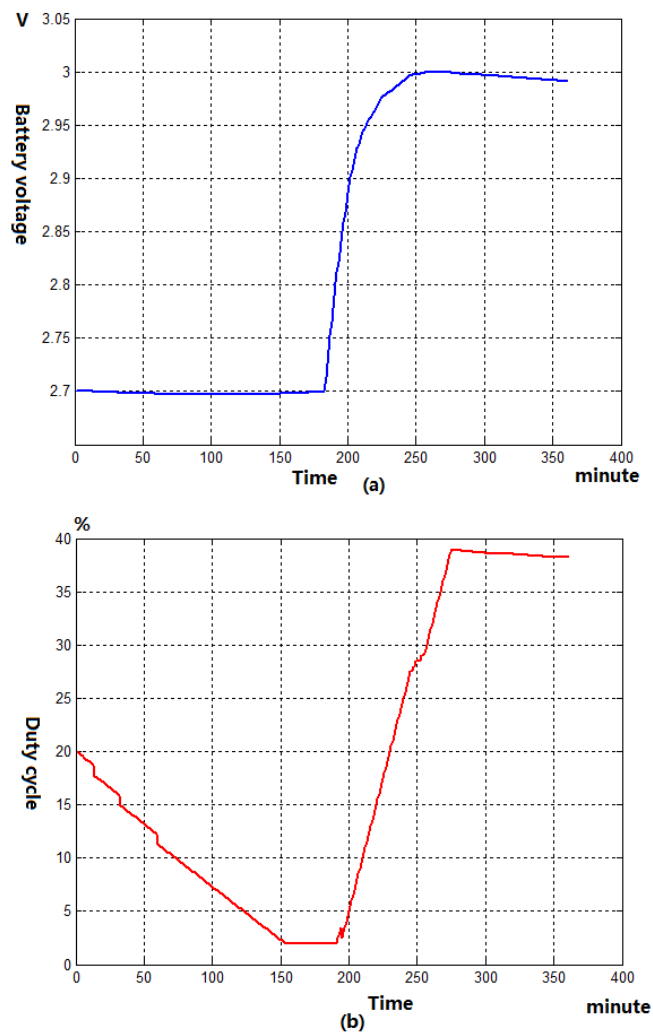


Figure 7.5 Testing results of Power management algorithm

The proposed power management system has been evaluated by using actual solar energy. Based on the system specifications and the characteristics of the solar energy, a 24 hours test window and a 30 minutes time slot have been set, respectively. The energy relationship is measured at each time slot. Based on the system specification,

shown in Table 7.2, the maximum duty cycle and the minimum duty cycle of the sensor node are 20% and 0.05%, respectively. The corresponding power consumptions of the system are 14mW and 7.5mW, respectively. Based on the duty cycle restriction, the parameters of the solar power management algorithm are shown in Table 7.5.

Table 7.5 The parameters of the solar power management algorithm

Parameters of the algorithm					
$V_{B,th1} = 2.2V$	$n_1 = 10$	$n_2 = 10$	$\Delta D_1 = 1\%$	$\Delta D_2 = 0.5\%$	$\Delta D_3 = 0.01\%$
$V_{B,th2} = 2.9V$					
$V_{b,th3} = 2.7V$					

In order to verify the system's efficiency and the performance, the proposed algorithm has been compared with two simple designs. The first design is to achieve energy neutral operation by sampling the battery voltage. It is based on the principle that the sensor node increases/decreases its duty cycle when the battery voltage increased/reduced. The second approach is using two fixed duty cycles based on the diurnal cycle of solar energy and two constant duty cycles 10% and 1% are set by the system during the day and night, respectively. In order to maintain the same experimental conditions for these three systems, the same solar cells has been connected with them and placed at the same environment. The initial duty cycle 10% and the same residual battery energy 2.6V were uniformly set by the systems. The experimental tests were conducted at Loughborough University for 5 days and the results are shown in Figure 7.6 (a) and (b).

The battery voltages were recorded during these five days, as shown in Figure 7.6 (a). It can be observed that the systems with the prior two types of power management algorithms can achieve energy neutral operation, for which the terminal voltage of the battery is around 2.7V at the end of each testing window. But for the system with two fixed duty cycle algorithm, the battery voltage was not oscillating around the 2.7V and the battery voltage dropped below 2.6V at the last testing window. Based on this trend, it seems that the system has not had an energy neutral operation that it cannot survive for a long term operation. The corresponding duty cycles of each design are depicted in Figure 7.6(b). It indicates that the proposed real time power management algorithm is able to achieve a performance level depending

on the energy availability. In addition, in order to show that the system with the power management algorithm can have the best system performance, the mean values of the duty cycle for each system during these five test windows are listed in Table 7.6. The comparison results demonstrate that the proposed power management algorithm has the largest mean duty cycle compared with the other two algorithms. This means the proposed power management algorithm can make the system has the higher system performance than other two approaches.

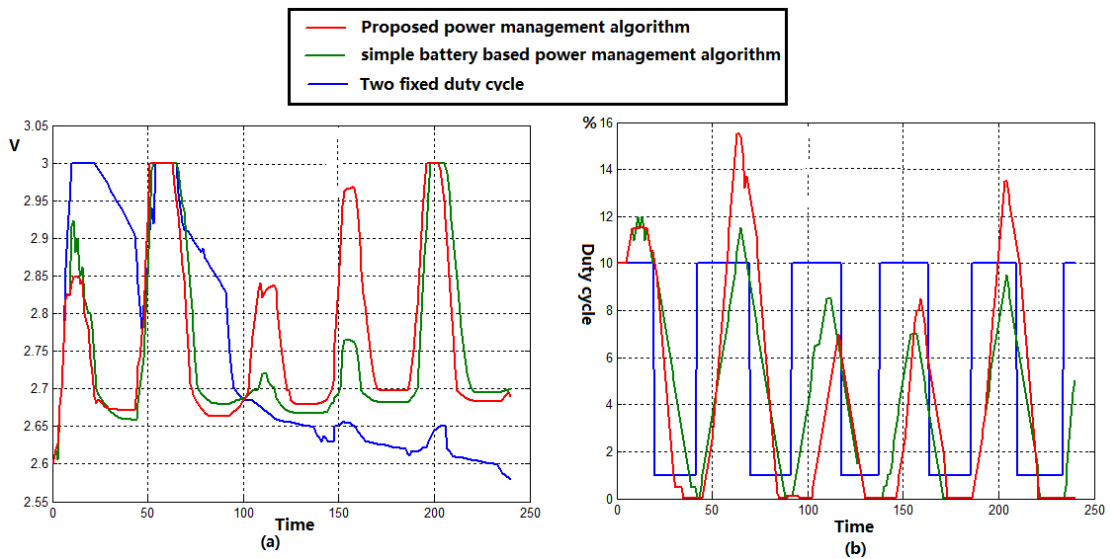


Figure 7.6 Experimental results of three different power management

Table 7.6 Performance comparison of the power management algorithms

Algorithm	The proposed	Simple battery based algorithm	Two fixed duty cycle algorithm
Mean value of duty cycles	5.515	5.15	5.5

7.5 Conclusion

In this chapter, an efficient power management unit has been designed. The various issues in power management for an energy harvesting system have been discussed. In order to cover the shortfalls of existing power management designs, the energy distribution unit and the power management algorithm have been designed. The proposed system has a significant advantage over currently used methods, which are based on estimating energy profile to adapt the sensor node's performance. The energy

relationship between the power generation and the power consumption can be indicated by the residual energy levels on the batteries and the super-capacitors. This makes the algorithm, which makes a decision of increasing or decreasing the power consumption of the system based on the real energy budget of the system. Moreover, the proposed algorithm is realized in most energy harvesting scenarios without making any assumptions about the profile of the harvested energy source. The system has been implemented in a real environment comparing with other two existing power management algorithms. The experimental results illustrate that the proposed algorithm can achieve the energy neutral operation in these test days and the system has the better system performance than other two approaches.

Chapter 8. Design a wireless Sensor node

8.1 Wireless sensor platforms

Before designing energy harvesting system, the characteristics of the target sensor node is very important. This is because that the energy consumption of the system is highly related to the power consumption of the sensor node. Hence deeply understanding a wireless sensor node and its platform is essential before designing an efficient energy harvesting system. According to this point, several wireless sensor nodes have been designed in this chapter for us to understand the characteristics of the wireless sensor nodes. Furthermore, in order to show how to design an energy harvesting system, two types of sensor nodes, developed in this chapter, have been selected as the target sensor nodes, which are powered by the solar and thermal energy harvesting systems in Chapters 9 and 10, respectively.

Wireless sensor nodes should be small, cheap and energy efficient because a large number of sensor nodes are deployed in the environment to construct a WSN. More in detail, the constraints in physical side decides that the sensor nodes cannot use a large capacity battery as the power source. The cheap and energy efficient requirements determine that a sensor node must use a low power consumption processor, a small radio with limited bandwidth and transmission range, and low power consumption sensors. Hence, wireless sensor nodes are constrained in terms of computation and communication capabilities. A generic wireless sensor node hardware structure is comprised of four main subsystems: a) a computing subsystem consisting of a microcontroller with memories to process data collected by the sensing subsystem; b) a communication subsystem consisting of a short range radio system for wireless data communication; c) a sensing subsystem consisting of a group of sensors and actuators to monitor the physical environment; d) a power supply subsystem, which normally use batteries to power the whole sensor node, as depicted in Figure 8.1. In order to

design a wireless sensor node, the system should be constructed based on these four subsystems.

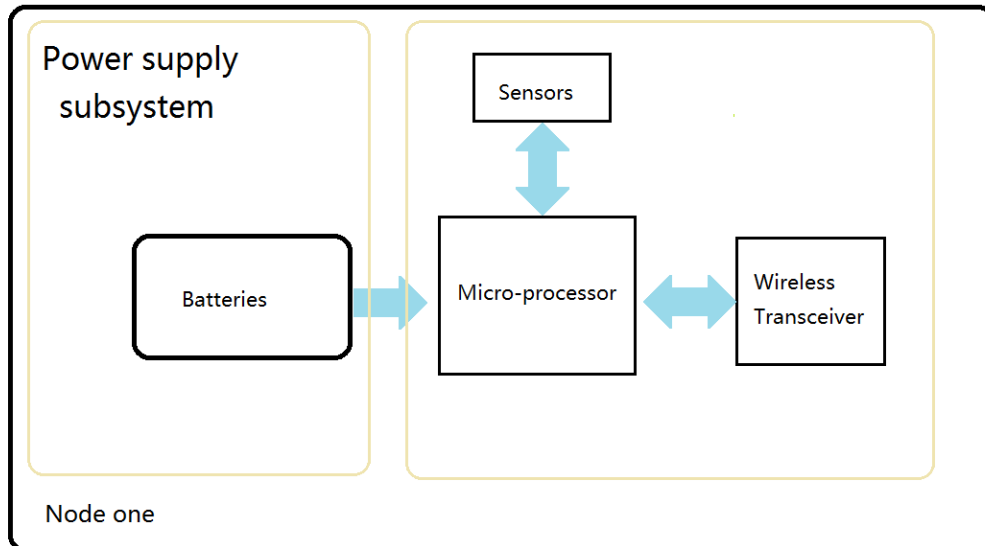


Figure 8.1 A generic Wireless Sensor node architecture

8.2 Data processing subsystem

A data computing and a data transmission subsystem can be seen as the data processing subsystem. Normally, these two modules are integrated into one chip as a module. In order to design a wireless sensor node, the first step is to select a microcontroller platform, which is the heart of all types of wireless sensor nodes. Nowadays, there are plenty of wireless modules in the market such as TI/CHIPCON's CC2430/CC2431, EMBER's EM250/260, FREESCALE's MC13211/212/213, MICROCHIP's MJ2440 and JENNIC's JN5121/5139/5148. Some of these microchips have integrated a built-in 2.4GHz IEEE 802.15.4 compliant radio transceiver. The comparison of different wireless MCUs is shown in Table. 8.1; the prices come from the DigiKey website.

Table 8.1 ZigBee Chips Comparison

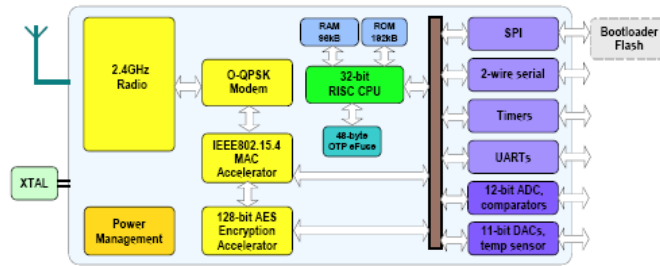
Manufacturer	Part Number	Supply voltage (V)	Sleep Current (UA)	TX Current (MA)	RX Current (MA)	TX Power (DBM)	RX Sensitivity (DBM)	Security	Price (USD)
ATMEL	AT86RF231	1.3-3.6	0.02	14.3	13.2	3	-101	AES	4.73
FREESCALE	MC13192	2.0-3.4	1	30	37	4	-91	None	4.67
TEXAS INSTRUMENTS	CC2420	2.1-3.6	20	17.4	18.8	0	-95	CTR CCM AES	8.75
MICROCHIP	MRF2J40	2.4-3.6	2	19	23	0	-95	CCM CTR AES	9.95
JENNIC	JN5139	2.7-3.6	2.6	37	37	2.5	-96	CBC CCM CTR AES	14.21
Ember	EM2420	2.1-3.6	0.5	17.4	19.7	10	-94	AES	17.23
ST	SN260	2.1-3.6	1.0	35.5	35.5	2.5	-100	AES	29.41

In this thesis, the Jennic JN5139 microchip (JN5139, 2009) is selected as the wireless MCU platform. There are three reasons to use this platform as an example. Firstly, the Jennic module is a ready-made component and the module integrates all of the 2.4GHz RF components, which removes the need to perform expensive RF design and test. This can extremely reduce the product developing time.

Secondly, the JN5139 module is a high capability wireless module, which is equipped with a 32-bit RISC processor, 192kB ROM, 96kB of RAM, and a rich mixture of analog and digital peripherals. This means that the sensor node has a high capability for handling different types of sensors and functions at the same time. The block diagram of JN 5139 wireless module is shown in Figure 8.2.



(a) JN 5139 modules



(b) Block diagram of JN 5139

Figure 8.2 JN5139 Module and the block diagram (Jennic 5139, 2009)

Thirdly, the Jennic module provides different power consumption modes for the end users to smartly control the power consumption of the sensor nodes. The controllable power consumption modes of the Jennic module can be divided into MCU part and wireless transceiver part. Based on the (Jennic 5139, 2009), the Jennic MCU has four different power consumption modes: active processing mode, doze mode, sleep mode, and deep sleep mode. Table 8.2 presents the resulting energy consumption for the JN5139 CPU at different modes. In active processing mode, all of the application processes take place and all of the peripherals are available to use. In this mode, the sensor node consumes the largest power. In order to reduce power consumption of MCU, the CPU can enter into doze mode, which CPU operation is stopped but the chip remains powering and digital peripherals continue running. In terms of the datasheet, the module in doze mode uses more power than sleep and deep sleep modes but it requires less time to restart the module. This mode can be used for radio communication, where the CPU operation is not required. The third mode is sleep mode, which the module can enter this mode to greatly save energy. When the CPU enters sleep mode most of the internal chip functions are shut down, the state of DIO pins is retained to preserve any interface to the external peripherals. Whilst in sleep mode, there is an option to quickly wake up the CPU by retaining the code in the RAM without reloading it from flash memory, but $2.4\mu\text{A}$ energy consumption will be added. In order to further reduce the power consumption, the module can be forced to the deep sleep mode. In this mode, the module just consumes 250nA current, but the module can only be waken up by using an external interrupt.

Table 8.2 Power consumption for the JN5139 microcontroller at different power mode (JN5139, 2009)

Mode	Current	Mode	Current
CPU active processing	2.85+0.295/MHz mA	Sleep mode with I/O wakeup	0.1uA
ADC	655 uA	Sleep mode with I/O and RC oscillator timer wake up	1.2uA
DAC	215/235 uA	The following current figures should be added to those above if the feature is being used	
Comparator	67.5 uA	RAM retention	2.4 uA
UART	95 uA	Comparator	1.2uA
Timer	65uA	Deep sleep mode (Waiting on chip Reset or I/O event)	250nA
2-wire serial interface	75uA		
CPU Doze mode	2.85mA		

Similar to the MCU, the 2.4GHz radio of JN5139 module can also have different power levels and power consumption modes. Table 8.3 shows the current draw from the 2.4GHz radio through different power levels and modes. The module provides seven different power levels for data transmission. This function can be used to further reduce the energy consumption by knowing the transmission distance between the two nodes.

Table 8.3 Different power level settings for 2.4GHz transceiver

Mode	Power level (dBm)	Current (mA)
TX	-30	8.4
	-24	9.8
	-18	12.3
	-12	19.4
	-6	25
	+1.5	38
	+3	42
RX		37
Idle		37

Fourthly, because almost all the peripheral devices are integrated on a small PCB board, the size of the module is small. The compact form makes Jennic modules highly suitable for many applications, including medicine, environmental monitoring, new computer human interface, and ambient intelligence.

8.3 Sensing subsystem

The sensing subsystem is a bridge which links a wireless sensor node to a physical world. It produces output signals in response to the value, quantity, or condition of some physical variables. Before selecting a sensor, the type of sensor and the output signal of the sensor should be determined. This process can be held by classifying the sensors. Normally, there are different ways to classify sensors. Based on the power supply point of view, the sensors can be divided into passive sensors and active sensors. The passive sensors do not need any additional power source to sustain the sensor operation. They directly generate an electrical signal in response to physical variables. A photodiode, which generates different analog signals with different light

illumination conditions, is a typical passive sensor. On the other hand, an active sensor needs an external energy source to maintain its operation. The temperature sensitive resistor is an outstanding example of the active sensor. The sensors also can be classified by their output signals, which are the digital or analogue signal. Normally, digital sensors provide simple ON/OFF or TRUE/FALSE commands or the binary signals to the controller. But an analog sensor generates an analogue signal, normally a voltage, to react the physical environment. In order to make the sensor readings can be read by the MCU, this type of sensor needs a peripheral device such as ADC to convert the analog signal to a digital one.

After sensor classification, the sensor selection process can be held. Normally, the sensor with high sensitivity, high accuracy, high repeatability, low power dissipation, low cost, and ease of using is considered as an idea sensor for the design. Unfortunately, it is very hard to have all these advantages in one sensor. Hence, selecting a proper sensor for a particular application necessitates prioritizing the requirements for that application. Sensor selection means balancing these requirements. There are several of the factors that play significant roles when selecting a sensor. These parameters can be conveniently collected from three aspects:

- Environmental condition: the operating temperatures, pressure, light, humidity and position.
- Design parameters: purpose of the measurement, human engineering requirements, data transmission technique to be used, data processing system to be used (JN5139), type of data display to be used, signal conditioning required and load on the transmission or data processing systems
- Sensor parameters: sensor package size, response time, accuracy of the measurement, transducer's effect on the measured, lifetime, power requirement, available accessories, temperature range, maximum error that can be tolerated during static conditions and during and after exposure to transient environmental conditions, transducer excitation voltage, current drawn from the excitation supply and cost.

In this chapter, an environment monitoring sensor node, which incorporates a temperature sensor and a Carbon Monoxide (CO) gas sensor, is designed as an example to show how to select a proper type of sensor for a type of application. The sensing subsystem design consists of a temperature monitoring circuit design and a

CO gas monitoring circuit design.

8.3.1 Temperature sensor selection

There are plenty types of temperature sensors in the market. Using one perspective, they can be simply classified into three groups: Thermocouple, Resistance Temperature Detector (RTD), thermistor and IC temperature sensors. Thermocouple, which was discovered by Thomas Seebeck in 1822, is one of the most common industrial thermometers. It consists of two dissimilar metals, joined together, and produces a small unique voltage at a given temperature. Thermocouples are considered as the smallest, fastest and most durable temperature measurement solution (Sensor selection, 2010). It can be used over an extremely wide temperature range and in harsh environmental conditions. The thermocouple junction can often be placed together to the desired point of measurement. There are three disadvantages with thermocouples. Firstly, temperature measurement with a thermocouple requires two temperature be measured. Secondly, the relationship between the process temperature and the thermocouple output voltage is not linear. Thirdly, thermocouple sensors need a special compensation technique if using it to approach temperature accuracies of 1%. RTD is basically a positive temperature coefficient device, which means that the resistance increases with temperature. Characteristics include high accuracy, low drift, wide operating range, repeatability, and reasonable linearity. A RTD is the most suitable type of the sensor when extremely stable and precise measurements are the most important criteria. A thermistor is also a type of resistor sensor whose resistance varies with temperature. But the difference between thermistors and RTDs is that the material used in a thermistor is generally a ceramic or polymer, while RTDs use pure metals. The most common thermistors have a negative temperature coefficient of resistance. Characteristics include moderate temperate range, low cost, poor but predictable linearity. Thermistors are ideal for measuring applications that require high accuracy sensitivity over a relatively narrow range of temperatures (Sensor selection, 2010). IC temperature sensors, which are produced in the form of ICs, are complete silicon based sensing circuits with either analog or digital outputs. The use of IC temperature sensors is limited to applications where the temperature is within a -55 centigrade to 150 centigrade ranges. But they have several advantages by comparing with other types of temperature sensors. Firstly, IC temperature sensors are considered as small, accurate, excellent linearity and inexpensive type of temperature sensors.

Secondly, they are easy to interface with other device such as amplifiers, and microcontrollers. All these factors are summarized in Table 8.4.

Table 8.4 Temperature sensors

Attribute	Thermocouple	RTD	Thermistor	IC temperature Sensors
Temperature range	-190°C to 1821°C	200°C to 850°C	-90°C to 130°C	-55°C to 150 °C
Accuracy	Poor	High	Medium	High
Response Time	Fast	Moderate	Fast	Fast
Stability	Not as stable	Stable over long periods	Moderate	Stable over long periods
Linearity	Moderate	Good	Poor	Best
Sensitivity	Low	Medium	Very high	Very High
Interchange ability	Moderate	Excellent	Poor	Moderate
Repeatability	Poor	Good	Moderate	Excellent
Size	Small to large	Medium to small	Small to medium	Small to medium

Because of the advantages of IC temperature sensors, Maxim IC temperature sensor DS18B20 (DS18B20, 2009) has been chosen as the temperature sensor in our design. The DS18B20 digital thermometer provides 9-bits to 12-bits Celsius temperature measurements and has an alarm function with non-volatile user-programmable upper and low trigger points (DS18B20, 2009). The DS18B20 requires one data line for communication with a central microprocessor. The features are shown in below:

- Power supply range: 3.0V to 5.5V
- Measures temperatures from : -55 °C to +125°C
- Accuracy: +/- 5°C from -10°C to +85°C
- Thermometer resolution is user selectable from 9 to 12 Bits
- Converts temperature to 12-Bit digital word in 750ms
- Available in 8-Pin SO (150 mils), 8-Pin SOP, and 3-Pin TO-92 packages

The application schematic diagram is shown in Fig.8.3. The DS18B20 chip is powered by an external power supply to the VDD pin. The current consumption of the temperature sensor is 1mA when it steps into active mode. And current consumption of the temperature sensor is dropped to 750nA when it operates in idle mode.

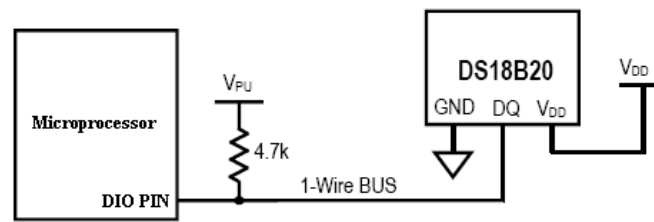


Figure 8.3 DS18B20 circuit

8.3.2 CO gas sensor selection

As mentioned in the previous part, the power consumption is a big issue in selecting a sensor for using in a wireless sensor node. Hence, an electrochemical gas sensor, which is a passive sensor, should be used in this work. Based on this point of view, a CO gas sensor TGS5042 (CO gas sensor, 2010) from Figaro company, has been selected. The features of the TGS5042 CO gas sensor are:

- Battery operable
- High repeatability/selectivity to CO
- Linear relationship between CO gas concentration and sensor output
- Simple calibration
- Long life
- Target gases: Carbon monoxide
- Typical detection range: 0 to 10,000 ppm
- Output current in CO: 1.2 to 2.4nA/ppm
- Operating temperature range: -40°C to +70 °C
- Response time (T90): within 60 seconds
- Weight: 12g

Fig.8.4 shows the basic measuring circuit of TGS5042, as recommended by the datasheet (CO gas sensor, 2010). The sensor generates a small electric current which is converted into sensor output voltage by an op-amp/resistor combination circuit. Hence, a low power consumption amplifier AD708 has been used in the circuit design. And the current consumption of the CO gas sensor circuit is 4mA when it works in active mode. The current consumption is dropped to 1 μ A when the sensor steps into sleep mode.

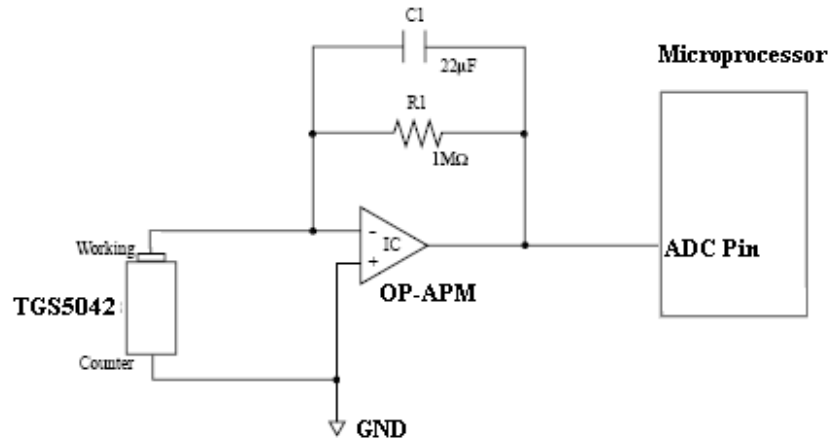


Figure 8.4 CO gas sensor circuit

8.4 Power supply subsystem

The power supply is a crucial component for wireless sensor nodes which determines the lifetime of the system. In most of the case, a battery is used as the power source. When selecting a battery for powering a sensor node, a number of factors should be considered.

- Average current consumption of the sensor node: this is the most significant factor that affects the choice of the battery. As the current drawn from the battery varies depending on the state of the wireless sensor node, it is necessary to determine the current consumption for each state of the system. By knowing the amount of time spent in each state, the average current consumption of the sensor node I_{average} can be calculated, as shown in Equation 8.1.

$$I_{\text{average}} = I_1 \times \frac{t_{\text{on1}}}{t_{\text{total}}} + I_2 \times \frac{t_{\text{on2}}}{t_{\text{total}}} + \dots + I_n \times \frac{t_{\text{onn}}}{t_{\text{total}}} \quad (8.1)$$

$$t_{\text{total}} = t_{\text{on1}} + t_{\text{on2}} + \dots + t_{\text{onn}}$$

where I_i ($i=1,2,\dots,n$) is the instantaneous current in the given state, t_{oni} ($i=1,2,\dots,n$) is the time spent drawing current in that status and t_{total} is the total time spent in a cycle of the state. In this thesis, the sensor node can be treated as working at two operation modes, sleep mode and active mode, for simplifying the calculation. Then Equation 8.1 can be rewritten as:

$$I_{\text{average}} = I_{\text{sleep}} \times \frac{t_{\text{sleep}}}{t_{\text{total}}} + I_{\text{active}} \times \frac{t_{\text{active}}}{t_{\text{total}}} \quad (8.2)$$

where I_{sleep} and I_{active} are the current consumption of the sensor node at sleep and active modes, respectively, and t_{sleep} and t_{active} are the total operation time during these two modes. By using a more common expression duty cycle to rewrite Equation 8.2, the average current consumption of the sensor node is

$$I_{\text{average}} = I_{\text{sleep}} \times (1 - D_{\text{active}}) + I_{\text{active}} \times D_{\text{active}} \quad (8.3)$$

where D_{active} is duty cycle of the sensor node when it works at active mode.

- Once the average current consumption has been calculated, Equation 8.4 can be used to calculate the capacity $C_{\text{battery,capacitor}}$ required to power the device over the desired battery lifetime T_{runtime} .

$$C_{\text{battery,capacitor}} = I_{\text{average}} \times T_{\text{runtime}} \quad (8.4)$$

- As mentioned in Table 5.2, there are plenty of battery technologies, which could be used. These technologies vary in price and size. As the wireless sensor nodes are low cost device, the cost of battery is another factor should be considered in the power supply subsystem design. In this application, as the sensor nodes are normally placed on the roof of a building, the size of the system is not critical. Hence, the small size of the battery is not a priority.

By considering these factors, two 1800mAh AAA batteries are employed as the power source for the sensor node. The schematic diagram and the PCB view of the sensor node are shown in Figure 8.5 and Figure 8.6, respectively.

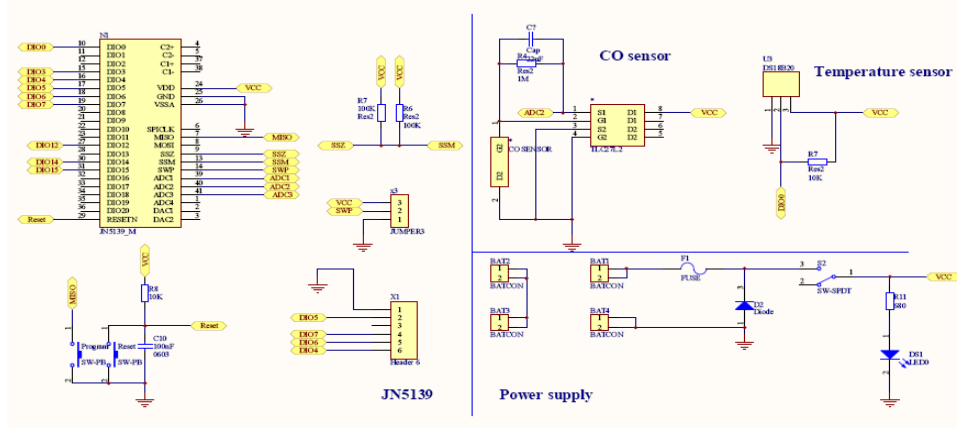


Figure 8.5 Schematic diagram of the Temperature & Co gas sensor

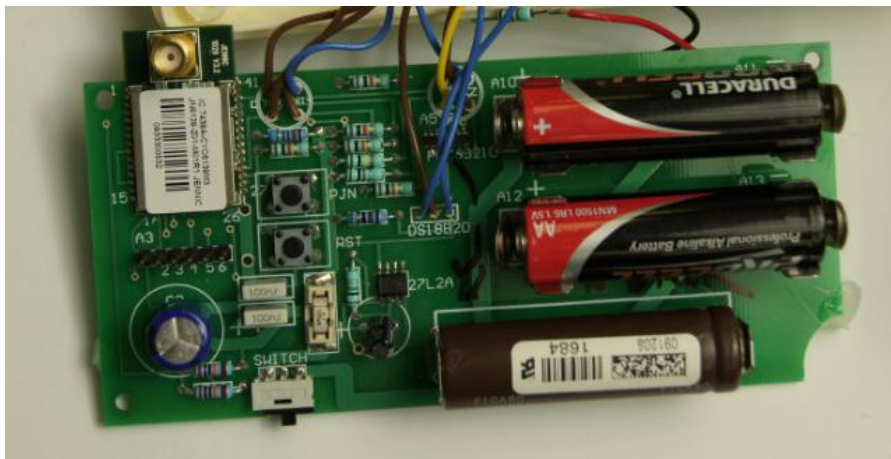


Figure 8.6 PCB view of the temperature & CO gas sensor

8.5 Lifetime calculation

Table 8.5 shows the based requirements of a typical sensor node. In order to evaluate the sensor node, the lifetime should be calculated.

Table 8.5 Specification of the door security sensor node

Priority	Description
1	System lifetime of at least 1 years
2	Minimum duty cycle: 0.05%
3	The maximum duty cycle: 100%
4	The mean duty rate of year $D_{mean}=10\%$

The current consumptions of the sensor node in active mode and sleep mode are 18mA and 0.006µA, respectively. A minimum duty cycle 0.05% is required by the sensor node. The average current consumption of the sensor node is calculated by Equation 8.3.



$$I_{average} = 18mA \cdot 0.05 + 0.006 \cdot 0.995 = 0.90597mA$$

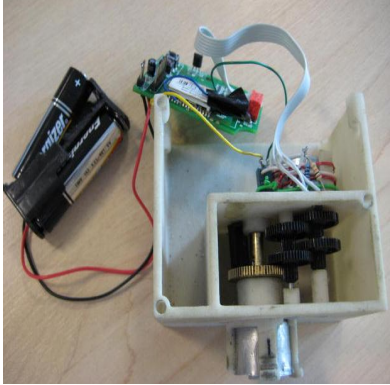




The lifetime of the system is



$$T_{runtime} = \frac{C_{battery, capacitor}}{I_{average}} = 1987\text{hours} \approx 83\text{days}$$

The lifetime of the sensor node is around 83days, which is far less than a year required by the application. Hence, a larger battery, a smart power management algorithm or an energy harvesting system should be added into the system. In this thesis, some more wireless sensor nodes for different applications have been developed, as depicted in Table 8.6. Most of them are powered by using two AAA batteries and the lifetime of them are constrained by this limited energy source. This causes some problems when these sensor nodes are used for outdoor applications.

Table 8.6 wireless sensor node designs

Name	Function	PCB board
ZigBee Enable Light Switch	Wirelessly control an electrical lamp. This is a demonstration of control a high power electrical device in a house.	
ZigBee Controller Board	This is a local controller to supply an interface for end users.	

<p>ZigBee Enabled Radiator Valve (ZBARV)</p>	<p>This device wirelessly controlled a residential radiator.</p>	
<p>ZigBee to USB adapter</p>	<p>This device is designed to link the ZigBee network to a personal computer.</p>	
<p>ZigBee to Wi-Fi adapter</p>	<p>This is a gateway board, which bridges the ZigBee network to the Internet.</p>	
<p>ZigBee Router board</p>	<p>This device is used to relay the wireless communication, when two devices are placed too far away.</p>	
<p>ZigBee sensor board</p>	<p>This device uses a temperature and a CO gas sensor to monitor environment.</p>	

Wireless based location tracking sensor node	The location tracking function is achieved by this device.	
Door security sensor node	This device monitors outdoor environment and door status	

8.6 Summary

Any energy harvesting system cannot be properly designed without knowing the characteristics of the target sensor node. In this chapter, some wireless sensor nodes without an energy harvesting system have been designed for deeply understanding the electrical characteristics of the sensor node. In order to show how to efficiently design a wireless sensor node, the temperature and CO gas sensors is selected as the case study. Then, other either types of sensor nodes have been designed and most of them are powered by the batteries. Based on the lifetime calculation, most of the systems last longer than the minimum lifetime requirement. Hence, several energy efficient efforts such as implementing a power management algorithm, using a larger capacitor battery or adding an energy harvesting system, should be considered. In the next two chapters, the door security sensor and the ZigBee Enable Radiator Valve have been selected as the target sensor nodes powered by the solar and thermal energy harvesting, respectively.

Chapter 9. Solar energy harvesting for wireless sensor nodes

9.1 Background and motivation

Solar energy is considered as the richest energy source in the environment. By comparing solar energy harvesting technology to other energy harvesting technologies, it has the most benefit and the least drawbacks for outdoor applications. Hence, solar energy harvesting becomes the most popular way of powering wireless sensor nodes in outdoor deployments.

9.2 Feature of the established system

In this chapter, a solar energy harvesting system is designed to power a wireless sensor node in a real environment. The system is designed based on the previous chapters. By determining and applying three factors of the system into the proposed theoretical model, developed in Chapter 5, the optimal size of each component of the solar energy harvesting system has been determined. By considering the MPPT based power conversion circuit and the power management subsystem, which developed in Chapters 6 and 7, a high system efficiency and nearly perpetual lifetime solar energy harvesting system has been designed. In order to evaluate the system, the proposed system has been evaluated both in the laboratory and outdoor.

9.3 System design considerations

Before designing an efficient energy harvesting system, some design considerations should be considered based on both entire system perspectives and the component perspectives. A block diagram of an energy flow of a solar energy harvesting system is shown in Figure 9.1.

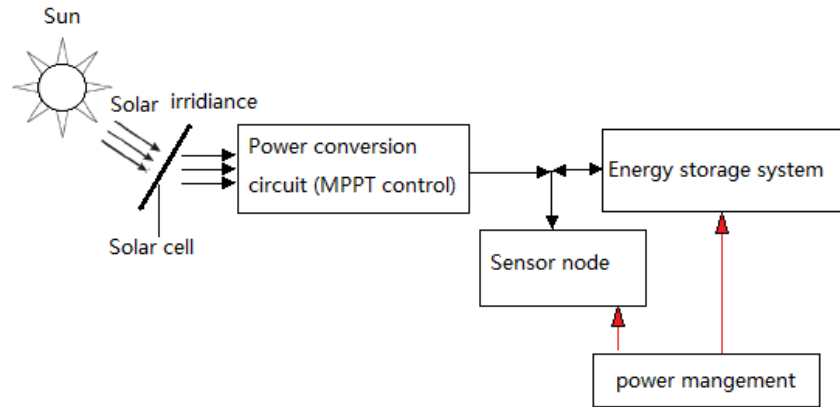


Figure 9.1 Energy flow diagram of solar energy harvesting system

In the diagram, the solar panel draws energy from the ambient environment and the harvested energy powers a sensor node through a power converter circuit, which includes an MPPT circuit to ensure the maximum power being transferred from the solar panel. This design minimizes the required size of the solar panel. The energy buffers are used to store the harvested energy when the system is placed in a sufficient light environment. At night time or when the system cannot harvest enough energy to power the system, the stored energy is drawn from the energy buffers. A power management control unit, which is used to monitor and control the energy distribution procedure, is employed to enhance the lifetime of the system. Hence, the proposed solar energy harvesting system includes the solar panel, the MPPT based power conversion circuit, the energy buffers with the power management unit and the target sensor node. According to the proposed design procedure shown in Figure 3.4, the system can be optimally sized by applying three factors of the system into the analytical model. Hence, the energy generation, the energy consumption and the power management strategy should be determined.

9.3.1 Energy storage vs. Energy generation

Normally, a simple trade-off, which is that the smaller energy storage is used when the larger energy transducer is employed, can be followed. A larger energy transducer means more system cost and on other hand a larger energy buffer means larger system size. Hence, the system designer should balance these two factors to optimize the system design. There is always an optimal balance point between these system parameters when the energy relationship between the energy generation and the energy consumption is known. Hence, in order to determine the size of the energy

harvester and the energy buffer, the energy relationship of the energy harvesting system through one year operation should be determined. The following sections show how to obtain the relationship in the real environment.

9.3.1.1 Energy dissipation of the sensor node

Normally, the energy consumption of the system can be calculated by knowing its load (sensor node), which is the main energy consumer in an energy harvesting system. In this chapter, a door security sensor node designed for an IEEE 802.15.4 based home automation system, as shown in Figure 8.3, is employed as the target sensor node to be powered by the proposed micro-scale solar energy harvesting system.

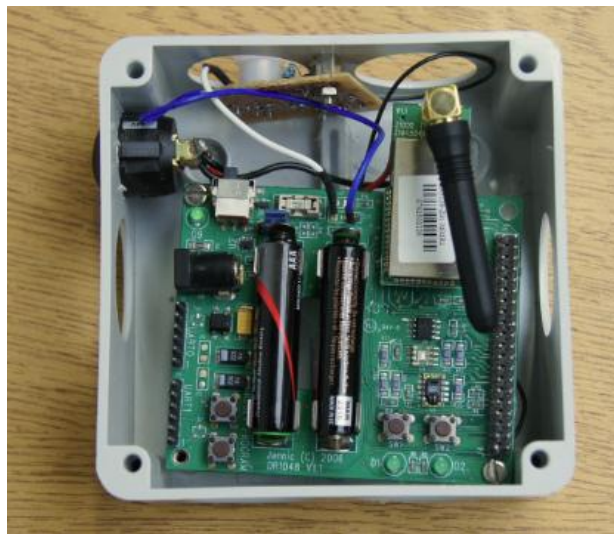


Figure 9.2 Prototype of Door security sensor node

The door security sensor is used as a micro-climate monitoring sensor for tracking outdoor environments such as light levels, temperature, humidity and door status. In order to achieve these functions, a temperature and relative humidity sensor SHT11 (SHT11, 2009), a light sensor TAOS TSL2550 (TSL2550, 2009) and a compact PIR sensor from Panasonic AMN14112 (AMN14112, 2010) are placed on the sensor layer. The Jennic 5139 wireless MCU is used to process the data and update the information through 2.4GHz wireless channel to the central controller, which determines how to control the whole home automation system. The DC current characteristics of the door security sensor node are shown in Table 9.1

Table 9.1 DC current consumptions of the components of the sensor node

Description	Current
CPU Sleep mode	0.0035mA
CPU active mode	7.41mA
Radio (Receiving mode)	37mA
Radio (Idle mode)	37mA
Radio (Transmission mode)	38mA
Temperature & Humidity sensor (Idle Mode)	3.5uA
Temperature & Humidity sensor (Sleep Mode)	0.3uA
Light sensor (active mode)	0.35mA
Light sensor (power down mode)	10uA
AMN14112 PIR sensor (Standby mode)	300uA
AMN14112 PIR sensor (detecting)	400uA

The power consumption of the sensor node can be calculated by knowing the system specification, as shown in Table 9.2.

Table 9.2 Specification of the door security sensor node

Priority	Description
1	System lifetime of at least 5 years
2	Minimum duty cycle: 0.05%
3	The maximum duty cycle: 50%
4	The mean duty rate of year $D_{mean}=10\%$

The power consumptions of the door security sensor in active mode P_{active} and sleep mode P_{sleep} are 43.5mW/s and 1.25mw/s., respectively. Based on the required

system design specification shown in Table 9.2, the duty cycle of the system D_{min} is 0.05%. Then the minimum average power consumption of the sensor node is calculated by introducing D_{min} into Equation 9.1

$$P_{average} = P_{active} \cdot D_{min} + P_{sleep} \cdot (1 - D_{min}) = 1.27mW \quad (9.1)$$

The lifetime of the sensor node is around 194 days when it is powered by 1800mAh battery. This is far shorter than the user requirement, which requires five years lifetime. Hence, using a battery as the power supply is not suitable for this application, which the battery replacement progress is very expensive and inconvenient. As this type of sensor node is normally used at outdoor, a solar energy harvesting system is considered as an ideal power replacement.

In order to calculate the power consumption of the sensor node over the course of a year, a mean duty cycle D_{mean} is introduced. By introducing $D_{mean} = 10\%$ into Equation 9.1, the average power consumption of the sensor node is 5.475mW. The energy dissipated by the sensor node in a certain month $M \in \{1, \dots, 12\}$ can be approximated by

$$E_{diss}(M) = P_{average}(\text{mean}) \cdot 24 \cdot n_{days}(M) \quad (9.2)$$

where n_{days} is the number of days in month M and the energy consumed by the sensor node can be expressed in Table 9.3.

Table 9.3 The energy consumed by the sensor node during each month of the year

Month	$E_{diss}(M)$ (mWh)
Jan	4047
Feb	3656
Mar	4047
Apr	3917
May	4047
Jun	3917
Jul	4047

Aug	4047
Sep	3917
Oct	4047
Nov	3917
Dec	4047
Total	47653

9.3.1.2 Available solar energy in a certain place

The second step of determining the energy relationship of the system is to calculate the energy available of the system through one year operation. This can be achieved by knowing the available solar energy in a certain place through a twelve month period, the solar cell's specifications and the power conversion efficiency of the MPPT approach based power conversion circuit.

As stated in previous chapters, solar energy varies significantly with the time-of-day and location of the solar cell. This is because the solar irradiance is continuously changing as a result of environmental factors such as latitude as well as the typical weather patterns at the deployment location. Moreover, the orientation to the sun and the environment temperature also affect the amount of energy that could be harvested from the environment. As the environmental factors play a crucial role in determining the harvested energy, the primary condition in deciding solar energy is the location in which the system is deployed.

By knowing the solar energy level in the certain place, the second factor to decide the harvested energy level is the solar panel's technology and its specifications. If the harvested energy from the solar panel is known, the energy availability of the system can be calculated by knowing the MPPT efficiency and the power conversion efficiency of the system. But unfortunately, the solar cell's manufacturers provide information about how much energy the panel can deliver under the defined laboratory light conditions that makes the amount of energy generated by a solar panel, when it is placed at outdoor environment, hard to be determined.

According to previous analysis, knowing the harvested energy level in a certain place and the electrical characteristics of the energy harvesting circuit are two critical

factors to determine the available energy of the system. In this chapter, a theoretical analysis model, based on previous chapters, is proposed to roughly predict the energy generation of the system. The historical solar insolation data from the solar irradiance calculator (Solar irradiance calculator, 2011) is adopted here as the input to approximate realistic solar energy level outdoor. Table 9.4 shows the average solar insolation figure, measured on a solar panel, which is set a 37° angle toward south in Loughborough, UK. The data is stated in mWh/cm^2 per month and a yearly cumulative radiation around $10.4\text{KWh}/\text{cm}^2$ is achieved in the table.

Table 9.4 Average monthly solar radiation for Loughborough, UK

Month	Daily solar radiation (mWh/cm^2)	Days in month	Monthly solar radiation (mWh/cm^2)
Jan	124	31	3844
Feb	206	28	5768
Mar	274	31	8494
Apr	357	30	10710
May	409	31	12679
Jun	405	30	12150
Jul	414	31	12834
Aug	399	31	12369
Sep	314	30	9420
Oct	240	31	7440
Nov	155	30	4650
Dec	106	31	3286
Total		365	103644

As the environment energy level is being determined, the energy conversion efficiency of the energy harvester should be obtained to calculate the harvested energy through a year in this place. In this chapter, an amorphous solar cell from Sanyo

AM5410, which has benefits of lower manufacturing costs and being produced in a variety of shapes and sizes, is employed as the solar energy harvester. According to the solar cell's simulation model, proposed in Chapter 4, the energy conversion efficiency α_{panel} is around 0.06. By introducing α_{panel} into Table 9.4, the harvested energy $E_{harvested}(M)$ in a certain month $M \in \{1, \dots, 12\}$ can be calculated as:

$$E_{harvested}(M) = \alpha_{panel} \cdot E_{solar}(M) \cdot A \quad (9.3)$$

where $E_{solar}(M)$ is the average monthly solar radiation illustrated in Table 1 and A is the effective area of the solar panel, which is around 12 cm^2 obtained from (SANY AM-5412, 2008).

Furthermore, in order to calculate the available energy of the system, the MPPT efficiency and the power conversion efficiency should be determined. Based on Chapter 5, the enhanced P&O MPPT technology based power conversion circuit, which has the most efficient in the rapidly changed environment, is adopted here to enhance the system efficiency. Based on the experimental results taken at the laboratory, the conversion efficiency of the circuit is around 71.8%, as mentioned in Chapter 6. By considering the worst case at outdoor, 70% conversion efficiency is employed in this chapter to calculate the energy generation of the system during a year. By applying these parameter in the proposed solar energy harvesting model, The energy generation of the system $E_{s-a}(M)$ in a certain month can be predicted as

$$E_{available}(M) = E_{harvested}(M) \cdot \eta_{MPPT} \cdot \eta_{converter} \quad (9.4)$$

By introducing the parameters, listed in Table 9.4, into Equations 9.3 and 9.4, the harvested energy and the energy generation of the system by using the single solar panel can be calculated. The results list in Table 9.5.

Table 9.5 The harvested energy and the available energy of the system in a certain month by using a single solar panel

Month	$E_{harvested}(M)$ (mWh)	$E_{available}(M)$ (mWh)
Jan	2767	1937
Feb	4383	3068
Mar	6455	4519
Apr	8139	5697

May	9636	6745
Jun	9234	6464
Jul	9754	6829
Aug	9400	6580
Sep	7159	5011
Oct	5654	3958
Nov	3534	2474
Dec	2497	1748
Total	78612	55028

9.3.1.3 Determining the energy relationship of the system

After calculating the total energy consumption and the energy generation of the system over a year, the energy relationship of the system can be created by knowing the power management strategy of the system. As introduced in previous chapters, the power management strategy in this thesis is to balance the energy usage and energy generation. The roughly calculation of the energy difference between these two factors can be expressed as:

$$E_t(M) = E_{available}(M) - E_{diss}(M) \quad (9.5)$$

Table 9.6 The comparison results of energy consumption and energy generation through a year by using a single solar panel

Month	$E_t(M)$ (mWh)	$E_{diss}(M)$ (mWh)	$E_{available}(M)$ (mWh)
Jan	-2110	4047	1937
Feb	-588	3656	3068
Mar	472	4047	4519
Apr	1780	3917	5697
May	2698	4047	6745
Jun	2547	3917	6464

Jul	2782	4047	6829
Aug	2533	4047	6580
Sep	1094	3917	5011
Oct	-89	4047	3958
Nov	-1170	3917	2474
Dec	-2299	4047	1748
Total	9760	47653	55028

By introducing Tables 9.3 and 9.5 into Equation 9.5, the energy difference between the energy consumption and the energy generation is obtained, as shown in Table 9.6. The excess 9760mWh energy can be calculated by comparing the total energy generated and the total energy consumed over a year. This means that a single solar panel can supply enough energy to power the system over a year. As the solar energy heavily varies over the year, the energy relationship may not be the same in these months. Hence, the comparison should take place at each month. By calculating the energy relationship in each month, the energy harvesting system cannot supply enough energy to power the system in five months in Loughborough, which are October, November, December, January and February. When the system operates in these five months, the system dissipated more energy than the energy generation and the energy shortage is compensated by the rechargeable battery. According to the calculation, 3495mWh energy shortage can be obtained by accumulating the energy shortages in these five months. In order to maintain the system working through these months, the minimum 4992mWh energy should be pre-stored in the rechargeable battery by considering 70% charging and discharging efficiency. On the other hand, for the remaining months, the energy generation is much bigger than the energy dissipation of the system. The excess energy stored in the rechargeable battery to cover the energy shortage of those five months. By calculation, the accumulated excess energy is 13906mWh through a year and the total 9734mWh energy can be stored in the battery by calculating with 70% charging efficiency. Based on the calculation, if the deficit energy during the cold months can be compensated by the energy stored in the battery at times when the system harvested more energy than it spent, the system can be seen as having a perpetual lifetime. By considering the self-discharging rate of the

battery, a much larger capacitance battery should be used. In this case, the minimum 5000mWh should be used.

As the battery dominates the primary part of the system volume, a larger battery being used means that the system size is being increased. This is not suitable for a micro energy harvesting system application. On the other hand, the energy deficit of the system can be reduced by using a larger solar panel. If a larger solar panel is used, the energy shortage of the year is reduced and small rechargeable battery could be used. Based on this point of view, a larger solar panel is considered in this application to reduce the size of the rechargeable battery. By calculating if two solar panels, which are connected in parallel, are used by the solar energy harvesting system, the energy relationship of the system can be rewritten, as shown in Table 9.7. In the table, the energy shortage can be found only in December and January, which total 724mWh energy deficit is calculated. By considering the charging/discharging efficiency and self-discharge rate of the NiMH battery, an initially 900mWh energy pre-stored on the batteries could cover the energy shortage. On the other hand, 62403mWh energy excess during a one year operation is calculated. Hence, a significantly larger battery should be used to store the excess energy making the system not waste energy. As the power management strategy, developed in Chapter 7, being used in this design, the power consumption of the system can be enhanced when the sufficient solar energy is harvested. By assuming the system is operated with a 50% duty cycle through a year, the total energy consumption is 84990mWh. By comparing this with the energy generation of the system, 17691mWh energy is excess through one year's operation. By considering the charging/discharging efficiencies of the super-capacitor and rechargeable battery respectively, two 1200mAh NiMH rechargeable batteries with 900mWh initial energy can satisfy the system requirements.

Table 9.7 The comparison results by using two solar panels

Month	$E_t(M)$ (mWh)	$E_{diss}(M)$ (mWh)	$E_{available}(M)$ (mWh)
Jan	-173	4047	3874
Feb	2823	3656	6136
Mar	5519	4047	9038
Apr	8143	3917	11394

May	10233	4047	13490
Jun	9767	3917	12928
Jul	10407	4047	13658
Aug	9883	4047	13160
Sep	6693	3917	10022
Oct	4331	4047	7916
Nov	421	3917	4948
Dec	-551	4047	3496
Total	62403	47653	55028

9.4 System design and implementation

Once the sizes of the solar panel and the rechargeable battery have been dimensioned, other components of the system can be determined. Based on the previous chapters, the system performance is substantially increased by applying both an MPPT based power conversion circuit and a power management subsystem. In this chapter, these two proposed works have been adopted. The schematic diagram of the solar energy harvesting system is depicted in Figure 9.3, which includes two solar cells, the enhanced MPPT based power conversion circuit, the power management subsystem and the sensor node.

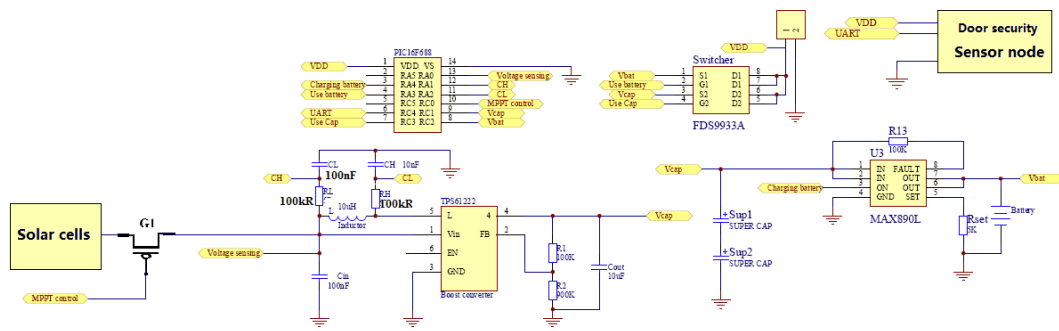


Figure 9.3 Schematic diagram of the solar energy harvesting system

9.4.1 Energy harvester

The energy harvester consists of two amorphous solar cells, which are connected in parallel, to harvest solar energy outdoor. In order to make the solar panels harvest as much solar energy as possible, the orientation and the facing angle of the solar panels are critical. Based on results shown in the solar irradiance calculator (2011), if the solar panel is set at a 37° angle in a Southward direction in Loughborough, it can harvest the maximum solar energy during a year. Hence, this setting has been adopted in thesis, as shown in Figure 9.4.

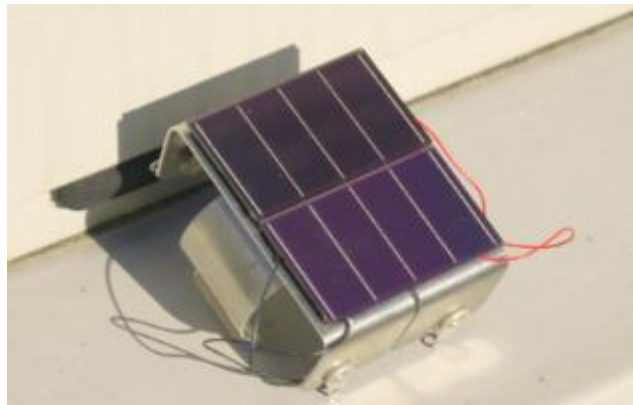


Figure 9.4 Solar cells design

9.4.2 MPPT based power conversion subsystem

For a long-term remote control application, the micro-scale energy harvesting system needs a high efficient and reliable power conversion system to harness the harvested energy in different situations. As the ultra-lower power is generated by the micro energy harvester during days with the weak light irradiations, the power conversion circuit should have low power consumption, simple circuitry, and high

efficiency. By considering the MPPT technologies listed in Chapter 6, the digital methods are strongly preferred due to the proliferation of low-power MCU and programmable logic devices. By comparing the system efficiency when the system is placed at the rapidly changed environment, the enhanced P&O MPPT method has the highest system efficiency. Hence, this type of MPPT approach has been selected to track the MPP of the solar panel in this work. As the same multifunction MCU PIC16F688 is used in both the power conversion subsystem and the power management subsystem, the complexity of the circuit and the power overhead of the system can be reduced by integrating all these functions into the one MCU.

9.4.3 Power management subsystem

As stated in Chapter 7, the main functions of a power management subsystem for an energy harvesting system should have:

- An intelligent distribution capability to increase the energy buffering efficiency and the energy usage efficiency,
- A battery care function, which can prevent over-charge and over-discharge, to maximize the lifecycle of the rechargeable battery,
- A monitoring function, which could reports the current information of the energy buffers,
- And a power management function, which can achieve the energy neutral operation and maximize the system performance based on a real-time energy relationship,

Based on these functions, the power management subsystem, developed in Chapter 7, is adopted here. A 24 hour window size and a 10 minute time slot are selected in the power management algorithm. By considering the maximum and the minimum power consumptions of the system in relation with the energy generation, the parameters of the algorithm are listed in Table 9.8.

Table 9.8 The parameters for the solar power management algorithm

Algorithm Parameters					
$V_{B,th1} = 2.2V$	D_{max} = 50%	D_{min} = 0.05%	$\Delta D_1 = 5\%$	$\Delta D_2 = 1\%$	$\Delta D_3 = 0.01\%$
$V_{B,th2} = 2.9V$					
$V_{b,th3} = 2.7V$					

When the time period of each time slot and the maximum power consumption of the system are determined, the minimum capacitance of the super-capacitor can be calculated by using Equations 7.2 and 7.3. The results are shown in Equations 9.6 and 9.7.

$$E_{system(maximum)} = \frac{(22.38 + 0.6)mW}{s} \times 600s = 13.788W \quad (9.6)$$

$$C_{min} = \frac{2 \times E_{system(maximum)}}{V_{w,th3}^2 - V_{w,th4}^2} = 4.27F \quad (9.7)$$

Based on the calculation, the minimum 4.27F super-capacitor should be used to maintain it at one status at each time slot. By considering the energy leakage and charging/discharging efficiency of the system in relation with the system size and efficiency, two 22F super-capacitors connected in series are used in this work as the primary energy buffer.

9.4.4 Energy consumer

As stated in previous sections, the door security sensor is employed as the target sensor node in this chapter.

9.5 System Evaluation

In this section, the solar energy harvesting system has been evaluated in both the laboratory and outdoors. The integrated system is shown in Figure 9.5.

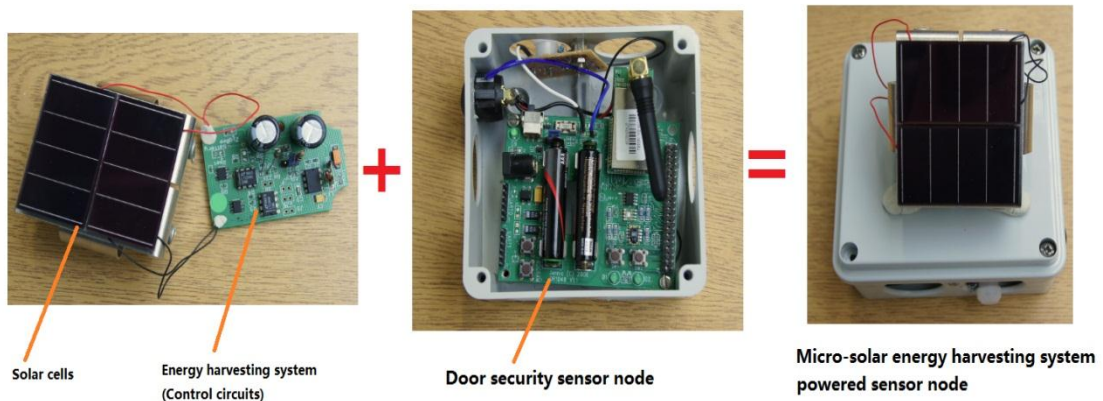


Figure 9.5 Micro-scale solar energy harvesting system powered door security sensor node

Since the performance of a solar energy harvesting system is extremely dependent on solar irradiance levels, weather conditions, dust and temperatures, which are hard to predict in outdoor conditions, the proposed energy harvesting system should be evaluated in the laboratory before the system is deployed in the real environment. A high power adjustable halogen lamp is used to produce a reproducible and controllable light source in the laboratory. An indoor experimental test setup has been developed by using a simple Zigbee based wireless network, which includes a network coordinator and an end device, as shown in Figure 9.6. In the network, a USB based sensor node has been configured as the network coordinator, which is designed to establish the wireless network. It has been connected to a laptop through USB port to display the obtained data from the end device. In this scenario, the solar powered door security sensor node has been employed as the end device, which gathers the environment data and sends to the coordinator. In order to make the experimental repeatable, the battery, the super-capacitor and the duty cycle of the sensor node are set at 2.7V, 0V and 10%, when the system is initialized. In order to emulate the diurnal characteristic of the solar energy, the system is illuminated by the desk lamp for 12 hours per day and the system keeps running without light in the rest of 12 hours. For further distinguishing the light levels of the day, four different light input levels, which are 50Klx, 35Klx, 10Klx, and 8Klx, are used to irradiate the solar panels for three hours at each testing day. The system has been tested for five days. The experimental results are depicted in Figure 9.7 (a) and (b).

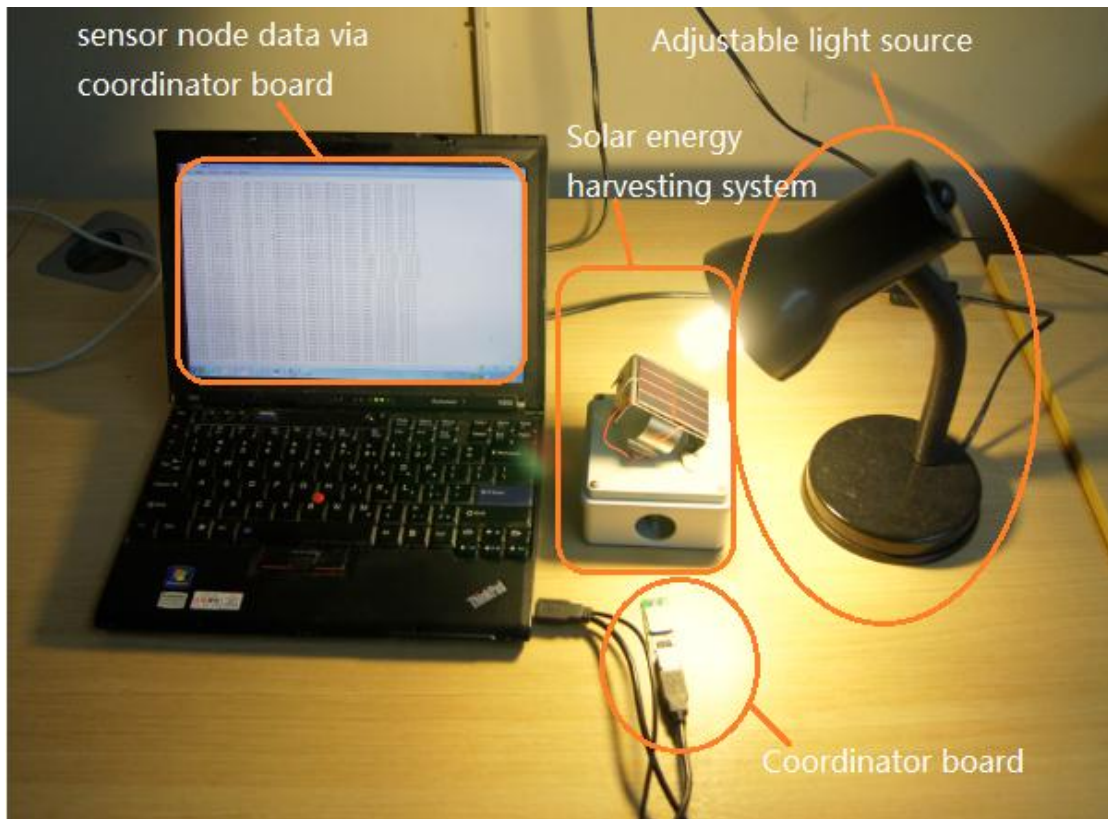


Figure 9.6 Indoor experimental test setup

Figure 9.7 (a) shows the terminal battery voltages of each time-slot during the five day test. All the data generated in the graph is sampled by the on-board ADC pins. Taking a close look at the graph, throughout the night, the batteries are drained and the battery voltage drops, and during the day time, the system charges the batteries when the energy generation is higher than the energy consumption. The energy neutral operation can be observed that the terminal battery voltage at the end of each test day is maintained around 2.7V, which is equal to the initial battery voltage. The corresponding duty cycle of the sensor node is depicted in Figure 9.7 (b). It can be observed that the duty cycle is adapted with the energy budget of the system. By using strong light to irradiate the solar cells, the sensor node increases its duty cycle rapidly in order to adapt to the energy generation. During the night, or if insufficient energy can be harvested, the sensor node reduces its duty cycle. During the five day test, the mean duty cycle of the sensor node is 24.9%, which is higher than 10% duty cycle requirement, mentioned in Table 9.2. It can be seen that the system performance is highly improved by using the solar energy harvesting system in relation with the power management algorithm.

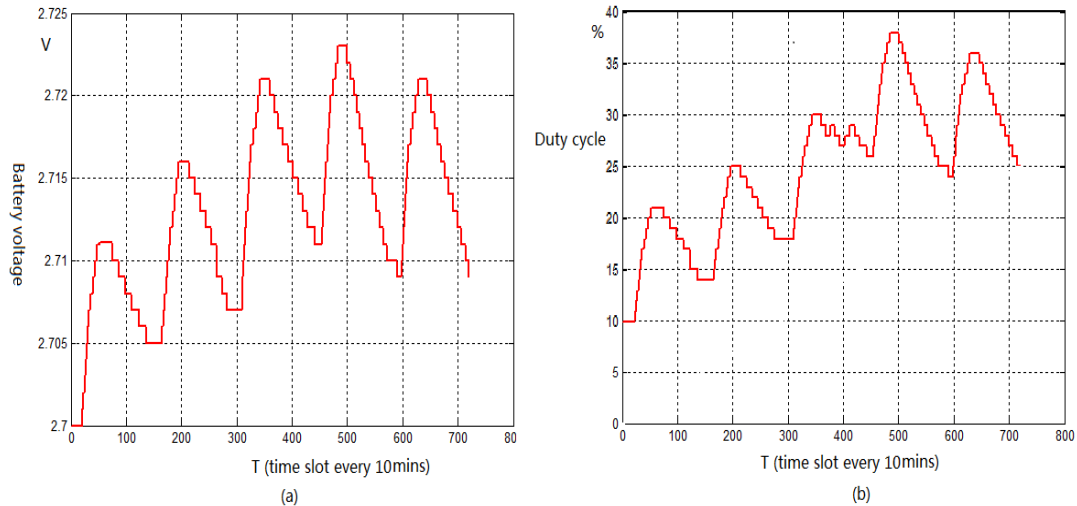


Figure 9.7 Five day indoor stress test

Because the main design criterion of the solar energy harvesting system is that the system can last through the limited solar radiation months, the time of the outdoor experiment has been chosen to be the dark period of the year at the given location. If the system could keep running during this month, it could survive for the rest of months and the lifetime of the system could be considered as everlasting. Based on the Table 9.4, December is the darkest month in Loughborough and the experiment is to examine if the proposed system that could survive in this month. Hence, the hybrid solar energy harvesting system has been deployed on the campus in Loughborough, UK, in December, 2010, as shown in Figure 9.8. The same wireless network, set at the laboratory, is used here to record the experimental data. According to the previous analysis, 800mWh energy pre-stored in the rechargeable batteries can cover the energy deficit during the coldest months of a year. By considering the energy lost and the charging and discharging efficiency, a much higher energy is pre-stored in the batteries. According to the battery model, described in Chapter 5, when 900mWh energy is stored on the battery, the terminal voltage of the two series connected 800mAh rechargeable batteries is 2.64V. Hence, the battery pack has been initially charged to 2.7V before the experiment has been held. The solar panel has been set at a 37° angle towards the south and a 10% initial duty cycle of the sensor node has been set by the system. The super-capacitors have been charged from the depleted condition when the solar energy was harvested by the solar panels. In order to observe and predict the system lifetime, the energy levels of the energy buffers in relation with the

duty cycle of the sensor node have been packed into the sensor data, which has been reported to the local server through a 2.4GHz wireless channel.

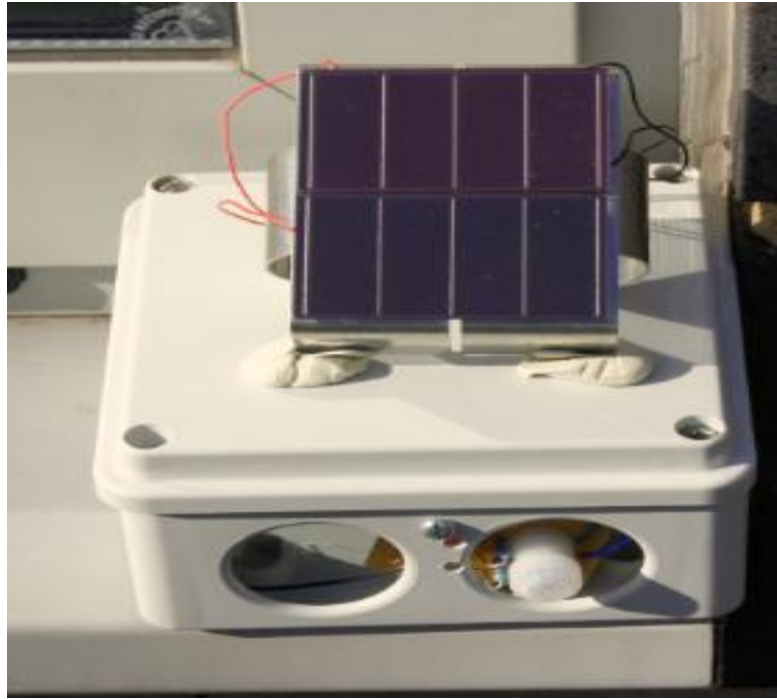


Figure 9.8 Depiction of the experimental setup at the deployment site

The 30 day measurement results are shown in Figure 9.9 (a) and (b), which the terminal voltages of the batteries in each hour are depicted in Figure 9.9 (a) and the duty cycle of the sensor node is recorded in Figure 9.9 (b). As it can be seen, the system has a periodical behaviour, in which the battery voltage increases at the day time and drops at night, mostly determined by the daily cycle of available solar irradiance levels. Because of using the adaptive power management algorithm, the sensor node's duty cycle is adapting with the residual battery energy level and energy relationship between the energy consumption and energy generation. The adaptive duty cycle of the sensor node is depicted in Figure 9.9 (b), which can be observed that the duty cycle is increased with the increasing battery voltage and it is decreased when a lower trend is detected. The recorded mean duty cycle is 2.9% through the 30 day experiment that is much smaller than the 10% duty cycle requirement. But according to the experiment taken at the laboratory, the mean duty cycle of the sensor node could be increased when the sufficient environment energy could be harvested. Hence, the minimum mean duty cycle of 10% through a year could be easily achieved by adapting a much higher duty cycle during the rest of months. After 30 days test, the terminal battery voltage has been recorded at 2.702V, which is almost equal to the

initial battery voltage 2.7V. This indicates that the solar energy powered door security sensor node could maintain the energy neutral operation during the darkest month and the lifetime of the system could be seen as eternal by neglecting the hardware lifespan.

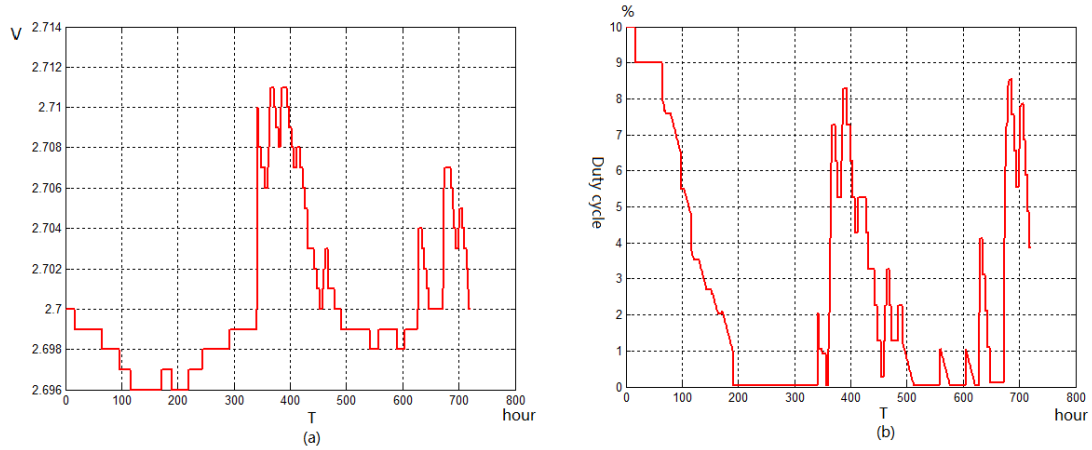


Figure 9.9 30 days outdoor testing

9.6 Summary

In this chapter, an efficient micro-scale solar energy harvesting system has been developed based on the previous chapters. The analysis model has been designed to determine the energy relationship of the solar energy harvesting system. Based on the energy relationship in relation with the energy harvesting design procedure, the sizes of the solar panel and the energy buffers are determined. In this work, the door security sensor node, whose lifetime is heavily restricted by the battery volume, has been chosen as the target sensor node to be powered by the solar energy harvesting system. By equipping the enhanced MPPT technology based power conversion circuit in relation with the power management unit, the energy efficiency and the performance of the system are significantly enhanced.

The proposed system has been evaluated in the laboratory before the system was implemented in a real environment. The experimental results show that the system can adapt its duty cycle to its energy generation. Then the system has been tested in the darkest month outside of the laboratory for 30 days to examine its performance. The experimental results show that the system works as expected and the lifetime of the system is as long as the lifetime of the hardware, which could be seen as eternal.

Chapter 10. Thermal energy harvesting for Wireless sensor nodes

10.1 Background and motivations

Similar to solar energy, heat is another major energy source which can be harvested from the environment. Normally, heat sources can take on many different forms, including hot surfaces such as radiators furnaces, exhaust gases, sunlight and even the human body. Recent developments on Thermoelectric (TE) materials have led to renewed interest in TE generator designs. There are two reasons to develop a thermal energy harvesting system in this thesis. Firstly, numerous investigations and some successful applications of thermal energy harvesting systems have been developed. But the efficiency, cost, size and lifetime of the systems are not satisfying the requirements of the sensor nodes. The situation becomes worse when a micro-scale thermal energy harvester is used. Secondly, the solar energy harvesting system based on the proposed system architecture and the design procedure has been developed in Chapter 9. In order to verify the proposed architecture and works, which can be easily expanded to other type of applications, the thermal energy harvesting system based on the same architecture and design procedure is developed.

10.2 Feature of the proposed system

Normally, a permanent energy harvesting system with high energy efficiency and a simple and compact construction is considered an ideal battery replacement for wireless sensor nodes. In this chapter, an efficient thermal energy harvesting system has been designed to power a wireless sensor node. The following contributions have been carried out:

- Based on the proposed system design procedure, a theoretical analytical model of a thermal energy harvesting system is established in order to optimize the sizes of thermal energy transducer and the energy buffers.
- Because of the low energy efficiency of the system, the proposed system enhances its energy efficiency by four parts: (1) Designing a TE generator to increase the energy conversion efficiency, (2) Using an MPPT technology based power conversion circuit to improve the energy transfer efficiency, (3) Employing a multiple energy buffer design to increase the buffering efficiency, and (4) Developing a power management algorithm to improve the energy consumption efficiency. The proposed works and efforts, described in previous chapters, are employed and verified in this chapter.
- The developed thermal energy harvesting system is used to replace the batteries to power a ZigBee based automatic radiator valve (ZBARV). The system is evaluated both in the laboratory and the real environment. The experimental results show that the system can survive for a long period operation without any human intervention.

10.3 System design considerations

Similar to the solar energy harvesting system design, the proposed thermal energy harvesting system is based on the same system architecture and design procedure. Three groups of the system parameters, which are listed below, are determined before knowing the energy relationship between the energy generation and the energy consumption of the system.

- Determining the energy consumption of the target sensor node
- Determining the characteristics of the energy source and the energy harvesting technology being used
- Determining the energy generation of the system when it is placed at the target environment

10.3.1 Energy consumption of the target sensor node

As stated in Chapter 9, the specification and electrical characteristics of the sensor node are used to decide the energy consumption of the system. In this chapter a practical wireless home automation application, a ZBARV, is employed as the target sensor node, as illustrated in Figure 10.1. It is used as the wireless temperature controller, which adjusts the room temperature by turning on/off the radiator. The command signals are sent by a local controller through a 2.4GHz wireless channel. The ZBARV sensor node provides two basic functions, which are adjusting the radiator based on the command sent by the local controller and measuring the room temperature and reporting it to the local controller. Hence, a SHT11 temperature sensor is used to measure the room temperature and a stepper motor connected to the rotary knob of the radiator is designed to adjust it.

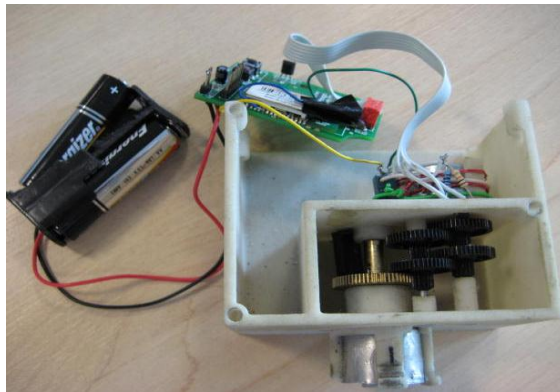


Figure 10.1 ZBARV sensor node

On board, a JN5139 wireless MCU is used as a control and communication microprocessor of the sensor node. The DC electrical characteristics of the ZBARV and the general system specification are described in Tables 10.1 and 10.2, respectively.

Table 10.1 DC current consumption of the ZBARV sensor node

Description	Current
CPU Sleep mode	3.5uA
CPU active mode	7.41
Radio (Receiving mode)	37
Radio (Idle mode)	37
Radio (Transmission mode)	38
Temperature & Humidity sensor (Active mode)	0.55mA
Temperature & Humidity sensor (Idle Mode)	3.5uA
Temperature & Humidity sensor (Sleep Mode)	0.3uA
Step motor	50mA
Step motor (sleep)	3uA

Table 10.2 General system specification of ZBARV sensor node

Priority	Description
1	System lifetime of at least 3 years
2	<p>Receive the control signal</p> <ul style="list-style-type: none"> ● The minimum duty cycle of the measuring the room temperature is 0.05% ● The minimum step motor working duration is 15 seconds per 30 minutes (duty rate is 0.83%) ● The maximum duty cycle for controlling step motor is 20%
3	<p>Receive switch off signal</p> <ul style="list-style-type: none"> ● Monitoring the room temperature at least every 30 minutes and sending the sensor reading to the local controller

- | | |
|--|---|
| | <ul style="list-style-type: none"> ● The maximum duty cycle is 20% |
|--|---|

As two functions, the temperature measurement and the temperature adjustment, have been achieved by the sensor node, respectively, the power consumptions of the sensor node at these two conditions are different. In the first condition, if no control signal has been received from the local controller, the sensor node just samples the room temperature by using the temperature sensor in every 30 minutes. The power consumption of the sensor node in active mode and sleep mode are 28.67mW and 21.45 μW . The average power consumption $P_{average}(1)$ can be calculated by introducing the minimum duty cycle 0.05% duty cycle into Equation 10.1.

$$P_{average}(1) = 28.67mW \times 0.05\% + 0.022 \times 99.95\% = 0.23mW \quad (10.1)$$

For the second condition, the sensor node has received a control signal, which has been sent by the local controller, it regulates the motorized radiator valve until the room temperature reaches the setting one. Based on the system specification, the sensor node powers the step motor for 15 seconds in every 30 minutes and the room temperature is also monitored in this cycle. The power consumptions at active mode and sleep mode are 192mW and 21.45 μW in this condition. By introducing the minimum duty cycle 0.83% into Equation 10.2, the average power consumption of the sensor node $P_{average}(2)$ is:

$$P_{average}(2) = 192mW \times 0.83\% + 0.022 \times 99.17\% = 1.62mW \quad (10.2)$$

By only considering the sensor node, which is working at the second condition, the longevity of the sensor node is around 152 days by using two 1800mAh batteries. This is much less than the lifetime required by the system specification and the battery must be changed at least every six months, which fails to allow the sensor node to be widely used in a normal house. A thermal energy harvesting system is considered as the best way to cover the shortfall of the battery powered ZBARV sensor node.

Similar to the solar energy harvesting system, knowing the energy dissipation of the sensor node over the course of a year is essential for designing a thermal energy harvesting system. As stated in previous section, the power consumption of the ZBARV sensor node is highly dependent on the functions the sensor node achieving. And these two functions are determined by the weather conditions, particularly the

temperature of the target area and the personal preference. In order to simplify the analysis model, the personal preference of the end users is neglected in this chapter. Hence, the temperature of the target place is the critical factor in deciding whether to turn the residential radiator on or off. Figure 10.2 shows the average monthly temperature of Loughborough, UK from 2009 to 2011 (Leicester weather station, 2012).

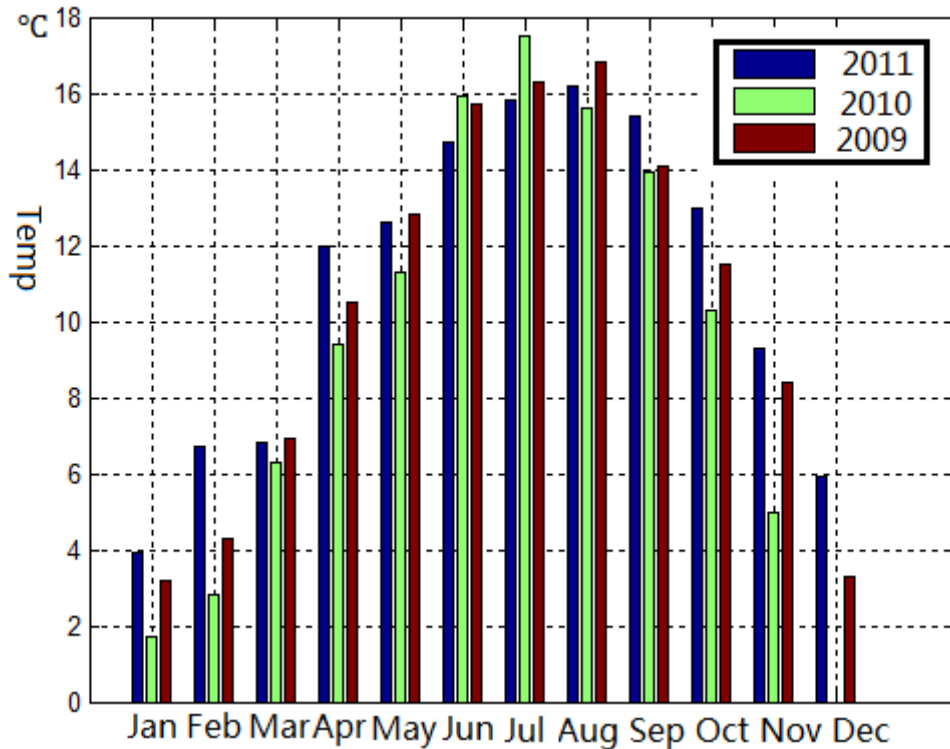


Figure 10.2 Average monthly temperature for Loughborough, UK

Based on the figure, Jun, July and August are normally the warmest months and December and January are the two coldest months in Loughborough. By assuming the house-holder turns off the central heating system when the monthly average temperature is higher than 14°C , and by examining the bar figure, based on the rule, the radiator is turned off in June, July, August and September. In these four months, the sensor node only measures the room temperature and the central heating system is turn off. The sensor node consumes $5.52\text{mW}\cdot\text{h}$ energy per day. Furthermore, if the monthly average temperature is in the range of $8^{\circ}\text{C} \leq T_{environment} < 14^{\circ}\text{C}$, it assumes that the radiator works 12 hours per day. By examining the figure, the average temperature in the months of April, May, October and November are satisfied this condition. Hence, the central heating system in a house can be assumed to operate

8 hours per day. In order to simplify the power calculation, the sensor node is assumed to adjust the radiator by using the duty cycle of 0.83% in the operation 8 hours. In the rest 16 hours the sensor node just measures the room temperature with the duty cycle of 0.05%. The energy dissipation of the sensor node is $22.2mW.h$ per day. The other four months are the coldest months in Loughborough and the radiator is assumed to work 16 hours per day. In these hours, it is assumed that the sensor node adjusts the radiator in every 30 minutes. For the rest of 8 hours, the sensor node just measures the room temperature with the duty cycle of 0.05%. Then the total energy consumption of the sensor node in these four months is $38.88mW.h$ per day. According to these assumptions, the energy consumed by the sensor node in a certain month can be approximated in Table 10.3.

Table 10.3 The energy consumed by the ZBARV sensor node during each month

Month	$E_{diss}(M)$ (W.h)
Jan	1205.28
Feb	1088.64
Mar	1205.28
Apr	666.6
May	688.2
Jun	165.6
Jul	171.12
Aug	171.12
Sep	165.6
Oct	688.2
Nov	666.6
Dec	1205.28
Total	8087.24

10.3.2 Characteristics of energy source

Determining the energy source and energy density in the environment, where the energy harvesting system is located, is the second consideration in designing an energy harvesting system. In this application, the sensor node is placed beside the radiator, which can generate tremendous thermal energy. Based on Fourier's law, a domestic hot radiator typically delivers approximately $1.4KW/m^3$ when it is heated from $21^\circ C$ to $50^\circ C$. Hence, if an energy harvesting device could harvest the thermal energy from the radiator and store the harvested energy to power the sensor node, the obstacle of the sensor node, mentioned previously, could be solved. According to the thermal law, extraction of energy from a thermal source requires a thermal gradient and the greater temperature difference the system has, the greater the thermal transfer efficiency of the system will be. In this work, a radiator is the heat source and the temperature gradient between the radiator and the ambient can be harvested by a TE generator. It is assumed that the radiator's temperature is maintained at $50^\circ C$ when it works, and the room temperature is $21^\circ C$, the thermal energy density of the radiator is $1.4KW/m^3$.

10.3.3 Energy generation characteristics

After understanding the energy source and the energy density, the energy generation of the system is determined by knowing the energy conversion efficiency of the energy harvester. In the thermal energy harvesting system, a good TE module usually plays the most important part to decide the energy conversion efficiency of the system. Hence, selecting a proper type of TE module is critical in the design of an efficient thermal energy harvesting system. Generally, TE materials and module construction of the TE modules are considered as the two primary issues in the TE module selection. In the natural world, there are many materials which can produce power from temperature differences, but they vary in cost, operation temperature and efficiency. Micropelt utilizes Bismuth(Bi), Antimony(Sb), Tellurium(Te) and Selenium(Se); all of which are compounds that have the best material properties with the operating temperature around the room temperature and up to $200^\circ C$ (Humida et al.,2009). Since the price of Bi_2Te_3 material is quite low, it is widely used in Peltier coolers and the Bi_2Te_3 module price is very cheap by comparing with other materials. Hence, this type of TE module has been chosen as the thermal energy harvester for this design. On the other hand, the module construction affects the maximum power and the

voltage/current characteristics of the TE generator. Normally, a TE module is composed of hundreds of TE elements, which are formed by P-type and N-type semiconductors, connected in series electrically and in parallel thermally between two ceramic layers. The voltage generated from the TE module is proportional to the number of elements since they are combined electrically in series. An interesting observation from (Masterbergen et al., 2005) shows that the power generated from the TE module increases as the thermoelement leg length decreases. Moreover, the test result from (Meydbray et al., 2005) illustrates that as the surface area of the TE generator increases, the power generated increases in parallel. Taking these into the considerations, a low cost Bi₂Te₃ TE module TEC1-12709 from Taicang company has been chosen as the TE module in this chapter to harvest the thermal energy radiated by the residential radiator. Assuming that a 10°C temperature difference can be maintained by both the hot side and the cold side of the TE module, a 1.2mW (0.09V) power $P_{generated}$ could be generated by using the simulation model proposed in Chapter 4. As the generated voltage (0.09V), which is significantly lower than the minimum start-up voltage 0.7V of the boost converter, 8 pieces of the TE modules connected in series should be used to increase the generated voltage. According to the simulation results shown in Chapter 5, the conversion efficiency of the boost converter circuit is around 68.8%. By assuming 90% MPPT efficiency of the MPPT circuit in the power conversion circuit and applying these parameters in the thermal energy harvesting model, proposed in Chapter 5, the total power transfer efficiency of the system is 61.92%. By considering the error of the model, a 55% conversion efficiency $\eta_{conversion}$ is used to calculate the energy generation of the system. It assumed the system works at this situation for one hour, the energy generated by the thermal energy harvesting system is:

$$E_{TE-a} = \eta_{conversion} \cdot P_{generated} \cdot T = 5.76mW.h$$

where T is one hour duration. According to the radiator operation assumptions, mentioned in the previous section, the energy generated in each month is listed in Table 10.4.

Table 10.4 The harvested energy and the available energy of the system in a certain month by using 8 pieces of the TE modules.

Month	$E_{TE-a}(M)$ (mW.h)
Jan	4285.44
Feb	3870.72
Mar	4285.44
Apr	2073.6
May	2142.72
Jun	0
Jul	0
Aug	0
Sep	0
Oct	2142.72
Nov	2073.6
Dec	4285.44
Total	25159.68

10.3.4 Energy and energy generation

As stated in Chapter 9, the volume of the energy storage elements can be determined by comparing the energy generation and the energy dissipation of the system. The comparison result is shown in Table 10.5. According to the comparison result, 17072.44mW.h energy slops over the energy consumption through one year period. This means that the thermal energy harvesting system with proper energy storage elements can harvest enough energy to power the sensor node. Based on the table, the energy deficit can be found in June, July, August and September, when the radiator is totally turned off and the total 761.28mW.h energy shortage is accumulated in these four months. By considering discharging efficiency and self-discharging rate of the NiMH battery, the energy deficit can be covered by storing 1200mW.h energy in the rechargeable battery before the system is used. The energy generation is greater

than the energy dissipation of the system in the other eight months and the excess energy will be stored in the battery. By considering the power management unit, the power consumption of the system will be adapted according to the energy budget of the system. If the system is working at the maximum duty cycle (20%) in these eight months, the power consumptions of the sensor node are 38.42mW and 5.75mW when it works at adjusting room temperature and measuring temperature modes, respectively. Then the total energy consumption of the sensor node in these eight months is 175313mW.h, which is higher than the total energy excess in a year (17072mW.h). Hence, the capacitance of the battery is only dependent on the energy deficit. By considering the charging and discharging efficiency in relation to the self-discharge rate of the energy buffers, a 1200mAh NiMH rechargeable battery, which has initially been stored 1200mW.h energy, can satisfy the system working at any situation.

Table 10.5 The energy consumed by the ZBARV sensor node during each month

Month	Energy difference (mW.h)	$E_{diss}(M)$ mean (mW.h)	$E_{TE-a}(M)$ (mWh)
Jan	3080.16	1205.28	4285.44
Feb	2782.08	1088.64	3870.72
Mar	3080.16	1205.28	4285.44
Apr	1407	666.6	2073.6
May	1454.52	688.2	2142.72
Jun	-165.6	165.6	0
Jul	-171.12	171.12	0
Aug	-171.12	171.12	0
Sep	-165.6	165.6	0
Oct	1454.52	688.2	2142.72
Nov	667.2	666.6	2073.6

Dec	3080.16	1205.28	4285.44
Total	17072.44	8087.24	25159.68

10.4 System design and implementation

After determining the sizes of the energy harvester and the rechargeable batteries, the rest of the system can be designed. Figure 10.3 shows the scenario diagram of the thermal energy harvesting system. The hot water is assumed to flow from side A to side B and the motorized valve is installed on side A to control the water flow rate. The radiator emits a large amount of thermal energy when the valve is open and the temperature gradient between the TE modules can be harvested and transferred into electrical energy, which is being stored in the energy buffer to drive the sensor node.

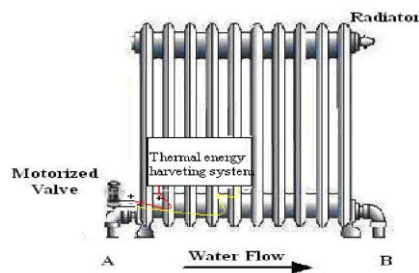


Figure 10.3 A scenario diagram of TE generator

By considering all aspects of ambient power sources in the light of the special characteristics of ZBARV, the thermal energy harvesting system has been designed. Figure 10.4 shows the general architecture of the thermal energy harvesting system powered ZBARV system, which is composed of four subsystems: the thermal energy generator, the MPPT based power conversion subsystem, the power management subsystem and the ZBARV sensor node. The thermal energy generator harvests thermal energy and converts it into electrical energy, which is delivered to the MPPT based power conversion subsystem. The output voltage of the conversion circuit is maintained around 5V, which is used to charge the energy buffers when there is extra energy available on the system. The power management unit is used to manage the energy generation and the energy consumption of the system. Energy neutral operation and maximizing the system performance are considered as two basic functions that should be achieved by the power management unit. The ZBARV sensor

node is the end device of the system which consumes most of the harvested energy. By comparing the thermal energy harvesting system with the solar energy harvesting system, the energy efficiency of the thermal energy harvesting system is much lower than the solar one. Hence, some efficient ways to improve the system efficiency are considered in this chapter. The details are given in the following sections.

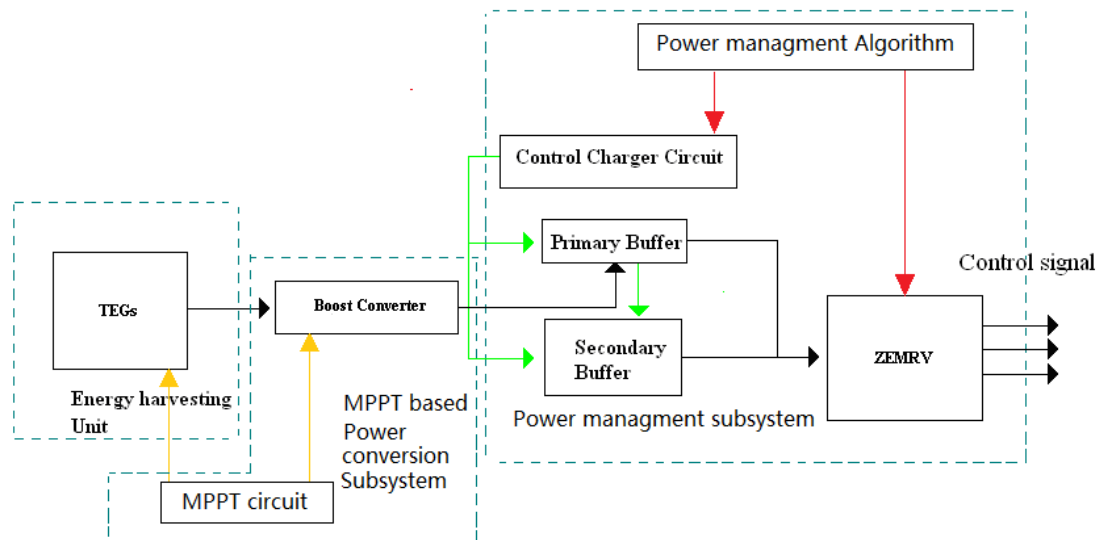


Figure 10.4 Function diagram of a Thermal Energy Harvesting System

10.4.1 Thermal energy harvesting subsystem

Since the thermal energy harvesting efficiency is a critical factor that constrains the use of any thermal energy harvesting system, a highly efficient thermal energy generator is the basic requirement for a successful energy harvesting system design. As stated in the previous parts, the conversion efficiency of the TE generator is dependent on the efficiency of the TE module and the thermal energy passing through the modules. Hence, the performance of a TE generator can be enhanced by increasing the TE material capability, maintaining a large temperature difference across the TE module and producing high thermal flows through the generator. Bi₂Te₃ TE module TEC1-12709 is employed as the thermal energy transducer. The physical properties of the TE module are shown in Table 10.6.

Table 10.6 Physical properties of the TE module

Parameter	Value
Dimensions (W × L × H)	40 × 40 × 3.2mm
Maximum temperature difference	77Kelvin
Number of thermocouple junctions	127
Device resistance	3.78 ohms
Resistivity	1.37 ohm cm

The temperature difference and the thermal flow are two critical factors. Based on Chapter 4, the temperature difference across the module is a significant factor in determining the efficiency of the entire harvesting system. In an environment in which a huge thermal gradient is present, the whole harvesting efficiency is raised while it drops where there are only small temperature differences. In order to maintain a large temperature difference across the module, a hot side heat exchanger and efficient heat dissipation on the cold side of the TE generator are needed. A good thermal conductor material such as metal is considered as an ideal heat exchanger for heat transfer. On the hot side of the module, a piece of aluminum plate has been chosen as the hot side heat exchanger. On the cooling side, because heat transfer is limited by air-cooling, a high efficiency heat sink is needed. A schematic diagram (Figure 10.5) shows the layout of the thermal energy harvesting subsystem.

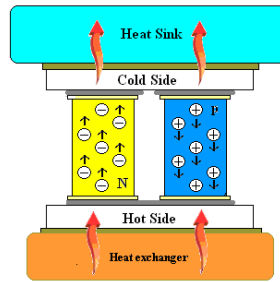


Figure 10.5 Thermal Energy Harvesting Subsystem

In order to choose a highly efficient heat sink as the cold side heat dissipation device, three types of heat sinks: a copper heat sink, an aluminum heat sink and a heat pipe type heat sink are compared in this chapter. To test the heat transfer efficiency, the same TE module is attached to three different types of heat sinks and tested in a similar environment where the room temperature is 20°C. The results of the experiments are summarized in Figure 10.6. From the graph it can be seen that the generated voltage of the TE module for the three different heat sinks varies, because the heat sink's ability to remove heat from the cold side varies. The heat pipe type heat sink is the most efficient one. Therefore, an Auras's 3 Heat pipes (Aura 3U heat sink, 2007) heat sink has been employed as the cold side heat sink.

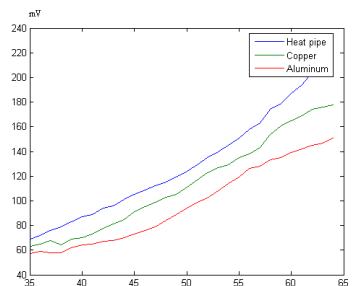


Figure 10.6 The comparison result of three Heat sinks

Furthermore, as shown in Chapter 4, the ambient air temperature around the heat sink is a crucial factor affecting the heat conductivity of the heat sink. There are three ways to reduce the temperature of the air surrounding the heat sink, which are considered in this chapter. When the heat sink is close to the heat source, the temperature of the air around the heat sink is higher. This reduces the heat transfer capability of the heat sink. Thus, the first way to enhance the efficiency of the heat sink is to increase the distance between the heat source and the heat sink. For this reason, in this design, a number of TE modules are attached together in a single stack and this has been used to increase this distance. To determine the capability, five

different TE module configurations have been tested and the experimental result output for each configuration is shown in Table 10.7. The temperature gradient between the heat source and heat sink is divided over each TE module. If too many TE modules are stacked, the temperature difference between each module is too small, and this small temperature gradient cannot generate enough electrical energy to overcome the energy consumed by the module itself. This is why the five-layer construction generates less power than the four-layer one. The experimental results show the most efficient stack is when four TE modules are attached together. Thus, a four layer design is employed in this work.

Table 10.7 Five different configurations of the TE generator (radiator temperature 323K and air temperature 294K)

Number of modules in stack	Voltage (V)	Current (mA)	Power (mW)
1	0.287	97	27.839
2	0.361	82.3	29.7103
3	0.482	78	37.596
4	0.547	72	39.384
5	0.586	58	33.988

Similar to the solar energy harvesting system, positioning the thermal energy generator also affects the harvesting efficiency. Empirically, the temperature of the air surrounding the radiator is not constant over the whole radiator surface area but varies at different positions on the surface. If the TE generator is located at the lowest temperature positions, the efficiency of the system can be significantly improved. In order to locate the lowest air temperature position, the ambient temperature distributions of the air surrounding the radiator have been tested. The result is shown in Figure 10.7. From the figure, the lowest air temperature position is at the bottom of the radiator, which is considered as the best position to place the TE generator.

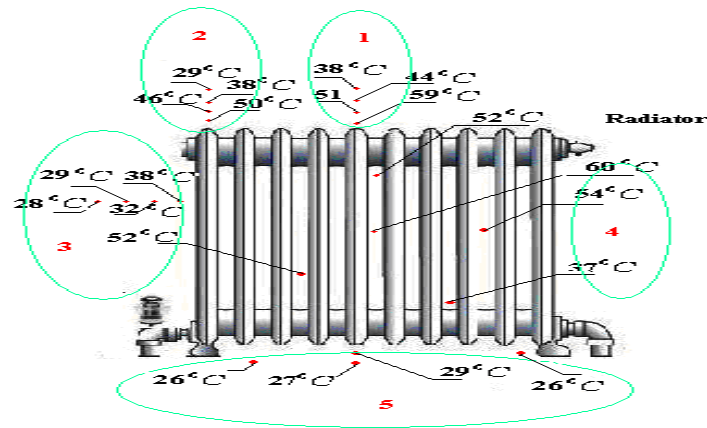


Figure 10.7 Temperature distribution of the radiator

In order to prove the concept, a four-layer TE generator with the heat sink was placed at five different positions, circled in Figure 10.7, and tested in a similar environment. The comparison results are shown in Table 10.8. By examining the results, when the system is placed at the bottom position of the radiator, it can harvest almost twice as much power as it being placed on the top of the radiator.

Table 10.8 Five different positions to locate TE generator (radiator temperature 323K and air temperature 294K)

Positions	Voltage (V)	Current (mA)	Power (mW)
1	0.475	65	30.875
2	0.547	70	38.29
3	0.503	68	34.204
4	0.487	67	32.629
5	0.715	89	63.635

Based on the same principle, if the heat from the radiator can be isolated from the air surrounding the heat sink, a larger thermal flow can pass through the modules. Some pieces of sponge or cotton material can be used to efficiently block heat flowing from a hot place to a cold place. Consequently some pieces of sponge were employed to surround the TE modules on the hot side heat exchanger to block heat from the radiator. The setup is illustrated in Figure 10.8.

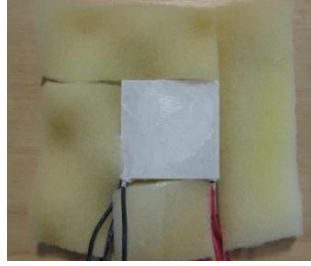


Figure 10.8 Hot Side heat exchanger with sponges

In order to evaluate the improved efficiency, a hot side heat exchanger without the sponge was compared with this design and the result is depicted in Table 10.9. From these results, the thermal conversion efficiency of the TE generator was increased by 50% or more by placing some pieces of sponges on the hot side heat exchanger to block the heat.

Table 10.9 Harvested power for different hot side heat exchangers

Radiator 323K & Air 294K	Voltage (V)	Current (mA)	Power (mW)
Heat exchanger without sponge	0.547	72	41.328
Heat exchanger with sponger	0.835	114	95.19

10.4.2 MPPT based Power conversion subsystem

The system efficiency can be enhanced by using a proper circuit to couple the harvested energy from the energy harvester. As mentioned in Chapters 5 and 6, the energy harvesting system performance is substantially increased if the maximum electrical power is available from the TE generator at all times given the available radiator temperatures. This is particularly critical if only minor temperature differences could be obtained by the TE generator. In the large temperature difference condition, any significant fraction of the available thermal electrical energy will recharge the system quickly; the MPPT circuit only affects how quickly the energy storage is replenished. However, the system performance can be substantially altered by maximizing the available thermal electric energy during short temperature gradient periods. The system volume and the energy overhead are two critical factors in determining which MPPT approach and circuitry should be used in the micro-scale energy harvesting system.

Due to the proliferation of low-power MCU, digital MPPT approaches are strongly preferred in order to deal with the system complexity and the power consumption of

the circuitry. Unlike the solar energy, which may change rapidly in an outdoor environment, the temperature gradient between the radiator and ambient varies steadily or keeps at a constant value. As illustrated in Chapter 6, the P&O MPPT method has higher efficiency than the enhanced P&O MPPT approach when the energy harvesting system is placed in a slowly changed environment. Hence, the P&O MPPT approach is adopted in this chapter to track MPP of the thermal energy harvesting system. The hardware circuit, proposed in Chapter 7, has been employed.

By comparing the power generation and the power consumption of the system, the output power of the TE generator is insufficient to directly power the sensor node. Hence a power converter interface circuit with a high power transfer efficiency needs to be developed in order to change the input power conditions into a suitable form for the target system. The same DC-DC boost circuit from Chapter 9 is used to boost the low input voltage from the thermal energy harvesting subsystem into a high output voltage. Because of the low harvested voltage, the DC-DC converter circuit might not work when it lower than the start-up voltage of the DC-DC converter circuit. In recent times, the start-up voltages of DC-DC converters have been scaled down more and more due to semiconductor technology development. Since almost all the step-up converters require input voltage of at least 0.7V to start up, there is a gap between the output of the thermal energy harvesting system and the minimum required input voltage of the DC-DC converter. Meeting this higher input voltage requires an additional circuit between the TE generator and the DC-DC converter. Conventional charge pumps are considered as an ideal component to increase the voltage in the circuit. The S-882Z charge pump IC from SEIKO (S-882Z charge pump, 2010) can work as the start-up circuit to deliver the required voltages for a boost converter. It is capable of stepping-up the input voltage from as low as 0.3V and outputs a boosted voltage of around 2.2V, sufficient to start-up a booster converter. Moreover, a built-in shutdown function can achieve significant power saving when the output voltage of the connected step up DC-DC converter rises above a threshold voltage. A schematic diagram of the DC-DC converter subsystem is shown in Figure 10.9. It consists of an S-882Z charge pump, which has a 2.5V discharge voltage, in conjunction with the TPS61222 boost converter. The charge pump starts to work when the input voltage is as low as 250mV. Once the output capacitor CPOUT of the charge pump has reached

2.5V, an internal transistor turns on and a 2.5V charge is delivered as an input source to the TPS61222 boost converter.

Subsequently, the booster converter starts to work and its output voltage rises. As soon as the output voltage rises beyond 0.7V, the booster converter supplies its own triggering power by feeding the output voltage to the input. Once the booster converter drives itself, the charge pump does not need to be considered in the design. According to Mateu et al (2006), a trade-off must be made when determining the value of the charge-pump capacitor, CPOUT. In order to provide the necessary start-up power for the booster converter, a high value capacity is required, but this extends the start-up time. In order to reduce the start-up capacitor to the minimum value at which it is still functional, two $50\mu\text{F}$ tantalum capacitors have been employed in parallel in this design. As the voltage of the thermal energy harvesting is very restricted and the generated current is quite high, a high value inductor may be used by the booster converter. It has the capability to reduce the minimal start-up voltage and provide high efficiency. Thus a high value inductor, $220\mu\text{H}$, was used in this design.

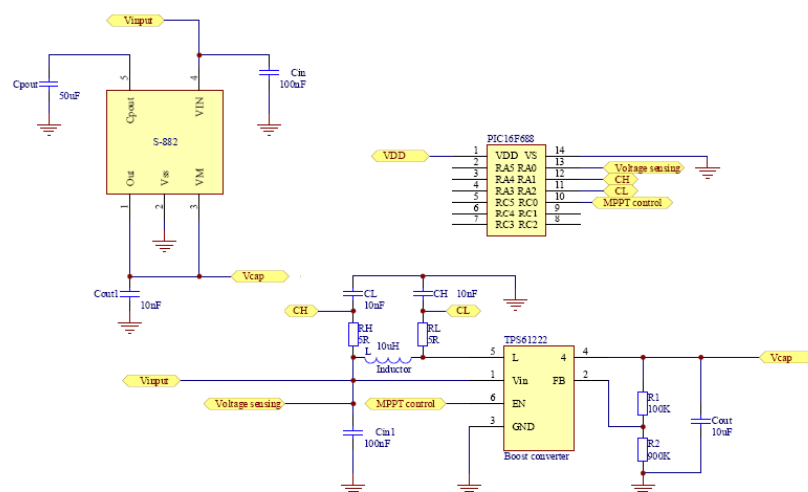


Figure 10.9 Schematic diagram of MPPT based DC-DC converter subsystem

10.4.3 Power management subsystem

For the power management part, the same hardware design, developed in Chapter 7 has been adopted. The following three main functions are achieved by the power management subsystem.

- It uses an intelligent control algorithm to distribute the harvested energy to each part of the system and store the available energy in the storage elements. In order

to prolong the system lifetime as long as possible, a hybrid dual energy buffers design has been used.

- The energy status of the rechargeable batteries and the super-capacitors are monitored by the PIC MCU. This indicates the energy relationship between the energy generation and the energy dissipation
- Based on the energy relationship, a power management algorithm is able to achieve the energy neutral operation in relation to maximize the system performance.

Following the same design procedure of the power management algorithm, described in Chapter 7, an adaptive power management algorithm for the thermal energy harvesting system has been developed. Based on the specification of the ZBARV sensor node, shown in Table 10.2, the window size and the time slot size are set for 24 hours and 30 minutes duration, respectively. In order to maintain the super-capacitor in only one state at each adjusting cycle, the size of the super-capacitor should be determined. Since the sensor node has two different functions, adjusting room temperature and measuring the room temperature, the power consumptions for these two functions are different. But the super-capacitor size calculation is only dependent on the maximum power consumption mode, which is the sensor node adjusting room temperature with the maximum duty cycle 20%. The maximum average power consumption of the sensor node is calculated as:

$$P_{average}(maximum) = 192mW \times 20\% + 0.022mW \times 80\% = 38.42mW$$

By assuming the power consumption of the thermal energy harvesting circuit is 1mW, the maximum energy dissipation by the system during a time slot is:

$$E_{system}(maximum) = 39.42mW \times 1800s = 69.16Joule$$

By assuming two voltage thresholds for the super-capacitor are set as $V_{w,th3} = 3.9$ and $V_{w,th4} = 2.7$, and then the minimum capacitance of the super-capacitor can be calculated as

$$C_{min} = \frac{2 \times E_{system}(maximum)}{V_{w,th3}^2 - V_{w,th2}^2} = 17.46F$$

Considering the energy leakage and charging/discharging efficiency of the system, the two 50F super-capacitors connected in series has been adopted in this work. As two separate functions have been achieved by the sensor node for different situations, the power management algorithm should have the ability to distinguish these two functions and adapt these two functions to the current energy budget. For the temperature measurement function, it happens when the sensor node detects the radiator being turned off or the room temperature is equal to the setting temperature, it only measures the room temperature in every 30 minutes. On the other hand, if the sensor node detects the room temperature being higher/lower than the setting temperature threshold, it adjusts the motorized radiator valve for 15 seconds in every 30 minutes.

The pseudo code of the proposed algorithm is shown in Table 10.10. Initially, the system sets basic parameters of the algorithm and measures the current energy buffers statuses. During the first time slot, the sensor node records the current battery voltage $V_{R-battery}$ and the status of the super-capacitor in n_{power} or n_{charge} . By comparing the current battery voltage with a 2.2V voltage threshold to determine the battery status, if the battery voltage is equal to or less than 2.2V, it indicates the battery is almost depleted and the system reports the error signal to the local server and then goes to sleep to protect the battery. On the other hand, if the battery voltage is higher than 2.2V that means the battery has stayed at the healthy status and thus the system goes to the next stage.

In the next stage, the sensor node checks the radiator status and if the radiator is totally turned off which indicates that no thermal energy can be harvested by the system, the system turns off the thermal energy harvesting system part to reduce system overhead. In this situation, the sensor node only measures the room temperature in every 30 minutes. If the sensor detects the radiator is in the turn on status, it compares the present room temperature to the user setting room temperature. If these two parameters are equal, the sensor node measures the room temperature without driving the step motor. Otherwise the sensor node adjusts the radiator to make the room temperature approach the setting one. The power consumption of the sensor node is adapted with the energy budget of the system by following the energy neutral operation and the maximum system performance rules. The detail of the algorithm is shown in Table 10.10 with a simple else-if statement.

Table 10.10 Power management algorithm pseudo code

	Driver
1	<p><i>Initial system</i></p> <ul style="list-style-type: none"> • <i>Masuring initial battery level $V_{R-battery}$, and set initial duty cycle $D_{initial}$ for sensor node</i> <ul style="list-style-type: none"> • <i>Setting $V_{B,th1}, V_{b,th2}, V_{b,th3}, D_{min}, D_{max}, \Delta D_1, \Delta D_2$, and ΔD_3</i> <ul style="list-style-type: none"> • <i>$n_{power} = 0$ and $n_{charge} = 0$</i>
2	<i>During time slot T, the system recorded $V_{R-battery}$, n_{power}, and n_{charge}, respectively</i>
3	<p><i>If $V_{R-battery} > 2.2V$</i> <i>Go to step 4</i> <i>Else go to step 8</i></p>
4	<p><i>Detecting the radiator status</i> <i>If radiator is turn off</i> <i>Turn off the thermal energy harvesting system</i> <i>Measure the room temperature in every 30 minutes</i> <i>Else</i> <i>Turn on the thermal energy harvesting system</i> <i>Comparing the current temperature with the setting room temperature</i> <i>If $T_{temperature\ sensor} = T_{setting\ temperature}$</i> <i>Go to step 5</i> <i>Else go to step 6</i></p>
5	<p><i>This step for the sensor node operates measuring room temperature function</i></p> <p><i>Comparing the final reading of the battery level $V_{R-battery}$ to previous battery level $V_{R-battery,i}$</i></p> <p><i>Case 1: If $V_{R-battery} < V_{R-battery,i}$</i> <i>{ If $V_{R-battery} < V_{B,th1}, D=D_{min};$</i> <i> Else If $V_{b,th1} \leq V_{R-battery} < V_{b,th3}, D = D_{initial} - \Delta D_1;$</i> <i> Else If $V_{b,th3} \leq V_{R-battery} < V_{b,th2}, D = D_{initial} - \Delta D_2;$</i> <i> Else If $V_{R-battery} \geq V_{b,th2}, D = D_{max} ;$</i> <i>}</i></p> <p><i>Case 2: If $V_{R-battery} > V_{R-battery,i}$</i> <i>{ If $V_{R-battery} < V_{B,th1}, D=D_{min};$</i> <i> Else If $V_{b,th1} \leq V_{R-battery} < V_{b,th3}, D = D_{initial} + \Delta D_2;$</i> <i> Else If $V_{b,th3} \leq V_{R-battery} < V_{b,th2}, D = D_{initial} + \Delta D_1;$</i> <i> Else If $V_{R-battery} \geq V_{b,th2}, D = D_{max} ;$</i> <i>}</i></p> <p><i>Case 3: If $V_{R-battery} = V_{R-battery,i}$</i> <i>{ If $V_{R-battery} < V_{B,th1}, D=D_{min};$</i> <i> Else If $V_{b,th1} \leq V_{R-battery} < V_{b,th3}$</i> <i> { If $n_{chairng,B} > 0, D=D_{initial};$</i> <i> Else If $n_{power,B} > 0, D = D_{initial} - \Delta D_1;$</i> <i> Else if $n_{chairng,B}, n_{power,B} = 0, D = D_{initial} - \Delta D_1;$</i> <i> }</i> <i> Else If $V_{b,th3} \leq V_{R-battery} < V_{b,th2}$</i> <i> { If $n_{chairng,B} > 0, D = D_{initial} + \Delta D_1;$</i> <i> Else if $n_{power,B} > 0, D = D_{initial} - \Delta D_1;$</i> <i> Else if $n_{chairng,B}, n_{power,B} = 0, D = D_{initial};$</i> <i> }</i> <i> Else If $V_{R-battery} \geq V_{b,th2}, D = D_{max} ;$</i> <i>}</i> <i>Go to step 7</i></p>
6	<p><i>This step is for the sensor node achieve adjusting room temperature function</i></p> <p><i>Comparing the final reading of the battery level $V_{R-battery}$ to previous battery level $V_{R-battery,i}$</i></p> <p><i>Case 1: If $V_{R-battery} < V_{R-battery,i}$</i> <i>{ If $V_{R-battery} < V_{B,th1}, D=D_{min};$</i> <i> Else If $V_{b,th1} \leq V_{R-battery} < V_{b,th3}, D = D_{initial} - \Delta D_1;$</i> <i> Else If $V_{b,th3} \leq V_{R-battery} < V_{b,th2}, D = D_{initial} - \Delta D_2;$</i> <i> Else If $V_{R-battery} \geq V_{b,th2}, D = D_{initial} - \Delta D_3 ;$</i> <i>}</i></p>

	Driver
	<p><i>Case 2: If $V_{R-battery} > V_{R-battery,i}$</i> <i>{If $V_{R-battery} < V_{B,th1}$, $D=D_{min}$;</i> <i>Else If $V_{b,th1} \leq V_{R-battery} < V_{b,th3}$, $D = D_{initial} + \Delta D_3$;</i> <i>Else If $V_{b,th3} \leq V_{R-battery} < V_{b,th2}$, $D = D_{initial} + \Delta D_2$;</i> <i>Else If $V_{R-battery} \geq V_{b,th2}$, $D = D_{initial} + \Delta D_1$;</i> <i>}</i></p> <p><i>Case 3: If $V_{R-battery} = V_{R-battery,i}$</i> <i>{If $V_{R-battery} < V_{B,th1}$, $D=D_{min}$;</i> <i>Else If $V_{b,th1} \leq V_{R-battery} < V_{b,th3}$,</i> <i>{If $n_{chairng,B} > 0$, $D=D_{initial}$;</i> <i>Else If $n_{power,B} > 0$, $D = D_{initial} - \Delta D_2$;</i> <i>Else if $n_{chairng,B}$, $n_{power,B} = 0$, $D = D_{initial} - \Delta D_3$;</i> <i>}</i></p> <p><i>If $V_{b,th3} \leq V_{R-battery} < V_{b,th2}$</i> <i>{If $n_{chairng,B} > 0$, $D = D_{initial} + \Delta D_2$;</i> <i>Else if $n_{power,B} > 0$, $D = D_{initial} - \Delta D_3$;</i> <i>Else if $n_{chairng,B}$, $n_{power,B} = 0$, $D = D_{initial}$;</i> <i>}</i></p> <p><i>If $V_{R-battery} \geq V_{b,th2}$, $D = D_{initial} + \Delta D_1$;</i> <i>}</i></p> <p>Go to step 7</p>
7	<ul style="list-style-type: none"> • $D_{initial} = D$ and $V_{R-battery,i} = V_{R-battery}$ • $n_{power} = 0$ and $n_{charge} = 0$ <p><i>Return to step 2</i></p>
8	<p><i>Else If $V_{R-battery} < V_{B,th2}$</i> <i>Report error to coordinator and enter sleep mode</i></p>

10.4.4 Integrated thermal energy harvesting system

After designing each subsystem of the thermal energy harvesting system, the integrated system is depicted in the Figure 10.10. As the same PIC MCUs are used in the power conversion circuit and the power management circuit, the circuit can be simplified and the power overhead can be reduced by using the one PIC MCU to integrate all the control functions.

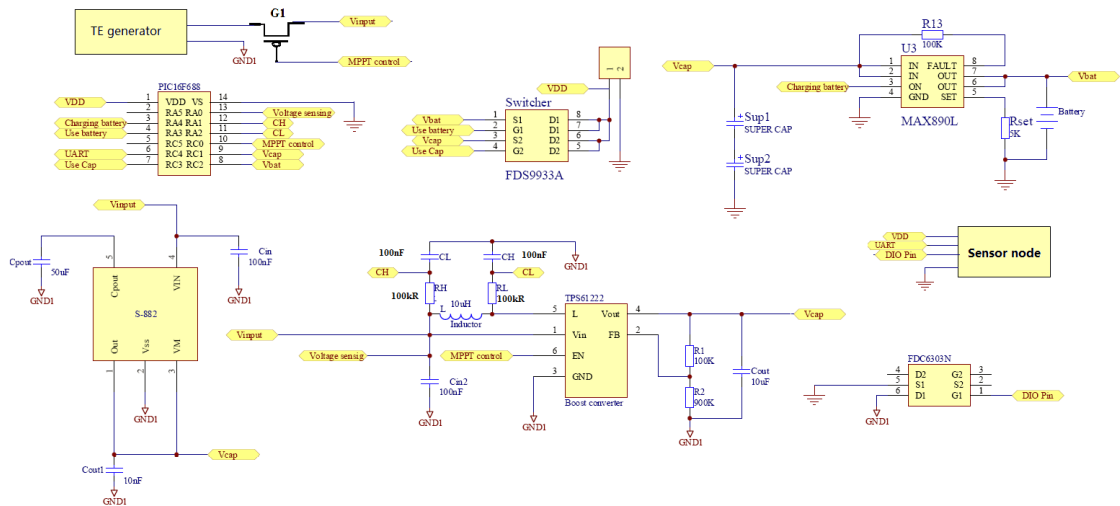


Figure 10.10 Schematic diagram of the proposed system

10.5 Evaluation

The use of the thermal energy harvesting system has been evaluated in terms of the four performance metrics of the system. A prototype of the TE generator has been developed and tested experimentally to identify its ability to capture thermal energy and convert it into electrical power. The MPPT based power conversion system has been evaluated and compared with a system without the MPPT scheme. The third approach is to verify the power management unit in order to see whether the system's performance and lifetime could be significantly improved or not. Lastly, after evaluating each subsystem of the prototype, the entire system has been integrated and tested in the real house to examine the performance of the system. The overhead caused by the thermal energy harvesting system's analog circuitry has been tested to identify the system efficiency.

10.5.1 Individual component evaluation

a) TEG operation

As stated in the previous sections, the harvesting efficiency of the TE generator is the critical factor in determining the entire system efficiency. Hence, the first evaluation procedure is to verify how much energy could harvest from the radiator by the developed TE generator. Since the temperature of the hot water radiator is hard to adjust, a 1.5KW electrical radiator, which can vary the heat output by adjusting an on board regulator, was employed to emulate the normal domestic radiator in the

laboratory. Figure 10.11 shows the experimental setup which was used to evaluate the proposed platform. In order to harvest enough thermal gradient energy from the radiator, two heat sinks and eight TE modules were used to fabricate the thermal energy harvester. In this design, four of eight modules were attached together in a stack by using high efficient thermal grease and then located between the heat sink and a thin copper plate. Additionally, some pieces of sponge were used to isolate heat from the radiator. For easy installation, the copper plate was formed to a U type and clamped on the bottom of the radiator. In order to monitor the temperature of the hot and cold sides of the TE Modules, an Omega CO-1 thermocouple (Omega CO-I thermocouples, 2010) with a Temperature meter was used.



Figure 10.11 Experimental setup for thermal energy harvesting system

In order to evaluate the thermal energy harvesting efficiency of the TE generator, the system was tested in the laboratory at different radiator temperatures with a fixed room temperature of 21°C. The experimental result is shown in Figure 10.12. The larger temperature difference the TE generator has, the greater the power that can be generated. It can be observed that the maximum harvested power is around 82mW when the hot side temperature is 55°C.

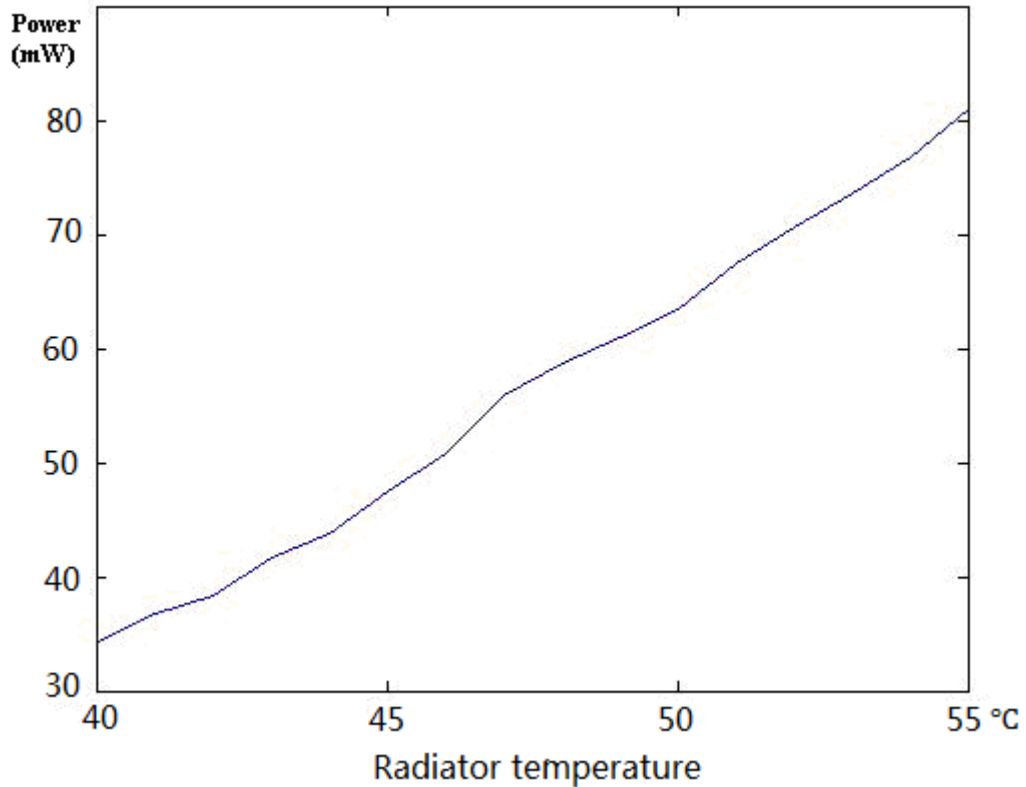


Figure 10.12 Output voltage of the TE generator as a function of the hot side temperatures

b) Efficiency of the MPPT based power conversion circuit

As indicated in Chapters 5 and 6, the efficiency of the MPPT based power conversion circuit is essential in determining the whole system efficiency, especially for micro-scale energy harvesting system. In this section, the efficiency of the MPPT based power conversion circuit can be divided into two parts: the efficiency of the boost converter circuit and the MPPT efficiency of the MPPT scheme. Firstly, a practical implementation of the DC-DC converter system without an MPPT circuit was tested with different input powers to evaluate efficiency and the result obtained is shown in Table 10.11. A DC power source was used to emulate different input power level and the output voltage of the booster converter was set to a constant voltage of 5V. The experimental results show that the efficiency of the booster DC-DC converter is related to input power and the converter system works even when the input voltage is as low as 0.32V and the average efficiency of the system is around 30%.

Table 10.11 Measurement Results of the DC-DC CONVERTER

Input Voltage (V)	Input Current (mA)	Output Current (mA)	Efficiency
0.32	59	1.1	29%
0.43	62	2.0	37.5%
0.47	65	2.4	39%
0.51	70	3.5	46%
0.63	89	5.5	49%
0.7	90	7.56	60%
0.75	110	10.8	65.4%
0.8	120	12.8	66.7%

Next the MPPT circuit was integrated with the boost DC-DC converter circuit to test MPPT efficiency. In order to evaluate the MPPT circuit enhancing the system efficiency, the same DC-DC converter circuit without MPPT circuit was compared with the system. The TE generator was connected with these two designs and the power outputs of the integrated systems were used to charge two 50F super-capacitors from 2V to 4V. The integrated system was tested in the laboratory with the electrical radiator where the room temperature was maintained at 21°C. Normally, the charging time provides a simple way to interpret efficiency. The experimental result is shown in Table 10.12. It can be observed that the charging time is around twice as fast as the system without MPPT circuit. For the MPPT based power conversion circuit, the maximum power conversion efficiency is 63.7% when the radiator is setting at 55°C. The conversion efficiency drops with the decreasing of the harvested power. The conversion efficiency is decreased more quickly when the radiator temperature is less than 50°C. This is because the efficiency of the boost converter drops rapidly when the input voltage is less than 0.7V. The system only can store 35.1% of the harvested energy into the energy buffer. But the conversion efficiency drop to 11.7% when the system without MPPT circuit is deployed in the same environment. Based on this

experiment, it can be observed that the MPPT circuit and the temperature difference are two critical factors in determining the system efficiency.

Table 10.12 Charging time and conversion efficiency of the two power conversion system

Harvested power (mW)	MPPT based power conversion subsystem (S)		Power conversion system without MPPT (S)	
	Charging time (S)	Efficiency	Charging time(S)	Efficiency
83mW (radiator temperature=55°C)	1456	63.7%	2610	35.5%
72.1mW(radiator temperature=52°C)	1612	62.1%	3101	34.4%
63.1 mW (radiator temperature=50°C)	1994	61.2%	3890	31.4%
58.4mW (radiator temperature=48°C)	2633	54%	5551	23.8%
48.7mW (radiator temperature=45°C)	3585	44.1%	8604	18.4%
35.1mW (radiator temperature=40°C)	6250	35.1%	18749	11.7%

C) Evaluation of the power management subsystem

In order to achieve longer life or even perpetual lifetime, a power management unit is a core component. The proposed power management subsystem with ZBARV was verified by simply connecting it to a DC power supply. Based on the functions of the power management unit, the system was divided into two parts. The first part was to verify the power distribution capability of the power conversion system. Initially, the ZigBee node was powered by the secondary buffer (two rechargeable batteries) while the DC power supplier charged the primary buffer. When the first threshold of 3.4V was met, the power management unit triggered the P-MOSFET to switch from the

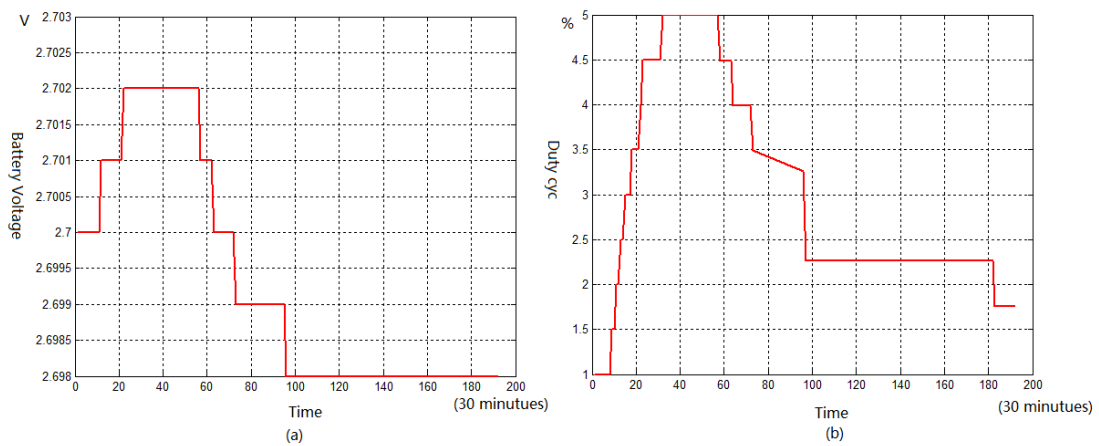
rechargeable batteries to the super-capacitors. Subsequently the entire system was powered by the super-capacitors. While the input power was increasing, the power accumulated on the super-capacitors was rising. Once the capacitor's voltage reaches 4.1V, the PIC16F688 MCU switches on the adjustable current limit switch and transfers the capacitor's energy to the rechargeable batteries. Next, the DC power supply is turned off and the voltage of the capacitors drops. When the voltage drops to less than 3.9V, the capacitors stop charging the rechargeable batteries. Furthermore, once the voltage is less than 2.7V, the rechargeable batteries again start to power the ZigBee chip. These phenomena correctly fit the design principle, which was mentioned in the power management subsystem. For the dynamic power management test, the power management algorithm was loaded into the sensor node.

The second stage involved the evaluation of the power management algorithm which can adapt the sensor node's power consumption to the energy generation. The system was powered by the DC power supply, which varies the output power level, for four days. The input voltage is maintained at 5V and the input powers are varied at 10mW, 5mW and 0mW, respectively. In the first day, the DC power supply was set 10mW constant output to charge the super-capacitor for 24 hours. Then the DC power supply adjusted its output power to 5mW and lasted for 48 hours. In the remaining 24 hours, the DC power supply was turned off. In order to make the experiment reproducible, the rechargeable batteries were initially charged to 2.7V and the super-capacitor was charged from a depleted condition. The initial duty cycle of the sensor node was set to 1%. Because the sensor node has two different functions based on different conditions, the experiment was tested with these two functions for two days, respectively. In the first two days, the sensor node was used to measure room temperature and adjust the step motor in each cycle. Next, the sensor node was operated in the simple mode, in which the sensor just measures the room temperature in each cycle, for another two days. Based on the specification of the sensor node, the parameters of the power management algorithm are shown in Table 10.13.

Table 10.13 The parameters of the power management algorithm

Algorithm parameters					
$V_{B,th1} = 2.2V$	$D_{max} = 20\%$	D_{min}	$\Delta D_1 = 1\%$	ΔD_2	ΔD_3
$V_{B,th2} = 2.9V$		$= 0.83\%$		$= 0.5\%$	$= 0.01\%$
$V_{b,th3} = 2.7V$					

The experimental results of the terminal battery voltage and duty cycle are depicted in Figure 10.13 (a) and (b), respectively. By examining these two curves, the duty cycle of the sensor node is increased with the increasing of the battery voltage, and vice versa. Moreover, because the battery has a very large capacity, the battery voltage cannot indicate the instantaneous energy relationship in each time slot. The status of the super-capacitor is introduced in order to indicate the instantaneous energy relationship. The duty cycle of the sensor node is dropped or increased when n_{power} or n_{charge} has been detected.

**Figure 10.13** The experimental result of the power management system

10.5.2 Integrated system evaluation

The integrated system, as shown in Figure 10.14, has been evaluated after each subsystem was evaluated. In order to measure the current consumption of the whole thermal energy harvesting analog circuit, the PCB board without the TE generator was tested. When a 3V battery is used to power the circuit, the current consumed by the analog circuit is around 700uA. This shows the importance of the power management

algorithm to switch off the energy harvesting circuit when there is no or insufficient power produced by the TE generator.

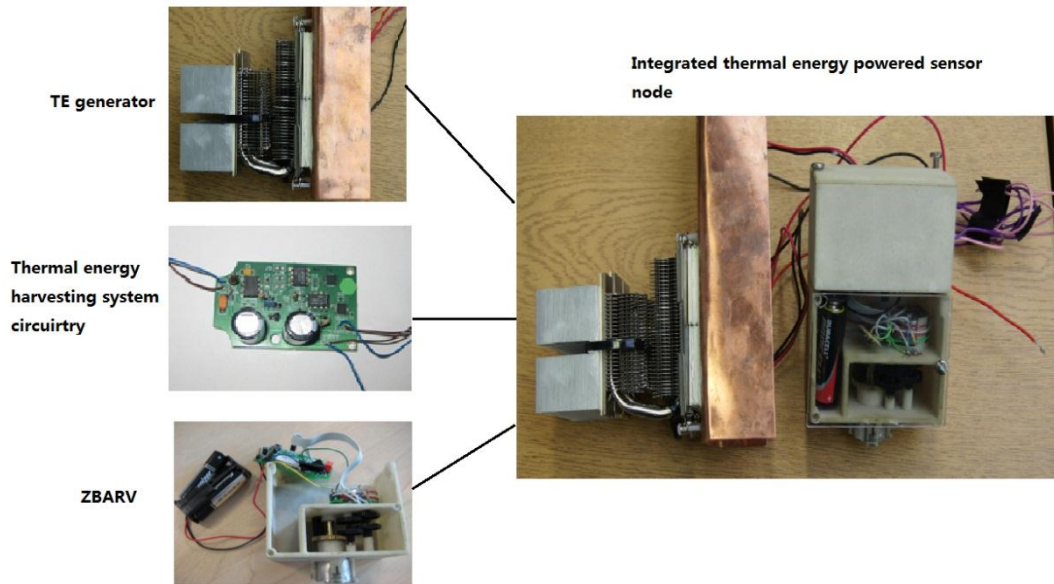


Figure 10.14 Integrated thermal energy powered ZBARV

Before the system was implemented in a real environment, the proposed system was evaluated with the electrical radiator in a house for seven days. The test setup is shown in Figure 10.15.



Figure 10.15 The thermal energy harvesting system with ZigBee Based Automatic Radiator

The terminal voltage of the rechargeable batteries and the duty cycle of the sensor node were recorded every 30 minutes over a period of seven days. The curves of the battery voltage and the duty cycle are shown in Figure 10.16 (a) and (b), respectively. The results show that the system worked autonomously as expected without any

additional power requirements. When the radiator was turned on, the thermal energy harvesting system harvested thermal gradient energy from the radiator and stored the excess energy into the rechargeable batteries. By examining two curves, the duty cycle of the sensor node is automatically adapted with the energy generation to perform energy neutral operation. The thermal energy powered ZBARV sensor node is considered to have a perpetual lifespan, which is limited only by the hardware lifetime.

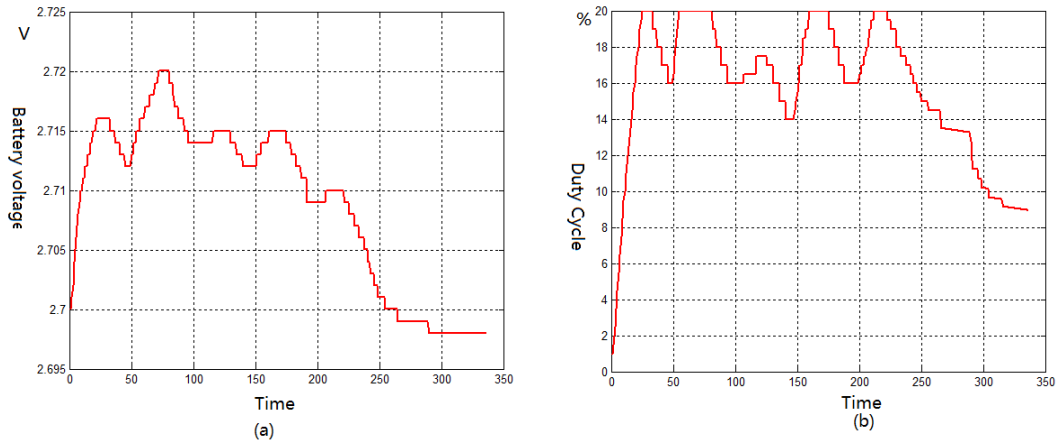


Figure 10.16 The proposed system test in a real house for 7 days

10.6 Summary

In this chapter, a highly efficient thermal energy harvesting system powered wireless sensor node, based on the proposed architecture and the design procedure, has been developed. The system is sizing optimally based on the theoretical model. Similar to the proposed solar energy harvesting system, the MPPT based power conversion circuit and the power management subsystem have been employed in the system to improve system performance both on the efficiency and lifetime sides. The experimental results show the system can harvest as low as 0.3V thermal energy from the environment, and that the lifetime of the sensor node is dramatically improved by using the thermal energy harvesting system. The system also shows that the proposed system architecture can be used for both solar and thermal energy harvesting systems. The system can be easily expanded to other types of applications by knowing the relationship between the energy generation and the energy consumption.

Chapter 11. Conclusion and Future work

11.1 Summary

Recently, new micro-systems like WSNs, which normally use ad-hoc wireless transceivers and micro-smart sensors, continue to integrate more and more functionalities in a smaller package size with lower power consumption. The compact size has many benefits and opens new application areas for WSNs but this deeply constrains the amount of power embedded on the system. The recent explosion in WSNs has not been matched by battery technology, which the slow growth of battery energy density has limited the lifetime of the wireless sensor nodes and added weight and volume to the system. Moreover, the lifetime and the energy consumption of the sensor nodes continue to remain a key challenge in the design process of battery powered sensor networks. Hence, energy is a limited resource in wireless electronics and power supplies and making sufficient energy available is perhaps the most challenging technological hurdle to be overcome in the widespread development of WSNs. Energy harvesting from environmental sources offers a promising alternative, which can reduce system weight and volume, and increase operating lifetime, and decrease maintenance cost, and hopefully solve the limitations arising from battery size constraints in sensor networks. In recent decades, a number of micro-scale energy transducers have been fabricated in order to convert energy from other modalities, such as solar radiation, thermal gradient energy, mechanical motions or vibrations, and radio frequency energy, etc. into electrical energy. By using energy harvesting techniques, the lifetime of the system is significantly prolonged and the energy limitation problem is mitigated in certain levels in some cases.

Despite the fact that significant research efforts have been put into this area, there are still a lot of problems when an energy harvesting system is deployed in the real environment, especially for a micro-scale energy harvesting system application. The traditional energy harvesting system design approach follows a developing manner of trial-and-error in which the proposed system performance heavily depends on the designer's experience. Unlike designing a battery powered embedded system, the energy harvesting system imposes a limit on the instantaneous power available based on the dynamic environmental energy level. Many designers use a worst case scenario to design the system, which means the system is typically oversized. Since the volume and price are two system restrictions for a micro-scale energy harvesting system, the oversized system results in inefficiency. Furthermore, since the amount of energy harvested from environments is typically small and highly variable, it requires system circuits and architectures with a low power consumption and sufficient stability for available energy generation. This means that the designers are faced with a great number of design parameter choices. They need to spend much time and effort in order to optimize system performance. In addition, quickly assessing and evaluating the entire system performance at the early stages is impossible. If the system evaluation shows that the system has a functional failure or poor efficiency, a new design cycle has to occur. Finally, different sensor nodes in a sensor network may also have different energy harvesting opportunities. A proposed energy harvesting system focusing on harvesting a typical energy source cannot be easily expanded to harvest another type of energy from the environment.

11.2 Contributions and future work

The research objective of this thesis is to investigate and design high efficiency micro-scale energy harvesting systems in order to power the wireless sensor nodes and give the system a perpetual lifetime. The main contributions and findings from the research are listed below:

1. A generic system architecture has been developed to fit various applications and requirements.

As stated in the literature review, different energy harvesting platforms have their own system architectures for harvesting a typical energy source. This is difficult in terms of placing an energy harvesting system powered sensor node in the environment where there are two or more energy sources available. Hence, a generic system architecture, which can be easily expanded for harvesting other types of energy sources and powering other types of sensor nodes, has been designed, implemented and evaluated. All the possible components to build up an efficient energy harvesting system have been taken into consideration. By employing the dual energy buffer design in the architecture, the performance and lifetime of the system is theoretically enhanced. Moreover, according to the different harvested energy types, the generic system architecture should have different components in the power conversion part. As solar and thermal are selected as the target energy sources, the generic system architecture for these two kinds of energy harvesting systems has been developed.

2. A simplified and optimized system design procedure has been developed for guiding the design of a cost-size effective and system efficient energy harvesting system.

As there is no clear design guideline in the existing literature to guide the complex system design procedure of a micro energy harvesting system, a clearly and simplified system design procedure, which is based on the generic system architecture, has been proposed. According this design procedure, the parameters of the system can be properly determined by knowing three factors of the system: the energy generation, the energy consumption and the power management strategy. By applying these factors in the simulation model, the energy harvesting system can be designed in the optimal way.

3. A general systematic model of micro-energy harvesting systems has been developed to bridge the gap between physical electrical level and simulation level to avoid a blindness design of energy harvesting system.

The traditional energy harvesting system design procedure is essentially the trial-and-error approach. A theoretical analysis is very important before designing and implementing an energy harvesting system in the real environment. A theoretical energy harvesting system model, based on the general systematic architecture, is proposed in this thesis to predict the system performances of solar and thermal energy harvestings. The model can be easily expanded to other types of energy harvesting resources by replacing modelling of an energy harvester. The models of each components of the system and the entire integrated system model are designed, respectively. In order to examine the model's accuracy, the corresponding test setup has been built in the laboratory for both solar and thermal energy harvesting systems. Based on the experimental results, the proposed model has around 80% accuracy in the worst case, which is considered. Moreover, the research findings also show that the system efficiency can be greatly improved by either improving efficiency of the energy harvester or using the MPPT based power conversion circuit.

4. Two ways of improving the system efficiency and performance have been developed in this thesis by following to improve the energy transfer efficiency, the energy buffering efficiency and the power consumption efficiency.

As the system efficiency is a critical factor in determining system performance, especially in designing a micro energy harvesting system, the research work here focuses on carrying out some possible ways to improve system efficiency by improving the energy transfer efficiency, the energy buffering efficiency and the power consumption efficiency. More in detail, the improvement actions are divided into two aspects: designing an MPPT based power conversion circuit to improve the energy transfer efficiency and developing an efficient power management subsystem to enhance the energy buffering efficiency and the power consumption efficiency. For the MPPT based power conversion circuit part, there are a lot a lot of MPPT approaches in the literature but the comparative results of which one has the most efficiency is not given. In order to show differences, three types of MPPT based power conversion circuit have been designed and evaluated. The experimental results show that the digital MPPT technologies are more suitable for the small scale system design. Furthermore, the enhanced P&O approach is suitable for rapidly changed environments and the classical P&O method is preferred for a constant or slowly

changed environment. According to this finding, the system designers can select a proper MPPT technology by knowing the characteristics of the environment source. For the power management subsystem part, this is designed to improve the lifetime and performance of the energy harvesting system. This subsystem is designed by following the rule of adjusting the system performance with the energy budget of the system. By using this type of subsystem, the lifetime of the energy harvesting system can be seemed as perpetual.

5. Design and implementation of three kinds of systems in the real environments to prove the proposed works

The thesis developed three case studies by using the proposed theoretical analysis and the proposed subsystems. The efficient design of any micro-energy harvesting system can only be achieved through fully understanding the electrical characteristics of the target sensor node. This is because the sensor node is the main energy consumer in the system. Any successful energy harvesting platform should fully satisfy the basic specification of the sensor node. Hence, several wireless sensor nodes, based on the JN5139 wireless platform, have been designed. The design procedure, which is based on the generic sensor node architecture, has been used. By using a theoretical lifetime calculation, the lifetime of the sensor nodes are not satisfying user requirements.

Then two energy harvesting systems (solar and thermal) have been developed to power two types of sensor nodes, which were designed previously. The system has been designed by using the proposed model and following the proposed design procedure. In the first case, a solar powered door security sensor node is developed. The parameters of the system are determined by knowing the characteristics of the energy generation and the energy dissipation of the system. By integrating the enhanced P&O MPPT based power conversion circuit in relation with the adaptive power management unit, a high efficiency solar energy harvesting system has been developed. The proposed system has been evaluated in the darkest month in Loughborough for 30 days and the experimental results show that the system can not only survive in these 30 days, but also adapt its energy consumption to the energy generation.

Based on the same design procedure and system architecture, a high efficiency thermal energy harvesting system has been designed to power a wirelessly controlled radiator valve. This is the second case study to show that the proposed system can be easily expanded to harvest other types of energy source such as thermal energy. Unlike the solar energy harvesting system, the harvest efficiency was initially quite low. Based on the TE generator model, a lot of efforts have been carried out to improve system efficiency. By integrating the classical P&O MPP approach based power conversion subsystem with the power management unit together, the entire thermal energy harvesting system has been developed. The evaluation results show that the system can efficiently harvest thermal energy from the radiator and the system has a perpetual lifetime by using a power management unit.

In summary, this thesis has achieved all of the proposed objectives described in Chapter 1. Future work in enhancing the lifetime of WSN based on energy harvesting systems should focus on the following parts.

Firstly, in this thesis, based on the proposed energy harvesting model and the design procedure, only solar energy and thermal energy have been considered. In future work, other common environmental energy sources such as vibration and radio frequency energy should be considered. The proposed design procedure for designing energy harvesting systems can be followed.

Secondly, the proposed energy harvesting system model only can predict the system performance of solar and thermal sources. In future work, the system model needs to expand in order to accept other kinds of energy harvesting technologies, such as RF energy harvesting, vibration and so on.

Thirdly, the circuitry efficiency is critical in deciding the entire system efficiency. Since the efficiency is the core part of any micro energy harvesting system, further research could be focused on how to improve the efficiency and reduce the size of the MPPT circuit and the power management circuit. Moreover, several commercially available DC-DC boost converters with built-in MPPT algorithm have been step into the market. In this thesis, the proposed MPPT based power conversion circuits have not been compared with these devices. In the future work, the commercial power conversion circuits and the proposed MPPT based power conversion circuits should be compared in order to examine the energy efficiency, power overhead, cost and size of these systems.

Finally, in this thesis, the author only considered how to use energy harvesting technologies to improve the lifetime of the individual sensor node in a WSN. As the network lifetime is more important and more realistic for a WSN, future study can focus on how to use energy harvesting technologies to extend the whole network lifetime.

References

- [1] Madden, S., Franklin, M.J., Joseph M. Hellerstein, J.M. and Hong, W., “ Tag a tiny aggregation service for ad-hoc sensor networks”, The fifth symposium on on Operating systems design and implementation (OSDI’02), Volume 36, pp 131-146, 2002.
- [2] Akyildiz, I.F., Su, W., Sankarasubramaniam, Y. & Cyirci, E., "A Survey on Sensor Networks", IEEE Communications Magazine, Vol. 40, No. 8, pp. 102-114, 2002.
- [3] Ganeriwal, S., Ganesan, D., Shim, H., Tsiatsis, V. and Srivastava, M.B., “Estimating Clock Uncertainty for Efficient Duty-cycling in Sensor Networks,” in Proc. Third ACM Conference on Sensor Networking Systems, pp. 130–141, 2005.
- [4] Dutta, P., Grimmer, M., Arora, A., Bibyk, S. and Culler, D., “Design of a Wireless Sensor Network Platform for Detecting Rare, Random, and Ephemeral Events,” in In The 4 th International Conference on Information Processing in Sensor Networks, pp. 497–502, 2005.
- [5] Liu, H., Chandra, A. and Srivastava, J., “eSENSE: Energy Efficient Stochastic Sensing Framework for Wireless Sensor Platforms,” in Proc. Fifth International Conference on Information Processing in Sensor Networks, pp. 235–242, 2006.
- [6] Gnawali, O., Jang, K.Y., Paek, J., Vieira, M., Govindan, R., Greenstein, B., Joki, A., Estrin, D. and Kohler, E., “The Tenet Architecture for Tiered Sensor Networks,” in Proc. 4th International Conference on Embedded Networked Sensor Systems. ACM, pp. 153–166, 2006.
- [7] Kumar, S., Lai, T.H. and Balogh, J., “On k-coverage in a Mostly Sleeping Sensor Network,” Wireless Networks, vol. 14, no. 3, pp. 277–294, 2008.
- [8] Ye, W., Heidemann, J. and Estrin, D., “An Energy-efficient MAC Protocol for Wireless Sensor Networks,” in INFOCOM 2002. Proc. Twenty-First Annual Joint Conference of the IEEE Computer and Communications Societies., vol. 3, pp. 1567–1576, 2002.
- [9] Heinzelman, W., Chandrakasan, A. and Balakrishnan, H., “Energyefficient Communication Protocol for Wireless MicroSensor Networks,” in Proc. 33rd Annual Hawaii International Conference on System Sciences., p p. 8020. vol.8, 2000.
- [10] Abusaimh, H., “ Energy-Aware Routing Protocols in Wireless Sensor Networks”, A doctoral thesis of Loughborough University, 2009.
- [11] Liu, W.L., Wang, Y., Liu, W., Ma, Y.C., Xie, Y., and Yang, H.Z., “ On chip hybrid power supply system for wireless sensor nodes” , Design Automation Conference (ASP-DAC), PP. 43-48, 2011.
- [12] Howell D., “ Progress Report for Energy Storage Research and Development”, U.S. Department of energy office of Vehicle technologies.
- [13] Tester, J.W., “Energy Transfer and Conversion Methods”, Sustainable Energy Lecture Notes, Topic on Energy Storage Modes, MIT, 2005.
- [14] Blomgren, G.E., “Perspectives on portable lithium ion batteries liquid and polymer electrolyte types”, Seventeenth Annual Battery Conference on Applications and Advances, pp.141-144, 2002.
- [15] Paradiso, J.A. and Starner, T., “Energy scavenging for mobile and wireless electronics”, IEEE Pervasive Computing, vol.4, issue 1, pp.18-27, 2005.

- [16] Mathna, C., O'Donnell, T., Martinez-Catala, R.V., Rohan, J. and Brendan, O., "Energy scavenging for long-term deployable wireless sensor networks", vol.75, no.3, pp.613-623, 2008.
- [17] Thomas, J.P., Qidwai, M.A. and Kellogg, J.C., "Energy scavenging for small scale unmanned systems", *Journal of Power Sources*, vol.159, pp.1494-1509, 2006.
- [18] Szewczyk, R., Polastre, J. Mainwaring, A.M., and Culler D.E., "Lessons from a sensor network expedition", In proceedings of EWSN 2004, PP. 307-322, 2004.
- [19] Sudevalayam S. and Kulkarni P., "Energy harvesting sensor nodes: Survey and implications," *IEEE Communications Surveys & Tutorials*, vol. PP, no. 99, pp. 1-19, 2010.
- [20] Kansal, A., Hsu, J. Zahedi, J. and Srivastava, M.B., "Power Management in Energy Harvesting Sensor Networks," *Trans. Embedded Computing Systems*, vol. 6, no. 4, pp. 32-37, 2007.
- [21] Wan Z.G., Tan Y.K. & C. Yuen, "Review on Energy Harvesting and Energy Management for Sustainable Wireless Sensor Networks", *IEEE International Conference on Communication Technology (ICCT2011)*, PP. 363-367, 2011.
- [22] Tan, Y.K., "Analysis, Design And Implementation of Energy Harvesting Systems For Wireless Sensor nodes", PHD thesis of National University Of Singapore, 2010.
- [23] Jeong, J. "A practical theory of micro-solar power sensor networks," Ph.D. dissertation, EECS Department, University of California, Berkeley, 2009.
<http://www.eecs.berkeley.edu/Pubs/TechRpts/2009/EECS-2009-49.html>
- [24] Randall J.F. & Jacot J., "Is AM1.5 applicable in practice Modelling eight photovoltaic materials with respect to light intensity and two spectra", *Renewable Energy*, vol.28, issue.12, pp.1851-1864, 2003.
- [25] Green M.A, Emery K., Hisikawa Y. & Warta W., "SHORT COMMUNICATION Solar cell efficiency tables (version 37)", *Progress in Photovoltaics: Research and Applications*, vol.15, issue.5, pp.84-91, 2010.
- [26] Jiang, X., Polastre, J., and Culler, D., "Perpetual Environmentally Powered Sensor Networks," in *Fourth International Symposium on Information Processing in Sensor Networks.*, pp. 463-468, April 2005.
- [27] Taneja, J., Jeong, J., and Culler, D., "Design, Modeling, and Capacity Planning for Micro-solar Power Sensor Networks," in *Proc. 7th International Conference on Information Processing in Sensor Networks*, 2008, pp. 407-418.
- [28] Raghunathan, V., Kansal, A., Hsu, J., Friedman, J., and Srivastava, M., "Design Considerations for Solar Energy Harvesting Wireless Embedded Systems," *Fourth International Symposium on Information Processing in Sensor Networks*, pp. 457-462, April 2005.
- [29] Park, C. and Chou, P., "AmbiMax: Autonomous Energy Harvesting Platform for Multi-Supply Wireless Sensor Nodes," *3rd Annual IEEE Communications Society on Sensor and Ad Hoc Communications and Networks*, vol. 1, pp. 168-177, Sept. 2006.
- [30] Simjee F. and Chou, P.H., "Everlast: Long-life, Super-capacitor-operated Wireless Sensor Node," in *Proc. 2006 International Symposium on Low Power Electronics and Design. ACM*, pp. 197-202, 2006.
- [31] Stanley-Marbell, P. and Marculescu, D., "An 0.9×1.2 Low Power, Energy-harvesting System with Custom Multi-channel Communication Interface," in *Proc. Conference on Design, automation and test in Europe. EDA Consortium*, pp. 15-20, 2007.
- [32] Laurier S., "Experimental analysis of photovoltaic energy scavengers for sensor nodes", Master thesis of University of Ghent, 2007.

- [33] Hill, J.L. and Culler, D.E., "Mica: A Wireless Platform for Deeply Embedded Networks," IEEE Micro, vol. 22, no. 6, pp. 12–24, 2002.
- [34] Polastre, J., Szewczyk, R. and Culler, D., "Telos: Enabling Ultra-low Power Wireless Research," in Fourth International Symposium on Information Processing in Sensor Networks, pp. 364–369, 2005.
- [35] JN5139 Data Sheet, 2009.
http://www.jennic.com/download_file.php?supportFile=JN-DS-JN5139MO-1v5.pdf
- [36] Venkatasubramanian, R., Siivola, E., Colpitts, T. and O'Quinn, B., "Thin-film thermoelectric devices with high room temperature figure of merit", Nature, Volume 413, Page(s) :597-602, 2011.
- [37] Kushch, A.S, Bass, J.C. and Eisner, N.B., "Thermoelectric development at Hi-Z technology", International conference on Thermoelectrics, 2001. Proceeding ICT2001. PP. 422-430, 2001.
- [38] Whalen, S.A., Apblett, C. A., and Aselage, T.L., "Improving power density and efficiency of miniature radioisotopic thermoelectric generators", ScienceDirect, Journal of power sources Volme 180, PP. 657-663, 2008.
- [39] Chen, L.G., Sun, F.R. and Wu, C., "Thermoelectric-generator with linear phenomenological heat-transfer law", ScienceDirect, Applied Energy, Volume 81, pp. 358-364, 2005.
- [40] Chen M., Rosendahl, L.A, Condra, T.J. and Pedersen, J.K., "Numerical modeling of Thermoelectric Generators with varing material properties in a circuit simulator", IEEE transactions on Energy conversion, Volume 24, Issue:1, pp. 112-124, 2009.
- [41] Nuwayhid, R.Y., Moukalled, F. and Noueihed, N., "On entropy generation inthermoelectric devices", Energy conversion & Management, Volume 41, pp. 891-914, 2000.
- [42] Gao M. and Rowe, D.M., "Conversion efficiency of thermoelectric combustion systems", IEEE. Transations of Energy Convers. 22 pp 528–534, 2007..
- [43] Lineykin, S. and Ben-Yaakov, S., "Modeling and analysis of thermoelectric modules", Industry Applications, IEEE Transactions on, Volume 43, Issue:2, pp. 505-512, 2007.
- [44] Altazin, S., Raphael, C. and Gwoziecki, R., "Analytical modeling of the contact resistance in top gate/bottom contact organic thin film transistors", Organic Electronics, pp.897-902, 2011
- [45] International Rectifier application note AN-1057, 2009,
http://www.freescale.com/files/microcontrollers/doc/app_note/AN1057.pdf
- [46] Marotta, E.E, Lafontant, S., McClafferty, D. and Mazzuca, S., " The Effect of Interface Pressure on Thermal Joint Conductance for Flexible Graphic Materials: Analytical and Experimental Study", the eighth Intersociety Conference on Thermal and Thermomechanical Phenomena in Electronic systems, pp. 663-670, 2002.
- [47] Wang, H., Hu, X.J., and Ng, K.M., "Reducing thermal contact resistance using a bilayer aligned CNT thermal interface material", Chemical Engineering Science Volume 65, pp.1101-1108, 2010.
- [48] Antonetti, V.W., Whittle, T.D., and Simons, R.E., "An approximate thermal contact conductance correlation", Journal of Electonic Packaging, Volume 115, Issue 1, pp. 131-135, 1993..
- [49] Hebei LTD, Thermoelectric cooler TEC1-12706, 2008,
<http://www.hebeiltd.com.cn/peltier.datasheet/TEC1-12706.pdf>.
- [50] Lineykin, S., and Yaakov, S.B., "SPICE Compatible Equivalent Circuit of the Energy Conversion Processes in Thermoelectric Modules", 23rd IEEE Israel Convention, pp. 346-349, 2004.

-
- [51] Egea-Lopez, E., Vales-Alonso, J., Martinez-Sala, A., Pavon-Mario, P. and J. Garcia-Haro, "Simulation scalability issues in wireless sensor networks," *IEEE Communications Magazine*, vol. 44, pp. 64-73, 2006.
- [52] Merrett, G. V., White, N., Harris, N., and Al-Hashimi, B., "Energy-Aware Simulation for Wireless Sensor Networks", In Proceedings of the 6th Annual IEEE Communications Society Conference on Sensor, Mesh and Ad Hoc Communications and Networks, pp.111-123, 2009.
- [53] Weddell, A.S., Merrett, G.V., Harris, N.R. and White,N.M., "Energy devices for sensor networks: Properties for simulation and deployment," in 1st International Conference on Wireless Communication, Vehicular Technology, Information Theory and Aerospace & Electronic Systems Technology, pp. 26–30, 2009.
- [54] Kruger, D., Buschmann, C. and Fischer, S., "Solar Powered Sensor Network Design and Experimentation," in 6th International Symposium on Wireless Communication Systems, pp. 11–15, 2009.
- [55] Kimball, J.W., Kuhn, B.T. and Balog, R.S., "A System Design Approach for Unattended Solar Energy Harvesting Supply," *IEEE Transactions on Power Electronics*, vol. 24, no. 4, pp. 952–962, 2009.
- [56] Taneja, J., Jeong, J. and Culler, D., "Design, modeling, and capacity planning for micro-solar power sensor networks," in Proceedings of the 7th international conference on Information processing in sensor networks, pp. 407–418, 2008.
- [57] Bader, S., Scholzely T. and Oelmann, B. "A Method for Dimensioning Micro-Scale Solar Energy Harvesting Systems Based on Energy Level Simulations", 2010 IEEE/IFIP International Conference on Embedded and Ubiquitous Computing, pp 372-379, 2010.
- [58] Lu, C., Raghunathan, V. and Roy, K., "Maximum Power Point Considerations in Micro-Scale Solar Energy Harvesting Systems", Fourth international symposium on information processing in sensor networks, pp. 273-276, 2005.
- [59] Xiao, W., Dunford, W. G. and Capel, A. "A novel modeling method for photovoltaic cells," in IEEE 35th Annual Power Electronics Specialists Conference, pp. 1950–1956, 2004.
- [60] Dezso, S., Remus, T. and Pedro, R., " PV panel model based on datasheet values", IEEE International Symposium on Industrial Electronics, pp. 2392-2396, 2007.
- [61] Farivar, G. and Asaei, B, "Photovoltaic module single diode model parameters extraction based on manufacturer datasheet parameters", 2010 IEEE International Conference on Power and Energy, pp. 929-934, 2010.
- [62] Villalva, M. G., Gazoli, J.R., and Filho, E.R., "Comprehensive Approach to Modeling and Simulation of Photovoltaic Arrays", *IEEE Trans. Power Electronics*, **24**, no. 5, pp. 1198-1208, 2009.
- [63] Petreus, D., Ciocan, I. and Farcas, C., "An improvement on empirical modeling of photovoltaic cells", 31st International Spring Seminar on Electronics Technology, Pp. 598-603, 2009.
- [64] SANY amorphous solar cell AM-5412, 2008,
<http://www.msc-ge.com/download/sanyo/glass/AM-5412.pdf>
- [65] Esram, T., Illinois U., Urbana, IL., and Chapman, P.L., " Comparison of Photovoltaic Array Maximum Power Point Tracking Techniques", *IEEE transactions on Energy conversion*, Issue: 2, Volume 22, pp. 439-449, 2007.
- [66] Liu, X., Lu, F., Diao, D., Guo, S., and Chang, Y., "Comprehensive power analysis and efficiency optimum design for step-up DC-DC converters", *IEEE Asia Pacific Conference on Circuits and system*, pp. 1868-1871, 2008
- [67] Aloisi, W., and Palumbo, G., " Efficiency model of boost dc-dc PWM converters", *International Journal of circuit theory and applications*, pp. 419-432, 2005.

- [68] Ribes-Mallada, U., Leyva, R. and Garces, P., "Optimization of DC-DC converters via geometric programming", *Mathematical problems in Engineering*, Volume 2011, pp.122, 2011.
- [69] Zhang, Y. and Yang, H. "Modeling and characterization of supercapacitors for wireless sensor network applications", *Journal of Power Sources*, Volume 196, Issue 8, Page(s) 4128-4135, 2011.
- [70] Guan, M.J. and Liao, W.H., "Characteristic of Energy Storage Devices in Piezoelectric Energy Harvesting Systems", *Journal of Intelligent Material Systems and Structures*, Vol. 19, PP 671-680, 2008.
- [71] Panasonic 22F super-capacitor, 2008,
<http://www.panasonic.com/industrial/components/pdf/ABC0000CE8.pdf>
- [72] MIT Electric Vehicle Team, "A guide to understanding battery specifications", 2008,
http://mit.edu/evt/summary_battery_specifications.pdf
- [73] Gomadam, P.M., Weidner, J.W., Dougal, R. A. and White, R.E., "Mathematical modeling of lithium-ion and nickel battery systems," *J. Power Sources*, vol. 110, no. 2, pp. 267–284, A 2002.
- [74] Rong, P. and Pedram, M., "An analytical model for predicting the remaining battery capacity of lithium-ion batteries," in *Proc. Design, Automation, and Test in Europe Conf. and Exhibition*, pp. 1148–1149, 2003.
- [75] Rakhmatov, D., Vruthula, S. and Wallach, D.A. "A model for battery lifetime analysis for organizing applications on a pocket computer," *IEEE Trans. VLSI Syst.*, vol. 11, no. 6, pp. 1019–1030, 2003.
- [76] Benini, L., Castelli, G., Macci, A., Macci, E., Poncino, M. and Scarsi, R. "Discrete-time battery models for system-level low-power design," *IEEE Trans. VLSI Syst.*, vol. 9, no. 5, pp. 630–640, 2001.
- [77] Buller, S., Thele, M., Doncker, R. W. D. and Karden, E., "Impedancebased simulation models of super-capacitors and Li-ion batteries for power electronic applications," in *Conf. Rec. 2003 Ind. Appl. Conf.*, vol. 3, pp. 1596-1600, 2003.
- [78] Valvo, M., Wicks, F.E., Robertson, D. and Rudin, S., "Development and application of an improved equivalent circuit model of a lead acid battery," in *Proc. Energy Convers. Eng. Conf.*, vol. 2, pp. 1159–1163. 1996.
- [79] Chen M. and Rincon-Mora, G. A., "Accurate Electrical Battery Model Capable of Predicting Runtime and I-V Performance", *IEEE Transactions on Energy Conversion*, vol. 21, no. 2, pp. 504-511, 2006.
- [80] Simunic, T., Benini, L., and Micheli, G.D., "Energy-Efficient Design battery-powered embedded systems", *IEEE Transactions on very large scale integration systems*, VOL.9 No.1, pp. 15-28, 2001.
- [81] Windarko, N.A., Choi, J., and Hyun, D., "SOC Estimation based on OCV for Continuous Charging/Discharging Process in NiMH Battery," *2nd Japan-Korea Workshop Joint Technical Workshop*, pp. 1-6, 2009.
- [82] DURACELL HR03 NiMH rechargeable battery, 2008,
http://www.bemoredog.cz/downloads/datasheets/product/Chargers/Chargers_Mini_Charger.pdf

-
- [83] Jennic DR1048 Controller Board, 2008,
http://www.jennic.com/files/support_files/JN-RM-2007-DR10480-Controller-Board-1v10.pdf
- [84] Kansal, A., Hsu, J. Zahedi, S. and Srivastava, M. B. ,“Power Management in Energy Harvesting Sensor Networks,” ACM Trans. Embed. Comput. Syst., vol. 6, no. 4, pp. 32, 2007.
- [85]Linear technology LTC1440, 2008,
<http://cds.linear.com/docs/Datasheet/144012fd.pdf>
- [86] PIC16F688, 2008
<http://ww1.microchip.com/downloads/en/devicedoc/41203b.pdf>
- [87] Max890L, High-side P-channel switch, 2007
<http://www.datasheetcatalog.org/datasheet/maxim/MAX890L.pdf>
- [88] Fairchild, FDS9933A, P-MOSFET, 2007
<http://www.fairchildsemi.com/ds/FD/FDS9933.pdf>
- [89] 62000P Series Programmable DC Power Supply, 2008
<http://www.chromausa.com/pdf/62000P-E.pdf>
- [90] Tanouti,J., Aziz, A. and Aziz, E.M.,“Design and implementation of DC-DC boost converter based on an analog MPPT technology”, EFEEA’s 10 International Symposium on Environment Friendly Energies in Electrical Applications, PP. 1-5, 2010.
- [91] Hasaneen, B.M. and Elbaset, A.A., “Design And Simulation of DC/DC Boost Converter” The Twelfth International Middle East Power System Conference, MEPCON’2008, South Valley University, Faculty of Eng., Aswan, Egypt, Vol. I, pp.335-340, 2008.
- [92] Masoum, M. A. S.,Dehbonei, H. and Fuchs, E. F."Theoretical and experimental analyses of photovoltaic systems with voltage and currentbased maximum power-point tracking," IEEE Trans. Energy Conversion, vol. 17, pp. 514-522, Dec. 2002.
- [93] Bekker B.and Beukes, H.J., "Finding an optimal PV panel maximum power point tracking method," in 7th AFRICON Conf. in Africa, pp. 1125-1129, 2004.
- [94] ESRAM, E. and Chapman, P.L.“Comparison of photovoltaic array maximum power point tracking techniques”, IEEE Transactionson Energy Conversion, vol. 22, No. 2, pp. 439-449, 2007.
- [95] Shao, H. Tsui, C.Y.and Ki, W. H. ,“The design of a micro power management system for applications using photovoltaic cells with the maximum output power control”, IEEE Transactions on Very Large Scale Integration (VLSI) Systems, vol. 17, pp. 1138-1142, 2009.
- [94] Sera, D.,Kerekes, T., Teodorescu, R. and Blaabjerg, F.,“Improved MPPT method for rapidly changing environmental conditions,” in Proc. IEEE ISIE, pp. 1420–1425, 2006
- [95] Hamamatsu technology, S1087 photodiode, 2009
<http://www.farnell.com/datasheets/104399.pdf>
- [96] 29L103C Inductor, 2007
http://www.murata-ps.com/data/magnetics/kmp_2900l.pdf

- [97] Pallo, R.C., N.A., Chan, W.R., Perreault, D.J., and Celanovic, I.L., “Low-power maximum power point tracker with digital control for thermophotovoltaic generators,” 25th IEEE Applied Power Electronics Conference, pp. 961–967, 2010.
- [98] Hohm, D.P. and Ropp, M.E., “Comparative study of Maximum Power Point Tracking algorithms”, Progress in Photovoltaics: Research and application, PP. 47-62, 2003.
- [99] Kar, K., Krishnamurthy, A. and Jaggi, N. “Dynamic Node Activation in Networks of Rechargeable Sensors,” IEEE/ACM Trans. Networking, vol. 14, no. 1, pp. 15–26, 2006.
- [100] Gatzianas, M., Georgiadis, L. and Tassiulas, L., “Control of wireless networks with rechargeable batteries,” IEEE Trans. Wireless Commun., vol. 9, no. 2, pp. 581–593, 2010.
- [101] Kansal, A., Hsu, J., Zahedi, S. and Srivastava, M. B. ,“Power Management in Energy Harvesting Sensor Networks,” ACM Trans. Embed. Comput. Syst., vol. 6, no. 4, pp. 1-35, 2006.
- [102] Hsu, J., Zahedi, S., Kansal, A., Srivastava, M., and Raghunathan, V., “Adaptive duty cycling for energy harvesting systems”, Proc. ACM/IEEE International Symposium on Low Power Electronics and Design (ISLPED), pp. 180-185, 2006.
- [114] Vigorito, C.M., Ganesan, D. and Barto, A.G., “Adaptive Control of Duty Cycling in Energy-Harvesting Wireless Sensor Networks,” in Proc. IEEESECON’07, San Diego, CA, pp. 21–30, 2007.
- [115] Aman Kansal, Jason Hsu, Mani B Srivastava, and Vijay Raghunathan. Harvesting aware power management for sensor networks. In 43rd Design Automation Conference (DAC), pp 112-118, 2006.
- [116] Solar irradiance calculator, 2011
<http://www.efficientenergysaving.co.uk/solar-irradiance-calculator.html>
- [117] Leicester weather station, 2012
<http://www.stormtrack.co.uk/Pages/Climateyr.aspx>
- [118] Humida,G.B., Ekuakille, A.L., Kachouri, A., Ghariani, H. and Trotta, A., “Extracting electric power from human body for supplying neural recording system”, International Journal on Smart Sensing and Intelligent system, Vol.2.No.2, pp. 230-245, 2009.
- [119] Mastbergen, D., Willson, B., and Joshi, S., “Producing Light from stoves using a thermoelectric generator, Engines and Energy conversion laboratory, Department of Mechanical Engineering, Colorado state University, pp 1-25, 2005
<http://www.bioenergylists.org/stovesdoc/ethos/mastbergen/Mastbergen ETHOS 2005.pdf>
- [120] Meydbray,Y., Singh, R., and Shakouri, A., “Thermoelectric module construction for low temperature gradient power generation”, International Conference on THERMOELECTRICS, pp 348-351 , 2005.
- [121] Auras's 3 U heat sink, 2007,
<http://auras.com.tw/ppdtview.asp?nid=230>
- [122] Seiko Instrumetns, S-882Z Ultra-Low Voltage operation charge pump, 2010,
<http://www.Eet-china.col11/ARTI VLES/2006MA Y/PDF/S882Z E.pdf>

-
- [123] Mateu, L., Codrea, C., Lucas, N., Pollak, M., Spies, P., “Energy harvesting for wireless communication systems using thermogenerators,” in Proc. of the XXI Conference on Design of Circuits and Integrated Systems (DCIS), Barcelona, Spain, pp.22–24, 2006.
- [124] Omega CO-I thermocouples, 2010,
<http://www.ll11ega.co.uk/Temperature/pdf/CO-k.pdf>
- [125] Aluminium Conductivity,2010,
http://www.ndt.ed.org/GeneralResources/MaterialProperties/ET/Conductivity_Al.pdf
- [126] Dan, M., Bryan, W., and Sachin, J., “Producing light from stoves using a thermoelectric generator”, Engineer and Energy conversion laboratory, Department of Mechanical Engineering, Colorado state university, 2005
http://www.bioenergylists.org/stovesdoc/ethos/mastbergen/Mastbergen_ETHOS_2005.pdf
- [127] SPV1020, 2010,
http://www.st.com/internet/com/TECHNICAL_RESOURCES/TECHNICAL_LITERATURE/DATASHEET/CD00275733.pdf
- [128] LTC3105, 2010,
<http://cds.linear.com/docs/Datasheet/3105fa.pdf>
- [129] SM72441, 2010,
<http://www.ti.com/lit/ds/symlink/sm72441.pdf>